Numerical and experimental analysis on microbubble generation and multiphase mixing in novel microfluidic devices

A dissertation submitted in the partial fulfilment of the requirements for

transfer to the degree of

Doctor of Philosophy

December 2017

by

Xiang Pan

Department of Mechanical Engineering

University College London

Torrington Place, London WC1E 7JE, UK

Contents

Table of tables

Table of figures

List of notations

m,m_{in},m_{out}	total mass, mass in/out of the object	μ, μ_l, μ_G	dynamic viscosity of the fluid
ρ, ρ_l	density of the fluid	v, v_l	velocity of the fluid
I	diagonal unit matric	ε,ε_{ij}	shear stress
f_{in}	internal forces	p	static pressure
τ_{ij}	viscous stress	c_v, c_p	specific heat of constant volume/pressure
γ	ratio of specific heats	M	Mach number
x,x_i,x_j	spatial coordinate	$\hat{n}$	unit vector normal at the interface
κ	curvature of the interface	σ	surface tension coefficient
$\delta(\Gamma, x)$	Dirac delta function	L	characteristic length scale/length of the immiscible slug
t	time scale	U, u,u_p,u_c,u_1,u_2	characteristic velocity or
		u_i, u_j	superficial velocity
ζ	molecular mean free path	ϕ, ϕ_f	scalar quantity or scalar quantity at the face
χ	void fraction	Δt,Δt^{n+1},Δt^n	time step
V, V_{P_C}	cell volume	f	cell face quantity as subscript
D_f	face diffusion term	0,1	quantity of cell-0 and cell-1 as subscript
m_f	face mass flow rate	Γ	interface
D	face diffusivity coefficient	v, v_l, v_g, v_f	velocity, grid/face velocity
x	position vector	G, G_f	grid flux

S_ϕ, S_f	source term	α	gradient limiting factor
ω	weighting factor	r	reconstructed value as subscript
$\hat{a}$, $\hat{a}_f$	face area/cell face surface vector	s	vector between cell face and cell centroids
v_{ls}	the contour level or isosurface value	Ω_1,Ω_2	two regions occupied by fluids
α_i	volume fraction of the i th phase	ρ_i	density of the i th phase
μ_i	molecular viscosity of the i th phase	$(c_p)_i$	specific heat of the i th phase
V_i	volume of the i th phase	S_{α_i}	source or sink of the i th phase
C_θ	angle factor	$D\rho_i/Dt$	material or Lagrangian derivative of the i th phase
ε_f, ε_C	normalized face value, central value	C_u, C_{u_l}, C_{u_u}	local Courant number
θ_w, θ_c	contact angle at the wall	θ	angle between the normal to the interface
h	liquid height	$\hat{n}_w$, $\hat{t}_w$	unit vectors normal and tangential to the wall
R	channel radius	g	gravitational acceleration
l, L	length scale or size of the given system or object	a	diameter of the particle
S	closed surface or cross-sectional area of the moving particle	f_{drag}	viscous drag coefficient
T	temperature	k	Boltzmann constant
Δp,ΔP_G	pressure drop	Q,Q_{in},Q_{out},Q_p,Q_c	volumetric flow rate in the pipe/capillary

w	width of the channel	β	constant of order one depending on geometry
l	bubble size	F_v,F_c	viscous force and capillary force
d	diameter of the pipe, channel	VBN	viscosity blending number
η	kinematic viscosity	C	viscometer constant
y_i	weight fraction of each component of the blend	A,A_p,A_c,A_1,A_2	cross-sectional of the pipe/capillary
$\hat{t}$	unit vector in the tangential direction to the interface	α_D, α_C, α_U, α_f	nodal variable values for the downwind, central, and upwind positions
$(\nabla\sigma)_t$	gradient of surface tension coefficient in tangential direction	f_{st}, f_σ, $f_{\sigma,n}$, $f_{\sigma,t}$	surface tension force, surface tension in normal direction, surface tension in tangential direction
m_b,m_t	mass of empty density bottle, mass of density bottle and solution	v_b	specific volume of solution in the density bottle
Re	Reynolds Number	φ	level set function
Δt	time step		

Abstract

In this study, a novel K-junction microfluidic junction and a conventional cross-junction were investigated numerically and experimentally for microbubble generation and multiple fluids mixing. In the K-junction, liquid solutions were injected into the junction via three liquid inlet channels, along with inert nitrogen gas supplied via the gas inlet channel, to periodically generate microbubbles in a controlled manner at the outlet channel. Numerical simulations based on Finite Volume method and Volume of Fluid (VOF) technique and experiments of both the K-junction and the cross-junction were conducted. The effect of parameters such as contact angle, surface tension, viscosity, gas pressure and gas-liquid flow ratios on the microbubble size distribution was investigated. The process of microbubble generation, obtained through high speed camera imaging and the numerical simulation, has shown good agreement in both junctions as well as the influence of viscosity and gas-liquid flow ratios for the K-junction and cross-junction. It was indicated that parameters like solution viscosities, gas-to-liquid flow ratios, gas inlet pressure, and their combination have a significant influence on the microbubble diameter, which was found to be in the range of 70-240 μm when using micro capillaries of 100 μm inner diameter. The multiple fluids mixing study was investigated by using two or three different polymer solutions for the cross-junction and the K-junction respectively in simulations and experiments. It can be seen that the mixing process obtained from simulations agrees well with experimental results and chaotic mixing was found in the mixing area of the K-junction, with higher mixing efficiency than the cross junction. Fluorescent images of microbubbles generated by using polymer solutions with dyes inside have shown the devices' potential of encapsulating fluorescent dyes and polymers on the shell of bubbles and could be adopted as a method to encapsulate active pharmaceutical ingredients for potential applications in drug delivery.

Acknowledgements

The most important influence on the successful completion of this thesis has been two dear advisors, Prof. Mohan Edirisinghe, to whom I am deeply grateful for his support and guidance. He has had great professional influence on my development both in terms of human traits and professional scientific approach. As a mentor, he pushed to develop my weaknesses and exploit my strengths. Just like a father, he has his own way of directing the student into the right direction at the moments of cruciality. I would like to express my gratitude to Prof. Yiannis Ventikos with whom I started working in the all-new world of numerical simulation. I am grateful for his guidance as my second supervisor and friendly, warm character who always taught by inspiring me. His encouragement and motivation aroused my excitement, while for his boundless help and anytime assistance I am deeply grateful.

Life in the laboratory would be incomplete without friends and especially Keith Lau, inspiring me ever with their work discipline and helped with overcoming problems that often occur during the timespan of a thesis work. I would like to dearly thank Anjana Kothandaraman with whom we shared many moments and many common ideas. Many thanks for all the dear people whom I could not mention one by one.

Finally, I am deeply grateful to my family. Without their support and encouragement, none of what I have accomplished would be possible.

Publications and Conference Presentations

1. Xiang Pan, Mohan Edirisinghe, Anjana Kothandaraman, etc, Preparing microbubbles: computational and experimental analyse of microfluidic K-junction, International Pharm. Tech. Conference, 4 Nov 2016, Poster.

2. Xiang Pan, Anjana Kothandaraman, Numerical analyse in novel microfluidic junction, Molecular Biology Summit, 20-21 Oct 2016, Poster.

3. Xiang Pan, Yiannis Ventikos, Mohan Edirisinghe, Numerical and experimental analyse into a novel microfluidic K-junction, UCL Mechanical Engineering PhD Students Conference ’14, 17 July 2014, Oral Presentation and Poster.

4. Xiang Pan, Ahmet Alptekin Topcu, Mohan Edirisinghe, Yiannis Ventikos, Numerical and experimental investigation of multiphase flow in a novel microfluidic K-junction, Lab on a chip (under review).

Chapter 1 : Introduction

1.1 Background

1.1.1 Microbubble applications

Microbubbles are very small bubbles, with diameters under 100µm, that and have been investigated for various applications such as biomedical engineering, food science, cosmetic and agriculture technologies (Gordillo et al. 2004; Park et al. 2010; Kiessling et al. 2012; Blomley et al. 2001; Xu et al. 2008; Sirsi et al. 2009). The properties of the microbubbles like size, monodispersity, surface functionalization and stability for these applications vary a lot according to the requirements (Stride et al. 2009; Unger et al. 2001; Stride and Edirisinghe 2008). The ultrasound response character of microbubbles makes them possible to be used as contrast ultrasound imaging, molecular imaging and targeted drug and gene delivery (Sirsi et al. 2009). Microbubbles consisting of a gas core stabilized by a liquid shell and with controlled diameters less than 10µm (approximately equal to the size of a red blood cell) can pass through microvessels and capillaries throughout the body and are therefore useful to theranostics. The gas core takes most of the microbubble volume and provides the mechanism for ultrasound backscatter and drug delivery. Due to the instability of microbubbles of this size in an aqueous solution (caused by surface tension effects), a shell comprised of surfactants, lipids, proteins, polymers or mixtures of these materials is used to stabilize the bubbles.

1.1.2 Droplet based microfluidics

Several methods have been developed to produce microbubbles such as sonication, ink-jet printing, coaxial electrohydrodynamic atomization and gyration (Farook et al. 2009; Kukizaki et al. 2007; Mahalingam et al. 2015; Xu et al. 2008). However, the main problem of these methods is the instability of producing totally monodisperse microbubbles. In contrast to other microbubble generation methods, microfluidic technology is one of the most promising ones to produce micirobubbles due to its capability of consistently generating monodisperse microbubbles. But the control of microbubble size becomes difficult with this technology because of the significant dependence on the size of capillaries used under the high viscosity solutions (Gunther et al. 2006). Microfluidic devices which can be manufactured with

different internal geometries in micrometer size can help to generate monodisperse microbubbles (Chen et al. 2009; De Menech et al. 2008).

Several designs can be found in the latest literature for microfluidic devices to prepare monodisperse microbubbles and microdroplets by using two-phase fluids such as gas/liquid streams and two immiscible liquid streams. The main microfluidic devices used are cross-flowing devices for example T-junction (Zhang and Wang 2009; Xu et al. 2006a, b), flow focusing devices (Garstecki et al. 2005; Fu et al. 2009; Nie et al. 2008) and other co-flowing rupturing method dependent devices (Xiong et al. 2007), and the geometry controlled break up technique (Yasuno et al. 2004). For cross-flowing devices such as T-junctions, the continuous flow is sheared off by a dispersion flow in two perpendicular microchannels. The pressure drop through the bubble governs the break-up of gas-liquid threads and the ratio of the volumetric flow rates of the two fluids has significant influence on the bubble size (Xiong et al. 2007). While in terms of flow-focusing devices, two concentric channels are set upstream of a small orifice in order to produce a strong extensional flow and the bubble size is mainly determined by the size of the orifice integrated in the microchannles under specific conditions (Stone et al. 2004). Besides it can also generate drops which are produced by the break-up of threads with much smaller size than the orifice in other cases. Other co-flowing devices, used by Xiong et al. (2007), have a simple structure with only one splitter plate to separate the gas and liquid channel in a main microchannel so as to form bubbles and the bubble size is found to be dependent on the volumetric flow rate of gas and liquid as well.

A variety of experiments on controlling bubble size and uniformity generated in microfluidic devices have been conducted (Garstecki et al. 2005; Fu et al. 2009; Xiong et al. 2007; Yasuno et al. 2004; Xu et al. 2006a, b) and the factors which influence the bubble size are the ratio of gas/liquid flow rate, liquid viscosity and interfacial tension. Because of the controllability on bubble/droplet size and uniformity, also the cost-effectiveness and simplicity of the design, the T-junction is still one of the most widely used microfluidic device used to generate bubble and droplet. Research by using this T-junction has been developed in a variety of groups. For instance, Garstecki et al. (2006) described that the ratio of the gas/liquid rates is the main factor which influences the bubble size and the balance of hydrostatic pressure in the two immiscible fluids determines the break-up process of either the liquid or gaseous streams in the continuous fluids. Besides, Yamamoto et al. (2012)

conducted a visualization experiment to detect the effects of the T-junction size on bubble generation and air-water two-phase flow instability in 486 um circular mirochannels and reported that the bubble length can be predicted by a correlation derived from a scaling analysis which was invalid when the flow rate ratio of the two phases was either too high or too low as well as in the smallest T-junction. Investigation on the transition mechanism to the flow was analysed through the fluctuations in the Laplace pressure and water phase during the bubble generation process. In addition, Wang et al. (2013) used a co-flowing microfluidic device with propane, butane and air as the dispersed phases and different SDS-PEG solution as the continuous phases and the fluid dynamic mechanism of microbubble generation in a co-flowing microfluidic device was discussed. It was found that the average bubble diameters are dominated by the two-phase flow rates, the water phase viscosity and the experimental temperature, but independent of the gas component.

1.1.3 Numerical study on microfluidic devices

Numerical simulations of microbubble generation in microfluidics devices such as T-junction have been conducted with the aim to understand the mechanisms of the experiments. De Menech et al. (2008) investigated the dynamics of breakup of streams of immiscible fluids in a microfluidic T-junction by using a phase-field model to simulate numerically the flow of the two immiscible fluids at the T-junction. Three distinct regimes of formation of droplets were identified: squeezing, dripping and jetting and the influence factors which dominate each regime. Moreover, Rong et al. (2010) had applied a surface tension model which was improved by introducing a fourth order central difference scheme in Moving Particle Semi-implicit (MPS) method to simulate the microbubble generation in microchannel successfully and a good agreement with visualization experiment was achieved. Through the simulation in different microchannels they also found that bubble size will decrease with increasing liquid flow rate and increase with increasing gas flow rate. On the other hand, the latest research on numerical simulation of Taylor bubble formation in a microchannel with a microfluidic device by Dang et al. (2014) stated that they managed to use two different interface capturing methods implemented in ANSYS FLUENT (ANSYS, Inc., Canonsburg, Pennsylvania) which were Volume of Fluid (VOF) and Coupled Level Set and VOF (CLSVOF) method to simulate the bubble formation in a square microchannel with a converging shape mixing junction. It was

reported that the CLSVOF method was more accurate in capturing gas-liquid interface and the contact angle had affected the size of bubble length and shape.

1.2 Aim and Objectives of the research

Although conventional T-junction is widely used in generating microbubble and droplet, it is restricted to two fluids such as gas/liquid or two immiscible liquids. Inexpensive and simple method like lithography and wet etching (Garstecki et al. 2005; Zhang and Wang 2009) are commonly used to manufacture microfluidic devices, while the main drawback of the devices is the regular blockage and clogging of the flow channels which results in expensive cleaning process and replacement of the devices (Mustin and Stoeber 2008). The aim of this project is to investigate microbubble generation in novel microfluidic devices (K-junction and cross junction) created by embedded circular cross-section capillaries of fixed outer diameter in both experiments and numerical simulations. Therefore, less maintenance is required for generating bubbles/droplets in these devices so that blocked channels can be replaced by inserting new capillary tubes. More importantly, this novel K-junction is able to form bubbles/droplets contained multiple components layers with more than two phases of fluids mixing inside of the junction with high level control of bubble/droplet size. However, most of the previous numerical simulations on microfluidic devices were only focused on investigating microbubbles/droplets break-up mechanism and boundary conditions control over size variation with two-phase fluids in T-junction or other similar converging shape mixing junction fabricated by lithography and wet etching methods. In this project, numerical simulation was also aimed to study multiple fluids mixing during microbubble generation in these microfluidic devices.

The objectives of this project include conducting numerical simulations and experiments of mixing and bubble generating process by using microfluidic devices with multiple fluids (gas and three different liquids with different densities). The relationship between boundary conditions in bubble formation process and bubble size measured from simulation results was evaluated through numerical simulations. This novel circular capillary embedded microfluidic K-junction, which has a relatively bigger mixing area than conventional microfluidic junctions was used and several simulations were running under a variety of parameters especially gas/liquid flow ratio, surface tension, density and viscosity

were investigated numerically. Then experiments under relevant boundary conditions such as velocity and pressure inlet were conducted afterwards. The study on microbubble generation process and microbubble size distribution was investigated in detail by collecting videos inside of the microfluidic junctions captured by a high-speed camera and analysing microbubbles on glass slides produced by these junctions respectively. The results from both numerical method and experiment were compared so that the agreement and difference between them were presented. Thus, adjustments on both numerical and experimental methods were implemented to make sure good agreement on the findings was achieved. It will in return contributes to the establishing of a new numerical model based on this novel microfluidic K-junction and verifying the findings through experiment as well as modifying experiment procedures at the cost of less time and materials. Meanwhile, multiple fluids mixing process in both the K-junction and conventional cross-junction was investigated numerically. Therefore, a better understanding of the influence of the geometry structure of microfluidic device on multiple phase fluids mixing could be achieved and contribute to the improvement of this mixing process.

1.3 Structure of the thesis

This study aims to analyse microbubble generation mechanism and multiple fluids mixing processes with biodegradable polymers using various microfluidic devices like K-junction and cross junction. It is conducted through using computational fluid dynamic methods to simulate multiple fluids mixing and microbubble formation within these microfluidic devices, comparing with experimental results thus assessing the suitability and optimizing performance of a range of experimental conditions.

Chapter 1 starts with the background to the microbubble applications, microfluidic devices, numerical simulation that used to analyse microfluidic study, and summaries the aims and objectives of the research. The literature review is in Chapter 2, the numerical methods for microfluidic research on the slug/bubble/droplet and microbubble generation and microfluidic techniques in experiments are reviewed. Chapter 3 introduces the numerical methods applied in this study for the investigation of the K-junction and cross-junction in detail. The mathematic modelling, discretization methods, and interface tracking are illustrated. Chapter 4 describes the details of the experimental setup of the K-junction

including experimental materials, microfluidic junction design, and solution preparation methods used in the study. Chapter 5 introduces the preparation of numerical simulation of the K-junction. The geometry and mesh generation as well as the setup of numerical method such as Volume of Fluid were described. Validation simulation and grid dependence test were also mentioned. In Chapter 6, the influence of contact angle, surface tension and liquid viscosity on microbubble generation in the K-junction is discussed through numerical approach. The effect of the gas inlet pressure, liquid viscosity and gas-liquid flow ratio on microbubble formation in the K-junction is presented through experiments. The results and discussion obtained from experiments and numerical simulations of K-junction are finally presented and compared. Chapter 7 discusses the chaotic mixing process observed in the simulation of both K-junction and cross junction and multiple components distribution on microbubbles. Chapter 8 finalized the report with conclusions and future work.

Chapter 2 : Literature Review

2.1 Overview

This chapter provides the review of research into numerical and experimental methods of investigating this novel microfluidic K-junction. Among a series of numerical researches been proposed and developed for microbubble/droplet generation, it has been found that the finite volume and volume of fluid (VOF) methods are the most commonly adopted approaches for discretization and interface tracking in microfluidic study. In addition, experimental study on microbubble generation methods and mechanism have also been evaluated with their application of microbubbles produced by microfluidic devices being analysed.

Consequently, this chapter has covered numerical methods including Volume of Fluid, Level-Set and Lattice-Boltzmann method on simulations of bubble/slug and droplets generated by single-phase or two-phase fluids mixing in microfluidic devices in Section 2.2. The microbubble fundamentals have been reviewed in section 2.3 in different aspects including microbubble generation methods, principle, setup etc. This chapter is summarised in Section 2.4.

2.2 Numerical study on microfluidics

The numerical methods have been used by researchers to analyse the bubble/slug generation such as Volume of Fluid (VOF) method, Level-set method, and Lattice-Boltzmann method. In addition, numerical modelling is also used in the microfluidic study of slug flow which is defined as a gas-liquid flow where bubbles generated from. Therefore, a better understanding of the mechanism behind slug flow could be obtained and help analyse the bubbles/droplets formation. In 2005, Kashid et al. had conducted numerical modelling of single phase flow (internal circulation) and two-phase flow (slug flow) in a capillary microreactor. It was reported that the benefits of slug flow capillary microreactor shows that the ability to adjust two individual transport mechanisms such as convection inside the slug and diffusion between two consecutive slugs. Because of the shear between slug axis and continuous phase or capillary, internal circulation has increased the mass transfer rate. Moreover, the

circulation patterns of the slug also have a significant influence on designing a capillary microreactor. Despite of that, analysing the slug flow generation contributes to improving methodology to explore hydrodynamics and mass transfer inside of it. In their study, the investigation on the flow behaviour of each individual slug and generation of slug flow were conducted. The numerical simulations and experiments were carried out in a 120° Y-shaped mixing junction (Figure 2.1) made of PTFE (Poly-tera-fluoro-ethylene) with a diameter of 0.75mm at downstream and length of 1 m. Two piston high-precision piston pumps were connected to this junction and two different liquids were injected into it to generate liquid-liquid slug flow.

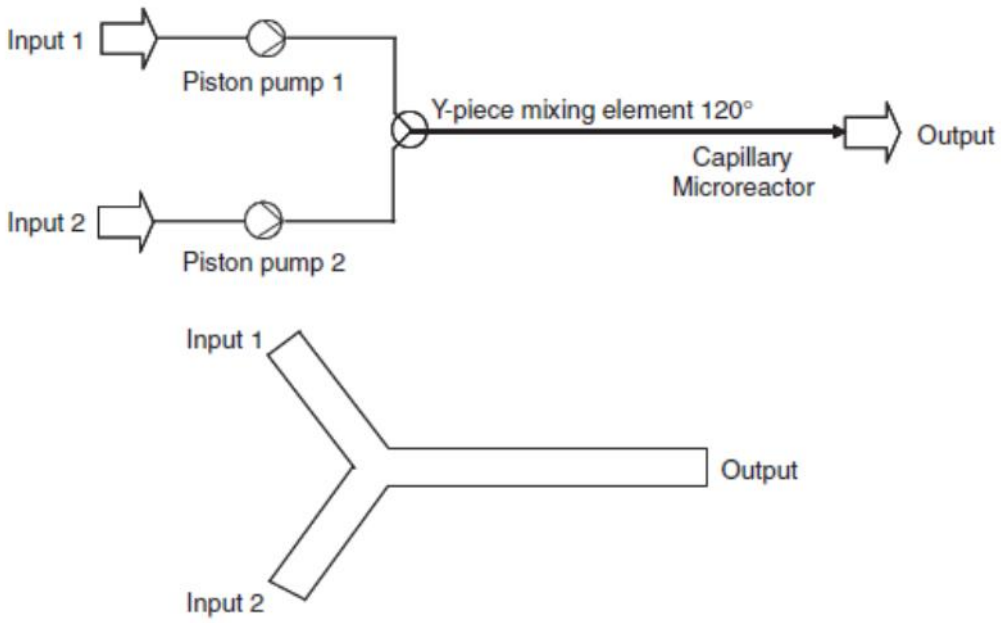

Figure 2.1 Experiment setup and simulation geometry of the Y-shaped mixing junction (Kashid et al. 2005).

The Volume of Fluid method was adopted to simulate the interface between different liquids and the numerical results of the effect on wall adhesion are shown in Figure 2.2 and 2.3.

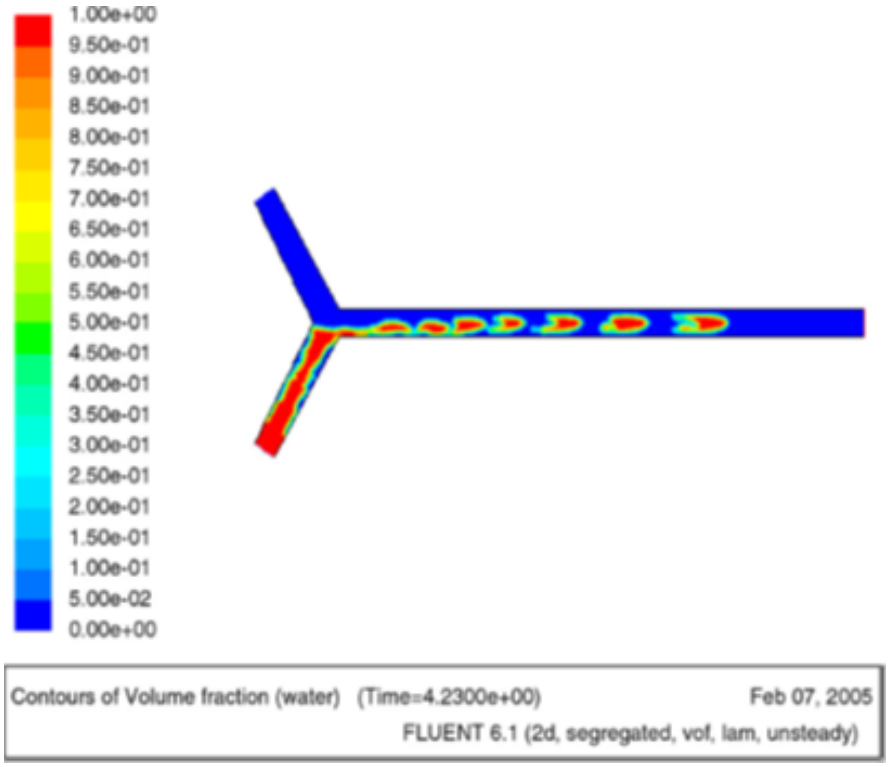

Figure 2.2 Flow simulation without wall adhesion in a Y-junction with diameter of 1 mm for oil-water system (liquid velocity u1=10 mm/s and u2= 10 mm/s) (Kashid et al. 2005).

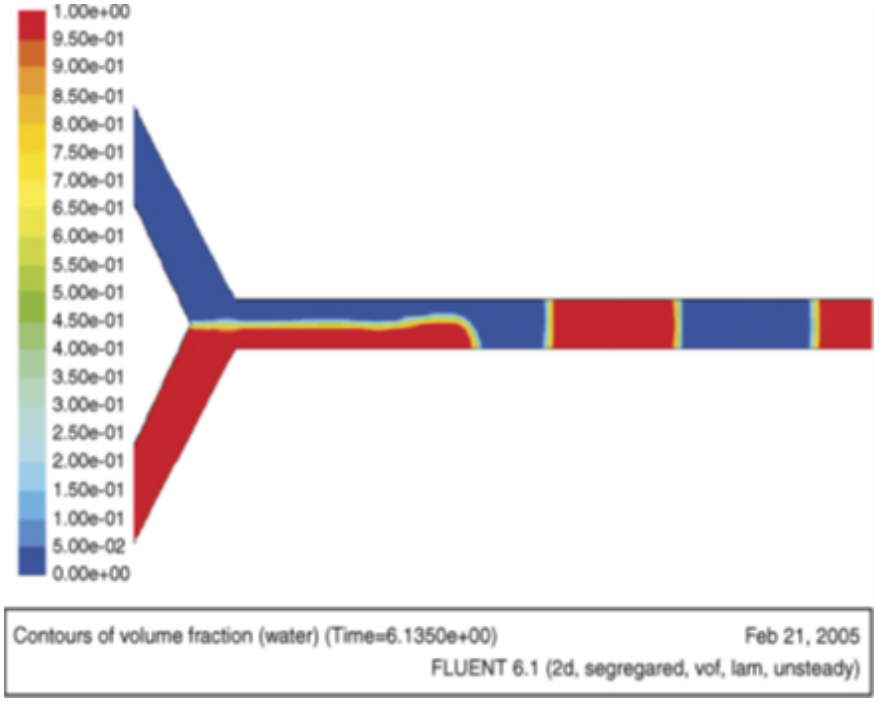

Figure 2.3 Slug flow generation with wall adhesion in a Y-junction with diameter of 1 mm for oil-water system (liquid velocity u1=10 mm/s, u2=10 mm/s, contact angle θ_w=90°) (Kashid et al. 2005).

In Figure 2.1, it shows that deformation arose on interfaces connected to the bottom of other slug and the connecting layer between two slugs reduced with the length of the capillary. In addition, it was observed that deformed drop was formed with no interaction with the wall when the surface tension and same flow rates were applied. While, in Figure 2.2, it reveals that wall adhesion has significant influence on slug flow generation. The slug flow was observed in both experiments with flow rate ranging from 1 ml/hr to 100 ml/hr and simulations with surface tension and wall adhesion for different immiscible fluid systems in 2D geometry which indicate the possibility of an appropriate step upon the generation of well-defined slug flow in numerical methodology.

The above research was mainly focused on the convection and diffusion mechanism inside and between slugs consist of liquid phase. Additionally, numerical research on gas and liquid slugs instead of liquid slugs for Taylor flow in a T-junction (Figure 2.4) by Qian et al. (2006) had extended the slug flow mechanism for two-phase fluid in a different geometry.

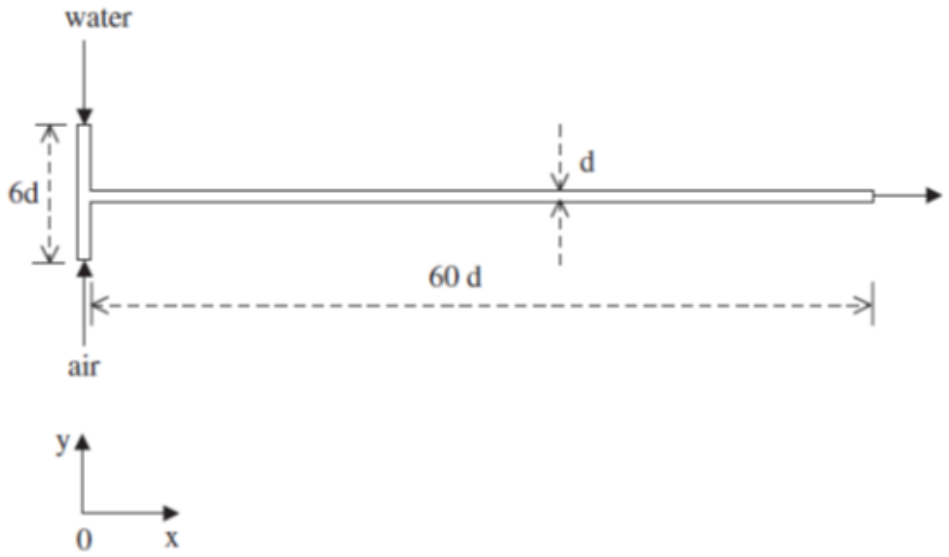

Figure 2.4 Geometry of T-junction used in simulation where d is the width and x, y are axis (Qian et al. 2006).

Their study presented the numerical simulation of the Taylor flow (gas and liquid slugs) in the microchannel of a T-junction with different cross section width by adopting Volume of Fluid method integrated in the computational fluid dynamics (CFD) software, FLUENT (ANSYS, Inc., Canonsburg, Pennsylvania). It was reported that the lengths of gas and liquid slug under

several operating and fluid conditions obtained from experiment had a good agreement with the literature data. According to the simulation results, some correlations in the microchannel of the T-junction were discovered. Slug flow within T-junctions with other cross section geometries and inlet conditions were investigated as well. The numerical predictions obtained from simulations were compared with the experiments on the coarse distributor which was performed by Heiszwolf et al. (2001) and Kreutzer et al. (2005). It was observed that the simulation results have a good agreement with the experimental results especially the slug length under specific conditions. In addition, the results claimed that the inlet configuration has vital influence on the slug length and the slug-uniformity becomes more evident with channel cross-sectional width over 1 mm as well as increase of gas or liquid flow rate. It was also found that the increase of gas velocity and decrease of liquid velocity results in the increase of gas slug length. On the contrary, the increase of liquid velocity and decrease of gas velocity leads to the increase of liquid slug length. In addition, Reynolds number (Re) and Capillary number plays an important role in determining the dimensionless slug length, thus with wider channel longer slug was formed at the same superficial gas and liquid velocities (Qian et al., 2006).

Comparing to the research presented above, Santos et al. (2009) had also conducted numerical modelling and experimental investigation of gas-liquid slug formation in a microchannel T-junction. However, they performed a three-dimensional modelling of slug flow and then found the agreement between simulation results and experiment data done by their own instead of using literature from others. It was discovered that the increase and oscillation of gas inlet pressure resulted in higher practical velocity slip which deviated the numerical predictions. Improvement had to be done by adjusting the contact angle, contact line slip and using dynamic boundary condition when simulating the compressible gas phase inlet reservoir. The experiment apparatus used in their study was made up of two syringe pumps, light, microfluidic T-junction, CCD camera and image acquisition computer (Figure 2.5). CFD software Fluent (ANSYS, Inc., Canonsburg, Pennsylvania) was used for the simulations and Volume of Fluid model was activated to capture and track the precise location of the interface between the fluids.

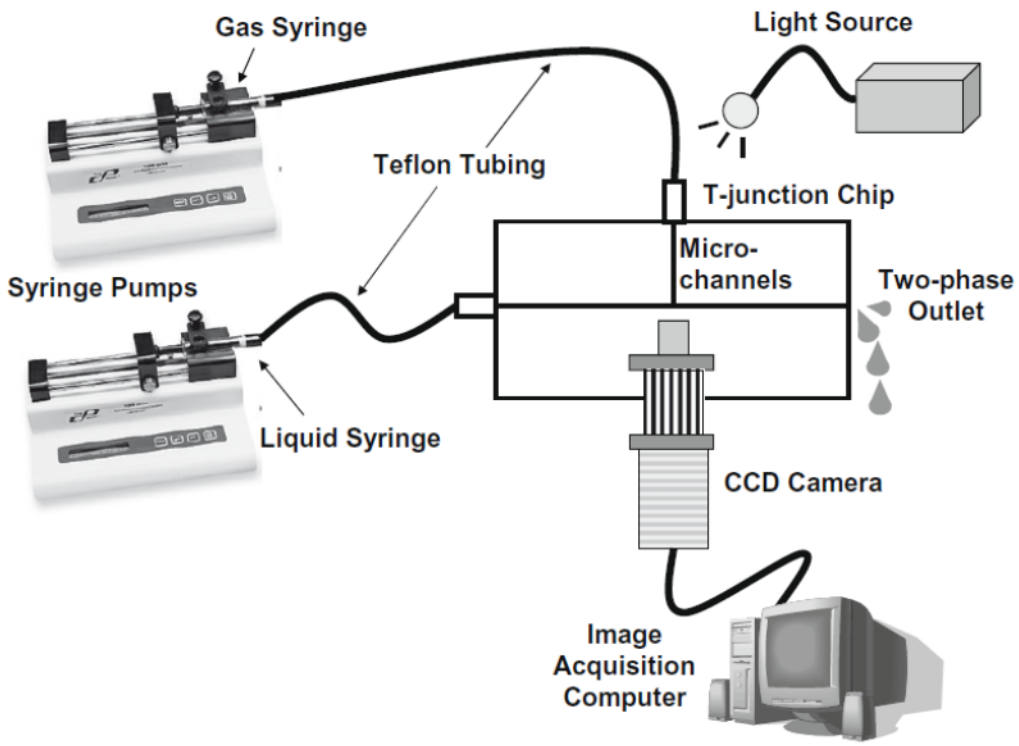

Figure 2.5 Experiment setup consists of syringe pumps, light source, T-junction chip, CCD camera, and image acquisition computer (Santos et al. 2009).

Comparisons of experimental and numerical results were focused on the void fraction, gas slug length and cross-sectional area of gas slug. It was concluded that numerical computed void fraction was related to the homogeneous void fraction in a linear fashion and compressible gas volume in the computational geometry or dynamic boundary condition had to be implement so as to accurately simulate experiment results and capture the break-up physics at the microfluidic junction. For the gas slug length shorter than $400\,\mu m$, the experimental and numerical results had good agreement with each other, while for longer slug length the results did not match well which is shown in Figure 2.6.

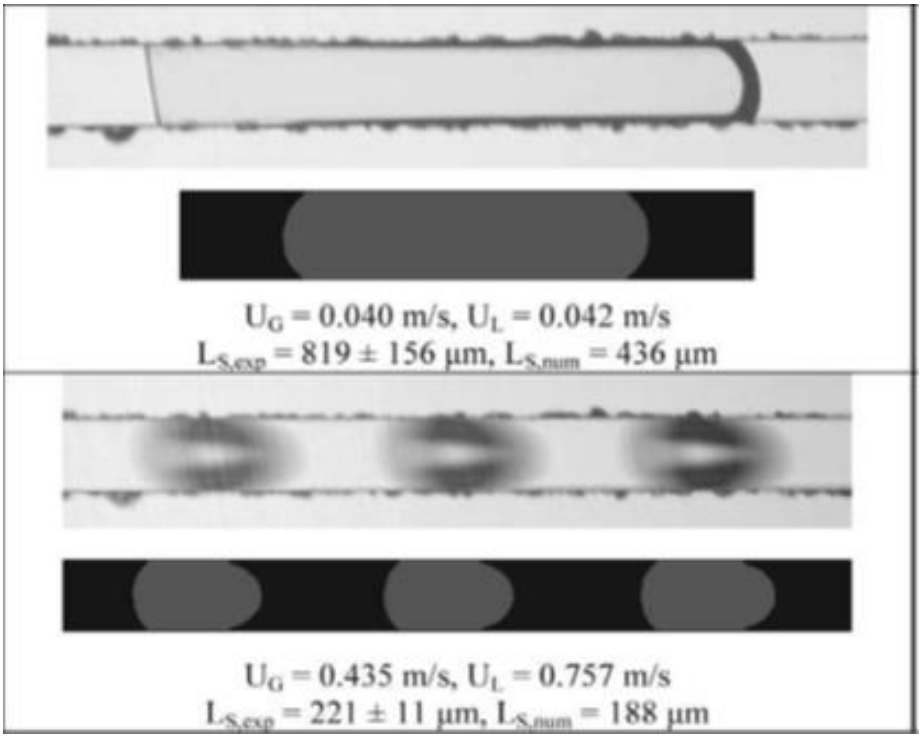

Figure 2.6 Comparison of gas slug with long and short size obtained for experiment and simulation (Santos et al. 2009).

Other than the VoF method which is quite popular used in tracking and locating interfaces between two different fluids, in 2011 Bashir et al. had performed simulations of microfluidic droplet formation in a microfluidic T-junction chip using the two-phase level set method. The level set method which is a robust and easy implementing scheme allows numerical computations of the objects to be proceeded on a fixed Cartesian grid without parameterizing them. In their research, the conservative level set method proposed by Olsson and Kreiss (2005) have been used and the 0.5 contour of the level set function ϕ is chosen to describe the position of the water-oil interface. The main channel is filled with oil as continuous phase and water as dispersed phase in the inlet channel as shown in Figure 2.7. $\phi = 0$ represents the continuous phase and $\phi = 1$ represents the dispersed phase.

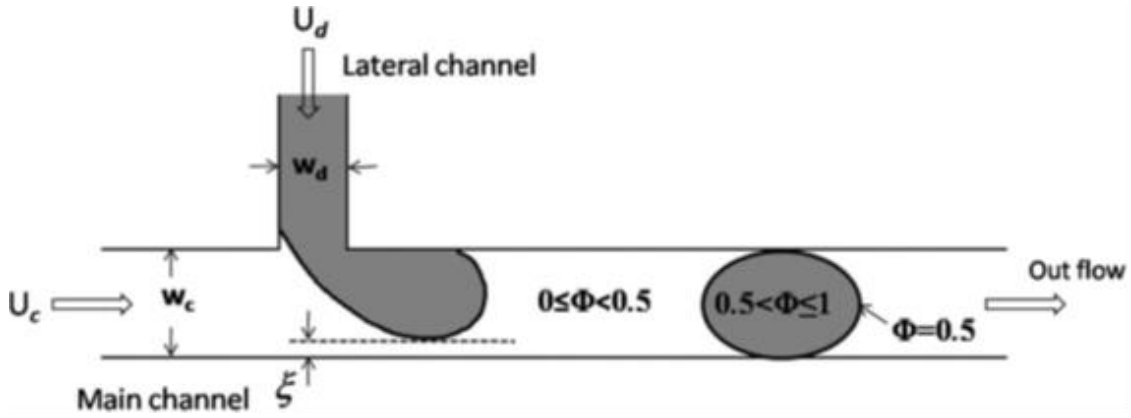

Figure 2.7 Geometry of the T-junction. The continuous phase (oil) is in the horizontal main channel and the dispersed phase (water) is in the perpendicular inlet channel (Bashir et al. 2011).

Numerical simulations of water droplets generation in oil in a T-junction were conduct with various value of oil/water flow ratios u_c/u_d using the two-phase level set method were conducted and compared with the laboratory experiments as shown in Figure 2.8.

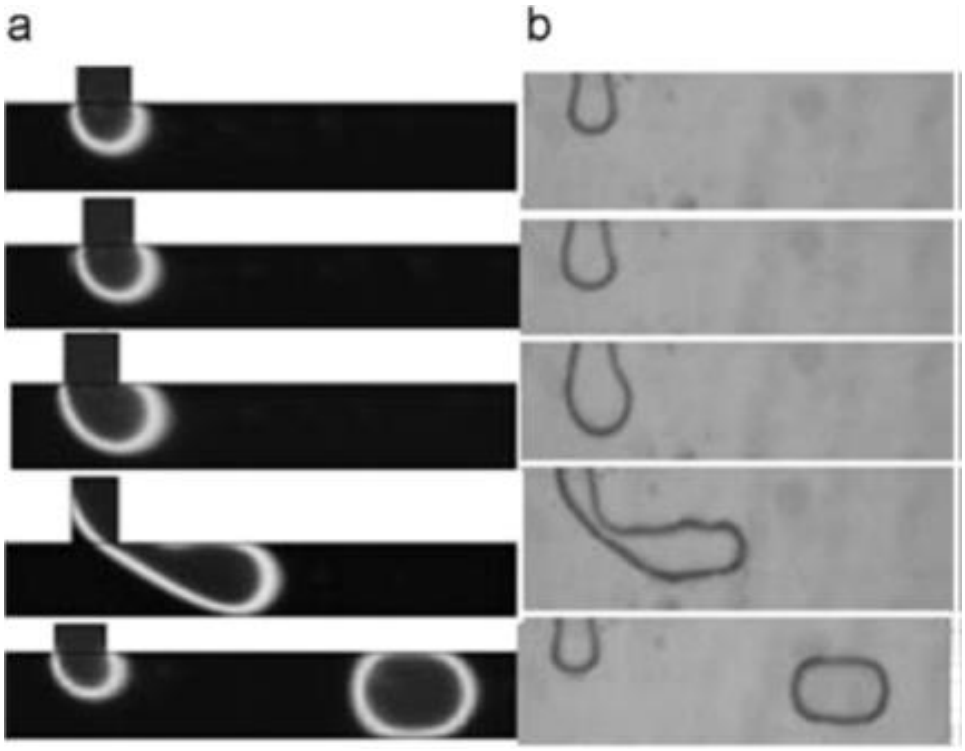

Figure 2.8 Comparison of level set method (a) and experiment (b) results of water droplet breakup process in n-dodecane oil with fixed droplet velocity u_d=0.012m/s and capillary number Ca=0.01(Bashir et al. 2011).

The effect of contact angle on size and generation rate of droplets were investigated by varying the contact angle of water droplets with the channel walls from 120° to 180° under different values of Capillary Number Ca and constant viscosity ratio λ which is the ratio of the viscosity of dispersed phase (water) and continuous phase (oil). Besides, the effects of both viscosity of carrier fluid and contact angle on the size of droplet were also studied by plotting droplet length against contact angle from 120° to 180° under different viscosity ratio of fluids which is shown in Figure 2.9.

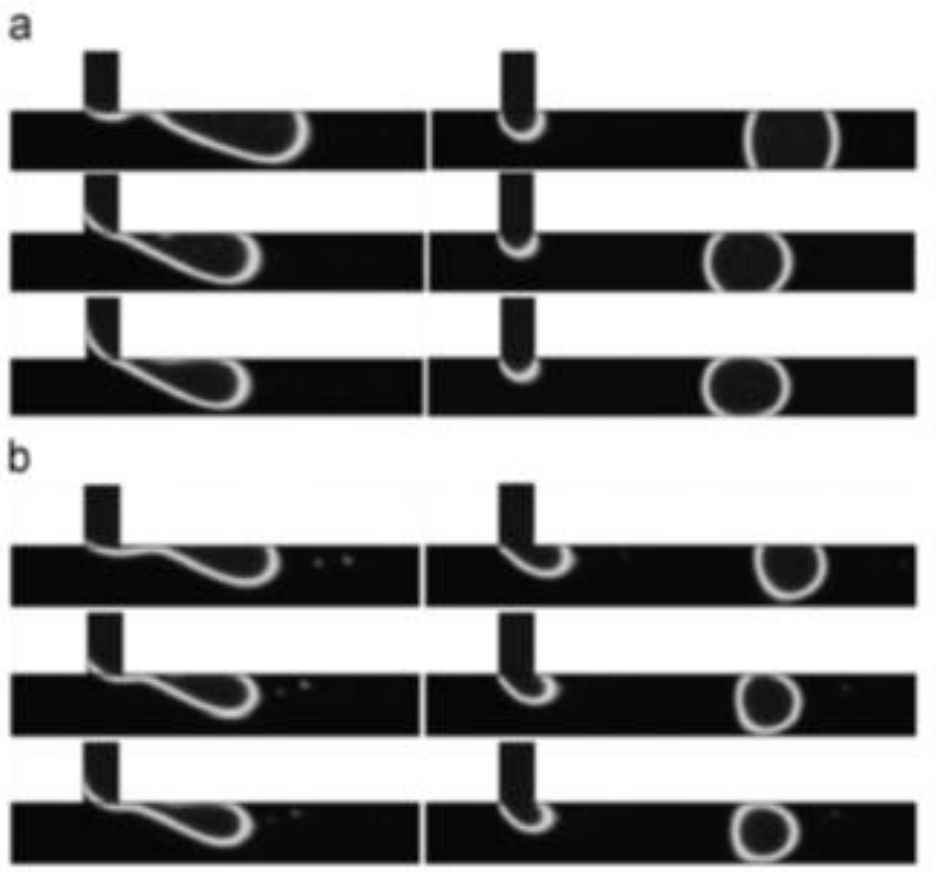

Figure 2.9 The influence of contact angle on droplet formation and sizes for (a) oil with low viscosity (λ=0.8) and (b) oil with high viscosity (λ=0.1) with droplet velocity u_d=0.012m/s, surface tension σ=5 mN/m and contact angle θ=120°, 150° and 180° from top to bottom respectively for both (a) and (b). Time interval between each left and right image is 5 ms (Bashir et al. 2011).

It was found in their study that with the increasing of contact angle from 120° to 180°, the droplet breakup time decreases almost linearly and the frequency of droplet generation increases. The effect of contact angle on droplet size can be ignored when the capillary

numbers are above 0.02, while for capillary numbers below 0.02 the contact angle plays an important role especially within the region of hydrophobic wetting. It is predicted by the numerical simulation that the droplets keep symmetry on a line which is perpendicular to the length of the channel when the viscosity ratio λ=0.8 and the length of droplet increases with the increasing of interfacial tension. The numerical simulations of the formation in a microchannel T-junction of aqueous droplets in an oil-based continuous phase by using two-phase level set method compared well with experimental observations and also gave results consistent with numerical studies of droplet formation from the literature.

Unlike the mesh and Navier-Strokes based numerical method such as VOF method and Level Set method, the latest numerical method called Lattice Boltzmann method (LBM) which solves the discrete Boltzmann equation instead of the Navier-Stokes equations in order to simulate the flow of a Newtonian fluid with low Reynolds number and collision models like Bhatnagar-Gross-Krook(BGK) was applied to analyse the bubble/slug flow as well. In this method, the interior particle interactions indicate viscous flow behavior in microscope that is applied to the greater mass through the simulation of a limited number of particles in streaming and collision processes. Therefore, Yu et al. (2007) has carried out experiment and Lattice Boltzmann simulation of two-phase gas-liquid flows in microchannels in 2007 that evince the feasibility of this method. Their study is conducted by using gas-liquid flow in microchannels with two types of geometries including the cross-shape and the converging shape channels which are shown in Figure 2.10.

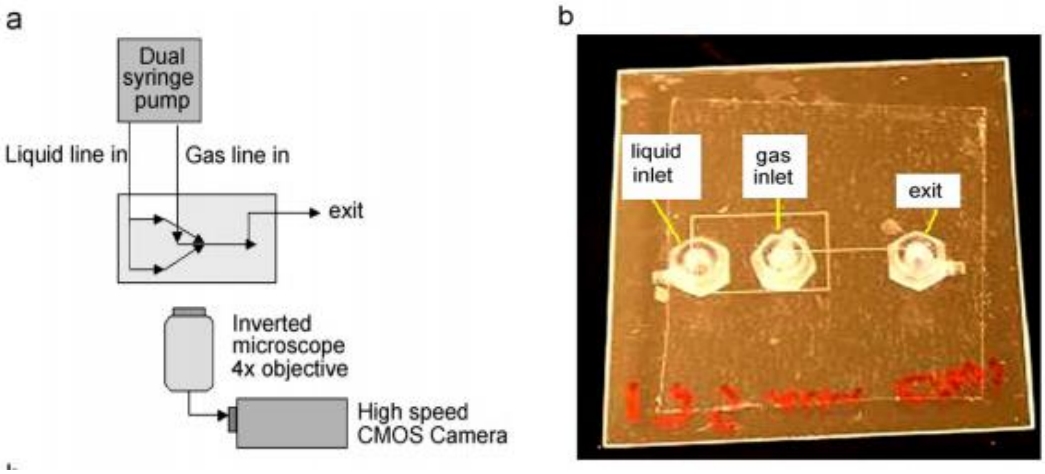

Figure 2.10 (a) Schematic illustration of the experiment setup. (b) Channel with cross-shape intersection. (c) Channel with smooth (converging) intersection (Yu et al. 2007).

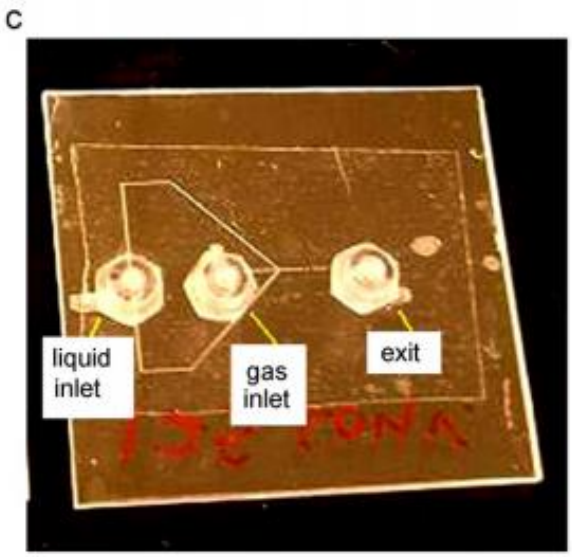

Figure 2.10 (a) Schematic illustration of the experiment setup. (b) Channel with cross-shape intersection. (c) Channel with smooth (converging) intersection (Yu et al. 2007) (continued).

The microchannels were made of polymethyl methacrylate (PMMA) with 125 and 250 μm for the channels and 1 mm for the inlet and outlet. All channels were 125 μm deep and were sealed by thermobonding a transparent thin film of PMMA. A dual syringe pump was used to inject the liquid and air streams into the microchannels with a set of flow rate and a high-speed CMOS camera was used to capture the images.

The effect of Capillary Number Ca was investigated by using air, silicon oil and sugar solution for simulations and experiments with a variety of surface tension, velocity and viscosity. The simulation results of bubble formation and the comparison between simulation and experiment are shown in Figure 2.11 and Figure 2.12.

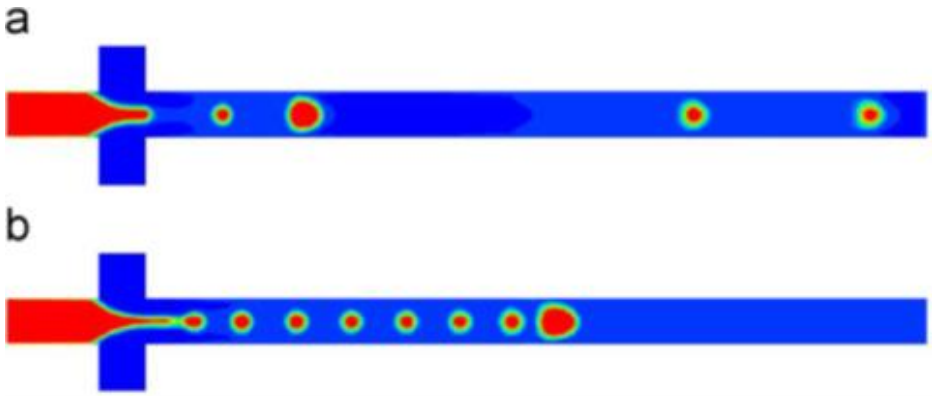

Figure 2.11 Simulation results for Ca=0.2 with gas/liquid flow ratio of (a) Q_g:Q_l=1:8; (b) Q_g:Q_l=1:4 in which red represents the gas and blue represents the liquid (Yu et al. 2007).

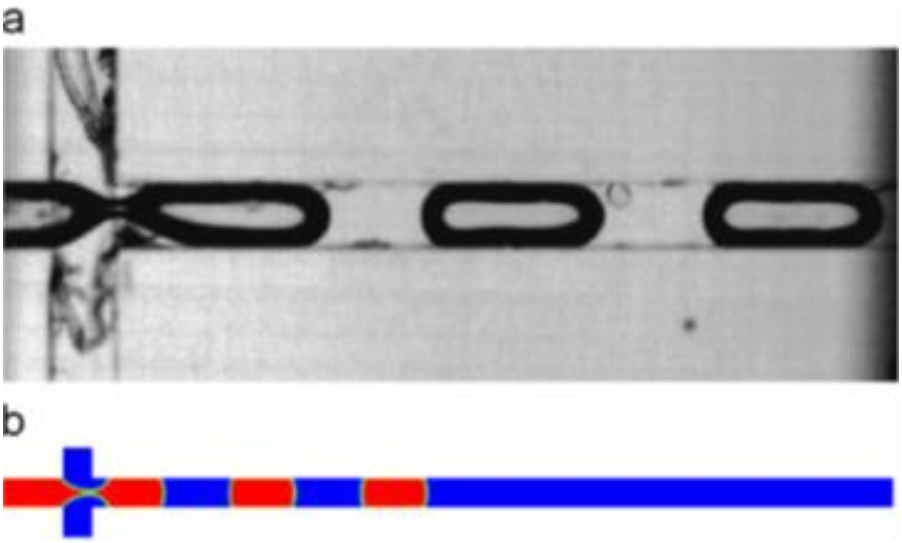

Figure 2.12 Comparison between (a) experiment and (b) simulation result of air-silicon oil in 125 μm channel with Ca=0.003, flow ratio Q_g:Q_l=1:1 (Yu et al. 2007).

The geometry effect on the bubble generation was also studied by both experiment and simulation and comparison was made in Figure 2.13.

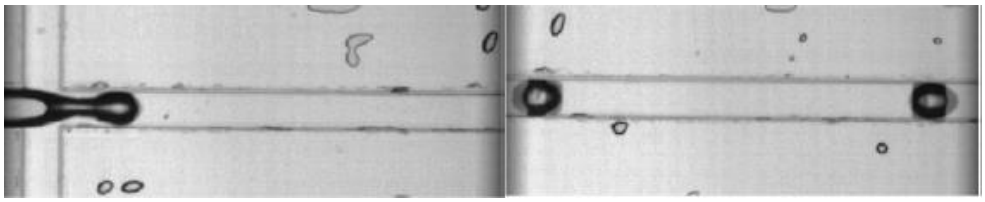

(a)

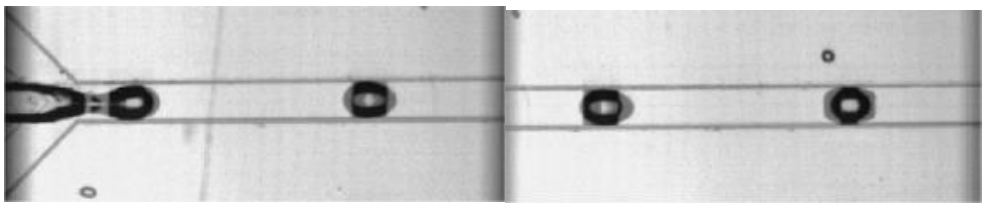

(b)

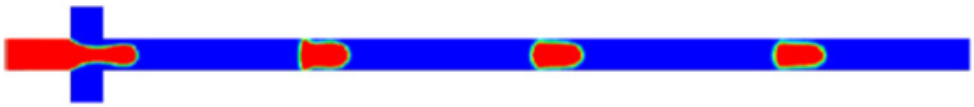

(c)

Figure 2.13 Comparison of experiment results in: (a) cross shape channel; (b) converging shape channel, and simulation results in: (c) cross shape channel; (d) converging shape channel for bubble formation in air-sugar system (Yu et al. 2007).

(d)

Figure 2.13 Comparison of experiment results in: (a) cross shape channel; (b) converging shape channel, and simulation results in: (c) cross shape channel; (d) converging shape channel for bubble formation in air-sugar system (Yu et al. 2007) (continued).

It was notated that the simulation results have a reasonable agreement with experiments in both cross and converging shape channels. The bubble generation mechanism differs due to Capillary Number Ca; therefore, the bubbles were formed by shear instability governed by the stretching of the gas stream when Ca number is above 0.03 and were pinched off by the pressure difference in the two phases when Ca is below 0.01. In addition, the geometry of the microchannels in mixing section also has a significant influence on the bubble size and the distance between the bubbles.

2.3 Fundamental of microbubbles

2.3.1 Introduction to microbubbles

Microbubbles are represented as bubbles of gas in a liquid of diameter smaller than one millimetre but larger than one nanometre (Zimmerman et al. 2011; Prevenslik, 2011) and are widely encountered in nature and used in industry and medicine. The component of the bubble shell and filling material play an important role in the characteristic features such as buoyancy, crush strength, thermal conductivity, and acoustic properties.

They are used as contrast agent for ultrasound imaging in medical applications (Blomley et al., 2001). The microbubbles with gas core such as air or perfluorocarbon oscillate and vibrate when a sonic energy field is applied and respond to ultrasound waves which make the microbubbles different from other tissues. Because of the lack of stability that results in quick dissolution in liquid, microbubbles have to be encapsulated in a solid shell made from a polymer or a protein to avoid the bubble break up.

To date, microbubbles can also be used for drug delivery (Sirsi et al. 2009), biofilm removal (Mukumoto et al. 2012), membrane cleaning (Agarwal et al. 2012), biofilm control and water/waste water treatment purposes (Agarwal et al. 2011). In other application, (out of a staggering range), they can be arranged to form a bubble layer near ships' hulls to reduce ship drag by using these small bubbles (Kumagai et al. 2015).

2.3.2 Microbubble generation methods

There are three generally used ways to produce microbubbles. The most common one uses compression of a gas to dissolve it into a liquid, which is subsequently released through a specially designed nozzle system, to nucleate small bubbles as potentially nanobubbles, based on the cavitation principle. These bubbles subsequently grow into much larger bubbles through the rapid dissolution of the supersaturated liquid. This method is called adsorptive bubble system operation and has many significant industry applications such as liquid industrial effluent treatment, water treatment, activated sludge thickening, oil-water separation, cellulose fibre concentration, etc. The most important factor of controlling air solubility in this method is the air pressure for generation of the air bubbles and the total volume and size of air bubbles produced on depressurization is proportional to the pressure of the process stream, the rate of flow, and the pressure reducing mechanism. The use of dissolved air which fulfils the requirements of air volumetric flow rate, bubble rising velocity, and power consumption results in an adequate air pressure generation system that produced optimum condition in the bubble generation process. For example, in the study of Hosokawa et al in 2009, they used a pressurized dissolution device to generate bubbles and measure the diameter of bubbles by using phase Doppler anemometry and an image processing method. The experiments were conducted several times with different mass flow rates of dissolved gas and air bubbles entrained in the upstream of the decompression nozzle were measured on bubble diameter. The schematic of the experimental apparatus and the dissolution tank are shown in Figure 2.14.

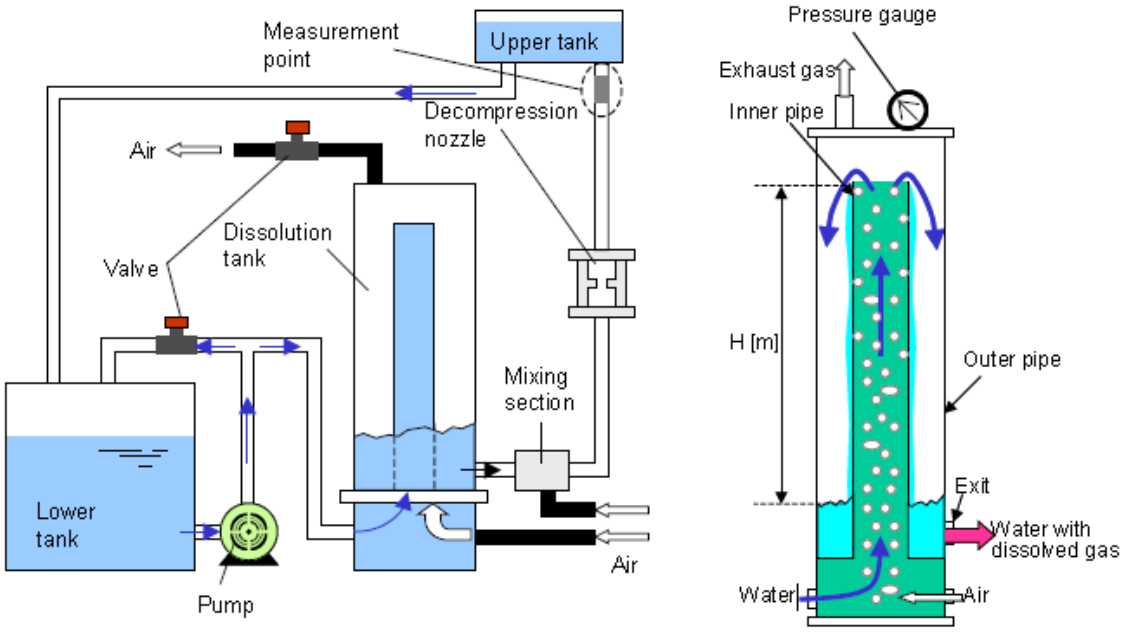

Figure 2.14 Experimental apparatus (left) and dissolution tank (right) (Hosokawa et al. 2009).

It was shown that air is supplied from a compressor and flows into the dissolution tank where the mixing process occurs with water supplied from the pump. One part of air dissolves in water through the air-water interface in the dissolution tank and the other part of air is exhausted from the tank. Bubble flow is generated in the inner pipe and flows over at the top of the pipe in the dissolution tank. The falling film is formed at the on the outer surface of the inner pipe and water flows to decompression nozzle through the tank exit located at the bottom of the outer pipe. Experiments are conducted for several mass flow rates of dissolved gas and of air bubbles entrained in the upstream of the decompression nozzle to examine effects of the entrained bubbles on the diameter and number density of micro bubbles generated by the pressurized dissolution method. It was found that the mean diameter of microbubbles generated by gas dissolution is smaller than that generated by breakup of air bubbles entrained in the upstream of the decompression nozzle and its diameter increases with the entrainment of air bubbles in the upstream of the decompression nozzle at a constant mass flow rate of dissolved gas.

The second class of bubble generation method uses ultrasound to induce cavitation locally at points of extreme rarefaction in the standing ultrasonic waves. Microbubble generator using a hollow cylindrical ultrasonic horn was developed by Makuta et al. 2013 and

it was found that microbubbles with diameter of less than 100 μm could be generated (Makuta et al., 2013). However, this method cannot satisfy industrial requirement of gas flow rate so that the available gas flow rate has to be increased to make the technique commercially viable. Further study has been conducted by Numakura et al. 2014 to modify this method by applying orifices that can be changed to the microbubble generator and the effect of the orifice shape on the time evolution of the dissolved gas concentration in bubbled water and the bubble diameter distribution have been evaluated. The microbubble generator above consists of an ultrasonic generator, an ultrasonic transducer, a gas supply source, and the hollow cylindrical ultrasonic horn which is shown in Figure 2.15.

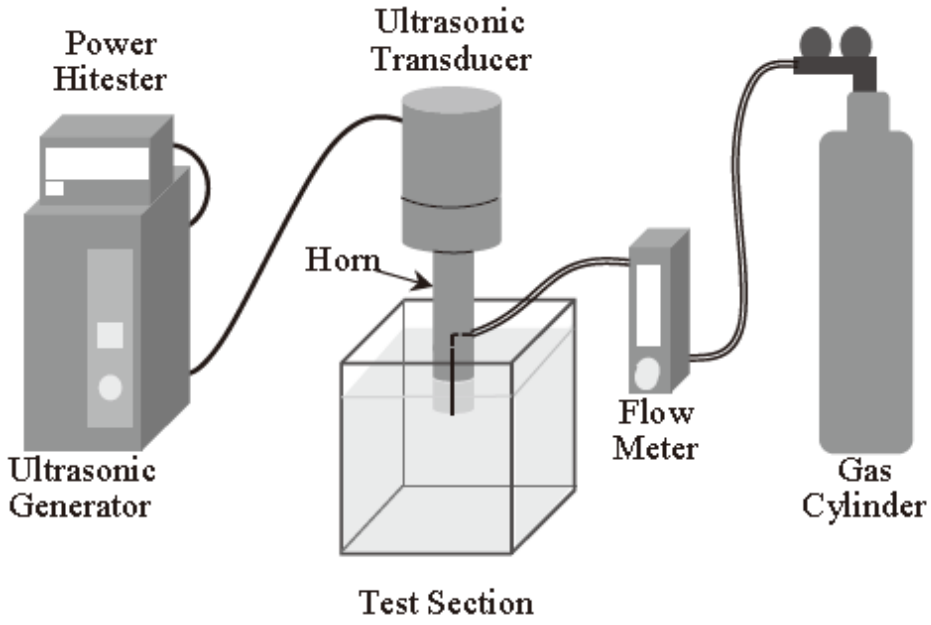

Figure 2.15 Configuration of the microbubble generator (Makuta et al., 2013).

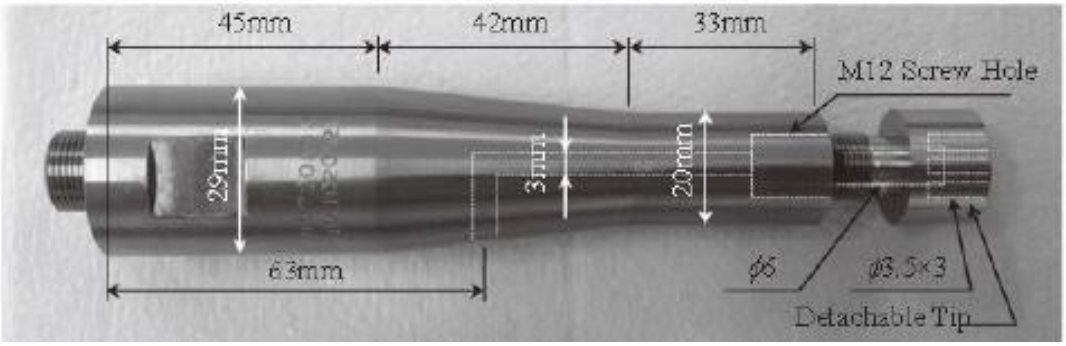

Figure 2.16 The internal and external shape of the hollow cylindrical ultrasonic horn

(Makuta et al., 2013).

The hollow cylindrical ultrasonic horn (Figure 2.16) in this device which is made of titanium alloy has a flow path with an inner diameter of 3mm and a detachable tip. Gas is supplied from the inlet located on the side of the ultrasonic horn to the end of the horn where the gas-liquid interface is formed when the gas the liquid. Then a large number of microbubbles are generated when the end oscillates ultrasonically in response to the electrical power input. Microbubbles generated from the hollow cylindrical ultrasonic horn come from the fragmentation of a capillary wave on the gas-liquid interface formed near the orifices at the end of the horn. Therefore, the increase of the contact area between the water, gas and horn help to improve microbubble generation and the effect of the orifice shape on microbubble generation has been investigated. It was found that the microbubble generator above with multiple orifices which were sufficiently apart to prevent the generated bubbles from coalescing could satisfy the requirement of microbubble generation and sonochemical reactions. This method can be applied to a sonochemical reactor (Makuta et al. 2013), which relies on the high temperatures and pressures generated in the ultrasonically oscillating microbubbles (Suslick et al., 1990). Besides, microbubble generator with multiple orifices for sonochemical applications by studying the degree of degradation of indigo carmine (Numakura et al., 2014).

The third method uses an air stream delivered under low offset pressure, and aim to break off the bubbles due to an additional feature such as mechanical vibration, flow focussing, fluidic oscillation, and other microfluidic devices. Small bubbles were generated by conventional air diffusers through the nozzles with the structure of porous material. Fluidic oscillation helps to break off the forming bubble while it is still a hemispherical cap which is likely to occur under the strong adverse effect of surface tension at higher curvatures from a pore. Membrane made of different materials was applied as porous filtration film to form microbubbles under the crossflow introduced by the continuous phase. Several studies were conducted to investigate the gas-liquid bubble formation process by using this method. It was reported that Khirani et al. has used commercial porous filtration membranes made of alumina or zirconium oxides to investigate microbubble generation characteristics in aqueous or organic liquid (heptane) under a liquid crossflow with different combinations of dispersed phases (air or nitrogen) by using the experimental apparatus shown in Figure 2.17.

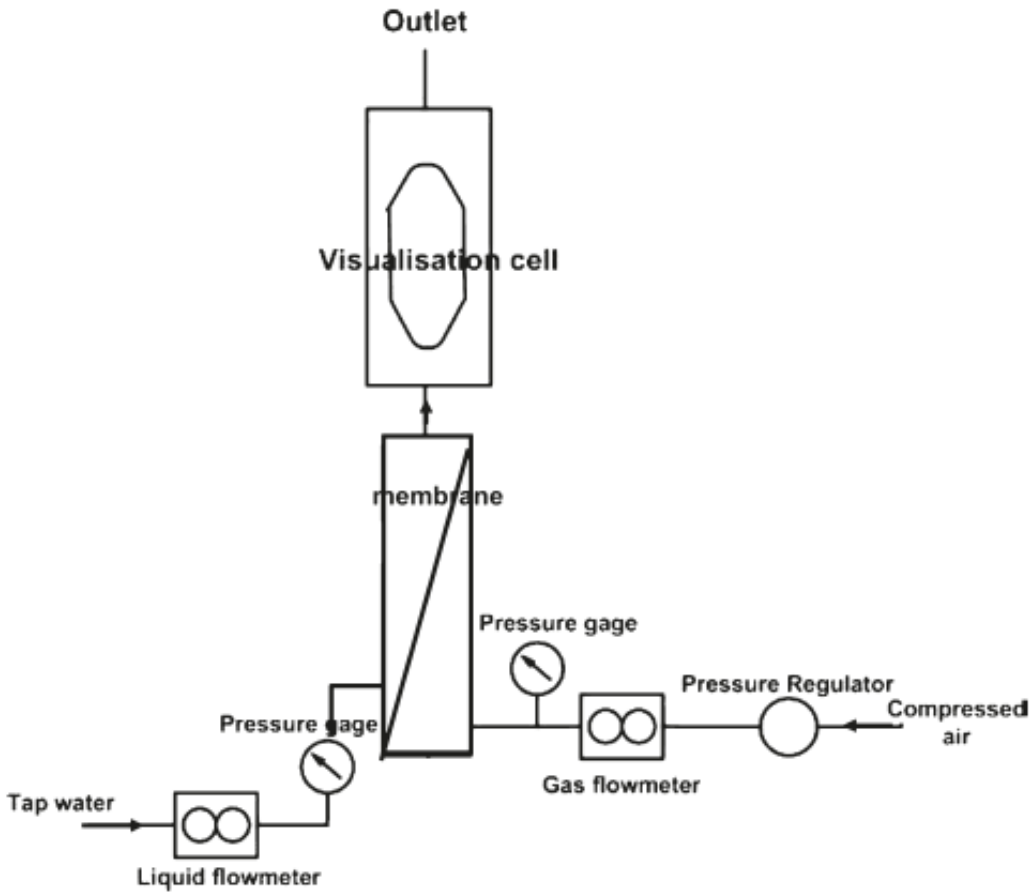

Figure 2.17 Schematic diagram of the microbubble generation apparatus under various conditions of water flow (Khirani et al.,2012).

It was found that these membranes were capable of generating microbubbles in heptane under the application of liquid crossflow. When zirconium oxide membranes with pore size varying from 20-100 nm was used, microbubbles with diameters ranging from 100-200 and 500-550 μm in heptane were obtained under a shear stress varying from 27 to 39 Pa with a gas fraction of nearly 3%. Therefore, this method has the potential to generate microbubbles that could be applied to improve the usual gas/liquid mass transfer operation. In addition, Kukizaki et al. also discovered the nanobubbles/microbubbles generation from Shirasu-porous-glass (SPG) membranes with uniform pores in a system filled with gas and water as disperse and continuous phases individually by using the experiment setup shown in Figure 2.18.

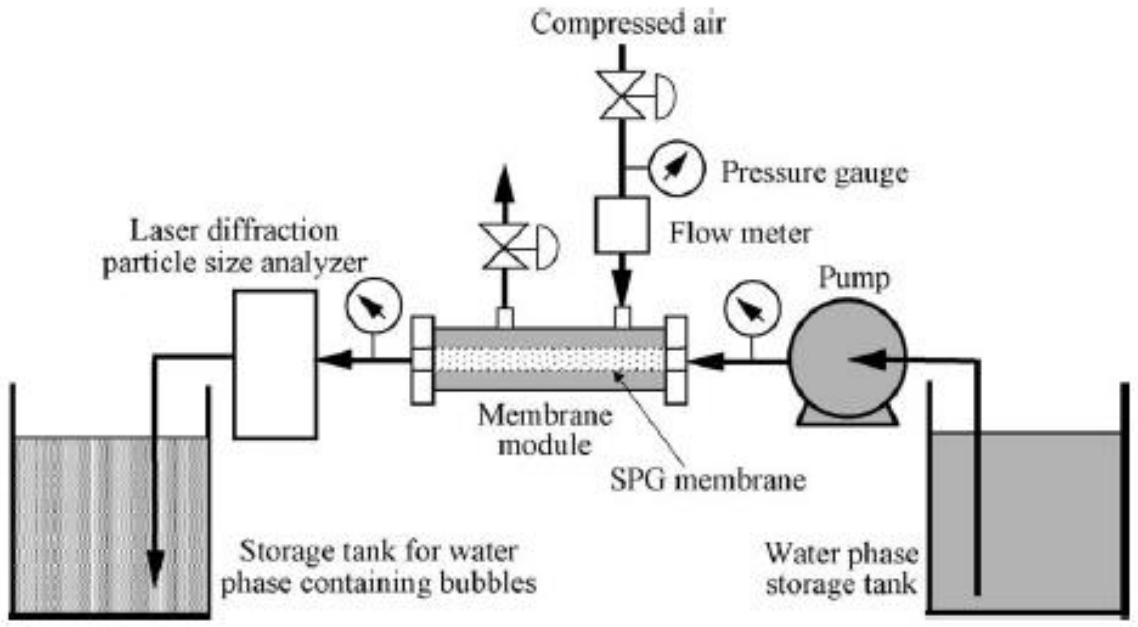

Figure 2.18 Microbubble generation experimental setup by using SPG membranes (Kukizaki et al.,2006).

In their study, air was pressurized into a sodium dodecyl sulfate (SDS) solution ranging from 0.05 to 0.5 wt% flowing through a SPG membrane with transmembrane/bubble point pressure ratio of 1.1-2.0. It was observed that monodispersed nanobubbles could be stably generated from membranes and the average bubble diameter was found to be 8.6 times larger than the average pore diameter. Therefore, the nanobubble diameter strongly depends on the membrane pore size but less influenced by the flow velocity or the surface tension between air and SDS solution.

The Microfluidic devices based on cross flowing, flow focusing and other co-flowing methods have also been commonly used in microbubble generation and the most commonly used types of designs are flow-focusing structure and T-junction. Researchers use gas as disperse phase and liquid as continuous phase for generation of microbubbles. Figure 2.19 has shown planar flow focusing microfluidic devices developed by Garstecki et al. which allows simultaneous, independent control over the size of the individual bubbles and volume fraction of the dispersed phases.

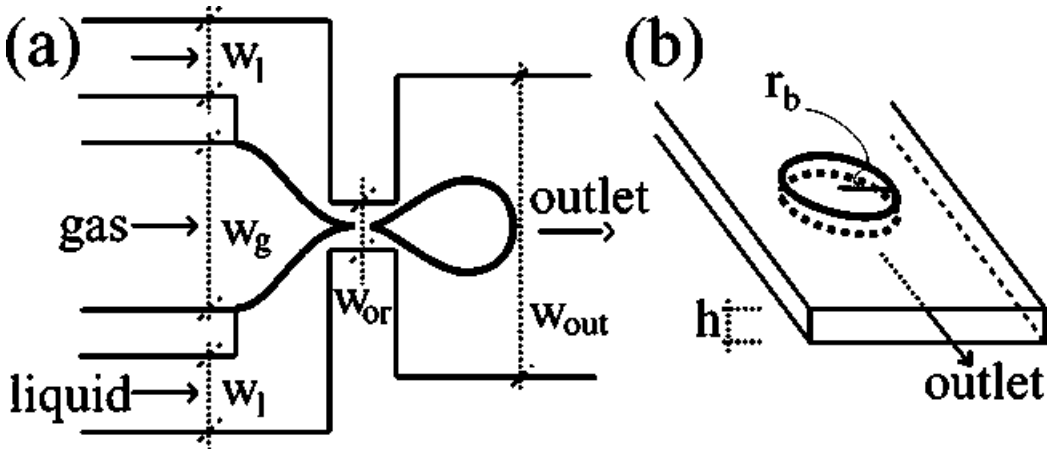

Figure 2.19 (a) The microfluidic flow-focusing device with rectangular cross sections of the channels (b) description of bubble in the outlet channel as bubbles are squeezed between the top and bottom wall with cylinder geometry.

The gas flows into the inner channel as disperse phase and the liquid flows into the outer channel as continuous phase. The two phases meet at the orifice and the gaseous thread is surrounded by continuous liquid film due to the hydrophilic character of the channel walls. The thread is unstable because of the high surface energy in this configuration and then breaks and release a bubble into the outlet channel periodically. Such flow-focusing microfluidic devices are widely applied for generation monodisperse microbubbles (Gordillo et al., 2004; Wan and Stone, 2010; Wan and Stone, 2011) because of its highly controllability on bubble size.

T-junction as shown in Figure 2.20 is another widely used for generating microbubbles due to its simplicity. Generally, there are two types of T-junction based on the difference of manufacture methods. They can be classified as lithography thus the whole junction is integrated in a microfluidic chip (shown in Figure 2.20a), and mechanical machining over materials like PDMS and glass blocks which allows capillaries of fixed inner and outer diameter inserting into these blocks (shown in Figure 2.20b). In both types of T-junction, the gas phase acts as disperse phase and the liquid phase acts as continuous phase. The gas phase injected into one of the channels is pinched off by continuous liquid phase and breaks into microbubble in the outlet channel. Due to the limit of the T-junction design, microbubbles with size below 10 μm are difficult to achieve by using this device.

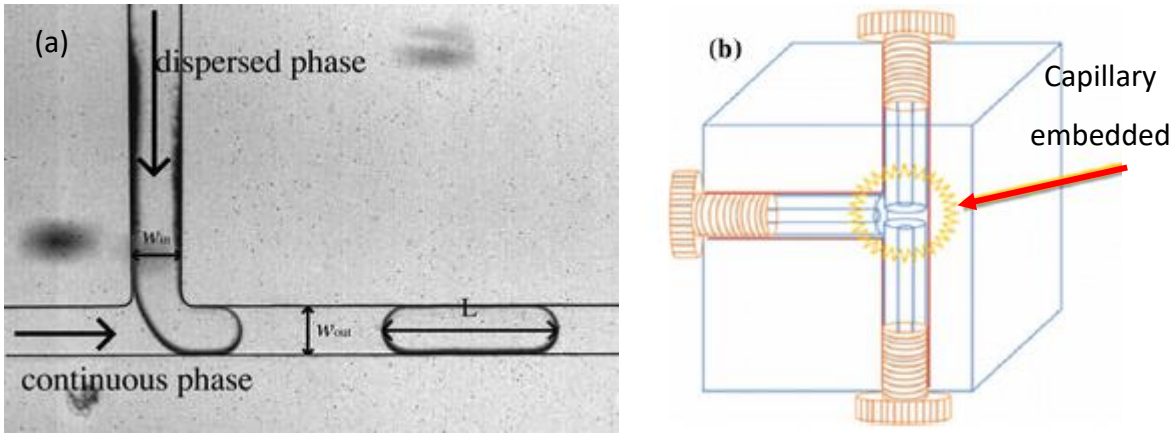

Figure 2.20 (a)Example of droplet production in a T-junction with dispersed phase and continuous phase (Baroud et al., 2010) (b)capillary embedded T-junction with fixed channel diameter manufactured by mechanical machining (Parhizkar et al.,2013).

Other than these conventional microbubble generation methods mentioned above, it is also reported that pressurized gyration device has been applied for generating microbubbles with multiple functions. Mahalingam et al. (2014) has developed a one-pot single-step novel process to produce microbubbles up to 250 μm in diameter using a pressured rotating device shown in Figure 2.21.

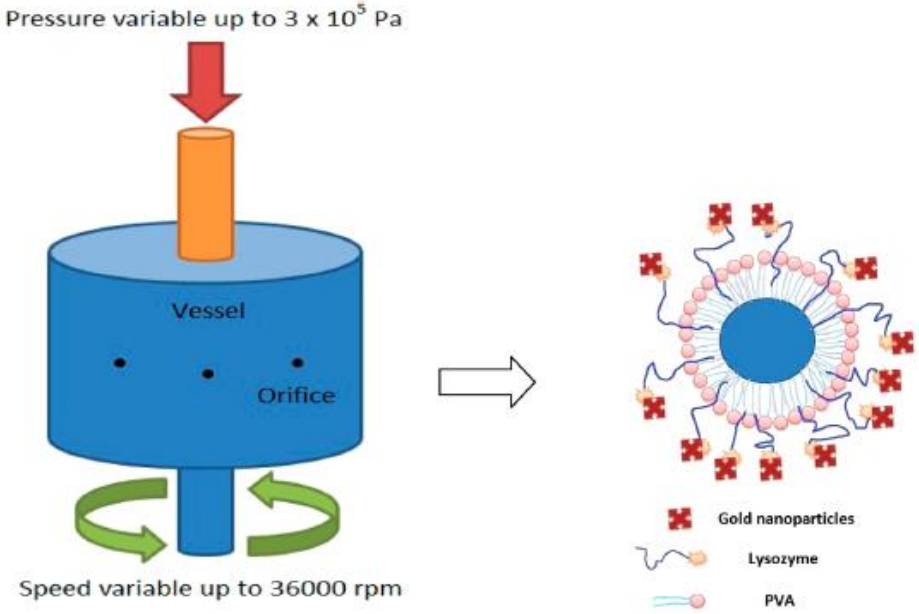

Figure 2.21 Schematic diagram describing the microbubbles formation by pressurized gyration of lysozyme solutions and microbubbles with multiple components coating were generated from the orifices (Mahalingam et al., 2014).

The device consists of a rotary aluminum cylindrical vessel with orifices on its face and the dimensions of the vessel and orifices can be adjusted to suite. The vessel is connected to a motor which can generate speeds up to 36000 rpm on one end and the other end is connected to a gas stream with pressure up to 3×10^5 Pa. A jet is generated when the vessel rotates with high speed and then breaks up into microbubbles due to the centrifugal force. It was observed that the breakup mechanism is influenced by the rotating speed of the vessel. Bare protein (lysozyme) microbubbles were generated by this method and revealed a morphological change which caused microcapsules over a period of time. Microbubbles containing gold nanoparticle at the bubble surface formed in this way also showed better stability over a time period and retained the same morphology. In addition, PVA-lysozyme microbubbles with and without gold nanoparticles were formed using the same pressurized gyration device. It was found that these microbubbles have shown antibacterial activity against Gram-negative Escherichia coli (E.coli) and biosensing capabilities when conjugating with alkaline phosphatase (Mahalingam et al., 2015). The functionalization of microbubbles generated by this method has great potential on applications in imaging, biosensing, and diagnostics (Mahalingam et al., 2014).

Researchers also interest in developing other novel microbubble generation methods such as electrogydrodynamic method which has been modified for producing microbubbles. Farook et al. (2006) reported a novel method based on co-axial electrohydrodynamic jetting for the preparation of microbubble suspensions made of bubbles with size less than 10 μm by using glycerol solution as liquid phase.

The experimental setup shown in Figure 2.22 was used to conduct co-axial electrohydrodynamic atomization. It was shown that both needles were connected to the same applied voltage relative to an earthed ring electrode placed 12mm below the outer needle. The inner needle is located 2mm above the tip of the outer needle. The outer diameter was 20mm and the inner diameter was 15mm. The flow rates of gas and liquid (glycerol) were controlled by high precision Harvard syringe pumps using plastic syringes. The glycerol solution was flowing in the outer needle of the co-axial twin needle configuration and undergoing electrohydrodynamic atomization in the stable cone-jet mode meanwhile air flowed in the inner needle. When zero voltage was applied, a hollow stream of liquid flow occurred from the outer needle. While, with the increasing of voltage applied, the hollow

stream became a stable cone-jet and released a microthread of bubbles, which were collected in a container filled with glycerol to obtain microbubble suspensions. It was found that microbubble size distribution was highly depended on the ratio of flow rates of liquid/air, especially the flow rate of the air.

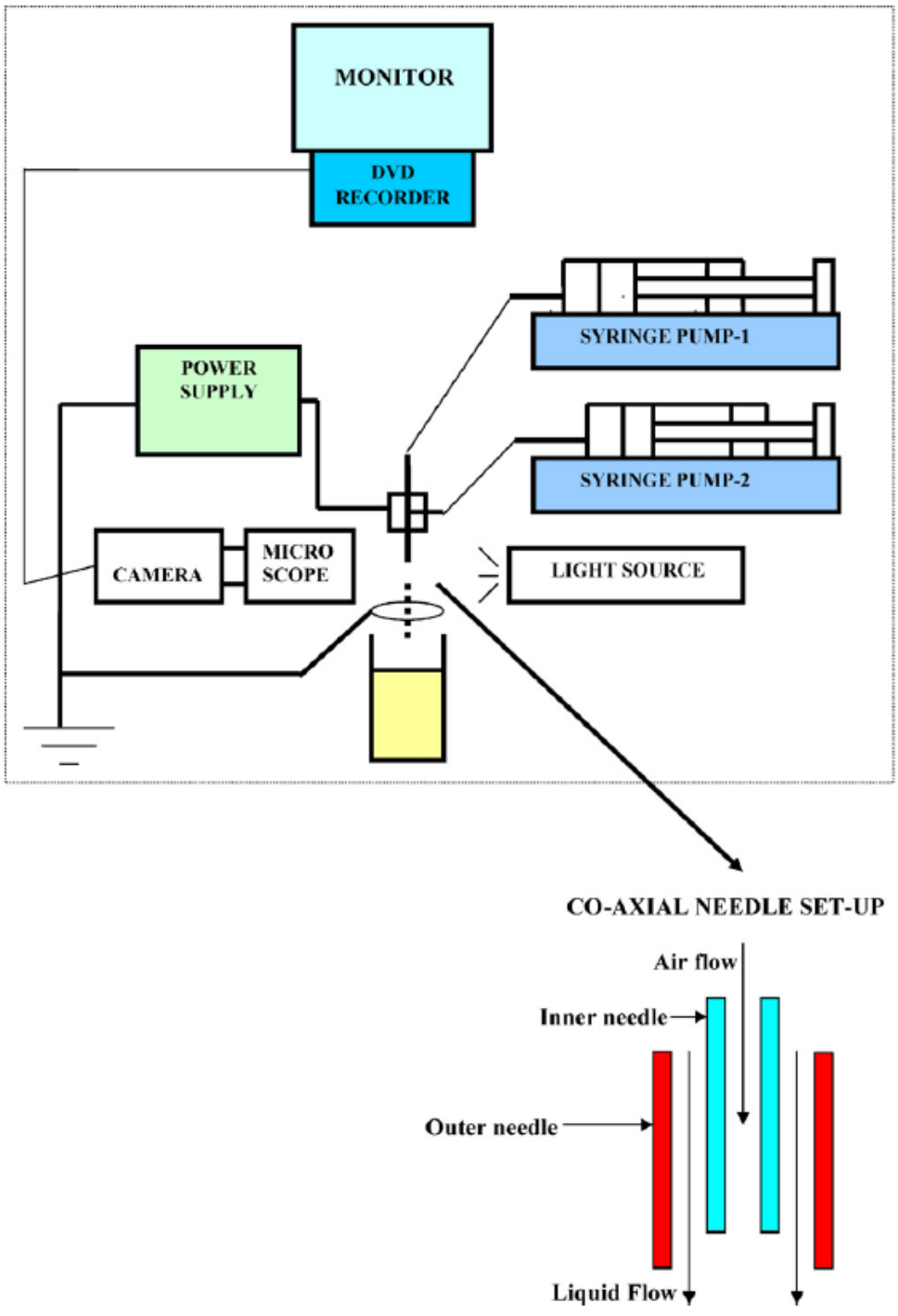

Figure 2.22 Equipment setup and needle arrangement used for co-axial electrohydrodynamic atomization (Farook et al., 2006).

Furthermore, the eletrohydrodynamic process has also combined with microfluidic device to generate microbubbles. It is noticed that Parhizkar et al. (2014) has investigated the microbubble generation using a microfluidic T-junction device modified by applying an electrical potential difference across the outlet channel as shown in Figure 2.23.

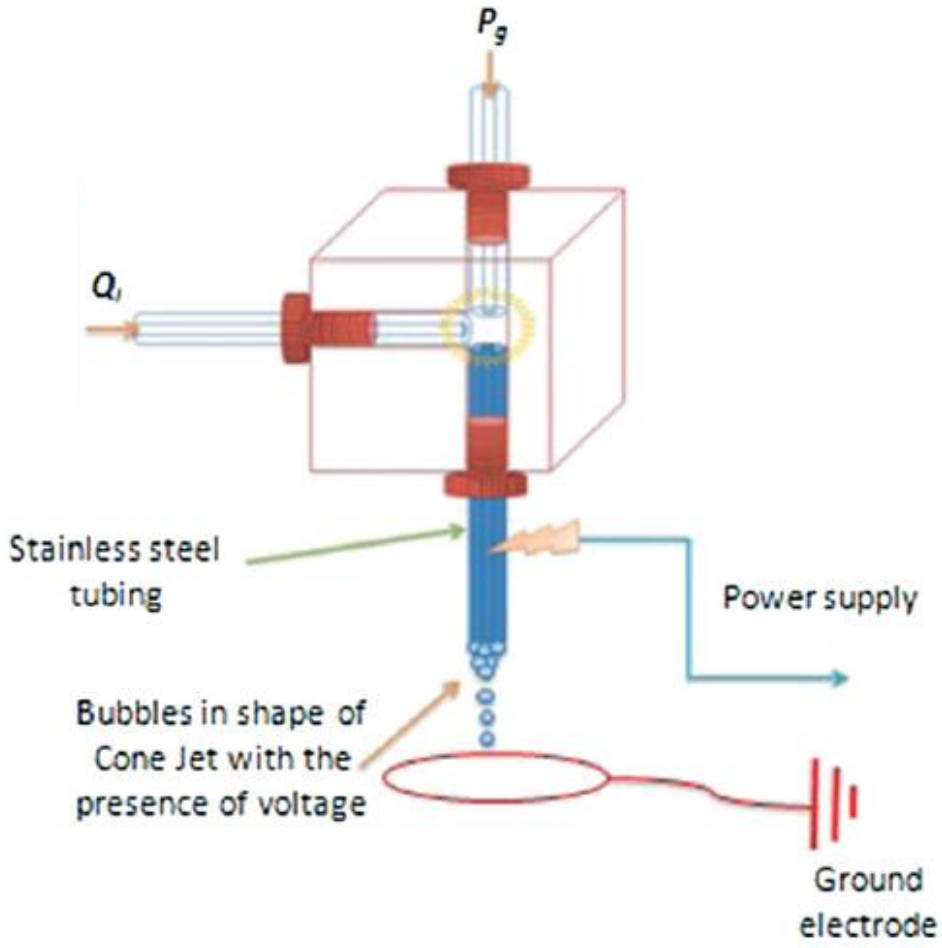

Figure 2.23 Schematic diagram of T-junction combined with eletrohydrodynamic process for microbubble generation (Parhizkar et al., 2014).

The experiment apparatus consisted of an embedded capillary T-junction with two Teflon FEP (Fluorinated Ethylene Polypropylene) capillaries as inlet channels for the gas and liquid phase and a stainless-steel capillary embedded in the T-junction co-axially aligned with the gas inlet channel where an electrical potential difference was applied by a high voltage power supply. The ground electrode was placed 100 mm below the tip of the outlet channel where an electric field was built. Microbubbles were firstly formed in the T-junction by the pinch-off process of the gas and liquid phase and then went through the electric field for

further observation. It was found that the size of microbubbles reduced with increasing electrical potential difference and the viscosity of the solution had less effect on the final size of microbubbles generated by this device. In addition to reducing the microbubble size, the microbubble throughput increased when an electrical potential difference was applied.

2.3.3 Microfluidic technique and principle

Microfluidics is a multidiscipline subject including engineering, physics, chemistry, biochemistry, nanotechnology and biotechnology that focus on the behaviour, precise control and manipulation of fluid within a small, sub-millimetre scale. It came out in the beginning of the 1980s and is widely applied in the development of inkjet printheads, DNA chips, lab-on-a-chip technology, micro-propulsion, and micro-thermal technologies. The volume of fluids used in microfluidic systems is relatively small, ranging from μl to nl(nanolitre) and even further. The surface tension such as capillary, adhesion and wetting which can be employed through specific design is dominating the microfluidic system because of miniaturization. Thus, sample and reagent volumes is reduced and efficiency and mobility can be improved as the microfluidic process are usually conducted in a miniaturised single chip. The behaviour of fluids at the microscale is different from normal scale fluids in the aspects of surface tension, energy dissipation, and fluidic resistance has significantly influenced the system. Microfluidic investigates the change of these behaviour, and the how they can be worked around or utilized for new applications. At micro scale, the Reynolds number can become very low which leads to the fact that co-flowing fluids could not mix in the traditional sense properly as flow becomes laminar instead of turbulent and molecular transport between them has to be through diffusion.

Besides, better reaction conditions and higher quality products in single and multi-step reactions can be achieved because of the high specificity of chemical and physical properties like concentration, pH, temperature, etc are generated in this microfluidic system. Microfluidic structures include micropneumatic systems such as microsystems for controlling fluids outside like liquid pumps and gas valves, and microfluidic structures for the handling of nanolitre (nl) and picoliter (pl) volumes (Nguyen et al., 2006). Recently, the most successful commercial application of microfluids is the inkjet printheads (Demello, 2006) and the devices can be produced in low cost plastics (Pawell et al. 2013) due to improvement of microfluidic

manufacture. The development of microfluidic technologies has led to the exploitation of application areas in continuous-flow microfluidics, droplet-based microfluidics, digital microfluidics, DNA chips etc. The new fields known as microelectron-mechanical system (MEMS) has also been adopted to fabricate microfluidic devices with sizes varying between 20-1000 micrometers for these applications above and made it possible to manipulate fluids in micrometer scale.

The channel in a microfluidic device is around the same width as a human hair, 70 μm, thus the fluid behaviour at this micrometric scale is closely related to surface, interfacial and capillary forces instead of macroscopic physics which depend on gravitaty.

The behavior of fluids and gases in static and dynamic conditions is based on the discipline of fluid mechanics and the physics at the microscale is mainly dependent on surface, interfacial and capillary forces instead of gravitational laws in macroscopic physics. Surface tension is the elastic tendency of a fluid to minimize its energy state by maintaining the least volume at the surface-air interface. Capillary forces occur when a liquid flow in narrow spaces such as microchannel or porous material and the fluid moves without the assistance of, or even in opposition to, external forces like gravity. It is caused by intermolecular forces between the liquid and surrounding solid surfaces and surface tension and adhesive forces work together to drive the liquid when the diameter of the channel is sufficiently small. The rise and fall of a liquid within a thin capillary channel can be expressed by Jurin's law as:

$$h = \frac{2\sigma \cos\theta_c}{R\rho g} \tag{2.1}$$

where h is the liquid height, σ is surface tension, θ_c is the contact angle of the liquid on the channel wall, ρ is the liquid density, R is the channel radius, and g is the gravitational acceleration.

When analyzing the physical properties of systems in microscale like channels in microfluidic devices, the scaling laws or size reduction effect is introduced. The variation of physical quantities is represented by the size l of the given system or object with constant time, pressure, temperature, etc in a scaling law. For instance, the volume forces such as gravity and inertia, and surface forces such as surface tension and viscosity are considered. The basic scaling law for the ratio of these two classes of forces can generally be present by:

$$\frac{surface forces}{volume forces} \propto \frac{l^2}{l^3} = l^{-1} \tag{2.2}$$

This scaling law reveals that the volume forces which are very important in our daily life become less significant than surface forces when scaling down to the microscale in microsystems. On the contrary, the surface forces have dominated the physical phenomenon and the most common types of forces and their scaling with size are shown in Table 2.1.

Surface tension	**Fluid force/electrostatic force**	**Weight/inertia/electromagnetic**
$F \propto l^1$	$F \propto l^2$	$F \propto l^3$

Table 2.1 Scaling of the most common forces with system size l.

Furthermore, other dimensionless parameter to investigate surface related phenomena such as the flow of a fluid through a microfluidic channel includes the Reynolds number (Re) which is represented by the ratio between inertial forces over viscous forces defined as:

$$Re = \frac{\rho_l v_l L}{\mu_l} \tag{2.3}$$

where L is the most relevant length scale, μ_l is the dynamic viscosity of the liquid, ρ_l is the liquid density, and v_l is the relative velocity. For microchannels, L is equal to $4A/P$ where A is the cross-sectional area of the channel and P is the wetted perimeter of the channel. The Reynolds number is usually much less than 100 and often less than 1 because of the small dimensions of microchannels. Therefore, the flow in this low Reynolds number regime is completely laminar and turbulence flow which occurs when Reynolds number is above the transition point in the range of 2000 will not exist. In laminar flow, molecules can be transported in a relatively predictable manner through microchannels. However, momentum-based phenomena such as flow separation still occur even at Reynolds number below 100.

The movement of an object through a fluid or a fluid moves through it bring viscous drag force. This force is caused by displacement of fluid element from the volume that the object occupies when it flows through and it can be expressed as:

$$F_{drag} = Sf_{drag} = \frac{\pi a^2}{4} f_{drag} \tag{2.4}$$

where S is the cross-sectional area of the moving particle, a is the diameter of the particle, f_{drag} is the viscous drag coefficient that is determined by the value of Reynolds number varying from 10^{-4} to 10^{5} (Zhang et al., 2016). In this study, the range of Reynolds number changes from 0.2 to 20 and the drag force can be denoted as:

$$F_{drag} = 3\pi\mu a v_l (1 + 0.15Re^{0.687}) \tag{2.5}$$

where μ is dynamic viscosity, a is the diameter of the particle, v_l is the relative velocity, and Re is Reynolds Number. During the mixing process of different fluids, diffusion plays an important role in the microscale. Molecules suspended in a fluid present random frequent collision because of Brownian motion. The mean square distance that a particle diffuses at time t can be represented by the Einstein-Smolechowski expression as:

$$\langle r^2 \rangle = 6Dt \tag{2.6}$$

where t is time scale, D is the diffusion coefficient, which is expressed according to Stokes-Einstein relationship as:

$$D = \frac{kT}{3\pi\mu a} \tag{2.7}$$

in which T is the temperature, k is the Boltzmann constant ($1.38064 \times 10^{-23}\mathrm{JK}^{-1}$) which represents the interplay between the temperature and diffusion that have positive correlation, μ is dynamic viscosity, and a is the diameter of the particle. Furthermore, smaller diffusion occurs in the microchannels with larger particle size a or higher viscosity μ. Another dimensionless number Peclet number, which stands for the system length and the diffusion length, is a useful parameter when fluid is mixing in microchannels. Peclet number is expressed as:

$$Pe = \frac{Lv}{D} \tag{2.8}$$

where L is characteristic length (dimension of the channel), v is average velocity (fluid velocity) and D is diffusion coefficient. It can be used to evaluate and compare the importance of convection to diffusion. If $Pe \gg 1$, the diffusion length is much shorter than the system size and gradients can be very high thus convection has dominated particle transport in flow. On

the other hand, if $Pe \ll 1$, the diffusion length is much longer than the system size which means diffusion is the primary component (Clift, Grace, & Weber, 2005).

The pressure drop can be evaluated by using the Poiseuille equation in a laminar flow of viscous and incompressible fluid as shown below:

$$\Delta p = \frac{8\mu LQ}{\pi R^4} \tag{2.9}$$

where Δp is the pressure drop, Q is the volumetric flow rate, L is the length of the channel, R is radius of the channel and μ is the dynamic fluid viscosity.

The fluid driven through microchannels can be achieved by two common methods. In this study, the fluid is pushed through the device via positive displacement pumps, such as syringe pumps which is called pressure driven flow. According to the basic laws of fluid mechanics for pressure driven laminar flow, the fluid velocity at the walls must be zero which is called no-slip boundary condition. This results in a parabolic velocity profile within the channel shown in Figure 2.24.

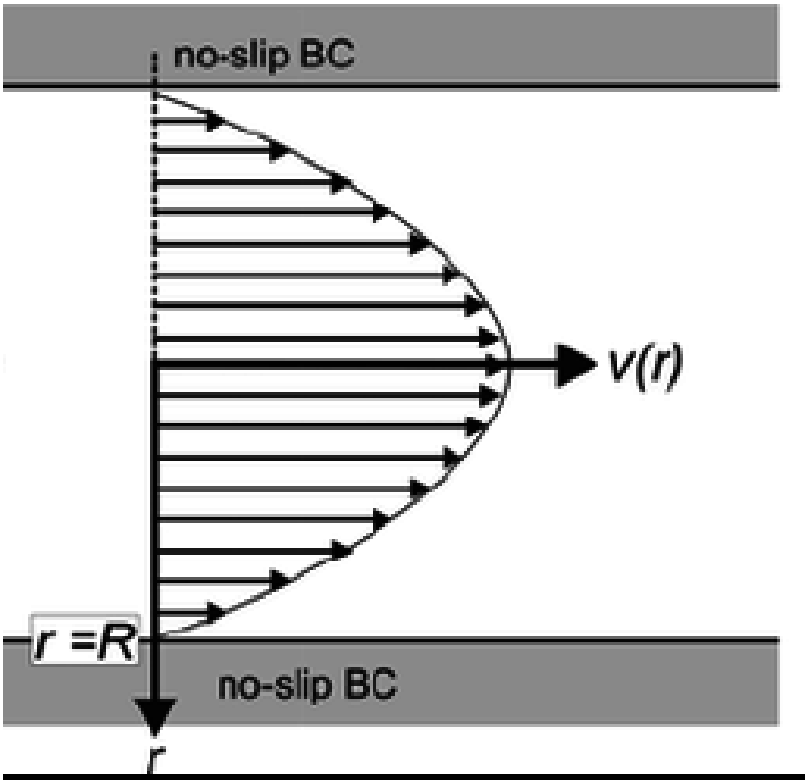

Figure 2.24 Fluid flow in the channel with no-slip boundary condition.

The parabolic velocity profile has played an important role in the distribution of molecules transported with a channel. Pressure driven flow has advantage of low cost and repeatability to pump fluid through microdevices compared to other approaches such as electrokinetic flow. Therefore, pressure driven flow has been used in miniaturization with increasing efforts at developing microfluidic devices.

2.3.4 Microfluidic processing setup

A microfluidic system to generate microbubbles comprises several components which consists of a microprocessor controlled pump for injecting the fluids into the system actuating fluid inside the microfluidic chip, microchannels for fluid transport, valve controlled gas tank which brings pressure the fluid and drive the flow mixing, and a high-speed camera which is used to observe the microbubbles generated and capture images (see Figure 2.25).

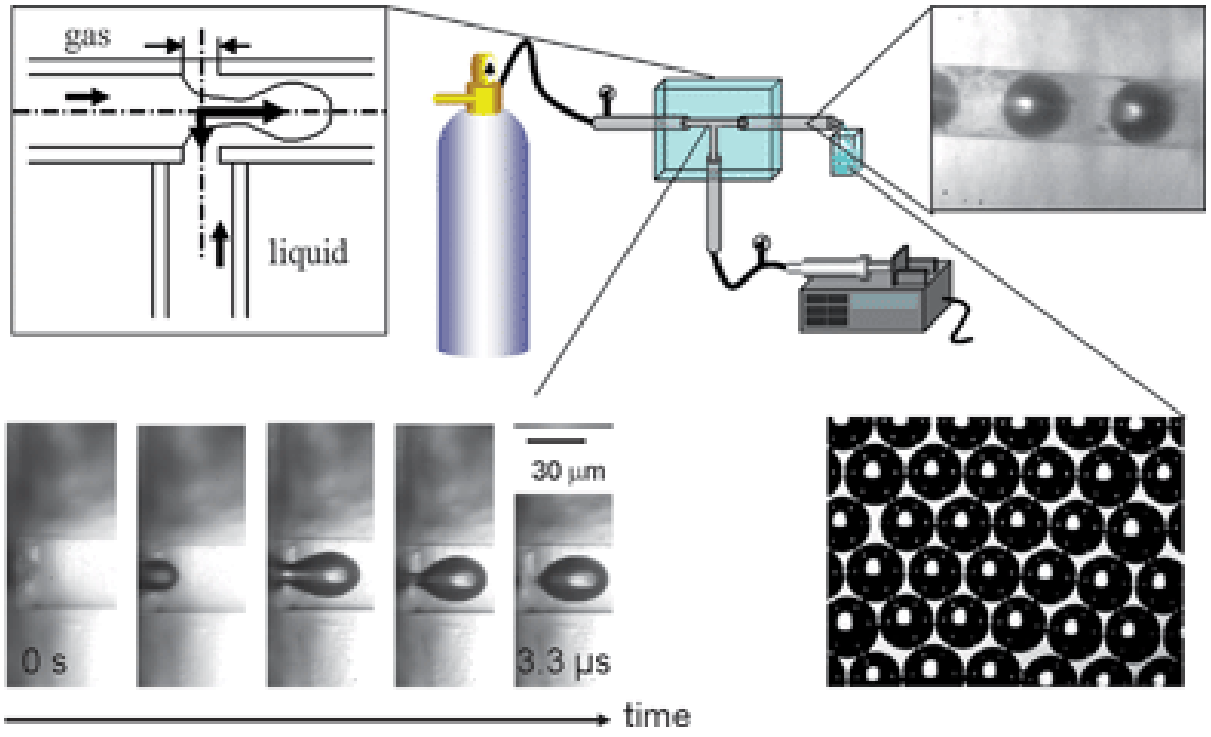

Figure 2.25 The experimental setup generation microbubbles with a T-junction device

(Stride & Edirisinghe, 2008).

Therefore, microbubbles can be frequently generated in this microfluidic system because of precise control on gas pressure, flow rate of the liquid phase, mixing and residence time (Garstecki, 2010). Microfluidic chips are the most commonly used in microfluidic systems

and they can be manufactured using methods such as soft lithography and mechanical processing with materials like PDMS, gas and silicone (Iliescu et al., 2012; McDonald & Whitesides, 2000). To date, various microfluidic chips with different designs and geometries such as flow focusing, co-axial capillaries, co-flow, and capillary inserted junction like T-junction have been investigated in microfluidic field. In terms of a simple T-junction microfluidic chip, the gas phase and liquid phase flow through microchannels and are forced to meet at the outlet of the junction by fluid flow and pressure. The tip of the gas stream forms a cavity and then turns to a growing bubble until it is pinched off and releases as a bubble in the outlet channel which is shown in Figure 2.26.

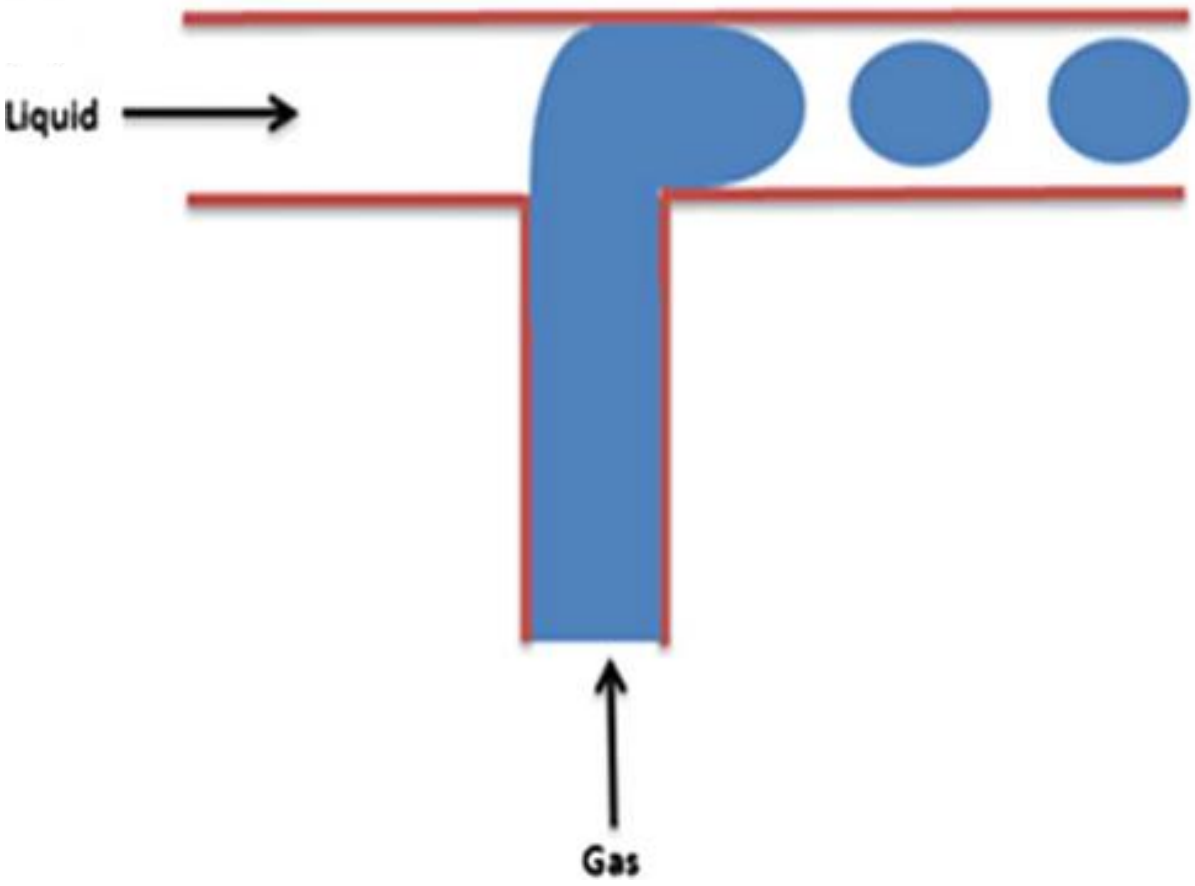

Figure 2.26 Gas-liquid streams in a T-junction device.

Hence, the gas-liquid interface at the outlet of this microfluidic device becomes unstable and the impact of a liquid and a gas happened there leads to microbubble generation. Moreover, the pinch-off process where the gaseous tip enters the outlet orifice, inflates a bubble, breaks and retracts upstream in the channel shows a periodic manner due to the

instability (Garstecki & Whitesides, 2006) and uniformly sized, monodisperse microbubbles can be generated periodically in this process. (Kumacheva & Garstecki, 2011).

2.3.5 Microbubble generation mechanism

As microfluidic techniques for high controlled formation of droplets and bubbles become a growing interest, a simple T-junction has been the most frequently used microfluidic geometry to generate immiscible fluid segments. Therefore, the process of break-up and quantitative analysis of the sizes of the droplets/bubbles have attracted a lot of attention. Essentially, for a T-shaped microfluidic junction with rectangular cross-sections of the channels (see Figure 2.27), it was found that at low values of the capillary number which means the interfacial forces have dominated the shear stresses the immiscible threads break-up process in T-junctions is dominated by the pressure drop across the droplet or bubbles as it forms. The break-up process is similar to the rate-of-flow controlled break-up in this squeezing regime for flow-focusing geometries. The size of the droplets or bubbles is determined only by the ratio of the volumetric rates of flow of the two immiscible fluids regardless of fluid material parameters such as viscosities and interfacial tension. Thus, the scaling law for the size of the discrete fluid segments can be expressed as:

$$L/w = 1 + \beta\, Q_{in}/Q_{out} \tag{2.10}$$

where L is the length of the immiscible slug, w is the width of the channel, $Q_{in/out}$ are the rates of flow of the dispersed and carrier fluids respectively, and β is a constant of order one which depends on the geometry of the T-junction. Because the capillary number is typically small, there are not sufficient shear stresses applied on the interface of the emerging droplet/bubble to distort it significantly. As a result, the droplet/bubble blocks the whole cross-section of the microchannel and forced the flow of the carrier fluid to form thin wetting films on the wall of the channels. The pressure upstream of the emerging droplet/bubble increases due to the blockage of the channel and thus the neck of the immiscible thread is squeezed under this pressure. The squeezing process continuous at a rate which is proportional to the rate of flow of the carrier fluid while the growth of the droplet/bubble continuous at a rate which is proportional to the rate of flow of the dispersed phase in turn. In this specific microsystem, the squeezing mechanism of break-up is achieved by the

blockage of the channel using a liquid or gas slug and contribute to the formulation of a simple scaling law which predicts the size of droplets and bubbles generated in microfluidic T-junction (Garstecki et al.,2006).

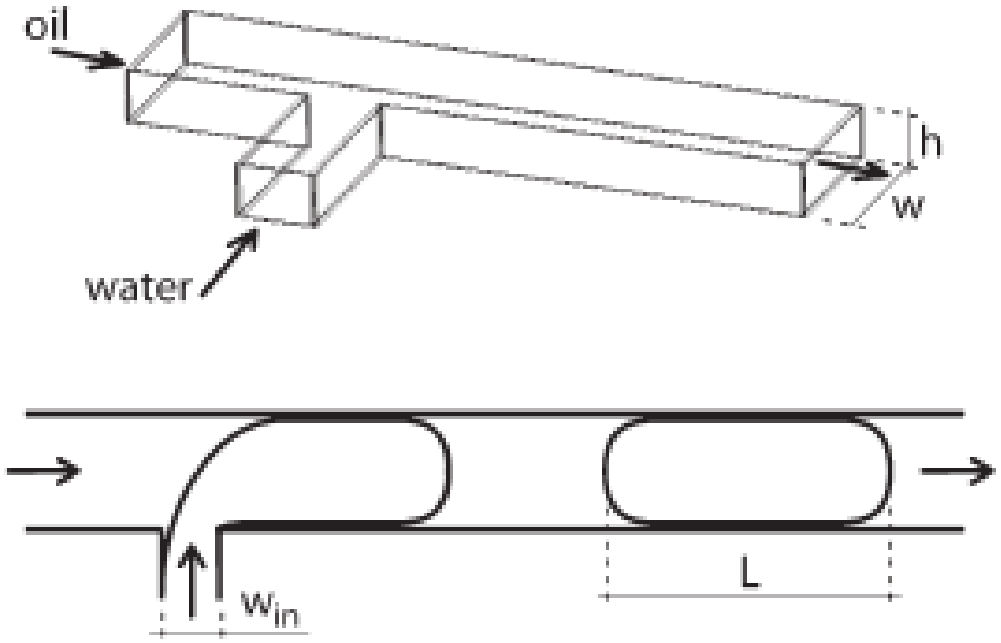

Figure 2.27 The illustration of the microfluidic T-junction with rectangular channels (Garstecki et al.,2006).

2.5.6 Multiple phase flow in microchannels

The flow types can be classified into simple mono-phase flows like single fluid flow, and complex multiphase flows which contains more than one phase or component (liquid/gas, solid/gas or gas/particle) based on device and application types. Generally, the majority of multiphase refers to the two-phase flow and because of the potential in heat and mass transfer the two immiscible phases are often circulated in microfluidic systems. Several engineering applications based on this concept such as microexchangers for cooling integrated circuits have been investigated and the micronization of the system becomes possible. The microexhanger can mitigate passive cooling stress with increasing power needs

and heat emission from any transistor based device by using liquid to absorb the heat while flows inside a copper channel through the energy-consuming array of transistors and subjected to phase transition to gas. Thus, the system becomes a typical flow of two immiscible phases in a microchannel (Kee et al.,2011). Besides, the application in emulsion bases system such as microdroplet dispensers have also been developed, however, due to the complexity of physics in liquid-liquid systems compared to singe liquid phases, it is often found in inkjet printers (Umbanhowar et al., 2000).

In macrometric system, two-component flows are also known as diphasic flows and have been studied mainly in power industries. Instead of ignoring gravitational forces at the microscale, the directions of flow parameters are commonly used in macrometric systems. The behavior of diphasic flow is generally complex as interfaces can generate elaborate forms and regimes need to be classified in phase diagrams with unclear boundaries. Several regimes of flow can be identified as bubble, slug/plug, annular, churn and wispy annular (see Figure 2.28) in diphasic flow based on the ratio of two phases co-flowing in the channel. Different flow regimes can be obtained by regulating the flow rates, characteristics of the fluids and diameter of the channel depending on the specific applications if necessary (Tabeling &Chen, 2010).

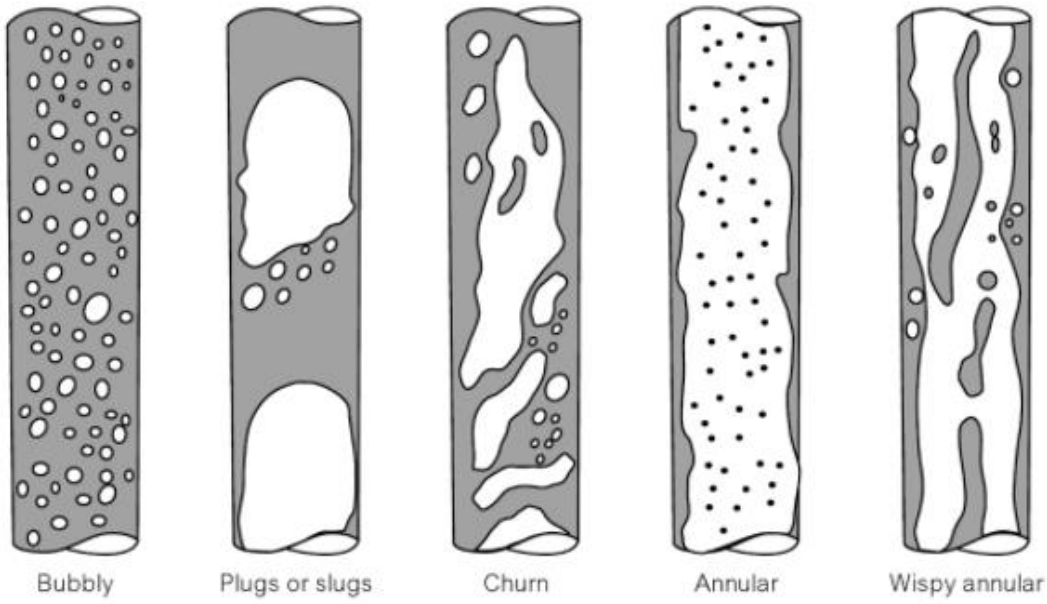

Figure 2.28 Schematic illustration displaying a typical microbubble (Tabeling &Chen,2010).

In microchannel multiphase flow, viscous stress and capillarity are more significant than in macroscopic systems. The viscous and capillary forces F_v and F_c respectively applied on a bubble can be expressed as:

$$F_v \sim \mu l U \quad \text{and } F_c \sim \sigma l \tag{2.11}$$

where l is the bubble size, U is the flow velocity in a microchannel, μ is the fluid viscosity and σ is the surface tension. The dimensionless parameter capillary number Ca is introduced to describe the competition of these two forces:

$$Ca = \frac{\mu l U}{\sigma l} = \frac{\mu U}{\sigma} \tag{2.12}$$

where l is the bubble size, U is the flow velocity in a microchannel, μ is the fluid viscosity and σ is the surface tension. According to the scaling law mentioned before, it can be concluded that both of these forces are single dimensional and vary proportionally to l:

$$Ca \sim l \tag{2.13}$$

It can be noticed that in microscale, when $l \ll 1$ capillary, interfacial forces are relatively more significant than the viscous forces and the microchannels becomes low capillary number systems. Normally, the capillary number can be considered to vary between 10^{-3} and 10^{-1} for microchannel based systems. While, in order to achieve well-defined structures (such as spherical drops) and reduce interfacial tension surfactants are usually used in both liquid-liquid and water-oil systems. Thus the contribution from surfactant has to be considered. When Ca is small, surface tension is has dominated the system generating spherical bubbles and drops. The flow plays a kinematic role in maintaining spherical drops without deformation along with the fluid flux. When Ca is moderate, the effect of viscous forces become obvious and structures is will be subjected to deformations. The flow can influence interfaces along stream lines thus affecting morphologies. The study of this influence was conducted in a diphasic system of tetradecane-water demonstration that spherical, stratified regimes, pears, necklace types of droplet morphology depended on the presence of a surfactant which used to maintain interfacial boundaries (Dreyfus et al., 2003).

2.6 Summary

A review of the numerical approaches used in the recent computational fluid dynamic research on microfluidic studies and microbubble fundamentals have been given in this chapter. Most of the literature (Kashid et al., 2005; Qian et al., 2006; Santos et al., 2009) chose mesh based Volume of Fluid (VOF) method integrated in commercial CFD software like ANSYS FLUENT and other in-house developed fluid dynamic numerical tools, except for Bashir et al. (2011) who used two-phase Level Set method, and Yu et al. (2007) who implemented the Lattice Boltzmann method which simulated flow and collision process via a limited number of particles. Moreover, it is found in the literature above that the velocity patterns like internal circulations and slug flow generation have been studied in the work of Kashid et al. (2005). Besides, Qian et al. (2006) also investigate the effect of gas/liquid velocity, Reynolds number and Capillary number on the slug length while Santos et al. (2009) focused on the flow patterns, slug fraction in the channel and the influence of surface tension on the slug length in a 3D simulation. In addition, Bashir et al. (2011) and Yu et al. (2007) also found out the correlations between the characters of bubble/slug, such as shape and size produced by these microfluidic devices, and the inlet boundary conditions such as gas/liquid velocity and gas/liquid ratio as well as other physical properties through 2D or 3D numerical simulations. These simulation results were then compared with the experiments and reasonable agreement was achieved. Therefore, the bubble/slug generation process can be predicted by numerical simulation with acceptable accuracy.

For experimental study of the fundamentals of microbubbles, microbubble generation methods and mechanism, microfluidic techniques and principles, processing setup and multiple phase flow in microfluidic devices have been discussed. It can be found that microfluidic techniques such as microfluidic chips are widely used in microbubble/droplet generation research.

The computational modelling helps to analyse multiple fluids mixing and microbubble generation phenomenon in microfluidic devices which can’t be observed clearly in experiments. Physical parameters change such as velocity, viscosity, and surface tension during these phenomena can be monitored for further investigation. It also saves more time and money instead of experiments and has the potential to predict the experiment

expectation. Meanwhile, experiment helps to validate the reality of computational simulation and experimental procedures can be modified from numerical prediction. Therefore, in this thesis, a combination numerical simulation and experiments approach is used to investigate a novel capillary embedded microfluidic K-junction microbubble generation and multiple fluids mixing. Quantitative comparison between computation simulation and experimental measurements under varies gas to liquid velocity flow ratio and liquid viscosity will be conducted. In addition, the agreement and difference from the comparison will be discussed in this study.

Chapter 3 : Numerical Methods

3.1 Overview

In this chapter, numerical methods applied in this study for microfluidic research have been introduced in detail. The mathematic modelling of basic physical phenomena is presented in section 3.2. Different numerical treatment for solving the Navier-Stokes equations including temporal and spatial discretization are discussed in section 3.3. Section 3.4 presents the interface tracking method commonly used to solve fluid problems with moving boundaries and interfaces. The Volume of Fluid (VOF) method which is used in this work has been presented particularly in this section along with the surface tension and contact angle model. Section 3.5 will summarise this chapter.

3.2 Mathematic Modelling

Partial differential equations are commonly used to describe physical phenomena such as heat transfer, wave propagation, structural stresses, and fluid dynamics. These equations involve rates of change with respect to continuous variables in an infinitesimal volume.

3.2.1 Conservation Laws

The fundamental conservation laws in computational fluid dynamics are the continuity, momentum and energy conservation equations. The three basic physical principles, which are obeyed by general fluid dynamics, are:

(1) Mass is conserved;

(2) Momentum is conserved: the change of momentum equals the sum of forces on a fluid particle/volume;

(3) Energy is conserved: First law of thermodynamics, the change of energy equals the sum of rate of heat addition to and work done on fluid particle.

For example, the change of mass in a volume is shown as:

$$\frac{dm}{dt} = m_{in} - m_{out} \tag{3.1}$$

If $m_{in} - m_{out} = 0$, then

$$\frac{dm}{dt} = 0 \tag{3.2}$$

which means

$$m = const \tag{3.3}$$

where m stands for the total mass, m_{in} and m_{out} are the mass in/out of the object respectively, and t is the time scale.

3.2.2 Navier-Stokes Equation

In many cases, fluids such as plain water, air, alcohol can be treated as Newtonian, in which the viscous stresses arise from the fluid's flow, and at every point are linearly proportional to the local strain rate. Also, it's the fluid's deformation changes over time. In terms of the non-Newtonian fluids including blood, toothpaste, and soap solutions, the fluid's viscosity changes with the applied stress. For Newtonian fluids the change of shear stresses is proportional to the velocity gradients, and such a relationship is expressed shown in:

$$\varepsilon_{ij} = \mu(\frac{\partial u_i}{\partial x_j} + \frac{\partial u_j}{\partial x_i}) \tag{3.4}$$

where μ is the dynamic or molecular viscosity of the fluid, u_i and u_j are velocity profiles, x_j and x_i are spatial coordination.

Based upon the mass, momentum and energy conservation, the continuity, momentum and energy equations can be derived as follows:

Continuity equation: $$\frac{\partial \rho}{\partial t} + \nabla \cdot (\rho u) = 0 \tag{3.5}$$

Momentum equation: $$\frac{\partial}{\partial t}(\rho u) = -\nabla \cdot (\rho u u) + f_{in} + \nabla \cdot (-pI + \varepsilon) \tag{3.6}$$

Energy equation: $$\rho c_v \frac{\partial T}{\partial t} + \rho c_v u_i \frac{\partial T}{\partial x_i} = -p \frac{\partial u_i}{\partial x_i} + \lambda \frac{\partial^2 T}{\partial x_i^2} - \tau_{ij} \frac{\partial u_j}{\partial x_i} \tag{3.7}$$

where ρ stands for density, u u_i, u_j stand for velocity profiles, I denotes the diagonal unit matrix, ε is the shear stress, f_{in} is the internal force, p is the static pressure, T is the temperature, t is the time scale, x_j and x_i are spatial coordination components, c_v is specific heat, λ represents thermal conductivity, and τ_{ij} is the viscous stress.

Assuming that the fluid is also incompressible, which means that the density ρ does not depend on pressure and $\frac{\partial \rho}{\partial t} = 0$ – then continuity equation (3.5) reduces to $\nabla \cdot u = 0$, the first term on the right-hand side of the momentum equation (3.6) can be rearranged as:

$$\nabla \cdot (\rho u u) = u \cdot \nabla(\rho u) + \rho u(\nabla \cdot u) = \rho(u \cdot \nabla)u \tag{3.8}$$

Then the Navier-Stokes equations can be rewriten as:

$$\rho\left(\frac{\partial u}{\partial t} + (u \cdot \nabla)u\right) = -\nabla p + \nabla \cdot \left(\mu(\nabla u + \nabla u^T)\right) + f_{in} \tag{3.9}$$

$$\nabla \cdot u = 0 \tag{3.10}$$

where ρ represents density, u is the velocity profile, p is the static pressure, t is the time scale, μ is the dynamic viscosity, and f_{in} is the internal force. These equations represents flows of incompressible Newtonian fluids in a mathematic form.

3.2.3 Boundary and initial conditions

When solving the Navier-Stokes equations, appropriate boundary and initial conditions which are usually specific in nature and other studies should be applied. These conditions are able to confine the problem to a smaller spatial sub region or domain and a specific temporal extent, which helps to simplify the modelling procedure and also reduce the required effort to obtain a solution. Boundary conditions are a necessary component of the mathematical model and are able to set the motion of flow and specify fluxes into the computational domain such as mass, momentum, and energy. It is of particularly advantage to utilize all existing symmetry axes to further shrink the computational domain, in which fluid and solid regions are represented by cell zones, material and the source terms are assigned to cell zones. Therefore, boundaries and internal surfaces are represented by face zones with boundary data being assigned to face zones as well.

Boundary conditions usually are divided into two distinct types: i.e. 1) the Dirichlet conditions, which prescribe the value of a variable at the boundary, e.g. $u(x) = constant$, and 2) the Neumann, also called natural, which prescribes the gradient normal to the boundary of a variable at the boundary, e.g. $\partial_n u(x) = constant$. When using a mixed boundary condition, a function of the form $au(x) + b\partial_n u(x) = constant$ can be applied. These conditions are usually prescribed at inlets to set inflow velocities or at impermeable walls to fix the velocity of the fluid to the domain of the wall. Besides, a range of boundary conditions types allowing the flow to enter and exit the solution domain are as follows:

1) **General**: pressure inlet, pressure outlet.

2) **Incompressible flows**: velocity inlet, outflow.

3) **Compressible flows**: mass flow inlet, pressure far-field.

For pressure inlet boundary, we usually define the total gauge pressure, temperature, and other scalar quantities at flow inlets:

$$p_{total} = p_{static} + \frac{1}{2}\rho u^2 \tag{3.11}$$

$$p_{total} = p_{static}(1 + \frac{\gamma-1}{2}M^2)^{\gamma/(\gamma-1)} \tag{3.12}$$

where equation (3.11) is for incompressible flows and equation (3.12) is for compressible flows, γ is the ratio of specific heats (c_p/c_v), M is the Mach number, ρ represents density, and u is the velocity. If the inlet flow is supersonic, the static pressure should also be specified. The pressure outlet boundary is defined as the static/gauge pressure of the environment at the outlet which the flow exhausts and usually keeps constant.

Another commonly used inlet condition is the velocity, which defines velocity vector and scalar properties of flow with uniform profile as the default. The total properties of flow are not fixed and the stagnation properties vary to accommodate prescribed velocity distribution.

An outflow boundary condition is used to specify how flow exits the computational domain. The exit flow is usually considered as fully developed, where all flow variables except

pressure is assumed as a zero-normal gradient and an overall mass balance correction is applied. Other inlet and outlet boundary conditions include mass flow inlet, pressure far field, exhaust fan/outlet vent, and inlet vent/intake fan which could be used in other specific cases.

Besides, wall boundaries are also used to bound fluid and solid regions. In viscous flows, no-slip condition is applied at walls meaning that tangential fluid velocity equal to wall velocity and normal velocity component is set to be zero. Alternatively, the shear stress can be specified as well. When heat transfer is involved, thermal boundary condition is adopted and the wall material and thickness can be defined for 1-D or in-plane through heat transfer calculations. When field and geometry is symmetric which means zero normal velocity at symmetry plane and zero normal gradients of all variables at symmetry plane, a symmetry boundary condition could be used to reduce computational effort in the simulation and also to model slip walls in viscous flow.

Initial conditions, such as specified velocities and pressures, must be prescribed throughout the domain, in addition to the boundary conditions, expecially for applications where the temporal evolution needs to be simulated (unsteady simulations). It is advantageous to define a good initial assumption so that the nonlinear solver will converge faster for stationary calculations. The fluid region parameters, boundary conditions, and initial conditions work together to specific the model problem.

3.2.4 Multiple phase flow

Generally, the concept of phases includes properties like velocity, temperature, or characteristic length scale of the matter. For example, if the case involves the bubbles with gas core and liquid shell which are very close to each other and have different diameter, and /or move with different velocities, and/or have different temperatures, they could also be considered different phases. In most cases, two-phase flows are the most widely used model in investigating multiple phase flow problem. It can be treated in the same method as single-phase flows that two different fluids can be handled either by using two separate sets of Navier-Stokes equations for each fluid, or alternatively using the same set of equations for both fluid but with variable density and viscosity fields as shown below:

$$\rho(x)\left(\frac{\partial u}{\partial t} + (u \cdot \nabla)u\right) = -\nabla \mathrm{p} + \nabla \cdot \left(\mu(x)(\nabla u + \nabla u^T)\right) + f_{in} \tag{3.13}$$

$$\nabla \cdot u = 0 \tag{3.14}$$

where $\rho(x)$ and $\mu(x)$ are density and dynamic viscosity depending on the spatial coordinate x respectively, u is the velocity, t is the time scale, p is the static pressure, and f_{in} is the internal force. Then the next step is to apply a method to locate the position of each fluid so that the correct value of the density and viscosity is chosen at each point, and such a step is used by the interface tracking techniques. If the two fluids are immiscible, interfaces separating the different fluids or phases will exist. Internal boundary conditions have to be defined to link the different fluids together on these interfaces. As there is no loss or gain mass (no chemical reactions) for incompressible fluids, the normal velocity on both sides of the interface must be equal and therefore there is no need for the extra modelling of inter-phase interaction.

3.2.5 Surface tension

Immiscibility of two fluid is a result of strong cohesion forces between their molecules depending on the nature of the fluids. The experimentally determined surface tension coefficient σ expresses the ease with which the fluid can be mixed. σ is defined as the amount of work necessary to create a unit area of free surface which refers to the interface between two immiscible fluids. Surface tension effects are included in a phase interaction when the surface tension force model is active. There are in general two methods to integrate surface tension effects into the Naiver-Stokes equations. The force balance boundary condition can be applied directly to the interface Γ as follows:

$$[-pI + \mu(\nabla u + (\nabla u)^T)] \,|_\Gamma \cdot \hat{n} = \sigma\kappa\hat{n} \tag{3.15}$$

where $\hat{n}$ represents the unit normal at the interface, p is the static pressure, I denotes the diagonal unit matrix, u is the velocity, μ is the dynamic viscosity, σ is surface tension coefficient, and κ is the curvature of the interface. It has been revealed that the difference between the combination of pressure and viscous forces has to be equal to the result of σ and κ. The surface tension coefficient σ is significantly influenced by the two fluids in contact, temperature and chemical impurities on the interfaces. The internal force boundary condition can also be evaluated as a volumetric force in the form of:

$$f_{st} = \sigma\kappa\hat{n}\delta(\Gamma, x) \tag{3.16}$$

where $\delta(\Gamma, x)$ is the Dirac-delta function distributing the surface tension force to the interface, σ is surface tension coefficient, κ is the curvature of the interface, and $\hat{n}$ is the unit normal at the interface. This method is commonly used by the computational fluid dynamic research because of feature of easy. The detail of the interface conditions is derived by A. Smolianski (2001).

The surface tension coefficient varies across the free surface when Marangoni convection occurs as a concentration or temperature gradient exists across the free surface and this effect can be neglected if the spatial variation of surface tension coefficients is small enough. Surface tension always exists between a given pair of fluids and its magnitude depends on the nature of the fluids in contact and temperature.

When an interface is in contact with a wall or solid boundary, a *contact angle* will be present. The contact angle is influenced by several factors such as the two fluids, the material properties, roughness of the solid boundary, and the magnitude and sign of the contact line velocity (in the non-static case). A value of contact angle smaller than $90°$ represents that the phase is wetting the wall, as described in the Figure 3.1.

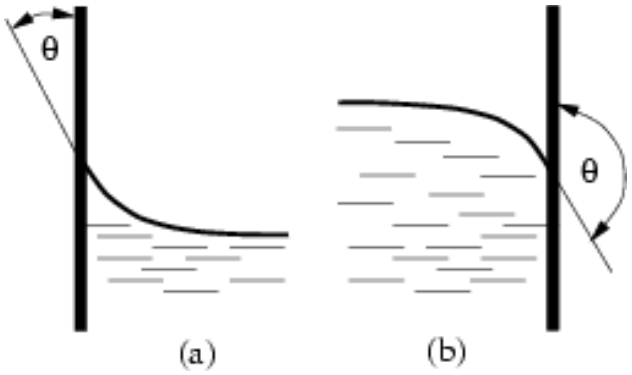

Figure 3.1 *Free surface in contact with a solid wall (a) contact angel less than* $90°$ *(b) contact angle more than* $90°$.

3.2.6 Nondimensionalization

Dimensionless numbers are used to identify which physical effects are dominating, and also assist with classifying different model problems. The length scale L, characteristic velocity U, and the subsequent scaling of the variables involved are introduced as follows:

$$x_i' = \frac{x_i}{L}, \mathrm{u}' = \frac{u}{U}, p' = \frac{p}{\rho U^2}, t' = \frac{tU}{L} \tag{3.17}$$

where L is the length scale, U is the characteristic velocity, ρ is the density, x_i is the spatial coordination, u is the velocity profile, p is the static pressure, and t is the time scale. The Navier-Stokes equations can be rewriting in the form of

$$\rho(\frac{U^2}{L}\frac{\partial u'}{\partial t'} + \frac{U^2}{L}(u' \cdot \nabla')u' = -\frac{\rho U^2}{L}\nabla' p' + \nabla' \cdot \frac{U}{L^2}\left(\mu(\nabla' u' + \nabla' u'^T)\right) + S_f \tag{3.18}$$

$$\nabla' \cdot u' = 0 \tag{3.19}$$

where L is the length scale, U is the characteristic velocity, ρ is the density, x_i is the spatial coordination, u is the velocity profile, p is the static pressure, t is the time scale, μ is the dynamic viscosity, and S_f is the source term. After multiplying the factor $L/\rho U^2$, the equation above is rearranged as

$$\frac{\partial u}{\partial t} + (u \cdot \nabla)u = -\nabla p + \nabla \cdot \left(\frac{\mu}{\rho U L}(\nabla u + \nabla u^T)\right) + \frac{L}{\rho U^2} S_f \tag{3.20}$$

$$\nabla \cdot u = 0 \tag{3.21}$$

where u is the velocity profile, t is the time scale, p is the static pressure, μ is the dynamic viscosity, L is the length scale, U is the characteristic velocity, ρ is the density, and S_f is the source term. The prime notation has been dropped in equation (3.21) and (3.22). The Reynolds number can then be identified as the inverse of the nondimensional group in front of the viscous term which is:

$$Re = \frac{\rho U L}{\mu} \tag{3.22}$$

where ρ is the density, L is the length scale, U is the characteristic velocity, and μ is the dynamic viscosity. It is an important dimensionless factor in fluid mechanics used to help predict flow patterns in different fluid flow situations such as laminar and turbulent flow based on the transition-critical Reynolds number value. This scale factor also reveals inertial forces to viscous forces making high Re number represent that the nonlinear convective terms dominate over the viscous terms and turbulent if its value exceeds the transition point; whereas, for a low Re number the flow is viscous and laminar.

The source term S_f on the right-hand side in equation (3.20) indicates that all imposed forces relevant to two-phase flow applications such as gravitational and surface tension forces will be considered. The gravitational and volume force formulation of the surface tension forces equation (3.16) result in the source term below:

$$S_f = \rho g + \sigma \kappa \hat{n} \delta(\Gamma, x) \tag{3.23}$$

where ρ is the density, g is the gravitational acceleration, $\delta(\Gamma, x)$ is the Dirac-delta function distributing the surface tension force to the interface, σ is surface tension coefficient, κ is the curvature of the interface, and $\hat{n}$ is the unit normal at the interface. When introducing the scaling of variables above gives:

$$S_f{}' = \frac{Lg}{U^2} + \frac{\sigma}{\rho U^2 L} \kappa' \hat{n} \delta(\Gamma, x) \tag{3.24}$$

in which L is the length scale, U is the characteristic velocity, g is the gravitational acceleration, σ is surface tension coefficient, ρ is the density, $\delta(\Gamma, x)$ is the Dirac-delta function distributing the surface tension force to the interface, κ is the curvature of the interface, and $\hat{n}$ is the unit normal at the interface. κ is proportional to $\partial^2 f / \partial x_i^2$ and thus scales as $\kappa' = L^2 \kappa$. Other two nondimensional parameters can be defined which are the Froude and Webber numbers:

$$Fr = \frac{U^2}{gL}, We = \frac{\rho U^2 L}{\sigma} \tag{3.25}$$

in which L is the length scale, U is the characteristic velocity, g is the gravitational acceleration, ρ is the density, and σ is surface tension coefficient. They illustrate inertial to gravitational effects where g is the gravitational constant and inertial to surface tension effects. Additionally, the capillary number is also further used to reveal the relative effect of viscous forces versus surface tension across an interface between two immiscible fluids, which is defined as:

$$Ca = \frac{\mu u}{\sigma} \tag{3.26}$$

where u is the characteristic velocity, and μ is the dynamic viscosity, and σ is surface tension coefficient. The value of capillary number is independent of units in the system and low

capillary number (usually less than 10^{-5}) represents that capillary forces have dominate the flow while high capillary number means that the capillary forces are negligible compared to the viscous forces. In this study, the range of capillary number varies from 0.005 to 0.02 therefore the viscos forces relatively less significant than interfacial forces.

Besides, another helpful dimensionless number which will determine whether the continuum mechanics formulation of fluid dynamic is valid, namely the Knudsen number Kn is defined as

$$Kn = \frac{\zeta}{L} \tag{3.27}$$

in which ζ is the molecular mean free path and L is the characteristic length of the body. For high Reynolds number, the Knudsen number is:

$$Kn = \frac{M}{Re}\sqrt{\frac{\gamma\pi}{2}} \tag{3.28}$$

where M is the Mach number which represents the ratio of flow velocity past a boundary to the local speed of sound, γ is the ratio of specific heats, and the Reynolds number Re is dependent on the length L. Flow situations can be classified into four general regimes as rules of thumb based on the Knudsen number shown below:

$Kn < 0.01$	Continuum
$0.01 < Kn < 0.1$	Slip flow
$0.1 < Kn < 3$	Transitional
$Kn > 3$	Free molecular flow

Navier-Srokes equations are valid when the flow is in the continuum regime and in the slip flow regime with good results and the effects of rarefaction because of slip velocity boundary conditions and temperature increase on the surface. While, for transitional flows a statistical method such as a direct simulation Monte Carlo approach. In the free molecular regime, the molecular collisions can be ignored as the flow is sufficiently rarefied. Hence the

continuum assumption that is built into the Navier-Stokes equations is not applicable to these gas regimes.

3.3 Numerical treatment

The Navier-Stokes equations are difficult or impossible to solve analytically even for simple configurations. For example, the flow in a straight and smooth circular pipe with low flow rate can be predicted and classified as laminar thus an analytical solution called Hagen-Poiseuille flow profile can be derived (White, 1999).

To solve the Navier-Stokes equations by computer, numerical techniques are commonly applied so that these equations are transferred into discretized form. Large amount of couple sub problems were consists of these discrete equations which satisfy the discretion scheme spatially into smaller sub regions and temporally into time steps. This can be then represented as a large inverted matrix system with corresponding discrete and approximate solutions.

3.3.1 Discretization method

The typical discretion methods are finite difference, finite element and finite volume methods. The finite difference method is one of the simplest and the oldest methods to solve differential equations by approximating them with difference equation in which finite differences approximate the derivatives. It was first presented by L. Euler (1707-1768) in one dimension of a space and developed by C. Runge (1856-1927) to two dimension and first used in numerical applications in the early 1950s and further developed by the emergence and proliferation of computers that offered a convenient framework for dealing with complex problems of physics. Today, the finite difference method is an important approach to numerical solutions of partial differential equations (Grossmann et al., 2007). The principle of finite difference methods is similar to the numerical schemes used to solve ordinary differential equations. The derivatives in the equations are replaced by differential quotients in order to approximate the differential operator. The approximations of the solution are calculated at the space and time points which are partitioned from the domain. The error between the numerical solution and the exact solution is determined by the error that is committed by going from a differential operator to a difference operator. This error is called

the discretization error or truncation error which involves that a finite part of a Taylor series is used in the approximation.

The Finite Element Method is a numerical method which is first recognized at the start of the 1940s by Richard Courant for solving problems of engineering and mathematic physics including structural analysis, heat transfer, fluid flow and mass transport. The analytical solution of these problems generally requires the solution to boundary value problems for partial differential equations. These partial differential equations can be solved with analytical methods for most of geometries and problems. Therefore, an approximation of the equations can be constructed based on different types of discretization which approximate the partial differential equations with numerical model equations. The solution to the numerical model equations are approximate values of the real solution to the partial differential equations at discrete number of points over the domain (Logan, 2011). In the Finite Element Method, a large problem is subdivided into smaller, simpler parts namely finite elements and the equations that model these finite elements are then assembled into a larger system of equations that model the whole problem. Variational methods from the calculus of variations are used to approximate a solution by minimizing an associated error function. The benefits of using the finite element method are that it offers great freedom in the selection of discretization, both in the elements that may be used to discrete space and the basic functions and the theory is well developed because of the close relationship between the numerical formulation and the weak formulation of the partial differential equation problem. For example, error estimates or bounds for the error are provided in this method when the numerical model equations are solved on a computer.

In this study, the present numerical simulations are built on the CFD software STAR-CCM+ (CD-adapco Ltd, Melville, New York) which is based on Finite Volume Method. The Finite Volume Method (Ferziger & Peric, 2012) divides the solution domain into a finite number of small control volumes, corresponding to the cells of a computational grid. Application of Gauss' Divergence Theorem on the governing equations converts the volume integrals into surface integrals across the faces of each control volume (i.e. fluxes). These discrete versions of the integral form of the continuum transport equations are applied to each control volume. The object is to obtain a set of linear algebraic equations, with the total number of unknows in each equation system corresponding to the number of cells in the grid.

The resulting linear equations are then solved with an Algebraic Multigrid solver (Shapira, 2008). The governing equation, based on the Finite Volume method, integrated and treated with Guss' Divergence Theorem is expressed as:

$$\frac{d}{dt}\int_V \rho\chi\phi\, dV + \oint_S \rho\phi\left(v - v_g\right)\cdot d\hat{a} = \oint_S \mathrm{D}\Delta\phi\cdot d\hat{a} + \int_V S_\phi\, dV \qquad (3.29)$$

where ρ is the density, ϕ is a scalar quantity, χ is the void fraction, V is the cell volume, v and v_g are velocity and grid velocity respectively, S is the closed surface, $\hat{a}$ is face area vector, D is face diffusivity coefficient, and S_ϕ is the source term. The equation describes the transport of a scalar quantity ϕ in a continuum and the transient term, the convective flux, the diffusive flux, and the volumetric source term have been shown in it from left to right.

As the solution domain has been distributed into small computational cells, the continuous form equation can be rearranged in discrete form after applying to a cell-centred control volume cell-0 as:

$$\frac{d}{dt}(\rho\chi\phi V)_0 + \sum_f[\rho\phi(v\cdot\hat{a} - G)]_f = \sum_f(\mathrm{D}\nabla\phi\cdot\hat{a})_f + (S_\phi V)_0 \qquad (3.30)$$

in which G is the grid flux calculated in equation (3.47), ρ is the density, ϕ is a scalar quantity, χ is the void fraction, v is velocity, $\hat{a}$ is face area vector, D is face diffusivity coefficient, S_ϕ is the source term, and V is the cell volume. In the following chapter, the issues of approximations used to represent each term of this equation will be addressed within the framework of finite volume method.

3.3.2 Temporal discretization

Temporal discretization is a mathematical technique used to solve transient problem that occur in the fields of applied physics and engineering. In the numerical discretization process, an important stage is to choose an appropriate time stepping scheme. It should be accurate in time and consider the convenience and computational effort and cost. Temporal discretization involves the integration of every term in different equations over a time step Δt on the general discretized equation. First and second order schemes are available in steady and implicit unsteady forms for temporal discretization. The algorithms described above were implemented in STAR-CCM+ (CD-adapco Ltd, Melville, New York). Explicit temporal schemes

are only available for a limited flow modelling schemes, such as the laminar coupled energy model. The problem in this study is unsteady flow problem, and therefore requires solutions in which position varies as a function of time. The integration of transient terms is shown below as a generic expression for the time evolution of a variable ϕ is given by:

$$\frac{\partial \phi}{\partial t} = F(\phi) \tag{3.31}$$

where ϕ is a scalar quantity and t is the time scale. The function F incorporates any spatial discretization. If the time derivative is discretized using backward differences, the first-order accurate temporal discretization can be written as:

$$\frac{\phi^{n+1}-\phi^{n}}{\Delta t} = F(\phi) \tag{3.32}$$

and the second order discretization is written as:

$$\frac{3\phi^{n+1}-4\phi^{n}+\phi^{n-1}}{2\Delta t} = F(\phi) \tag{3.33}$$

where ϕ is a scalar quantity, $n+1$ is the value at the next time level at $t+\Delta t$, n is the value at the current time level at t, and $n-1$ is the value at the previous time level at $t-\Delta t$. The function $F(\phi)$ can be evaluated using time integration which can be classified as explicit and implicit scheme based on the integral form of the equation:

$$\frac{\phi^{n+1}-\phi^{n}}{\Delta t} = \omega \cdot F(\phi^{n+1}) + (1-\omega) \cdot F(\phi^{n}) \tag{3.34}$$

where ω is a weighting factor between 0 and 1, ϕ is a scalar quantity, $n+1$ is the value at the next time level at $t+\Delta t$, n is the value at the current time level at t, Δt is the time step, and t is the time scale. The value of $\omega = 0$ means the fully explicit scheme, $\omega = 1$ means the fully implicit scheme, and $\omega = 0.5$ means the Crank-Nicolson scheme. This integration is valid for any discretized variable at any control volume. When applied to the full discretized diffusion, convection, and source terms, the following equation is obtained:

$$\int_{t}^{t+\Delta t} F(\phi)dt = [\omega \cdot F_{\phi}^{t+\Delta t} + (1-\omega) \cdot F_{\phi}^{t}]\Delta t \tag{3.35}$$

where ϕ is a scalar quantity, t is the time scale, Δt is the time step, ω is a weighting factor. For the implicit time integration, the function $F(\phi)$ can the evaluate at the future time level:

$$\frac{\phi^{n+1}-\phi^{n}}{\Delta t} = F(\phi^{n+1}) \tag{3.36}$$

where ϕ is a scalar quantity, t is the time scale, Δt is the time step, $n+1$ is the value at the next time level at $t + \Delta t$, and n is the value at the current time level at t. This is referred to as implicit integration since ϕ^{n+1} in a given cell is related to ϕ^{n+1} in neighbouring cells through $F(\phi^{n+1})$:

$$\phi^{n+1} = \phi^{n} + \Delta t F(\phi^{n+1}) \tag{3.37}$$

where ϕ is a scalar quantity, t is the time scale, Δt is the time step, $n+1$ is the value at the next time level at $t + \Delta t$, and n is the value at the current time level at t. The implicit equation can be solved iteratively at each time level before moving to the next time step with the advantage of unconditionally stability.

For the explicit time integration, this method evaluates $F(\phi)$ at the current time level:

$$\frac{\phi^{n+1}-\phi^{n}}{\Delta t} = F(\phi^{n}) \tag{3.38}$$

where ϕ is a scalar quantity, t is the time scale, Δt is the time step, $n+1$ is the value at the next time level at $t + \Delta t$, and n is the value at the current time level at t. Equation (2.39) is called explicit integration because ϕ^{n+1} can be expressed explicitly in terms of the existing solution values ϕ^{n}:

$$\phi^{n+1} = \phi^{n} + \Delta t F(\phi^{n}) \tag{3.39}$$

where ϕ is a scalar quantity, t is the time scale, Δt is the time step, $n+1$ is the value at the next time level at $t + \Delta t$, and n is the value at the current time level at t. The time step Δt is restricted to the stability limit of the underlying solver thus identical time step has to be used in all cells within the domain to keep time accuracy. Besides, the time step must be the minimum of all the local time steps in the domain to maintain stability.

For temporal discretization in the work presented here, the implicit unsteady solver in STAR-CCM+ (CD-adapco Ltd, Melville, New York) is applied which offers two temporal discretization options: first-order and second-order. The First-order temporal scheme which is also called Euler Implicit discretizes the unsteady term using the solution at the current time

level, $n+1$, as well as the one from the previous time level, n, for cell-centred control volume cell-0:

$$\frac{d}{dt}(\rho\chi\phi V)_0 = \frac{(\rho\chi\phi V)_0^{n+1} - (\rho\chi\phi V)_0^n}{\Delta t} \tag{3.40}$$

where ρ is the density, ϕ is a scalar quantity, χ is the void fraction, V is the cell volume, t is the time scale, Δt is the time step, $n+1$ is the value at the next time level at $t+\Delta t$, and n is the value at the current time level at t. The second-order temporal scheme discretization of the unsteady term uses the solution at the current time level, $n+1$, as well as the solutions from the previous two time levels, n and $n-1$, as follows:

$$\frac{d}{dt}(\rho\chi\phi V)_0 = \frac{\{(\alpha^2-1)[(\rho\chi\phi V)_0^{n+1} - (\rho\chi\phi V)_0^n] + [(\rho\chi\phi V)_0^{n-1} - (\rho\chi\phi V)_0^n]\}}{\alpha(\alpha-1)\Delta t^{n+1}} \tag{3.41}$$

And:

$$\alpha = 1 + \frac{\Delta t^{n+1}}{\Delta t^n} \tag{3.42}$$

$$\Delta t^{n+1} = t^{n+1} - t^n \tag{3.43}$$

$$\Delta t^n = t^n - t^{n-1} \tag{3.44}$$

where ρ is the density, ϕ is a scalar quantity, χ is the void fraction, V is the cell volume, t is the time scale, Δt is the time step, $n+1$ is the value at the next time level at $t+\Delta t$, n is the value at the current time level at t, and α is the gradient limiting factor. On the first time-step of a second-order temporal simulation, a first-order discretization is used since only two time levels are available.

With a second-order discretization the source term has been approximated by the product of the value of the integrand, S_ϕ, evaluated at the cell centroid, and the cell volume V:

$$\int_V S_\phi dV = (S_\phi V)_0 \tag{3.45}$$

where S_ϕ is the source term, and V is the cell volume. In this study, a second-order temporal scheme discretization was used in the simulations as it is more accurate than first-order discretization although it is more difficult to converge.

3.3.3 Spatial discretization

First and second order upwind schemes are available options for spatial discretization, with additional possibilities, such as central differencing and bounded central differencing being available. In the CFD software STAR-CCM+ (CD-adapco Ltd, Melville, New York), a collocated mesh topology is used, which means that discrete values of any quantity ϕ are stored at the cell centers. Therefore, face values ϕ_f are required for the convection terms in the equation below and must be interpolated from the cell center values. The convection term at a face of the cell is discretized as:

$$[\phi\rho(v \cdot \hat{a} - G)]_f = (m\phi)_f = m_f\phi_f \tag{3.46}$$

where ϕ_f and m_f are the scalar values and mass flow rates at the face, respectively, G is the grid flux, ρ is the density, and v is velocity. G can be computed from the mesh motion equation:

$$G_f = v_g \cdot \hat{a}_f \tag{3.47}$$

where v_g is the grid velocity and $\hat{a}_f$ is the face area vector.

For the upwind scheme, the face value ϕ_f is derived from quantities in the cell upstream(upwind) relative to the direction of the normal velocity and the manner in which the face value ϕ_f is computed from the cell value has a profound effect on the stability and accuracy of the numerical scheme.

For a first-order upwind scheme, the convective flux is computed as:

$$(m\phi)_f = \begin{cases} m_f\phi_0 & for\ m_f \geq 0 \\ m_f\phi_1 & for\ m_f < 0 \end{cases} \tag{3.48}$$

where m_f is face mass flow rate, ϕ_0 and ϕ_1 are scalar quantities. In this scheme, a dissipative error is introduced to stabilize and help the solver achieve robust convergence. However, this

numerical dissipation also results in smearing discontinuities especially when those discontinuities are not aligned with the grids lines. Thus, the usage of this scheme is limited and would only be applied if the second-order scheme cannot obtain a solution. Actually, it is commonly used to obtain an initial solution using the first-order convection and then switch to the second-order one to obtain a more accurate, final converged solution.

For a second-order upwind scheme, the convective flux is computed as:

$$(m\phi)_f = \begin{cases} m_f \phi_{f,0} & for\ m_f \geq 0 \\ m_f \phi_{f,1} & for\ m_f < 0 \end{cases} \tag{3.49}$$

where m_f is face mass flow rate, $\phi_{f,0}$ and $\phi_{f,1}$ are facial scalar quantities. The face values $\phi_{f,0}$ and $\phi_{f,1}$, are linearly interpolated from the cell values on either side of the face as follows:

$$\phi_{f,0} = \phi_0 + s_0 \cdot (\nabla\phi)_{r,0} \tag{3.50}$$

$$\phi_{f,1} = \phi_1 + s_1 \cdot (\nabla\phi)_{r,1} \tag{3.51}$$

where:

$$\overrightarrow{s_0} = \overrightarrow{x_f} - \overrightarrow{x_0} \tag{3.52}$$

$$\overrightarrow{s_1} = \overrightarrow{x_f} - \overrightarrow{x_1} \tag{3.53}$$

in which $\phi_{f,0}$ and $\phi_{f,1}$ are facial scalar quantities, ϕ_0 and ϕ_1 are scalar quantities, $\overrightarrow{s_0}$ and $\overrightarrow{s_1}$ are vectors between cell face and cell centroids, $\overrightarrow{x_f}$, $\overrightarrow{x_0}$ and $\overrightarrow{x_1}$ are position vectors. $(\nabla\phi)_{r,0}$ and $(\nabla\phi)_{r,1}$ are the limited reconstruction gradients which is calculated using Hybrid Gauss-LSQ gradient method in cells 0 and 1, respectively. The advantage of this scheme over the first-order upwind scheme is that it is nominally second-order accurate. While, limited reconstruction results in the reduction of local extrema but introduces more dissipation than a central-differencing scheme. Generally, the accuracy of this scheme is usually as good or better than the first-order upwind scheme. However, the drawback is that the convergence properties are poorer than the first-order convection because of the reduced numerical dissipation in some situations. In many circumstance, poorer convergence is an acceptable trade-off.

For a central-differencing scheme, the convective flux is computed as:

$$(m\phi)_f = m_f[\omega\phi_0 + (1-\omega)\phi_1] \tag{3.54}$$

where the geometric weighting factor ω is related to the mesh stretching, m_f is face mass flow rate, ϕ, ϕ_0 and ϕ_1 are scalar quantities. It would have a value of 0.5 for a uniform mesh. The accuracy of this scheme is the roughly the same as the second-order scheme but dispersive error is more likely to occur as well as stability problems for most steady state situations. The discretization of positive definite quantities such as temperature or turbulent kinetic energy where overshoots cannot be tolerated becomes more difficult because of the dispersive errors. The advantage of the central-differencing over second-order unwinding is that it preserves turbulent kinetic energy when used to discretise velocity. Therefore, it is a useful scheme in large eddy simulation, where upwind schemes cause turbulent kinetic energy to decay unnaturally fast.

Other spatial discretization methods such as bounded central differencing, hybrid second-order upwind/central are not applied in this study and will not be discussed in this chapter.

Finally, for diffusion term D_f the discretization form is given by:

$$D_f = \sum_f (\mathrm{D}\nabla\phi \cdot \hat{a})_f \tag{3.55}$$

where D, $\nabla\phi$, and $\hat{a}$ represent the face diffusivity, gradient, and area vector, respectively. The second-order upwind scheme was used in the following simulations of the K-junction and cross-junction because of reasonable accuracy with considerable computational effort.

3.4 Interface tracking

3.4.1 Interface tracking methods

Interface tracking methods are widely used in computation of fluid problems with moving boundaries and interfaces. Generally, interface tracking methods can be classified into two main categories based on different fluid fields. The first category consists of Langrangian methods where the interfaces are tracked directly that the cell edges of the computational

grid are aligned with the interfaces which is represented by Lagrangian particles and its movement is tracked by the motion of these particles. Some parametrization or meshes of the interface are used to connect these particles in order. This type of method includes boundary integral methods (Power et al., 1995), boundary element methods (Ciskowski et al., 1991), and front tracking method (Tryggvason et al., 2001; Glimm et al., 1998; Hawker & Ventikos, 2012). The main advantages of this method are that the interface can be represented with efficiency and accuracy and the motion of particles can be easily monitored. However, the drawback of this method is that for a moving interface with complex geometry and large deformations or topological changes, it is difficult to keep a smooth global parametrization or a quasi-uniform mesh as breakup and merging occur. The algorithm is formed during the evolution and complicated reconnection through intervention (redistribution etc) when topology changes with constant reparameterization and remeshing.

The second category consists of capturing methods where a scalar field function defined on a fixed Cartesian mesh is used to represent the interface implicitly. The movement of the interface is monitored by the evolution of the scalar function under Eulerian framework which is also called Eulerian interface tracking methods. Fixed grids could be used which is more desirable from both computational and implementation points of view and coalescence and breakup is implicitly controlled by the grid resolution. The main advantages of these capturing methods are that the geometric problem is turned into the partial differential equation problem on a fixed grid with simple data structure which avoiding parametrization or surface mesh. Besides, merging or splitting of the grids can be easily solved in the viscosity sense. However, the accuracy and efficiency of these capturing methods are less than that of other tracking methods based on both interface representation and evolution. Additional numerical dissipation could be introduced during the computation and more computational effort is required to determine the interface explicitly as refined Cartesian grid has to be adapted to solve partial differential equations.

3.4.2 Eulerian interface tracking methods

Several Eulerian interface tracking methods have been used and each of them has its own advantages and disadvantages. The most popular methods applied to date are the level set, front tracking, and volume of fluid (VOF) methods.

The level set method was first developed by Osher and Sethian in 1980s and has been applied in a variety of fields such as image processing, computer graphics, computational fluid dynamics and etc. The principle of the level set method is to embed the interface $\Gamma(t)$ in a higher dimensional function φ (level set function), introduce implicit framework to solve problems which do not remain graphs and have variable topology, and develop multi-dimensional upwind scheme to approximate the relevant gradients (Osher and Sethian, 1988):

$$\Gamma(t) = \{x \in R^d | \varphi(x,t) = v_{ls}\} \tag{3.56}$$

in which v_{ls} is the contour level or isosurface value implicit represent the interface, x is position coordination, and t is time scale. The value of v_{ls} is usually taken as zero so that it is possible to identify the different phases based on the sign of φ. The function φ can be prescribed as a signed distance function properly:

$$\varphi(x,0) = d(\Gamma,x) = \begin{cases} dist(\Gamma,x), & x \in \Omega_1 \\ v_{ls}, & x \in \Gamma \\ -dist(\Gamma,x), & x \in \Omega_2 \end{cases} \tag{3.57}$$

where Ω_1 and Ω_2 represent the two regions occupied by the fluids, Γ is the interface, x is position coordination. The adoption of distance function helps to smooth the most part, simplify construction of regularized Heaviside and delta functions, and determine where to refine the grid when using local grid adaptation and grid deformation. The normal vector $\hat{n}$ and the curvature κ can be easily approximated through the derivative operators applied to the level set function, that is:

$$\hat{n} = \frac{\nabla\varphi}{|\nabla\varphi|}, \qquad \kappa = -\nabla\hat{n} \tag{3.58}$$

where $\hat{n}$ is the normal vector, φ is level set function, κ is the curvature. The advantages associated with this method are that it won't change in higher dimensions for surfaces propagating in three dimensions and maintain accurate curvature and good smoothness of discontinuous physical quantities near interfaces. However, the more numerical error and poor mass conservation may occur during the computation.

For front tracking method, a separate front is used to mark the interface and a fixed grid which is modified near the front to make a grid line follow the interface is used for the

fluid within each phase. The basic idea is discussed by Richtmyer and Morton (Richtmyer and Morton, 1968) and has been applied through the work of J. Glimm and coworkers (Glimm et al., 1988). The moving front is represented by a connected set of points which forms a moving internal boundary. Irregular grids are built and a special finite difference stencil is used on these grids in order to calculate the evolution inside the fluid. This method has been applied to solve a series of problems such as compressible flows of stratified fluids (Chernet al., 1986) and the motion of saturation fronts in porous medium (Maesumi et al., 1988). It is also reviewed by Moretti (Moretti, 1987) for aerodynamics calculations and has been developed by Peskin and collaborators (Peskin, 1977; Fauci and Peskin, 1988; Fogelson and Peskin, 1988) based on different ideas. The advantages of this method are higher accuracy but at the cost of considerable more complexity as the major drawback as well as the difficulty caused by merging and break up of interfaces.

The Volume of Fluid (VOF) method is a free surface modelling technique for tracking interfaces. It is an advection scheme that allows for tracking the shape and position of the interface but not an independent flow solving algorithm, thus the Navier-Stokes equations describing the motion of the flow have to be solved separately. This method was first based on marker-and-cell (MAC) methods and given the name as VOF in 1976 by Noh & Woodward where they introduced the *fraction function* while the first publication in a journal was by Hirt and Nichols in 1981. The fraction function is a scalar function which is identified as the integral of a fluid's characteristic function in the control volume called the volume of a computational grid cell. The volume fraction of each fluid is tracked through every cell in the computational grid and all fluids share the same set of momentum equations. Generally, a zero value of volume fraction indicates the cell is fully occupied by fluid one (say water), and when the value is 1 then the cell is fully filled with the other fluid (for example air). Values between 0 and 1, indicate a partially filled cell, implying that the interface separates the two fluids across this cell. This method has been used in numerous computer codes, both in house, research and commercial (such as ANSYS Fluent, STAR-CCM+, CFD-ACE and ANSYS CFX) for solving multiphase fluids problems with immiscible fluids (Khalili et al. 2016) and is now more or less the dominant method for addressing such problems. The main advantages of this method are good mass conservation with a sharp representation of the interfaces and less computational resources required. However, the drawbacks are low accuracy regarding interface curvature

estimation (since the interface has to be reconstructed based of the volume fraction) and difficulty to maintain the smoothness of the discontinuous physical quantities near the interfaces.

Many other methods such as phase field (Jacqmin,1999), immersed interface, level set (Sethian and Wiegmann, 2000), ghost fluid (Fedkiw et al., 1999), and lattice Boltzmann (Chen and Doolen, 1998) have been used. Some researchers have tried to combine two methods to improve the quality of interfaces. The CLSVOF method combines the level set and VOF methods to create a more accurate gas-liquid interface at the rupture stage of the emerging bubble (Dang et al. 2014). The particle level set method can be seen as a diffuse front tracking approach used to correct the level set method (Sethian, 1999). We shall describe the implementation of VoF variant used in our calculations in some detail in the next section, since it plays a central role in our computer model.

3.4.3 Volume of Fluid method

The Volume of Fluid method is a simple multiphase model which is generally used to simulate flows of several immiscible fluids on numerical grids capable of resolving the interface between the phases of the mixture. The model assumes that all phases share velocity, pressure, and temperature fields. Due to its numerical efficiency, this model is suited for simulations of flows where each phase constitutes a large structure with a relatively small total contact area between phases such as sloshing flow in a water tank, where the interface keeps smooth. When the movement is imposed to the tank, breaking waves, large number of bubbles in the water, and water droplets in the air will appear under a fine mesh with small modelling errors.

The spatial distribution of each phase at a given time is defined in terms of a variable called the volume fraction and the transport equation for the phase volume fraction is solved by a method of calculation such distributions. The second-order discretization is used to the obtain sharp interfaces between the phases and the HRIC Convection Discretization Scheme (Muzaferija et al., 1998) which is suitable for tracking sharp interfaces was applied in this study.

As all immiscible fluids phases present in a control volume share velocity, pressure, and temperature fields in the VoF model, the same set of basic governing equations describing momentum, mass, and energy transport in a single-phase flow is solved. The equations are solved for an equivalent fluid whose physical properties are calculated as functions of the physical properties of its constituent phases and their volume fractions which are shown below:

$$\rho = \sum_i \rho_i \alpha_i \tag{3.59}$$

$$\mu = \sum_i \mu_i \alpha_i \tag{3.60}$$

$$c_p = \sum_i \frac{(c_p)_i \rho_i}{\rho} \alpha_i \tag{3.61}$$

$$\alpha_i = \frac{V_i}{V} \tag{3.62}$$

where α_i is the volume fraction, ρ_i, μ_i, and $(c_p)_i$ are the density, molecular viscosity and specific heat of the i th phase and V, V_i are cell volume of fluid phase. The conservation equation which describes the transport of volume fraction α_i is:

$$\frac{d}{dt}\int_V \alpha_i dV + \int_S \alpha_i (v - v_g) \cdot d\hat{a} = \int_V \left(S_{\alpha_i} - \frac{\alpha_i}{\rho_i}\frac{D\rho_i}{Dt}\right) dV \tag{3.63}$$

where α_i is the volume fraction, V is cell volume, S is the closed surface, v and v_g are velocity and grid velocity, S_{α_i} is the source or sink of the i th phase, $\hat{a}$ is face area vector, and $D\rho_i/Dt$ is the material or Lagrangian derivative of the phase densities ρ_i. If there is a large time variation of phase volume α_i, there is a large time variation of the mixture density ρ which features in the continuity equation. Therefore, the continuity equation can be rearranged as:

$$\int_S (v - v_g) \cdot d\hat{a} = \sum_i \int_V \left(S_{\alpha_i} - \frac{\alpha_i}{\rho_i}\frac{D\rho_i}{Dt}\right) dV \tag{3.64}$$

where α_i is the volume fraction, V is cell volume, S is the closed surface, v and v_g are velocity and grid velocity, S_{α_i} is the source or sink of the i th phase, $\hat{a}$ is face area vector, and $D\rho_i/Dt$ is the material or Lagrangian derivative of the phase densities ρ_i. When the phases have constant densities and have no sources, the continuity equation can be reduced to:

$$\nabla \cdot v = 0 \tag{3.65}$$

where v is velocity.

3.4.4 Numerical treatment

In the VoF model of the CFD software STAR-CCM+ (CD-adapco Ltd, Melville, New York) implemented in this study, the normalized variable diagram (NVD) developed by Leonard (Leonard, 1991) is used to analyse boundedness properties of convective discretization schemes. Figure 3.2(a) below has shown that three cells in the vicinity of a cell face f, across which the velocity v_f is known. The nodal variable values are labelled α_D, α_C and α_U, standing for the downwind, central, and upwind positions relative to each other.

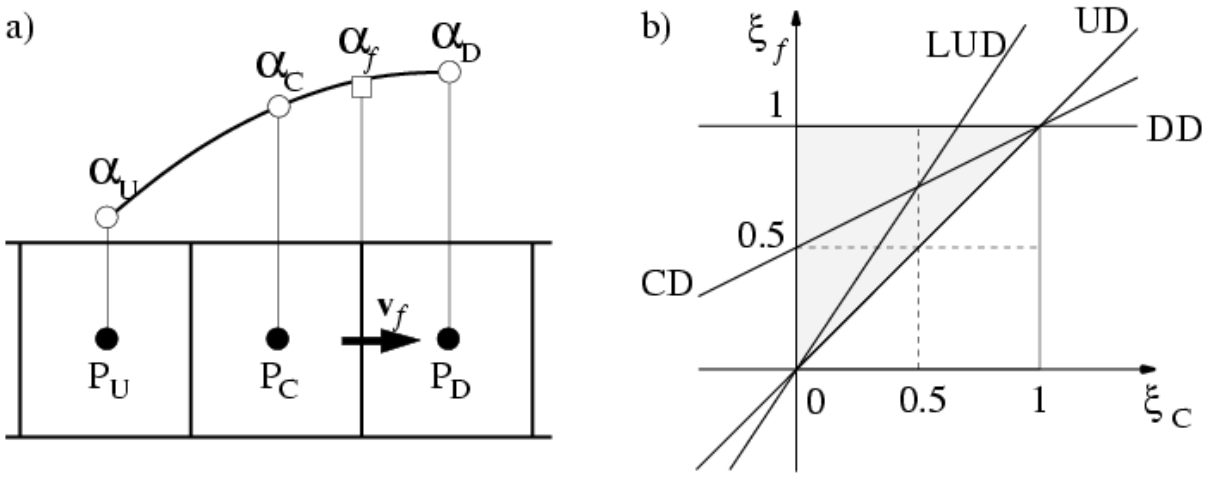

Figure 3.2 Upwind, downwind, and central cells that are used in the analysis on the left(a) and convection boundedness criterion in the NVD diagram on the right(b)

The normalized variable $\varepsilon(r,t)$ near face f is defined as:

$$\varepsilon(r,t) = \frac{\alpha(r,t)-\alpha_U}{\alpha_D-\alpha_U} \tag{3.66}$$

The normalized face value:

$$\varepsilon_f = \frac{\alpha_f-\alpha_U}{\alpha_D-\alpha_U} \tag{3.67}$$

Calculated by any differencing scheme that uses only nodal values of α at points U, C, and D as shown in Figure 3.2(a) can be written in the form:

$$\varepsilon_f = \varepsilon_f(\varepsilon_C) \tag{3.68}$$

where:

$$\varepsilon_C = \frac{\alpha_C - \alpha_U}{\alpha_D - \alpha_U} \tag{3.59}$$

in which $\alpha_C(\alpha_f)$, α_U and α_D are the nodal values of α at points C, U, and D, ε_f is the normalized face value and ε_C is the normalized central value. Non-physical oscillations may occur in the solution and α_C(and consequently α_f) have to be locally bounded between α_U and α_D to overcome its influence, meaning:

$$\alpha_U \leq \alpha_C \leq \alpha_D \text{ or } \alpha_D \leq \alpha_C \leq \alpha_U \tag{3.70}$$

in which α_C, α_U and α_D are the nodal values of α at points C, U, and D. If every point in the domain has satisfied this criterion, the effect of non-physical oscillations can be avoided.

The boundedness criterion for convection differencing schemes can be presented in the NVD diagram and the normalized face value ε_f can be expressed as a function of ε_C, as the hatch region in the Figure 3.2(b). It can also be illustrated through the following conditions: For $0 \leq \varepsilon_C \leq 1$ the bounded region lies above the line $\varepsilon_f = \varepsilon_C$ and below $\varepsilon_f = 1$ while for $\varepsilon_C < 0$ and $\varepsilon_C > 1$, ε_f is equal to ε_C. NVD is used to handle convective transport alone without sources or sinks, otherwise, the given condition in Equation (70) can be evaluated to false. The boundedness criterion becomes significant in the case of variables which have physical bounds such as the phase volume fraction cannot become negative or larger than unity.

The sharp interface that separates the fluid components is an important standard of an immiscible phase mixture such as air and water. Simple higher-order schemes, for example, central differencing (CD) or lower upwind differencing (LUD) may not capable to approximate large spatial variations of phase volume fractions which are represented by the Heaviside unit step function. On the other hand, the High-Resolution Interface Capturing (HRIC) scheme has more advantages over simple higher-order schemes above in mimic the convective transport of immiscible fluid components which makes it a suitable scheme for tracking sharp interfaces.

This scheme is based on the NVD diagram which have been described above and the normalized face value ε_f is calculated as:

$$\varepsilon_f = \begin{cases} \varepsilon_C & if \quad \varepsilon_C<0 \\ 2\varepsilon_C & if \quad 0\leq\varepsilon_C\leq 0.5 \\ 1 & if \quad 0.5\leq\varepsilon_C<1 \\ \varepsilon_C & if \quad \varepsilon_C\geq 1 \end{cases} \tag{3.71}$$

where ε_C is normalized central value. The calculated value of ε_f is further corrected according to the local Courant number:

$$C_u = \frac{v\cdot\hat{a}_f}{V_{P_C}}\Delta t \tag{3.72}$$

where v is velocity profile, $\hat{a}_f$ is the cell-face surface vector, V_{P_C} is the cell volume at point C shown in Figure 3.2, Δt is a given time step.

This correction has considered the availability criterion which describes the amount of one fluid that is convected across a cell face during a time-step is always less than or equal to the amount available in the donor cell. It can be expressed in the following:

$$\varepsilon_{f^*} = \begin{cases} \varepsilon_f & if \quad C_u < C_{u_l} \\ \varepsilon_C + \left(\varepsilon_f - \varepsilon_C\right)\frac{C_{u_u}-C_u}{C_{u_u}-C_{u_l}} & if \quad C_{u_l} \leq C_u < C_{u_u} \\ \varepsilon_C & if \quad C_{u_u} \leq C_u \end{cases} \tag{3.73}$$

where ε_C is normalized central value, ε_f is the normalized face value, C_{u_u}, C_{u_l}, C_u are Courant numbers. This equation is very important for transient simulations this correction. The values for C_{u_l} and C_{u_u} are set as 0.5 and 1 separately by default. They are used to control blending of HRIC and Upstream Differential (UD) schemes depending on the Courant number. The HRIC scheme is activated under the condition that $C_u < C_{u_l}$, for $C_{u_l} < C_u < C_{u_u}$ a combination of HRIC and UD are used, and for $C_{u_u} < C_u$ UD is used.

Compared to single HRIC or UD schemes, this blending results in stability and robustness to the scheme especially when the second-order time discretization is used in the case which large time variation of the interface shape is present and the time step is too large to resolve details of it. Convergence can be more easily achieved when the values of C_{u_u} and

C_{u_l} are small and the smaller values also help to activate UD sooner and make the calculation more stable. The interface becomes more fuzzy in regions with large C_u on the contrary.

For steady-state problems, the values of C_{u_u} and C_{u_l} should be large and the HRIC scheme is used no matter what time-step is chosen. Any number larger than the maximum CFL is appropriate.

When the interface is perpendicular to the flow, the front sharpening aspect of the downwind scheme is needed while for the interface parallel to the flow, the downwind scheme tends to wrinkle it. The interface between two fluids in this case was shown in Figure 3.3 and the angle θ between the normal to the interface n_i and the cell-face surface vector a_f are taken into account in the final correction of ε_f as shown below:

$$\varepsilon_{f^*}{}^* = \varepsilon_{f^*}(\cos\theta)^{C_\theta} + \varepsilon_C(1 - (\cos\theta)^{C_\theta}) \tag{3.74}$$

where ε_{f^*} is the cell-face value, ε_C is the cell-central value, θ is the angle between the normal to the interface n_i and the cell-face surface vector a_f, and C_θ is the angle factor. C_θ is set to 0.05 as the default value and its value will be increased of the interface is not smooth and not aligning with the grid lines. The cell-face value ε_f can be then calculated as:

$$\alpha_f^{HRIC} = \varepsilon_{f^*}{}^*(\alpha_D - \alpha_U) + \alpha_U \tag{3.75}$$

where $\varepsilon_{f^*}{}^*$ is the final correction of the cell-face value, α_U and α_D are the nodal values of α at points U, and D shown in Figure 3.3.

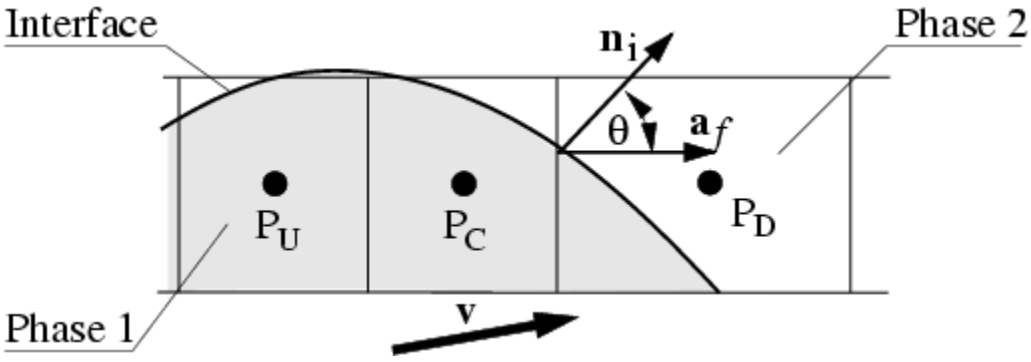

Figure 3.3 Interface between two fluids and the notation used.

3.4.5 Surface tension model

The surface tension force is the elastic tendency of a fluid surface to keep the least surface area possible. It is a tensile force tangential to the interface which separates two fluids and works to keep the fluid molecules at the interface in contact with the rest of the fluid. The value of surface tension is mainly influenced by the nature of the fluid pair and by temperature. In the case of a curved interface, the surface tension force f_σ can be divided into two parts:

$$f_\sigma = f_{\sigma,n} + f_{\sigma,t} \tag{3.76}$$

where:

$$f_{\sigma,n} = \sigma\kappa\hat{n} \tag{3.77}$$

$$f_{\sigma,t} = \frac{\partial\sigma}{\partial t}\hat{t} \tag{3.78}$$

in which σ is the surface tension coefficient, $\hat{n}$ is the unit vector normal to the interface which pointed to gas from liquid, $\hat{t}$ is the unit vector in the tangential direction to the interface, κ is the mean curvature of the interface, t is the time scale, $f_{\sigma,n}$ is surface tension force at normal direction, $f_{\sigma,t}$ is surface tension force at tangential direction. The coefficient of surface tension of the liquid is defined as the force acting in the surface of the liquid at right angles to a line of unit length in the surface of the liquid. For a constant surface tension coefficient σ, the tangential force is zero and the surface tension results in a force normal to the interface $(f_\sigma = f_{\sigma,n})$. However, for variable surface tension coefficient which is caused by temperature differences, the tangential force still exists. Therefore, Marangoni or Benard convection can be adopted to develop tangential to the interface.

In the VOF method used in this study, the surface tension force is computed based on the continuum surface force (CSF) model proposed by Brackbill (Brackbill et al. 1992). It can be described by using the smooth field of the phase volume fraction α_i to calculate a vector normal to the interface:

$$\hat{n} = \nabla\alpha_i \tag{3.79}$$

where α_i is the phase volume fraction. The curvature of the interface can be represented by using the divergence of the unit normal vector n below:

$$\kappa = -\nabla \cdot \frac{\nabla \alpha_i}{|\nabla \alpha_i|} \tag{3.80}$$

where α_i is the phase volume fraction. Then the normal part of the surface tension force $f_{\sigma,n}$ can be written as:

$$f_{\sigma,n} = -\sigma \nabla \cdot \left(\frac{\nabla \alpha_i}{|\nabla \alpha_i|}\right) \nabla \alpha_i \tag{3.81}$$

where α_i is the phase volume fraction, and σ is the surface tension coefficient. The tangential force is expressed below for a variable surface tension coefficient:

$$f_{\sigma,t} = (\nabla \sigma)_t |\nabla \alpha_i| \tag{3.82}$$

where $(\nabla \sigma)_t$ is the gradient of the surface tension coefficient in the tangential direction, and α_i is the phase volume fraction.

3.4.6 Contact angle model

The contact angle θ describes the influence of a solid wall on the interface which is show in Figure 3.4.

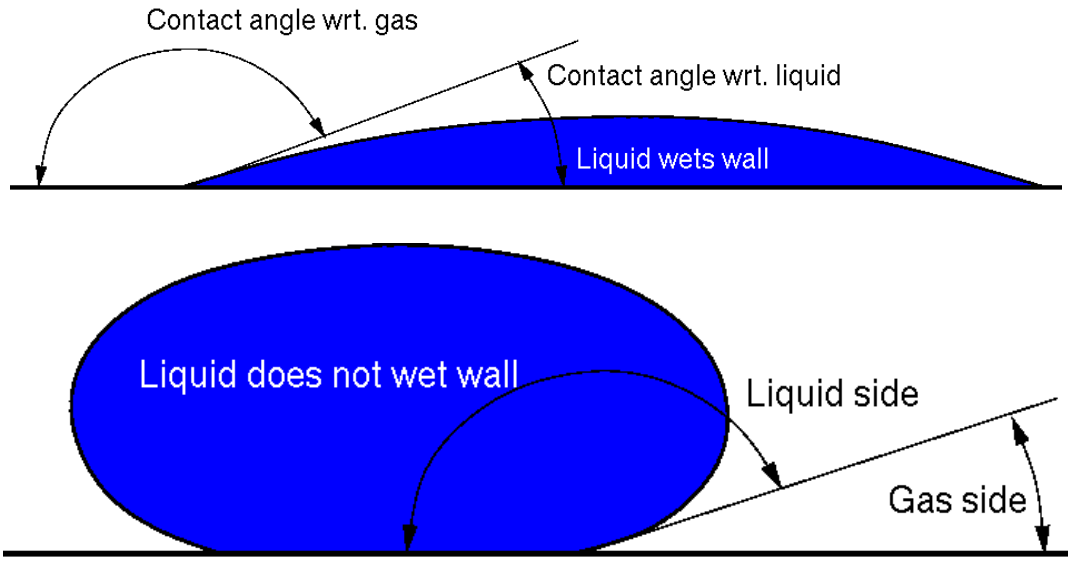

Figure 3.4 Measuring the contact angle between the wall and interface.

In the VoF model, the wall adhesion angle in conjunction with the surface tension model is specified. Instead of imposing this boundary condition at the wall itself, the contact angle of the fluid in contact with the wall is used to adjust the surface normal in cells near the wall. This dynamic boundary condition results in the adjustment of the curvature of the surface near the wall. If θ_w is the contact angle at the wall, the surface normal at the live cell next to the wall $\hat{n}_{fs}$ can be expressed as:

$$\hat{n}_{fs} = \hat{n}_w \cos\theta_w + \hat{t}_w \sin\theta_w \tag{3.83}$$

where $\hat{n}_w$ and $\hat{t}_w$ are the unit vectors normal and tangential to the wall separately as shown schematically in Figure 3.5, and θ_w is the contact angle at the wall.

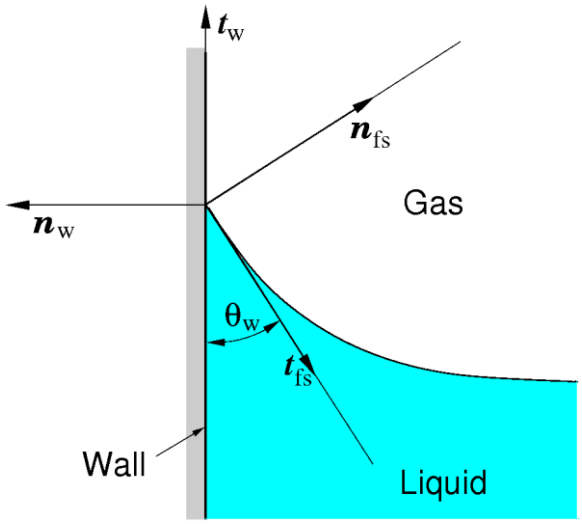

Figure 3.5 Contact angle and surface normal calculation illustration.

The combination of this contact angle with the normally calculated surface normal one cell away from the wall determine the local curvature of the surface, and this curvature is used to adjust the body for term in the surface tension calculation.

3.4.7 Mesh initialization

The starting point for mesh initialization is to create a geometry that describes the shape of the object used for analysis. The geometry can be created by performing logical operations on primitive shapes such as cylinders and spheres and customizing specific volumes by building vertices, edges, and faces. It can also be created using pre-processor software that is used to create the grid. Flow domains of the geometry created need to be divided into small

subdomains made up of geometric primitives such as hexahedra and tetrahedra in 3D and quadrilaterals and triangles in 2D to analyse fluid flow. The face mesh was created first in the flow domain and the mesh quality was checked to improve and repair face mesh created. The volume mesh was generated afterwards and further refined after checking the mesh quality. Then the governing equations can be discretized and solved inside each of these subdomains by using finite volume, finite element, or finite difference methods. In order to the keep proper continuity of solution across the interfaces between two subdomains, extra care has to be taken to split these subdomains so that the approximate solutions inside different positions can be put together to provide a complete picture of fluid flow in the whole domain. These subdomains are usually called elements or cells and the collection of all elements or cells is called a mesh or grid. For the same cell amount, hexahedral meshes will provide more accurate solutions especially if the grid lines are aligned with the flow. The mesh density should be high enough to capture all relevant flow features such as the mesh adjacent to the wall. The process of obtaining an appropriate mesh is called mesh generation and has long been recognised as a bottleneck in analysis process because of the absence of a fully automatic mesh generation procedure. The mesh quality was measured from skewness, smoothness and aspect ratio. Some specialized software programs have been developed to help improve mesh and grid quality which is vital to the success of the numerical model.

There are many categorisations of grids. A commonly used distinction classifies meshes as structured or unstructured, based on their connectivity. Structure mesh are characterized by regular connectivity that can be described as a two or three-dimensional array and thus confined to quadrilaterals in 2D and hexahedra in 3D; each cell has an easily defined neighbour in each of the 6 (4 in 2D) directions. The regularity of the connectivity point to a great advantage of such meshes, i.e., memory economy, since no connectivity information needs to be stored. For unstructured mesh, it is characterized by irregular connectivity that can't be expressed as a two or three-dimensional array in computer memory. In general, cells are numbers sequentially and any cell can have common faces with any other cell. The storage requirements for an unstructured mesh can be substantially larger since the neighbourhood connectivity must be explicitly stored. Meshes called hybrid, which contain structured portions and unstructured portions are also used. This definition requires knowledge of how the mesh is stored and used causes there is disagreement as to the correct

application of the terms "hybrid" and "mixed." In terms of mixed mesh, it is usually applied to meshes that contain elements associated with structured meshes and elements associated with unstructured meshes that probably stored in an unstructured fashion.

3.5 Summary

In this chapter, numerical methods applied in this study are described. Mathematic equations such as partial differential equations used for modelling basic physical phenomena such as fluid dynamics have been described. The fundamentals of computational fluid dynamics including conservation laws, Navier-Stokes equations, boundary and initial conditions etc. have been discussed in detail.

In terms of numerical treatment for solving the Navier-Stokes equations, three typical discretion methods including finite difference, finite element, and finite volume methods are discussed and compared. Temporal and spatial discretization methods provided by computational fluid dynamic software for solving transient problems which occur in the existence of applied physics and engineering in both time and space have been reviewed. In the meantime, the most commonly used interface tracking methods, for example, boundary integral, boundary element and front tracking methods based on Lagrangian framework, level set and volume of fluid (VOF) methods based on Eulerian framework are illustrated. According to the comparison between the numerical approaches mentioned above in the literature, the finite volume method is chosen as the discretion method along with the second order implicit unsteady and second order upwind scheme for temporal and spatial discretization respectively for following numerical study after considering the convenience, computational effort, cost and accuracy.

Chapter 4 : K-junction Experimental investigation

4.1 Overview

In this chapter, the materials, experimental procedures and setup used to obtain the results throughout this study are discussed. Methods used to prepare and analyse microbubbles are explained in detail. The materials used: polymers, solvents and dyes, and the corresponding suppliers and product details are described. The polymeric solution preparation procedures and characterisation methods are described as well. The design of microfluidic devices K-type junction has been illustrated. For analytical methods that are utilized, the theory and background details are briefly prepared. The methodology, materials and equipment descriptions mentioned in this chapter covers the following result chapters with some slight change in microfluidic device and materials used in some cases which will be illustrated in the corresponding section.

4.2 Material preparation

Primary materials used throughout the study are polymers, solvents, and dyes. Auxiliary materials include buffer solutions and surfactants which are referred to in this section.

4.2.1 Polymers

Polyethylene Glycol (PEG) produced by Sigma-Aldrich was used in this study. It is a polyether compound which is also known as polyethylene oxide (PEO) or polyoxymethylene(POE). However, PEG has a specific molecular range (8500-11500$gmol^{-1}$) otherwise it is known by PEO or POE despite having the same chemical composition. It is used as stabilizing polymer on the microbubble surface in microfluidic study (Dayton & Rychak, 2007) which makes it good for microbubble generation. The structure of PEG is commonly expressed as $H{-}(O{-}CH_2{-}CH_2)_n{-}OH$ and is shown in Figure 4.1.

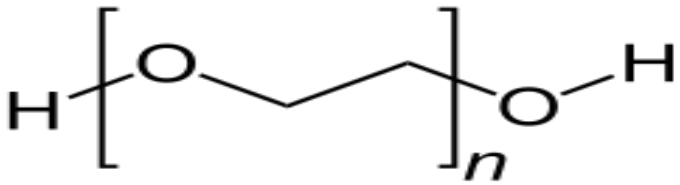

Figure 4.1 Chemical Structure of Polyethylene glycol(PEG).

PEG is a biocompatible, biodegradable polymer which is widely used in applications such as biomedical and pharmaceutical industries. It has excellent hydrophilic properties because of the existence of oxygen groups in the ethylene oxide monomer, making it suitable as a drug carrier matrix in biomedicine applications. It is easily dissolved in water and many other organic solvents such as toluene, methylene chloride, acetone and ethanol. Additionally, it is also generally considered biologically inert and safe thus has been approved for many medical applications. Covalent bonding of PEG to other molecules could increase the properties of other molecules like water solubility and protein rejection.

Polymethylsilsesquioxane(PMSQ) with molecular weight 10000 $gmol^{-1}$ is a biocompatible polymer with silicone ingredient and commonly used to generate polymeric nanoparticles for biomedical applications (Gunduz et al., 2013). The molecular formula of PMSQ is represented as (CH3SiO)n and the structure is shown in Figure 4.2.

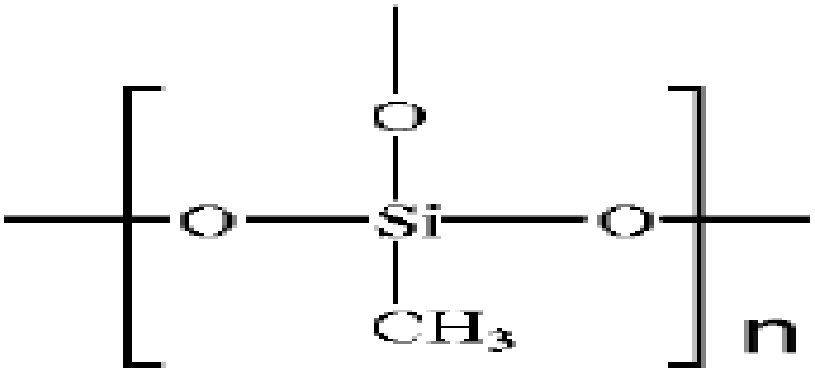

Figure 4.2 Chemical structure of Polymethylsilsesquioxane(PMSQ).

PMSQ is well known for its chemical and physical stability in biomedical application, low-toxicity profile and biocompatibility (Albijanic et al., 2010; Bhatt & Shah, 2012; Gunduz et al., 2012). It is also used in cosmetics industry (Xu et al., 2005) in skin care products as it creates a lubricating feel and increases the skin's ability to repel water. In addition, it has been applied in pharmaceutics, entrapment of drugs (Quintanar-Guerrero, 1998), encapsulation of cells and biomolecules.

Poly lactic-co-glycolic acid (PLGA) is a copolymer which has shown great potential as a drug delivery carrier and as scaffolds for tissue engineering. PLGA is a biodegradable and biocompatible polymer approved by FDA and has been widely investigated as drug delivery

carrier for proteins and other macromolecules like DNA. The excellent degradation characteristics, long experience interval in clinical studies and possibilities make it quite popular compared to other biodegradable polymers. The PLGA used in this study has molecular weight ranging from 24000 to 38000 $gmol^{-1}$ with a lactic/glycolic acid ratio of 50:50 and is purchased from Evonik Rohm GmbH(Essen, Germany). The chemical formula of PLGA is represented as (C4H4O4)x (C6H8O4)y and the structure is shown in Figure 4.3

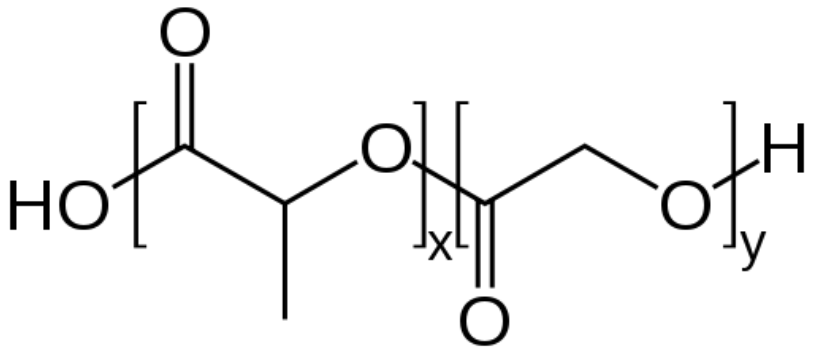

Figure 4.3 Chemical Structure of Poly lactic-co-glycolic acid(PLGA).

Poly (vinyl alcohol) (PVA) used in experiments was purchased from Sigma-Aldrich with molecular weight of 38000-46000 $gmol^{-1}$. It is a water-soluble synthetic polymer in the state of colourless and odorless beads and is usually used in industrial, medical and food applications such as lacquers, resins, surgical threads and food-contact materials. PVA is used in papermaking, textiles, coatings, and variety of medical applications such as transdermal patches and rapidly drying topical gels. It can also be biodegraded through enzymatic breakdown by several microorganisms. The acute oral toxicity of PVA is very low, with LD_{50} in the range of 15-20 g/kg, thus it is considered as nontoxic (Demerlis & Schoneker, 2003). Because of its solubility in both water and non-water based solvent with low cost, PVA is commonly used as a steric stabilizer in suspension and dispersion polymerization (Hong et al., 2007). It was regarded as a stabilizing agent to obtain increased compatibility between immiscible polymer macromolecules due to its film forming, adhesive and emulsifying properties. The molecular formula of PVA is described as (C2H4O)x and the structure is shown in Figure 4.4.

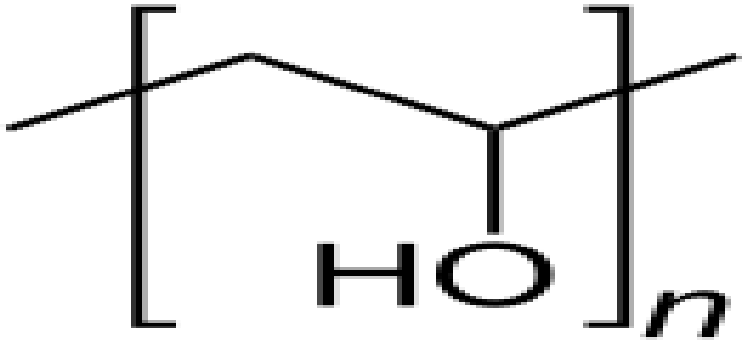

Figure 4.4 Chemical Structure of Poly (vinyl alcohol) (PVA).

4.2.2 Solvents

Three primary solvents used in experiments: acetone, ethanol and distil water (Table 4.1).

Acetone used in this study is laboratory grade (Laboratory Reagent, $\geq 99.5\%$) and was purchased from Sigma Aldrich, UK. It was mainly used for hydrophobic polymers and was selected as it is one of the least toxic among organic solvents.

Ethanol (denatured, Research grade, alcohol content 99-99.5%) was provided by BDH Laboratory, UK. It was used to dissolve PMSQ in microfluidics feed solutions, some of the chromophore dyes, and to clean microfluidic chips and syringes before and after experiments.

Pure distilled water was produced using Millipore Filtration device (Millipore, USA) to dissolve hydrophilic polymer feed solutions, prepare buffer solution and clean device. It is generally used as a solvent for all hydrophilic polymer feed solutions used in microfluidic bubble generation.

	Formula	**Molecular Weight ($\mathbf{gmol^{-1}}$)**	**Boiling Point (℃)**	**Density (kg/m^{-3})**	**Surface Tension (mNm^{-1})**	**Viscosity ($25℃$) (cP)**
Acetone	$(CH_3)COCH_3$	58.08	56	0.7845	23.3	0.33
Ethanol	H_3CCH_2OH	46.07	78	0.789	22.3	1.08
Water	H_2O	18.02	100	0.998	72.8	0.89

Table 4.1 Solvents used in the experiments and their properties (Clayden, Greeves, &Warren, 2012).

4.2.3 Dyes

Three fluorescent dyes were used to observe polymers in polymeric solutions with UV-Vis range chromophores and observation under fluorescent microscope.

Methyl Green (C27H35BrCIN3.ZnCl2) has a blue/green colour and was dissolved in ethanol. It was purchased from Sigma Aldrich, UK (Dye content 85%, Zinc chloride salt, certified by Biological Stain Commission. Its maximum absorption wavelength is at 629nm.

Neutral Red ($C_{15}H_{17}CIN_4$) has a dark red colour and is a water-soluble chromophore. It is purchased from Sigma-Aldrich with dye content 50-60% and maximum absorption wavelength is at 540nm.

Perlene (peri-dinaphtalene, $C_{20}H_{12}$) has a tallow colour with a slightly blue haze and can be dissolved in acetone. It is purchased from Sigma-Aldrich, UK with dye concentration $>$99% and used for blue staining in UV range. The maximum absorption wavelengths of Perlene are in the range of 400-440 nm.

4.3 Microfluidic junction design

CAD software CATIA (Dassault Systemes, France) was used to draw the microfluidic device design. The engineering draft of K-junction generated was sent to a properly equipped workshop for subsequent manufacturing of the microfluidic chips (see Figure 4.5).

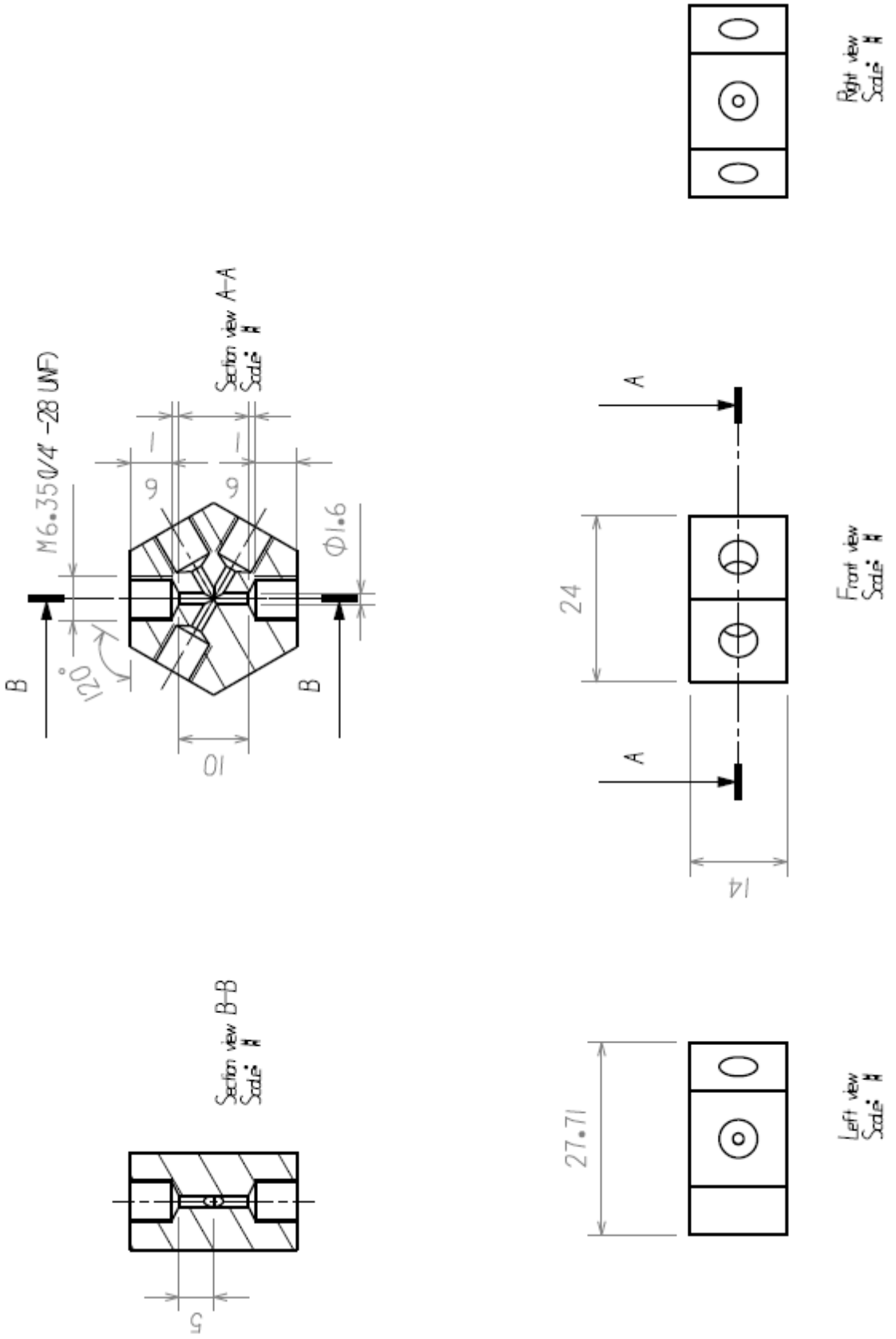

Figure 4.5 Drawing used for manufacturing of the K-type microfluidic device in unit mm.

Polydimethysiloxane(PDMS) was selected to manufacture microfluidic chips because of its low chemical activity, transparency, toughness and low cost compared to other materials such as glass, polymer mould, flexible web, paper wax or silicon. The manufacturing process determines the type and geometry of structures, tolerances and sizes of the chip. In this study, precision mechanical machining in the Mechanical Engineering workshop was chosen to produce microfluidic chips due to the low number of chips required and low set up cost. Microfluidic chips are made of several basic structures including channels, connectors and junction areas to achieve the functionality and microfluidic operation. The junction geometry changes with the numbers of channel and the complexity of junction geometry increases from commonly used T-shape and cross-shaped junctions to this novel K-shape microfluidic junction.

In the K-junction, there are five channels available which can be inserted with five capillaries as one for gas stream, three for liquid steam, and one for outlet. Therefore, the area where five capillaries meet was formed inside of the K-junction with irregular shape. The gas stream and liquid stream were mixed and microbubbles were generated in this area namely mixing chamber. Compared to typical used T-junction which only has three channels, the area where three channels meet for fluid mixing and microbubble generation is a simple square. Flow characteristics and multiple fluids mixing in this area with different geometries are influenced by the original geometry of the junction depending on the number of channel. Thus, less number of channel makes more simplify and regular area for mixing and microbubble generation while the increase of channels make this area more complex and irregular. Profile of channels, aspect ratio (height/width) and connector types have to be of suitable type for a chip to function at its designed capacity without any flaws or fluid leakages and blockages. The channels embedded in the chip have outer diameters (OD) of 1.6 mm (1/16”) and can be filled with capillaries with internal diameters (ID) of 100 µm. The angle between gas steam and liquid stream channels are set to 60 degree so that the connectors can be fitted in properly and make the junction more compactable. The K-junction shown in Figure 4.6 is transparent, rigid and can withstand the high pressures generated during bubbling up to 500 kPa.

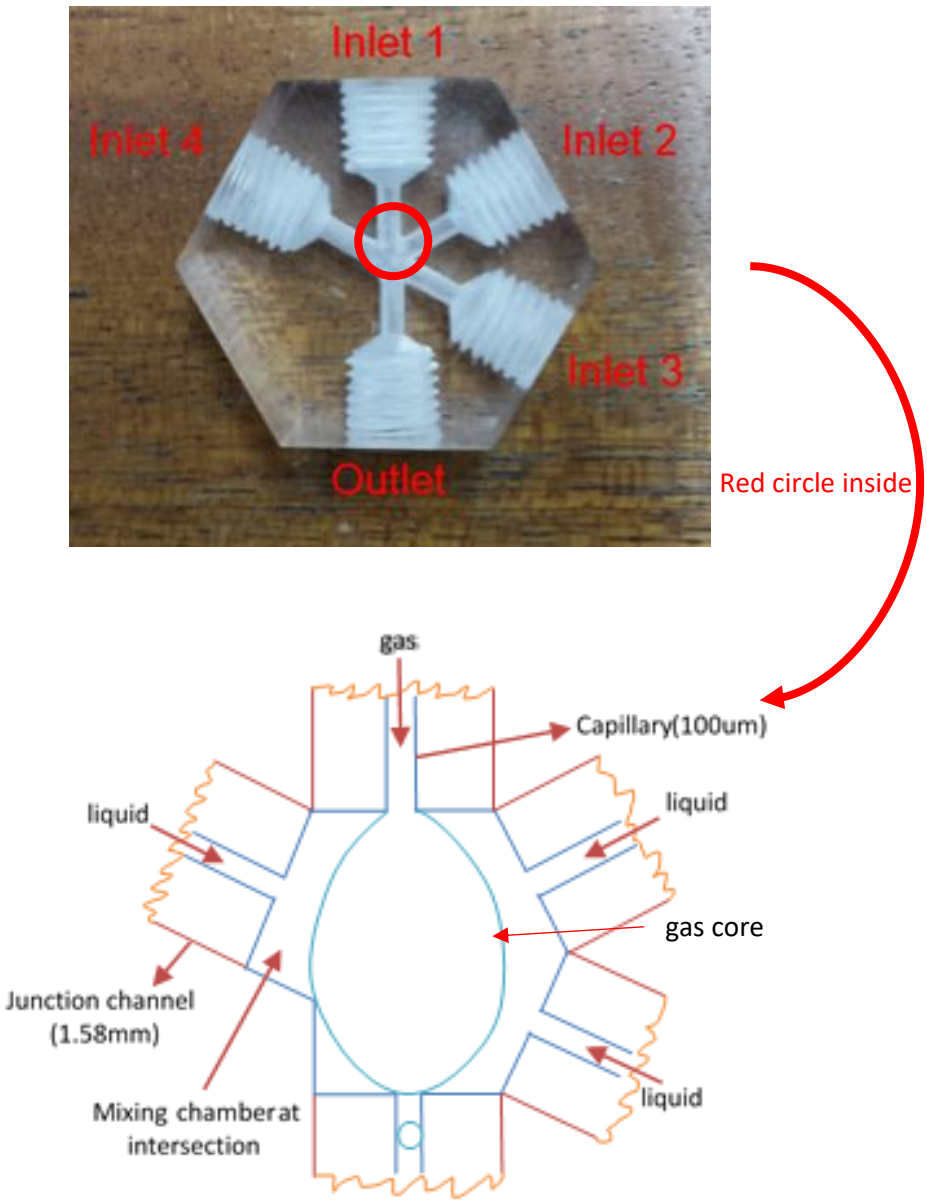

Figure 4.6 Picture of the K-junction used in the experiment (top) and cross-sectional representation of the device shown in the red circle (bottom).

The capillaries used are made of polytetrafluoroethylene (PTFE) with ID 100 µm/OD 1.6mm and standard lengths of 80mm were inserted in the microfluidic device made by PDMS block (22× 22 × 15 mm) through connectors at both ends. The connectors also connect microchannels with the chip and the liquid pumping device. Besides, flangless ferrules are adopted between connectors and the microfluidic chip contact points to avoid fluid leakages.

4.4 Physical properties

4.4.1 Density

The density of the polymer solutions was measured at an ambient temperature of 23°C using 10 ml standard glass density bottle of the Gay-Lussac type purchased from VWR International Ltd. The equation used for calculating density is shown as:

$$\rho = \frac{m_t - m_b}{v_b} \tag{4.1}$$

where m_t is the total mass of the bottle and solution, m_b is the mass of the empty bottle, and v_b is the specific volume of the solution in the bottle (10ml). The Kern EMS Basic Precision Balance purchased from SciQuip Company (UK) was used to measure the empty density bottle and bottle with solution. The balance was set to zero before each measurement to reduce error. The measurement of density was taken at least three times with a maximum deviation of approximately 0.05 % and the average value was used.

4.4.2 Viscosity

The Ostwald viscometer (Ubbelohde-type) supplied by VWR International, UK was used to measure the viscosity. It is made of a U-shaped glass tube held vertically with constant temperature at 25℃. The kinematic viscosity (η) was calculated using viscometer constant (C) and time measured for liquid to flow between two marks in the device (t);

$$\eta = Ct \tag{4.2}$$

where C is viscometer constant, and t is time scale. The dynamic viscosity (μ) for each polymer solution was calculated using kinematic viscosity and solution density (ρ);

$$\mu = \eta\rho \tag{4.3}$$

The viscosity measurements were taken three times and the average value after calculation was used.

4.4.3 Surface tension

The Krüss DSA 100 Shape Analysis System (Krüss, Germany) with a Wilhelmy plate tensionmeter was used to measure surface tension. It works as a stainless-steel plate is immersed in a liquid surface and the force exerted on the plate is measure using a delicate spring tensiometer. The glass beaker with liquid inside was slowly lowered away from the plate tip until the plate has only a slight contact with the upper portion of the liquid surface. The force measured at this point is read. Surface tension is an important parameter, thus the pressure from micropump could have problems to overcoming it if the surface tension value is too high and may cause difficulties in obtaining the bubbling regime (Zhao et al.,2004).

4.5 Microbubble generation preparations

4.5.1 Solution preparation

5% w/w of PEG and 2% w/w PVA were dissolved in distilled water and the solution was mixed using a magnetic stirrer at 60℃ for 1h. 5% w/w PLGA was dissolved in acetone under the same conditions. 5% w/w of PMSQ was dissolved in ethanol and magnetically stirred in a conical flask for 1h at room temperature 23℃. Similarly, other polymer solutions such as PEG, PVA with different mass fraction were prepared in an identical manner. The physical properties of these polymer solutions prepared and gas used are shown in Table 4.2.

	Density (kg/m^3)	**Dynamic viscosity (mPa s)**	**Surface tension (mN/m)**
Nitrogen at 20℃ and 1 atm	1.2	1.75×10^{-2}	N/A
5wt%PEG+2wt%PVA in water	986	4.14	54
5wt%PMSQ in ethanol	802	1.06	30
5wt%PLGA in acetone	788	9.37	30

Table 4.2 Physical properties of gas and liquids used in the experiment.

4.5.2 Experimental setup and microbubble generation

The schematic diagram of each components of the microfluidic processing setup and the details of it are provided in the Figure 4.7.

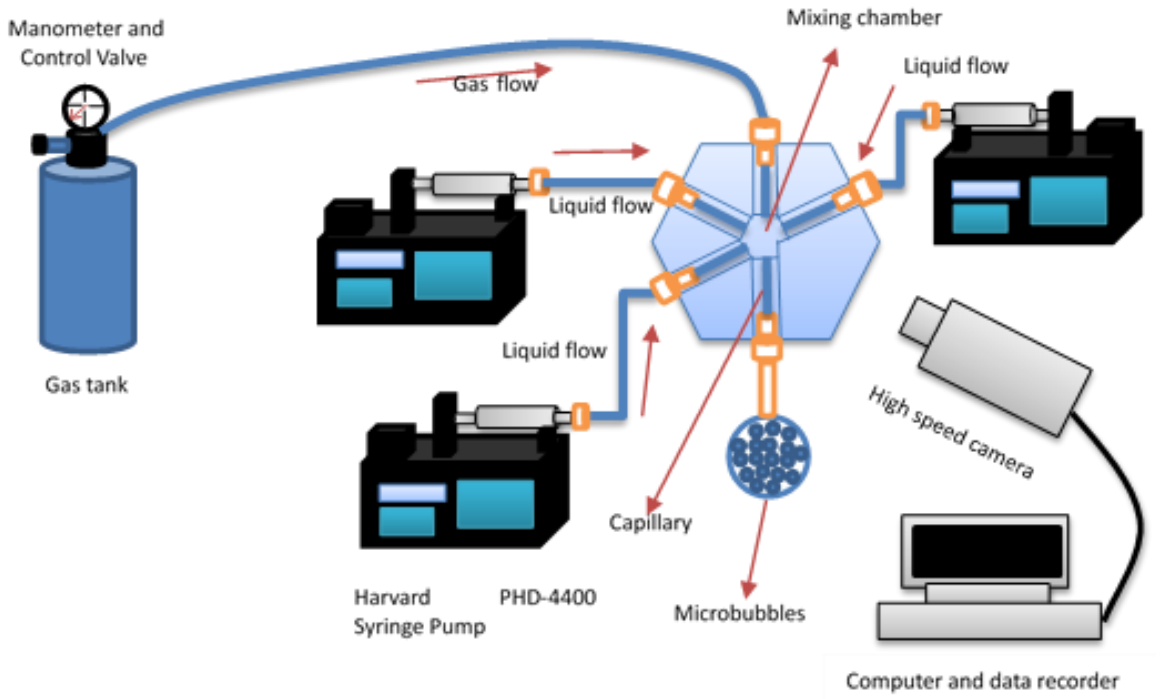

Figure 4.7 Schematic diagram of the complete experimental setup consisting of the K-junction, a high-speed camera connected to a computer and a data recorder, gas tank and three syringe pumps which infuse gas and liquids into the junction.

The microbubbles were generated using this setup and its slightly altered modifications with different microfluidic devices. Digitally controlled piston pumps (Harvard Apparatus PHD 4400) were used to control injection of polymer solutions in plastic syringes(10ml) with a liquid flow rate in the range of 150-200 $\mu l/min$ under a flow of nitrogen gas with pressures between 100-300 kPa. The details are shown in Figure 4.8. The microfluidic device was used to generate a constant flow regime formed by nitrogen and polymer solutions and the monodisperse microbubbles generated were collected on a glass slide with and without water coating as collection medium and then put under optical microscope for observation and measurement.

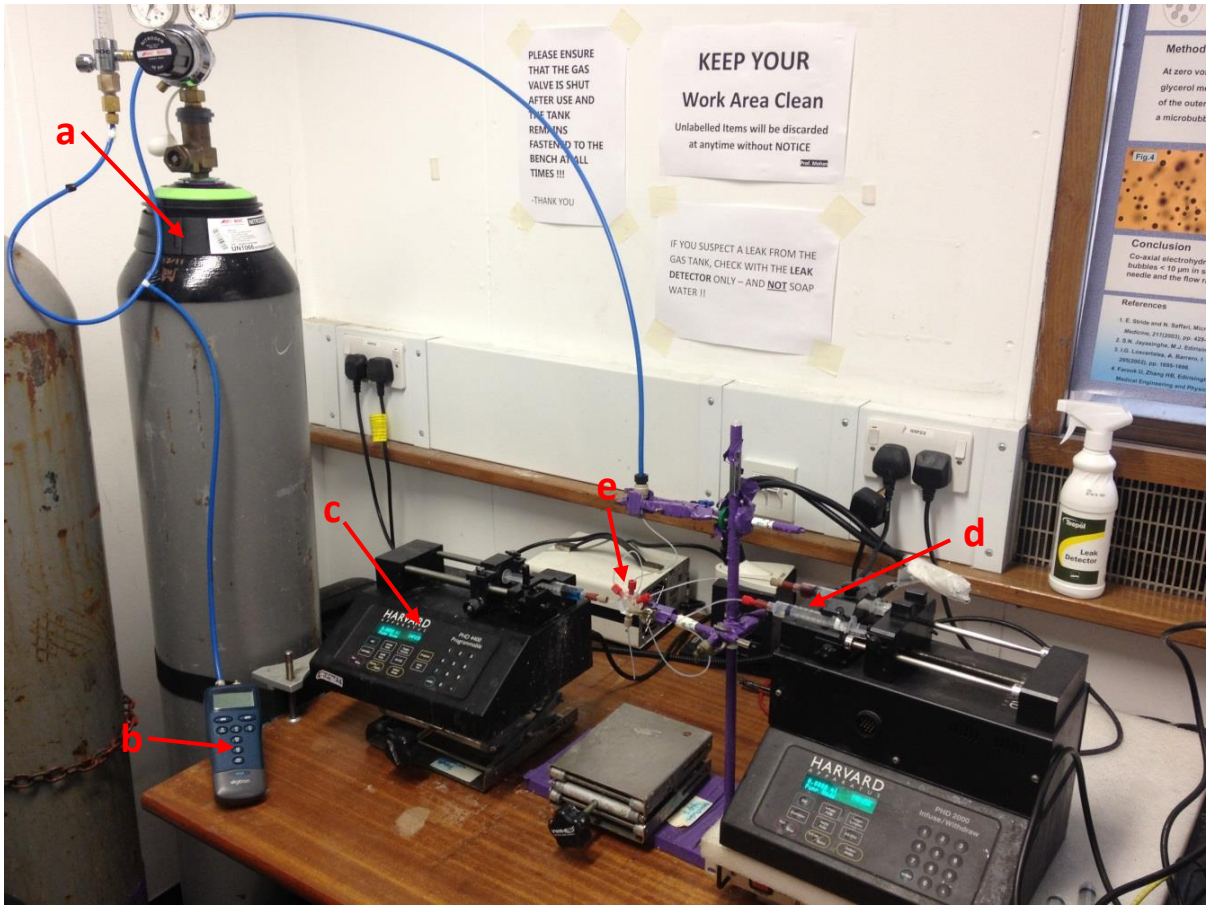

Figure 4.8 Experimental setup of microfluidic system a)Nitrogen gas tank b)Digital Manometer c)Harvard Syringe Pump d)Plastic Syringes e)Microfluidic K-junction.

Capillaries made of Telfon Fluorinated Ethylene Propylene (FEP) were used to connect the inlets and outlet of the microchannels which provide nitrogen gas and the polymer solutions. The top channel of the microfluidic K-junction was connected to a pressurized nitrogen gas tank under the control of barometer and flowmeter. A digital manometer (British Oxygen Company, Aldershot, UK) connected with a high-precision valve was used to control the supply of nitrogen.

Polymer solutions were supplied from 10 ml plastic luer lock syringes injected to microchannels using electronically controlled syringe pumps (model PHD 4400, Harvard Apparatus, UK). The flow rate of the polymer solutions (5 wt.% PLGA, 5 wt.% PMSQ and 5 wt.% PEG with 2 wt./v % PVA) was set in the range of 100-200 $\mu l/min$ using the syringe pumps under the flow of pressure gas ranging from 100 kPa to 450 kPa(see Figure 4.9).

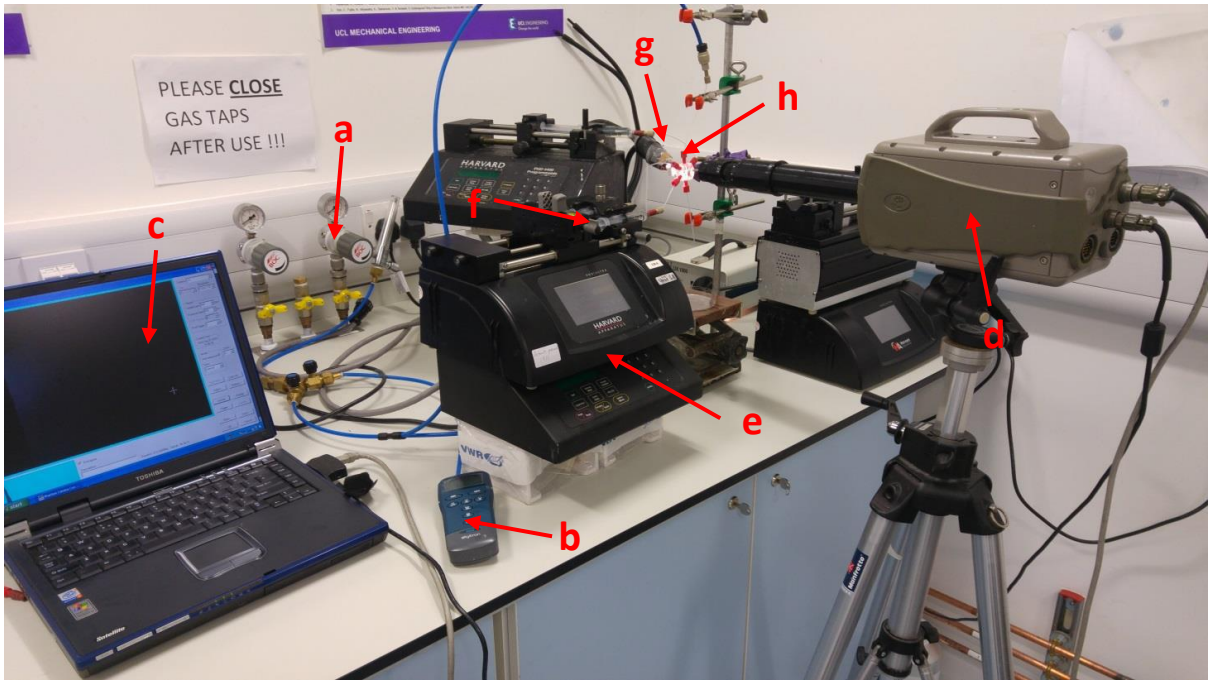

Figure 4.9 The whole experimental setup of this work a) Nitrogen gas valve and manometer b) Digital Manometer c) PC and Imaging capture software d) High Speed Camera e) Harvard Apparatus Pump f) Plastic syringes g) Optical light source h) Microfluidic K-junction.

The gas was supplied through the inlet channel on the top while liquids were infused through the three other inlet channels (see Figure 4.10). Microbubbles were generated at the mixing chamber where these channels join together in the junction and were collected from the outlet capillary at the bottom of the device (see Figure 4.10). The microbubbles collected on glass slide were then taken to optical microscopy for measurement. It was found that the microbubbles were easy to aggregate together resulting in microbubble collapse. In addition, the aggregation of microbubble makes it difficult to observe under optical microscope because of microbubble overlap. Therefore, glass slides were slightly wetted by distill water before collecting microbubbles so that microbubbles could spread homogeneously on the slides and more convenient for observation. The experiments were conducted at the ambient temperature (25℃) and the leakages of all connectors and the blockages of all capillaries were check before each of the experiments.

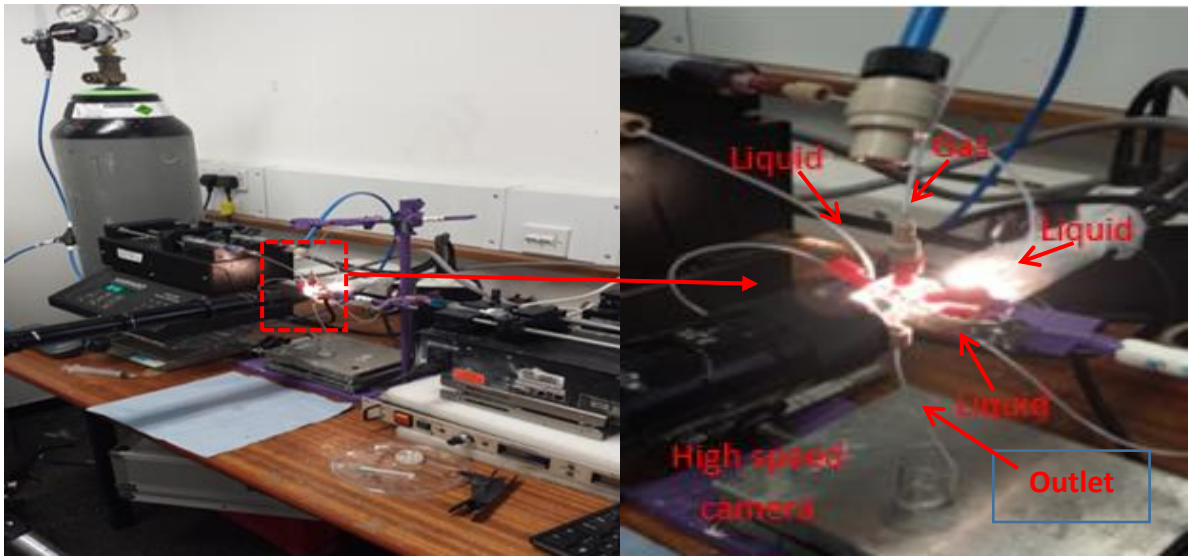

Figure 4.10 Close up images of the experimental setup for microfluidic device.

4.6 Characterization Methods

4.6.1 Optical Microscopy

Optical microscope is a device that depends on visible light to magnify images of samples in micro or submicron size by using different type of condensers and optical lenses. The image is usually captured by a high-resolution digital camera to generate micrographs. The resolution of optical microscopy is often limited to samples of sizes above 200nm because of its usage of visible light. In order to eliminate the dependence on lightwaves, a series of method have been adopted such as using oil immersion medium to remove chromatic aberrations caused by light, or illumination-based techniques such as contrast enhancing, phase contrast, bright/dark field or cross-polarized light illumination (Davidson &Abramowitz). In this study, a Nikon Eclipse ME-600 optical microscope (Nikon Co, Tokyo, Japan) was utilized to observe microbubbles collected on a glass slide immediately after generation. The digital imaging software integrated in the microscope provided different scale bars corresponding to the magnification of optical lenses. In each experiment, three samples were prepared for measurement. The image processing software Image J 1.48v (National Institute of Health, USA) was employed to analyse bubble size and shape from these optical micrographs.

4.6.2 High Speed Camera

The high-speed camera with the name of Phantom V5.1 high speed camera (Vision Research Ltd. Bedford, UK) was used for video recording. It has a maximum resolution of 1024×1024 pixels @1200 fps providing 6.8s of recording time.In this study the configuration of the high-speed camera was set as a resolution of 800×600 pixels with 1000 fps and 1s of recording time and has been used to obtain real-time video images of the microbubble generation process.

4.6.3 Fluorescence Microscopy

A fluorescence microscope is an optical microscope that uses fluorescence and phosphorescence instead of, or in addition to, reflection and absorption to study properties of organic or inorganic substances (Spring KR, Davidson MW, 2008) and is shown in Figure 4.11. It is one of the fastest growing areas of characterization based on optical microscopes. This type of microscope works using the fluorescence phenomenon (when incident light of sufficient energy strikes an object that emits light of a specific wavelength) as the source of light. Specific chemicals (fluorochromes) with delocalized electrons display this capacity and are usually used to stain specific materials to emit fluorescence. These may dye certain constituents of materials in polymeric samples selectively, which is called fluorescent labelling and is very popular in biomedical applications (Leng, 2008a).

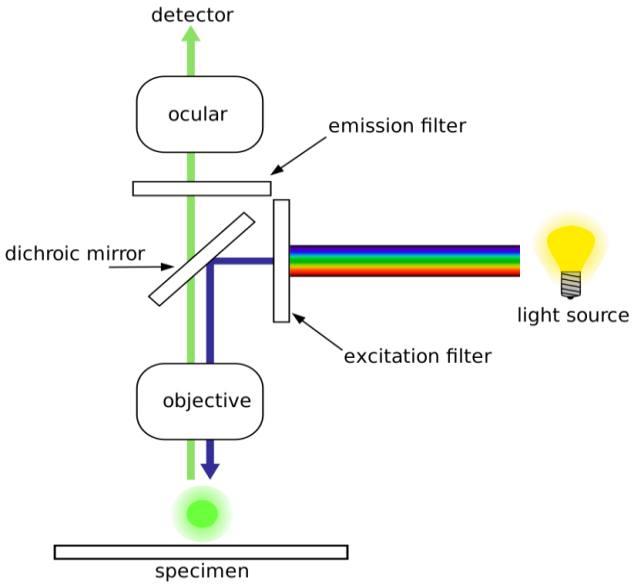

Figure 4.11 Schematic of a fluorescence microscope.

A fluorescence microscope (Life Evos XL, ThermoFisher Scientific) was used for the characterization of bubbles with the following excitation wavelengths for blue and red channels: λ_{DAPI}= 410nm $\lambda_{Texas\ Red}$= 570nm. PEG/PLGA were tagged with UV-active dyes, 100ppm NR/PER respectively.

4.7 Summary

In this chapter, the experimental investigation conducted on the novel microfluidic K-junction including materials, experimental setup design and microbubble generation preparations and characterization methods have been introduced. Several polymers, solvents and dyes used in the experiments are reviewed. Microfluidic junction design especially the novel microfluidic K-junction used in this study is introduced in this chapter in detail and the measurement of the physical property of polymer solutions has been presented. Microbubble generation preparation procedures such as solution preparation and experiment setup arrangement have been discussed and the characterization methods which are used for observing and analysing microbubbles produced by the K-junction have been stated. In the following chapter, preparation of numerical simulation part of this work will be presented and discussed comprehensively.

Chapter 5 : Numerical simulation of K-junction

5.1 Overview

In this chapter, preparation procedures of numerical simulation conducted for investigating the microbubble generation and multiphase fluids mixing in the K-junction are presented. A commercial computational fluid dynamic software STAR-CCM+ (CD-adapco Ltd, Melville, New York) has been applied in this numerical study. Physical and mathematic model provided by this software and used in the following numerical simulation is introduced. Geometry and mesh of the K-junction generated by using numerical tools integrated inside of the software are also stated. In addition, the Eulerian multiphase fluids properties, Volume of Fluid (VOF) model and boundary conditions settings have been explained and determined in order to guarantee proper numerical simulations. Different boundary conditions conversion such as gas pressure inlet to gas flow rate inlet have been discussed and compared. Meanwhile, the software validation of the numerical modelling is conducted by using simple T-junction and the grid dependence test by using the K-junction is also presented in this chapter.

5.2 Physical and mathematic model

A series of numerical simulations were conducted in a novel microfluidic K-junction which was utilized to replicate multiple fluids mixing and bubble generation process. The K-shaped microfluidic junction is made of PDMS with five fixed channels which can be inserted with capillaries and the joint part of the edges of capillaries creates an irregular shaped mixing chamber inside of the junction as shown in Figure 5.1.

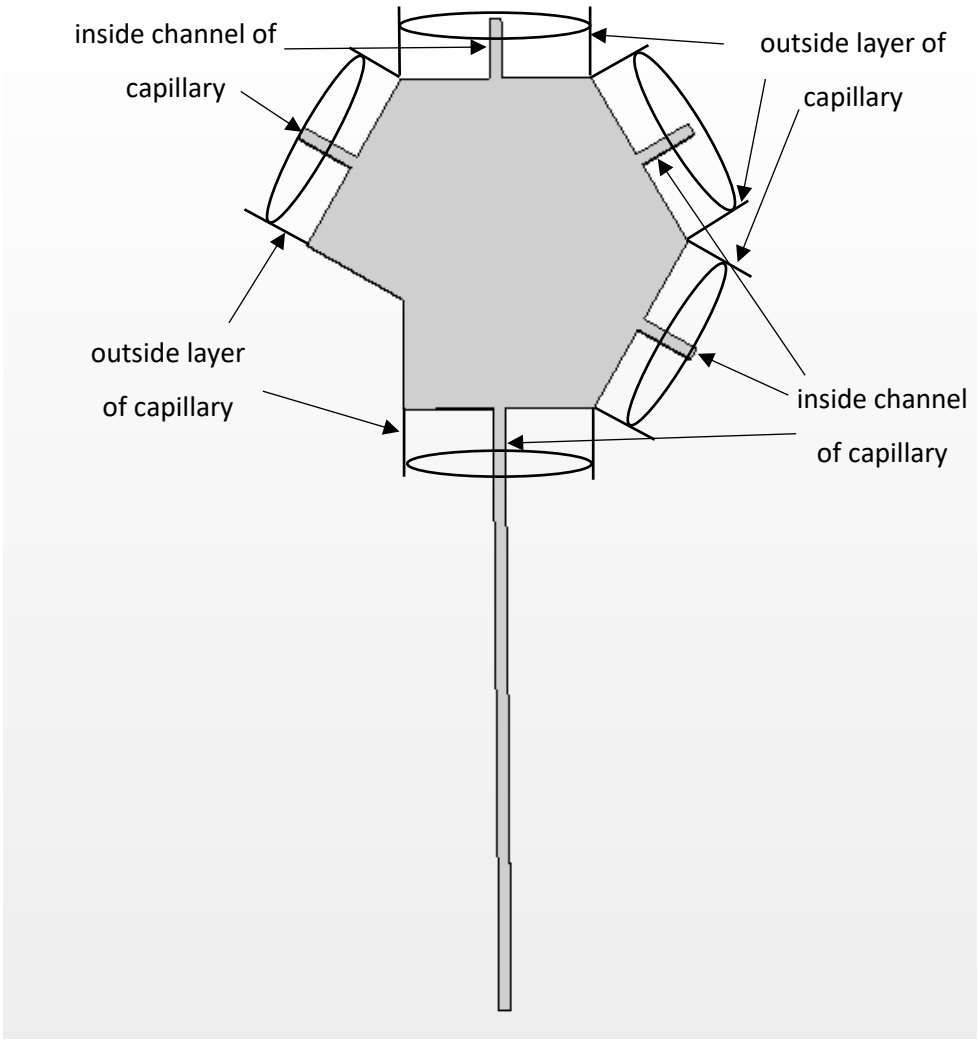

Figure 5.1 2D Geometry of K-junction created in the numerical simulation which is consist of five capillaries with inner channel.

The channel on the top is used as gas inlet, three channels on both sides are for liquid inlets and the last channel at the bottom is outlet where bubbles are formed. The flow is considered as pressure driven laminar flow, no-slip boundary conditions are applied on all walls. Both gas and liquid are treated as continuous phases and they meet at the mixing chamber inside the junction where the tip of the gas stream inflates a cavity which transforms into a growing bubble and breaks as a bubble and releases in the outlet channel. Multiple liquids with different density, viscosity and surface tension are used in the simulations and the diffusion of the liquid molecules is considered. To describe the mechanical processes inside this microfluidic K-junction, the dynamic of the fluid will be governed by the finite volume method and volume of fluid method as interface tracking technique when we extend the existing CFD software package STAR-CCM+ (CD-adapco Ltd, Melville, New York). It is a

multidisciplinary simulation environment that allows to represent most of the real-world physics in both research and industry with affordable computational resources. In these simulations, constant velocity inlets, pressure outlet and no-slip wall are considered as boundary conditions and the effect of fluid velocity, pressure and liquid diffusion are investigated in the simulations.

5.3 Numerical modelling

5.3.1 Geometry and mesh generation

Before running the simulations, the CFD software STAR-CCM+ (CD-adapco Ltd, Melville, New York) analysis requires a geometry to represent the actual object or scenario being modeled. The integrated 3D-CAD module is applied to prepare the geometry thus in this case the 3D geometry of the mixing chamber inside of the K-junction with five capillaries channels is built at first where different fluids movement, mixing and bubble break-up happen. Then a volume mesh is generated and a specific tool named badge for 2D meshing is used to identify part surface the lies on the symmetric plane of the 3D geometry of the K-junction. Therefore, a 2D mesh on this symmetric plane is generated and used in 2D simulations of the K-junction in this study. According to the design graph of the K-junction, five capillaries with internal and external diameters of 100 μm and 1.58 mm are inserted into the channels of the K-junction and an irregular shaped mixing chamber is created when the external edges of the capillaries meet. Gaseous phase and liquid phase flow through the internal channel in four of the capillaries and gas slug/bubble is collected at the end of the internal channel in the last capillary. Therefore, the physical geometry of the K-junction in this simulation can be simplified as five channels with diameter 100 μm and joints the irregular shaped mixing chamber with sider length of the 1.58mm. In consideration of the physics models applied, inlet boundaries are assigned to the tip of four channels, outlet boundary is assigned to the tip of the last channel, and the wall of the both channels and mixing chamber is set as surface boundary. The length of outlet channels which used to collect gas slug/bubble is extended compared to the rest channels in order to clearly observe the bubble generation and distribution and the whole geometry is shown in Figure 5.2.

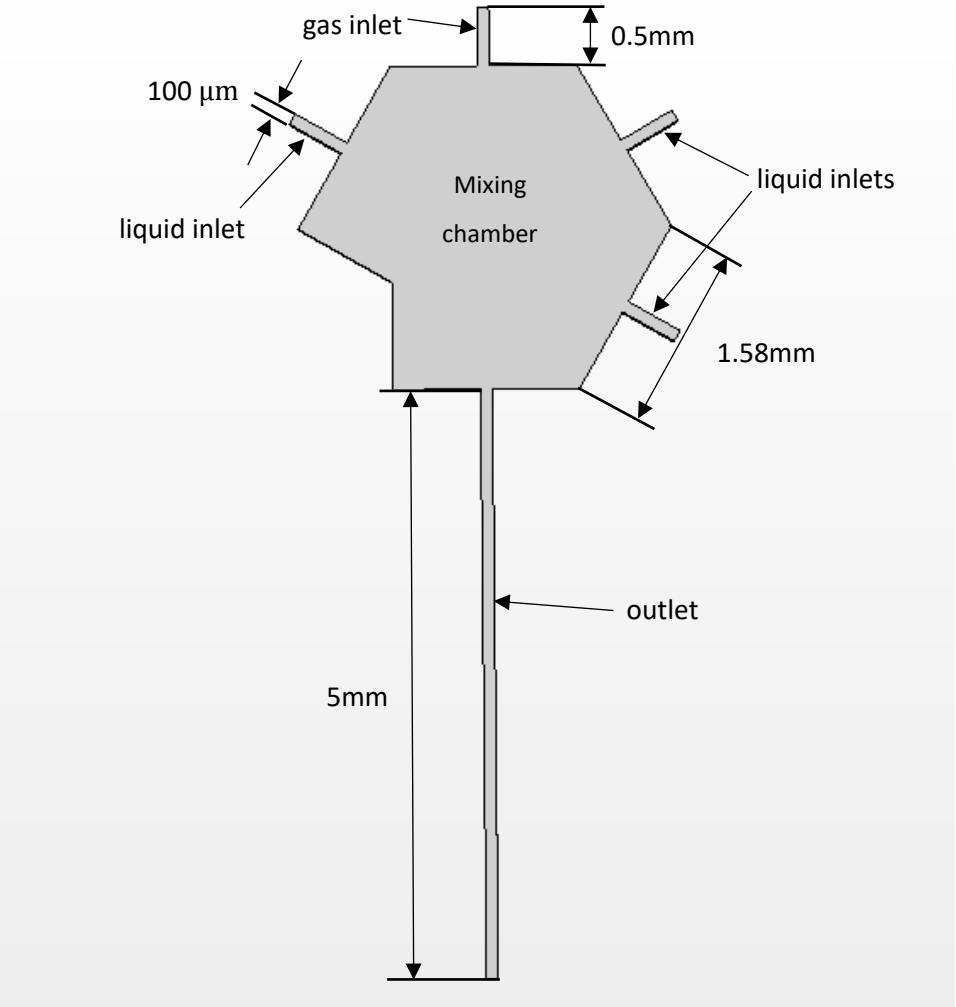

Figure 5.2 K-junction geometry generated in the simulation with dimensions in mm.

The mesh has to be generated afterwards with the geometry part created. Meshing models are split into two groups: surface mesh models and volume mesh models. Initially, the surface meshing models have to be used to create a high-quality surface mesh and then go on to choose volume meshing models to create volume mesh. The surface mesh is a discrete representation of the geometry of the individual regions that are used for the volume mesh generation. It consists of faces (triangles) and vertices. Besides, feature curves are included in surfaces that are created in some pre-processing packages. Internal feature surfaces such as baffles or interfaces are allowed. There are two surface meshing models provided in this numerical study: the surface remesher which is suit for geometries that have been imported from CAD models or created in 3D-CAD and the surface wrapper which can be used to extract fluid volumes, simplify complex assemblies or to provide a closed surface over poor quality CAD. Surface remesher is chosen to retriangulate the surface of the K-junction 3D geometry

generated before in this study and the remeshing is primarily based on a target edge length that is supplied and can also include feature refinement that is based on curvature and surface proximity. Localized refinement that is based on part surfaces or boundaries can also be included. Specific surfaces or boundaries can also be omitted form the process so that the original triangulation form the imported mesh can be preserved. The properties of the surface remesher model can be changed to provide additional meshing control during the meshing process such as volumetric control which allows the surface target size to be set for any of the allowable shapes that encompass the import surface and aligned meshing which can optimize the resulting surface triangulation further. The input values used for the surface remesher like the base size which is a characteristic dimension of the model can be adjusted to generate surface mesh with different mesh resolution. When a high-equality surface mesh of the K-junction is generated, the volume mesh models have to be implemented to create volume mesh. Several volume meshing models are provided in this software and the main models are as follows:

1)**Polyhedral mesher**: Suited to complex, multi-region geometries. It provides a balanced solution for complex mesh generation and can be built easily and efficiently without more surface preparation compared to tetrahedral mesh. The polyhedral meshing model utilizes and arbitrary polyhedral cell shape in order to build the core mesh and it also contains approximately five times fewer cells than a tetrahedral mesh for a given starting surface.

2)**Trimmer**: Uses a predominantly hexahedral mesh. It is efficient at filling large volumes and uses less memory per cell than the polyhedral mesh. It also provides a robust and efficient method of producing a high-equality grid for both simple and complex mesh generation problems. The trimmer meshing model utilizes a template mesh that is constructed form hexahedral cells from which it cuts or trims the core mesh using the starting input surface by default. The template mesh contains refinement that is based on the local surface mesh size and local refinement controls.

3)**Prism layer mesher**: Used with the previous two models to provide layers of prism cells next to the wall. The prism layer mesher is essential for turbulent flows. The prism layer mesh model is used with a core volume mesh to generate orthogonal prismatic cells next to

wall surfaces or boundaries. This layer of cells is necessary to improve the accuracy of the flow solution.

4)**Thin mesher**: For thin geometries (such as solid plates). The thin meshers are used to generate a prismatic type volume mesh for thin regions. However, the prismatic type mesh is only produced in portions of the geometry that the mesher recognizes as thin. Thick or bulk portions of the same geometry are meshed with polyhedral cells. The different portions of mesh are joined continuously without abrupt changes in the mesh between the bulk and thin portions of the geometry.

5)**Generalized cylinder**: For cylindrical geometries such as internal pipe flows. The generalized cylinder mesher is used with the polyhedral volume mesher to generate an extruded mesh along the length of parts that are considered to be generalized cylinders.

6)**Extruder**: Used to extend volume mesh as an offset from selected boundaries. The extruder mesher can be included with the core mesh when generating a volume mesh in order to produce orthogonal extruded cells for specific boundary surfaces. The extruder mesh is typically used for inlet and outlet boundaries to extend the volume mesh beyond the original dimensions of the starting surface, so that a more representative computational domain is obtained.

In this study, the meshing test comparison between polyhedral mesher and trimmer mesher was conducted. High quality polyhedral mesh was much easier to be generated than the hexahedral mesh although more time-consuming. It is probably caused by the complexity of the K-junction shown in Figure 5.2 such as the irregular shaped mixing chamber. The following convergence test also shows polyhedral mesh were more likely to converge than hexahedral mesh. Therefore, due to the results of meshing and convergence tests comparison between polyhedral mesher and trimmer mesher, the polyhedral mesher was chosen for the 2D simulations because it is relatively easy and efficient to build for this complex topology compared to other volume meshers. It has been noticed that the use of a 3D mesh is much less efficient than using a 2D mesh for 2D and axisymmetric simulations. Therefore, to expedite computational time and enable the computation of longer time histories and variety of conditions, we chose to implement the model on 2D-representation of the K-junction by

extracting a 2D mesh from its 3D volume mesh and the final 2D mesh of the junction is shown in Figure 5.3.

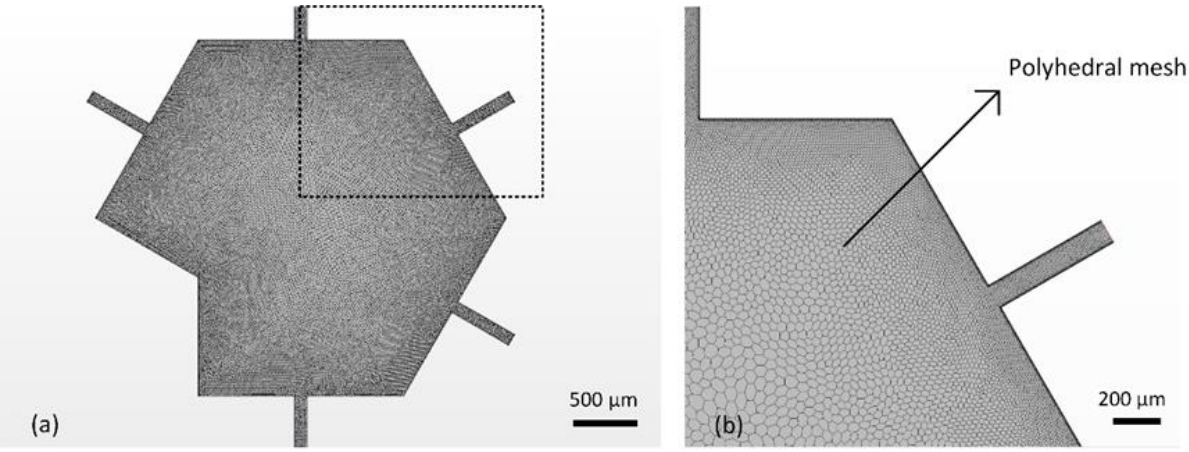

Figure 5.3 Geometry of the K-junction (a) and close-up of polyhedral mesh (b) in the dash line area.

5.3.2 Eulerian multiphase setup

Multiphase fluids will be used in these 2D simulations of the K-junction such as liquids with different properties and gas which are considered as Eulerian phases. Therefore, the Eulerian Multiphase model is used to create and manage those phase for these multiphase models that require multiple Eulerian phases. An Eulerian phase is defined as a phase that is modelled in a Eulerian framework and each Eulerian phase includes the set of models applicable to its material thus two materials constitute two different Eulerian phases. Each Eulerian phase has phase models that are associated with it such as gas, liquid, particle, multi-component gas and multi-component liquid. Here in this study, we choose nitrogen as the gas phase and different polymer solutions used in the experiments as liquid phases, whose physical properties are discussed in the experiment section. It determines the representation of a physical phenomenon in a phase, the primary variable of the simulation and usage of mathematical formulation to generate the solution. The phase materials can be found in the default model base and can also be customized with more appropriate data like replacing the physical properties like density, viscosity and surface tension of the liquid phase material to the ones that we used in the experiments. In addition, a Eulerian phase requires its own Equation of State model to define how the density of the material is computed. Several

equations of state have been provided such as constant density, ideal gas, polynomial density, and user defined density. For simplification, we assume all Eulerian phases used in the simulations as constant density Eulerian phase model that the density is invariant throughout the continuum and all the phases are in laminar flow based on the low Reynold number (below transition point) after calculation.

5.3.3 VOF multiphase setup

Volume of Fluid (VOF) multiphase model is selected to simulate flows of several immiscible fluids on numerical grids which are able to resolve the interface between the phases of the mixture. The spatial distribution of each phase at specific time is defined in terms of a variable that is called the volume fraction. The 2^{nd}-order discretization scheme with appropriate sharpening factor parameter is selected in order to obtain well-defined gas-liquid interfaces and implicit unsteady is chosen as temporal discretization. In terms of multiphase interaction model, after activating the VOF model the VOF phase interaction is applied to define the phase interactions where we can choose primary phase as liquid (continuous phase) and secondary phase as gas (dispersed phase). As the results by using VOF model could be influenced by the initial volume, it is necessary to set the initial volume fraction of each phase properly. According to the experience of numerical study on microfluidic device like T-junction from literature (Qian et al., 2006), we assume that the initial condition is set to be filled with one of the liquid phase in the entire flow domain of the K-junction and the velocity of the liquid phase is set to zero which help to obtain a convergence results.

5.3.4 Boundary condition initialization

Boundary conditions tell the STAR-CCM+ (CD-adapco Ltd, Melville, New York) solvers how the substance within the region interacts with its environment. For example, the solvers realize that an amount of substance is being added to the fluid domain at a certain rate from a velocity inlet boundary. There are three types of inlet boundary available in the software which differs depending on the properties used to define the inlet flow: velocity, mass flow rate and stagnation inlet. For outlet boundary, two types of outlet boundary are provided: flow-split and pressure. The only parameter required for flow-split ratio expressed as a value between 0 and 1 with the sum of flow-split ratio values for all flow-split outlet boundaries in

the region equal to 1. For the K-junction in this study, four fluid inlets in which one for gas and the other three for liquids are set as velocity inlets and the outlet is set as flow-split outlet with the flow-split ratio of 1. In order to transfer gas pressure and liquid volumetric flow rate we used in the experiments to velocity in the simulations, mathematic calculations have to be conducted. For the gas flow rate, since gas was controlled by a valve fitted on the gas tank and only pressure was measured from the pressure meter near the tank, the Poiseuille equation and Bernoulli's equation were used to calculate the value of gas flow rate as well as its superficial velocity. The fluid was assumed as incompressible and Newtonian with laminar flow inside of the pipe for the application condition of Poiseuille equation which is described in standard fluid dynamics notation:

$$\Delta \mathrm{P} = \frac{128 \mu L Q}{\pi d^4} \tag{5.1}$$

where $\Delta \mathrm{P}$ is the pressure loss, L is the length of pipe, μ is the dynamic viscosity, Q is the volumetric flow rate, d is the pipe diameter. Therefore, two digital pressure meters were used to measure the gas pressure between the gas pipe with the length of L to obtain the pressure loss ΔP_G, then the gas volumetric flow rate Q_p in the pipe can be rewritten as:

$$Q_p = \frac{\Delta P_G \pi d^4}{128 \mu_G L} \tag{5.2}$$

in which d is the diameter of the gas pipe connected to the gas tank, μ_G is the dynamic viscosity of gas (nitrogen), L is the length of pipe, and ΔP_G is the pressure loss. As the superficial velocity u can be defined as:

$$u = \frac{Q}{A} \tag{5.3}$$

where Q is the volume flow rate, A is the cross-sectional area. So, the superficial velocity u_p of the gas in the pipe can be expressed as:

$$u_P = \frac{Q_p}{A_p} \tag{5.4}$$

where A_p is the cross-sectional area of the gas pipe, and Q_p is the volume flow rate of the pipe. The gas pipe with large inner diameter is used to connect gas tank and capillary through

a tube convertor in experiments. According to the Bernoulli's equation in company with the one-dimensional continuity equation, it can be derived that:

$$A_1 u_1 = A_2 u_2 = \text{constant} \tag{5.5}$$

where A_1, A_2 are the cross-sectional areas in pipe 1 and pipe 2 with different diameters, respectively. u_1, u_2 are the superficial velocities in the two different pipes and the schematic diagram to illustrate this equation is in Figure 5.4.

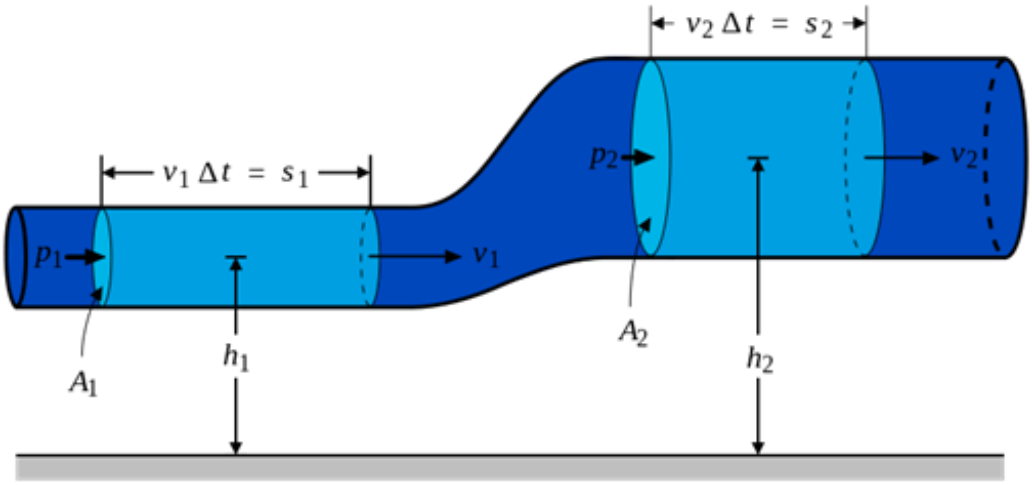

Figure 5.4 Diagram illustrating a derivation using Bernoulli's Law.

It is observed that the volumetric flow rate in gas pipe 1 which is represented as $Q_1(Q_1 = A_1 u_1)$ remains the same in capillary pipe 2 which is $Q_2(Q_2 = A_2 u_2)$. In order to calculate the superficial velocity and volumetric flow rate of the gas in capillary flowed from pipe, the derivation formula mentioned above can be developed as:

$$A_p u_p = A_c u_c = \text{constant} \tag{5.6}$$

in which A_p, A_c are the inner cross-sectional areas in the pipe and capillary, separately. u_p, u_c are the superficial velocities in the pipe and capillary as well. Thus, the superficial velocity in the capillary u_c can be expressed as: $u_c = \frac{A_p u_p}{A_c}$ which is considered as the gas velocity at the gas inlet of the junction and the inlet gas flow rate in the capillary which was written as:

$$Q_c = A_c u_c \tag{5.7}$$

where A_c are the inner cross-sectional areas in the capillary, and u_c are the superficial velocities in the capillary. During the experiment, it was observed that at 200 kPa the pressure drop (ΔP_G) between barometer on the gas tank and digital pressure gauge on the plastic pipe connected to the tank was about 0.01 Pa. The length of pipe (L) between two pressure gauges was measured as 0.6m and the inner diameter of the tube (d) was found to be 0.003 m. According to Equation (5.2), the volumetric flow rate of gas (Q_p) was calculated to be 114 $\mu l/min$ which was very close to liquid volume flow rate of 100 $\mu l/min$ which was used in the experiment. As the volumetric flow rate in both plastic pipe and capillary was the same based on Equation (5.6), the volumetric flow rate of gas in the capillary (Q_c) remained the same as Q_p. Then the velocity of gas in the capillary (u_c) at 200 kPa with inner diameter of 100 μm was obtained as 0.24 m/s by using Equation (5.3). Therefore, the Reynolds number of gas and liquids used in the experiment with volumetric flow rate of 114 $\mu l/min$ and 100 $\mu l/min$ respectively was calculated and shown in Table 5.1.

	Volumetric flow rate ($\mu l/min$)	**Reynolds number**
Nitrogen at 20℃ and 1 atm	114	1.65
5wt%PEG+2wt%PVA in water	100	5.05
5wt%PMSQ in ethanol	100	15.6
5wt%PLGA in acetone	100	1.78

Table 5.1 Reynolds number of gas and liquids with constant volumetric flow rate.

The rest of the boundaries are set as no-slip boundary condition with contact angle option activated if necessary. As the VOF model uses multiple Eulerian phases, it is necessary to set the volume fraction of each phase at appropriate boundaries thus the volume fraction at the gas inlet is set as 0 (gas phase) while the liquid inlets are set as 1(liquid phase). The gas inlet was defined as fixed velocity normal to the interface as well as liquid inlets which were both ranging from 0.01 to 0.5 m/s under a gas/liquid ratio of 0.5,1, and 2. Due to the

significant influence of Capillary Number (Ca) which illustrates the ratio between the viscous force and the surface tension on the flow patterns, particularly the mechanism of the generation of bubbles/slugs, simulations were conducted with different values of Ca in order to investigate the effect on bubbles/slugs formation.

It is reported by Gunther and Jensen (2006) that in flow-focusing devices, when Ca is below 0.01, the pressure drop across the bubble dominates the bubbles formation while when Ca is large, the effect of the viscous force is more obvious than the surface tension and serious deformation appears in the shape of the interface. Besides, previous experiment done by Garstecki et al. (2006) has shown that the length of the bubble/slug generated in a microchannel T-junction is also influenced by the flow rate ratio between the dispersed and carrier fluids significantly. In addition, the study of mesh dependence on the simulations was initially conducted so that the difference of the plots on the interface with various mesh resolutions was investigated and appropriated mesh resolution with reasonable accuracy was established. Therefore, the variables in the simulations were Capillary number (Ca), flow rate ratio between gas (Q_g) and liquid (Q_l) and mesh resolution. The simulations were categorized as different Ca of 0.005, 0.01, and 0.016 with constant flow rate ratios (Q_g/Q_l) of 1, different flow rate ratios (Q_g/Q_l) of 0.5, 1, and 2 with constant Ca of 0.01, and constant Ca and flow rate ratio (Q_g/Q_l) of 0.01, 1 repectively with coarse and refined mesh on the geometry. Three different kinds of liquids which were mentioned in experiment part were used in the final mixing simulation in the K-junction and the velocity of each liquid with different Ca is by using each liquid shown in Table 5.2.

Ca	Velocity of 5wt%PEG+2wt%PVA solution(m/s)	Velocity of 5wt%PMSQ solution(m/s)	Velocity of 5wt%PLGA solution(m/s)
0.005	0.065	0.14	0.016
0.01	0.13	0.28	0.032
0.016	0.21	0.45	0.051

Table 5.2 Velocities of different liquids with various Ca.

In addition, the corresponding gas and liquid velocities of these liquids with constant Ca of 0.016 and various flow rate ratios is also shown in Table 5.3.

	5wt%PEG+2wt%PVA solution		**5wt%PMSQ solution**		**5wt%PLGA solution**	
Flow ratio	Gas velocity (m/s)	Liquid velocity (m/s)	Gas velocity (m/s)	Liquid velocity (m/s)	Gas velocity (m/s)	Liquid velocity (m/s)
0.5	0.105	0.21	0.225	0.45	0.0225	0.051
1	0.21	0.21	0.45	0.45	0.051	0.051
2	0.42	0.21	0.9	0.45	0.102	0.051

Table 5.3 Gas and liquid velocities used in the simulation with different liquids and constant Ca.

The simulations of K-junction were carried out in 2D by using these three different liquids separately for researching the influence of Ca and flow rate ratio on bubble/slug generation at present. The flow rate of both gas and liquid phase was taken as volumetric flow rate which can be derived from each velocity and the flow rates of all liquid inlets in the K-junction were kept the same. The total number of simulation by using each liquid was 8 including 3 for different Ca, 3 for different flow rate ratios, and 2 for different mesh resolutions. Each simulation cost about 2-4 days depending on the running platform (4 for desktop and 2 for UCL Legion) thus the total time for simulation using three different liquids plus the waiting time consumed in the queue of Legion for submission and other disconnection problems was estimated around two months at least. For the K-junction, simulations need to be performed in 2D first by using three different liquids at the same time with various gas/liquid flow ratios which will take 5 days with coarse mesh and 10 days with refined mesh if running on my desktop or 3 days with coarse mesh and 6 days with refined mesh of running on the Legion. Then 3D simulations of the K-junction should be conducted

on the Legion with refined mesh and it will take 4-6 months approximately. Finally, it will take around 6-8 months for the simulation work.

5.4 Validation of the numerical model

5.4.1 Comparison with conventional microfluidic device

In order to confirm whether the CFD software STAR-CCM+ (CD-adapco Ltd, Melville, New York) is appropriate for this study, simulation of bubble or slug generation in a conventional microfluidic T-junction has to be modeled first and then compared with previous published work. It is reported that Guo and Chen (2009) have conducted a numerical study on Taylor bubble formation in a micro-channel T-junction by using VoF method and good agreement between simulation results and visualization experiment was achieved. Therefore, simulations using this software which is chosen for this project are performed for conditions that are practically identical to those described in the publication mentioned; then comparisons will be conducted to validate the numerical method chosen. Following the Guo and Chen (2009) model, the 2D geometry of the rectangular microchannel T-junction is shown in Figure 5.5.

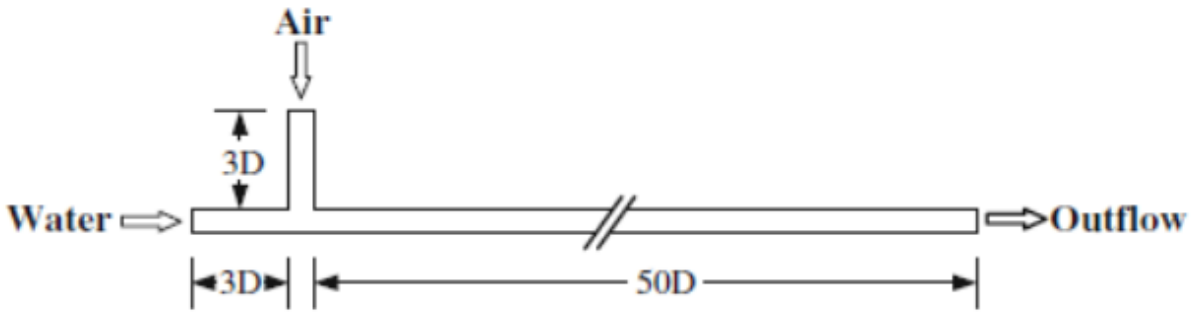

Figure 5.5 T-junction used in the simulation, adapted from Guo and Chen (2009).

The width D of both the straight and intersecting channels is 200 μm and the lengths of inlet channels for both water and air which are considered as continuous phase and discrete phase respectively are 3D. The length of outlet channel is 50D.

In the Guo and Chen (2009) work, the initial condition of the simulation was set as fully water-filled channels; then air and water were injected into the channels at constant velocity from their respective ports. Structured rectangular uniform grid blocks were used to

mesh the geometry and the flow inside was regarded as fully developed flow which means the velocity profile does not change in the fluid flow direction hence the momentum also does not change in the flow direction at the outlet. In terms of numerical methodologies employed, the Volume of Fluid(VOF) model (Noh and Woodward, 1976) accounted for the tracking and locating of the interface and the Continuum Surface Force (CSF) model (Brackbill et al. 1991) was used for accounting for surface tension. The Interface Reconstruction and Pressure Interpolation, Piecewise-Linear Interface Calculation (PLIC) (Youngs, 1982) and Pressure Staggering Options(PRESTO!) (Patankar, 1980) methods were employed for obtaining smooth and reliable contact line description. The pressure-velocity coupling was calculated by using the Pressure-Implicit with Splitting-Opeartions(PISO) algorithm (Issa, 1986) and momentum equation was solved by adopting a second-order upwind scheme. Series of simulations were conducted with the boundary conditions for the velocity of gas and liquid ranging from 0.01 to 0.9 m/s.

Our simulations implemented in the CFD software STAR-CCM+ (CD-adapco Ltd, Melville, New York) were conducted under the same conditions as the previous work done by Guo and Chen (2009) mentioned above by using the VoF method. In addition, the HRIC scheme (Muzaferija et al., 1998) which was designed to mimic the convective transport of immiscible fluid components was used in order to track sharp interfaces as an important quality of an immiscible phase mixture instead of PLIC algorithm. The simulation results for the various combinations of a set of gas (U_G) and liquid (U_L) inlet velocities are shown in Figure 5.6 depicting the void fraction contour.

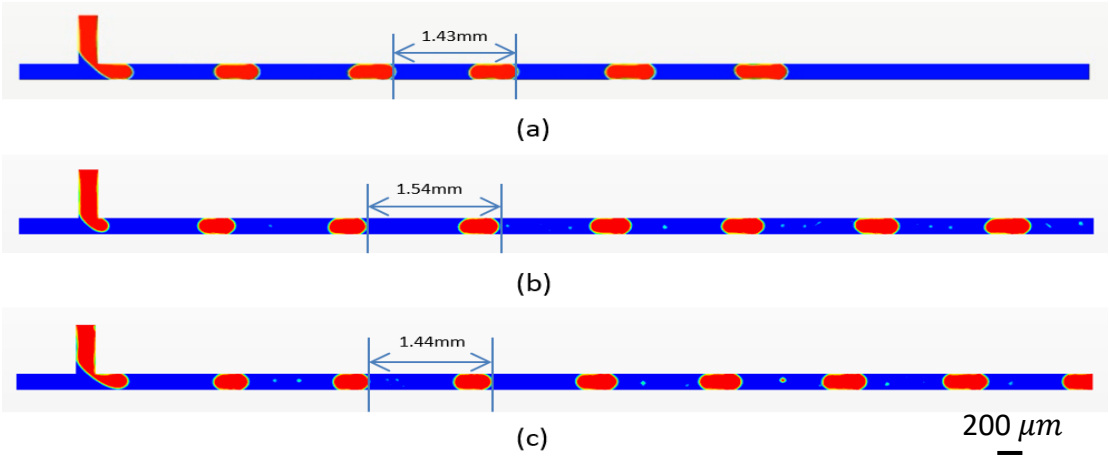

Figure 5.6 Our simulation results of bubble flow at different inlet velocities (a) u_G=0.06m/s, u_L=0.012m/s. (b) u_G=0.08 m/s, u_L=0.240 m/s. (c) u_G=0.10m/s, u_L=0.300 m/s.

It was found that the bubbles are generated at the intersection area and pinch off at by the corner between vertical and horizontal channels, then the bubbles flow to the outlet by continuous phase liquid without collision or merging. An important comparator in this case is the length of the bubbles and the number of bubbles observed per unit length. Figure 3.6 presents such results for our simulations, whereas Figure 5.7 shows the distribution obtained by Guo and Chen (2009), for identical flow and geometric conditions. For both the overall distribution and for the bubble tip to bubble tip lengths, the comparisons are made and differences are calculated.

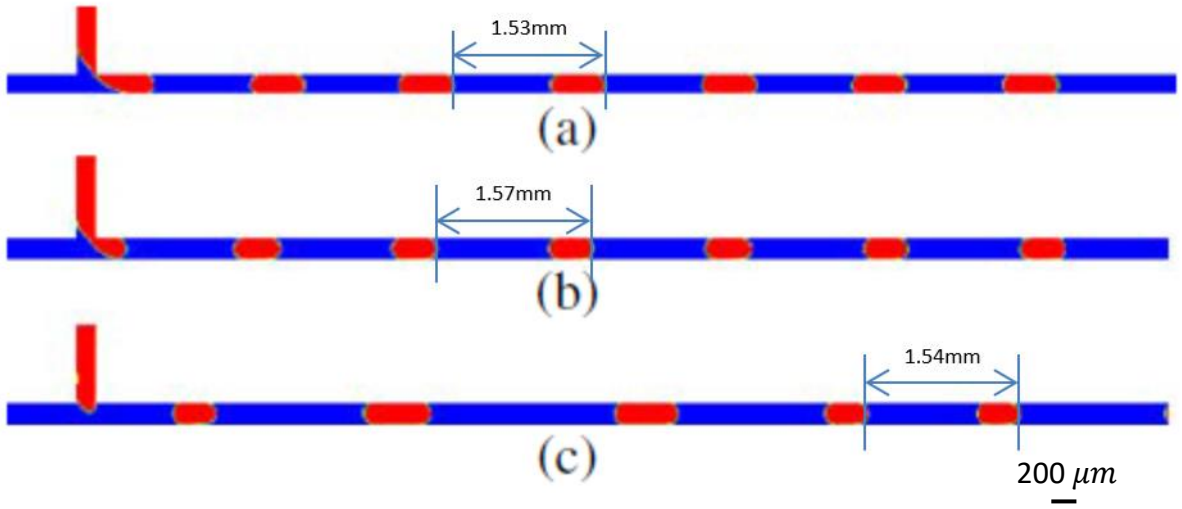

Figure 5.7 Simulation results by Guo and Chen(2009). (a) u_G=0.06m/s, u_L=0.012m/s. (b) u_G=0.08 m/s, u_L=0.240 m/s. (c) u_G=0.10m/s, u_L=0.300 m/s (Guo and Chen, 2009).

It is notated that the differences of the bubble tip to tip lengths between our simulations in Figure 4.6 and the simulations done by Guo and Chen (2009) in Figure 4.7 are 6.5%, 1.9%, and 6.5% for different conditions (a), (b) and (c) respectively which means the comparisons are deemed excellent.

The time sequence of the bubble generation at the intersection channel is also investigated under the same conditions as in the literature and the comparison of available experimental and simulation results (Guo and Chen, 2009) with our numerical simulations is shown in Figure 5.8.

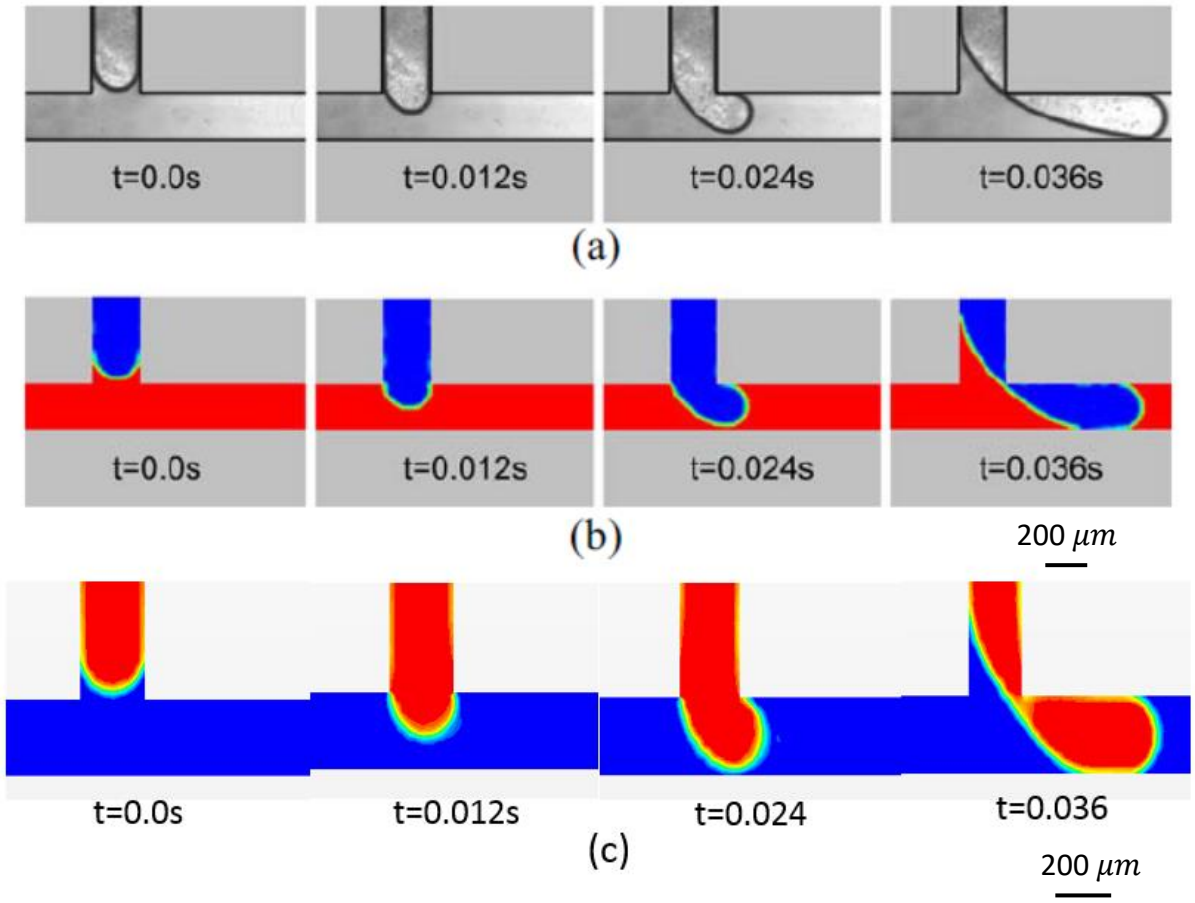

Figure 5.8 Experimental and numerical result of bubble generation by Guo and Chen (2006) at gas and liquid velocity of u_G=0.035m/s, u_L=0.09m/s. (a) and (b) are experimental result and numerical simulation of Guo and Chen (2006), (c) is our simulation results.

It is observed our numerical results have slightly difference compared to both experimental and numerical results obtained by Guo and Chen which is mainly caused by the difference in mesh refining and image capture error in real-time simulation. However, it still matches well with the bubble generation trend in the literature, confirming that numerical method we have chosen is appropriate for the task of capturing gas-liquid interfaces and bubble formation with reasonable accuracy. Therefore, we postulate that bubble generation in microchannels with more complex geometries such as K-junctions, where experimental data at this level of detail are not available, can indeed be replicated numerically by this methodology.

5.4.2 Grid independence test

The grid independence was conducted to investigate the influence of mesh size on the simulation results, six sets of polyhedral mesh cell ranging from 10^5 to 2.5×10^6 were used under the same boundary condition in the simulations. The inlet gas velocity v_g and other three liquid inlet velocity v_l were set as 0.1m/s and 0.01m/s separately. The physical properties of continuous and discontinuous phases were set as aqueous solution consist of PEG and PVA with 5% and 2% weight percentage individually and nitrogen. In order to minimize the measurement error, dimensionless parameters were adopted in this test. Dimensionless lengths of a microbubble, a liquid slug and the whole microbubble and liquid slug which are represented as L_b/D, L_l/D and $(L_b + L_l)/D$ individually are shown in Figure 5.9 with different number of mesh cells. It was found that the changes of these length parameters are not significant when the mesh cell count is above 5×10^5. Therefore, as a compromise of computation effort and the accuracy of the results, the mesh number of at least 5×10^5 cells with a grid size of 1E-4m are mostly used in this study in order to visualise the bubble generation and liquid mixing in the microchannels of the K-junction in a more physically realistic approach.

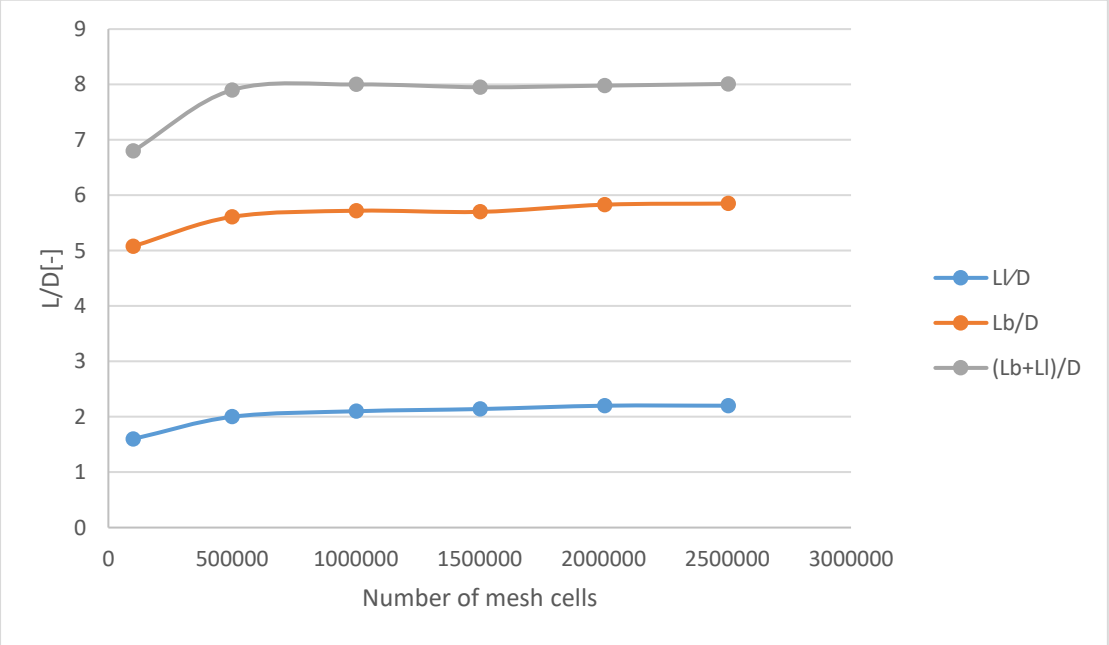

Figure 5.9 Grid dependence of the microbubble length/channel diameter, liquid slug length/channel diameter and the total length of both liquid and microbubble/channel diameter.

Therefore, numerical simulations with the number of 5×10^5 mesh cells by using the multiple liquids were then conducted which allowed further analysis, improved insight regarding the processes at play and a direct comparison of experimental and numerical results.

5.5 Analyzing numerical results

Results can be visualized using scenes. Scenes are composed using one or more displayers, where each displayer can be created independently of the others. The following displayer types are available such as geometry which is used to display geometry and change colour, opacity, and shading, scalar which is used to plot field function like density on parts and display filled, smooth filled contours, vector which is used to plot vector quantities like velocity and alter vector styles and distribution, streamline which can only be used to display streamlines and plot streamlines as tubes, lines, or ribbons and also animate streamlines using the toolbar. Derived parts including plane sections, isosurfaces, threshold-based parts, streamlines, probes and vortex cores are provided as alternative options to display simulation data if the model geometry has not enough surfaces.

5.6 Summary

This chapter has presented the numerical preparation for the simulation of the K-junction by using commercial computational fluid dynamic software STAR-CCM+ (CD-adapco Ltd, Melville, New York) provided. The geometry and mesh generation of the K-junction have been illustrated and appropriate multiphase fluids properties, Volume of Fluid (VOF) settings, and boundary conditions have been determined. It is found that there is still slightly difference when transforming gas pressure boundary condition to gas flow rate boundary condition although it is feasible in the simulations. Validation of the numerical model used for the K-junction are conducted on the conventional microfluidic T-junction and shows good agreement with the literature. The convergence analysis performed has also shown mass and momentum balance and a decrease in residual by three orders of magnitude without any divergence. Therefore, numerical model provided by this software are proofed to have the ability of solving these microfluidic problems such as microbubble generation and multiple

fluids mixing. Besides, grid dependence study also shows the most proper mesh cell number for the numerical simulations of the K-junction. The numerical results of the K-junction will be discussed and analysed in the following chapter.

Chapter 6 : Numerical and experimental results of the K-junction

6.1 Overview

In this section, results and discussion for the numerical simulation and experimental results of microfluidic K-junction have been discussed. The microbubble generation process is simulated under a series of operation conditions and the results are then used to investigate the external influences on this process and microbubble distribution. Besides, a parametric study is conducted to study the effects of liquid viscosity, surface tension and contact angle on the microbubble generation and size variation. Finally, the numerical simulation results are compared and verified with experimental observations, which contribute to the optimisation of the design of microfluidic device and operation conditions in the future.

In terms of experimental results of the microfluidic K-junction, the microbubble generation process inside of the K-junction under specific gas and liquid flow rate is captured by high-speed camera for the comparison with numerical results. Meanwhile, the influence of inlet gas pressure, liquid viscosity, gas-liquid flow ratios on microbubble size distribution and multiple fluids mixing have also been investigated from experimental results. The microbubble throughput and diameter distribution under different gas-liquid flow ratios are compared with numerical results with the same condition.

6.2 Numerical results

6.2.1 The test simulations

Test simulations of three different kinds of liquids and one gas which are used in the experiments were performed in the K-junction with simple geometry that only has microchannels with inner diameter of 100 μm and gas/liquid flow ratio of 0.5, 1 and 2 respectively. In terms of mixture property, the molecular diffusivity between these three liquids was determined by Schmidt number which is described as the ratio of momentum diffusivity (viscosity) and mass diffusivity, other material properties such as density, and dynamic viscosity were treated as volume-weighted mixture. In the simulations, it was

assumed that the diffusion only happened between water and ethanol in these solutions and the Schmidt number was found to be 540. The velocities of all liquid inlets were kept the same and gas velocities were ranged from 0.02 m/s to 0.04 m/s. The inlets of the K-junction were set as inlet 1 for gas (nitrogen) and inlet 2, 3, 4 for three different liquids 5wt%PEG+2wt%PVA water solution, 5wt%PMSQ ethanol solution, and 5wt%PLGA acetone solution (Figure 6.1).

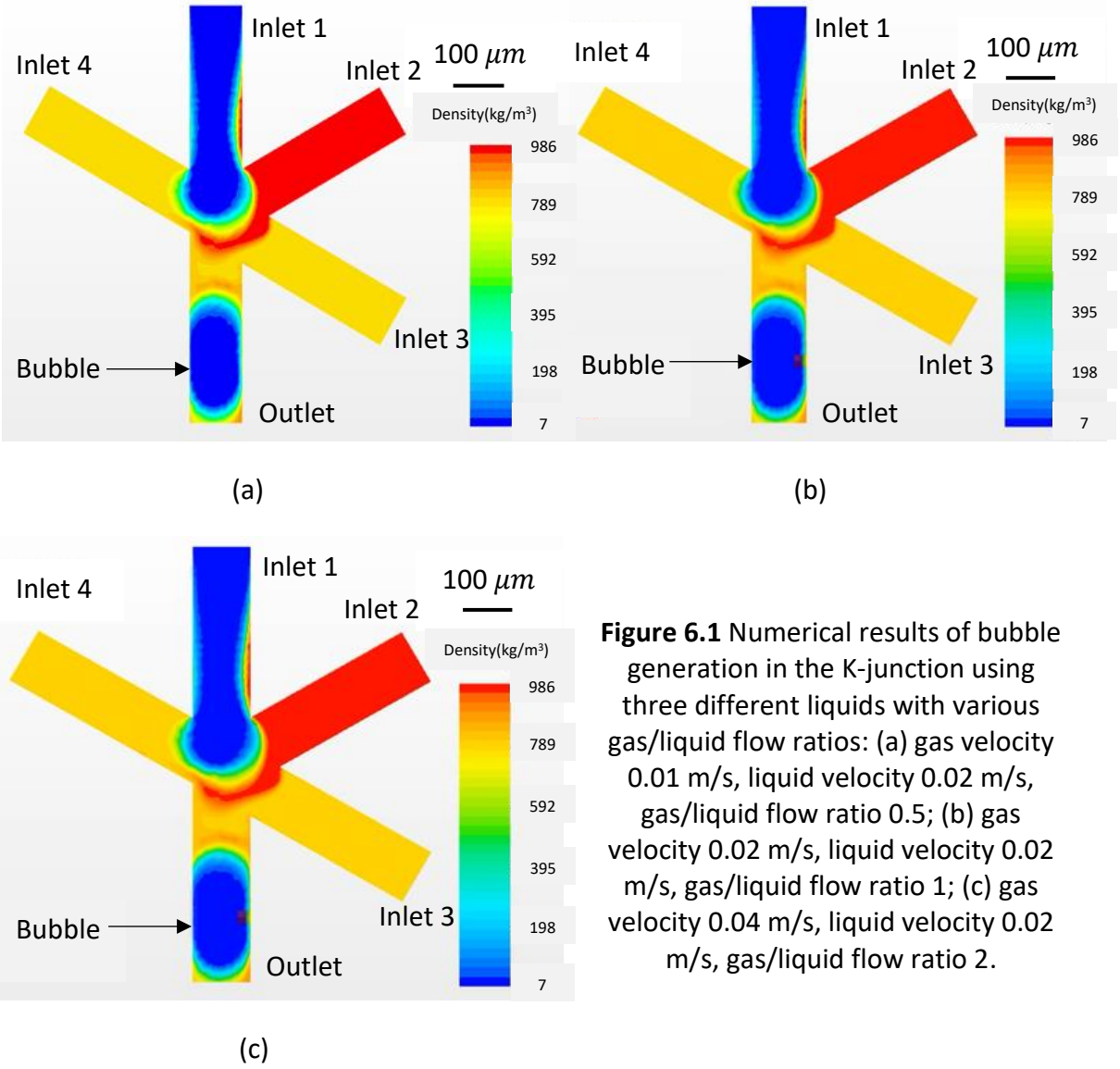

Figure 6.1 Numerical results of bubble generation in the K-junction using three different liquids with various gas/liquid flow ratios: (a) gas velocity 0.01 m/s, liquid velocity 0.02 m/s, gas/liquid flow ratio 0.5; (b) gas velocity 0.02 m/s, liquid velocity 0.02 m/s, gas/liquid flow ratio 1; (c) gas velocity 0.04 m/s, liquid velocity 0.02 m/s, gas/liquid flow ratio 2.

The bubble sizes and throughput under each gas/liquid flow ratio in the K-junction were measured and listed in Table 6.1 below.

Gas/liquid velocity flow ratio	Bubble size (μm)	Outlet throughput(bubble/s)
0.5	230	0.8
1	232	1.125
2	240	1.2

Table 6.1 Bubble sizes and throughput variations with different gas/liquid flow ratios in the numerical simulations of the K-junction.

It was observed that microbubbles were generated in the simulations of this simple K-junction geometry with various gas/liquid flow ratio by implementing mixing module with Volume of Fluid method in the software STAR-CCM+ (CD-adapco Ltd, Melville, New York). The bubbles were formed through the process that the liquid mixture phase pinched off the gas phase inside of the junction and then squeezed the bubble to the outlet by the force of liquid mixture and the bubble size increased slightly with the increasing gas/liquid ratio as well as the generation rate of bubbles. The test simulations indicated that it is feasible to use this software and numerical method to model multiple fluids mixing and bubble generation in this simplified K-shaped junction. However, the interface between gas and liquid can only been visualized with low resolution as obvious numerical diffusion occurred due to coarse mesh and big time step adopted in the simulations.

6.2.2 Effect of the contact angle

First, we investigated the effect of the contact angle on the bubble length, bubble volume and pressure drop under various gas-liquid flow ratios as shown in Figure 6.2a-b. It was indicated that the bubble length increases (Figure 6.2a) with the increase of the gas-liquid flow ratio, which is qualitatively consistent with the existing correlations for the bubble length in the literature (Fu et al., 2010; Garstecki et al., 2006). In this study, the bubble length was measured as the distance between the top and the bottom of a bubble at the centre line of the microchannel. The bubble length changes little along the main channel; therefore, the bubble and gas slug were only measured at the outlet of the main channel.

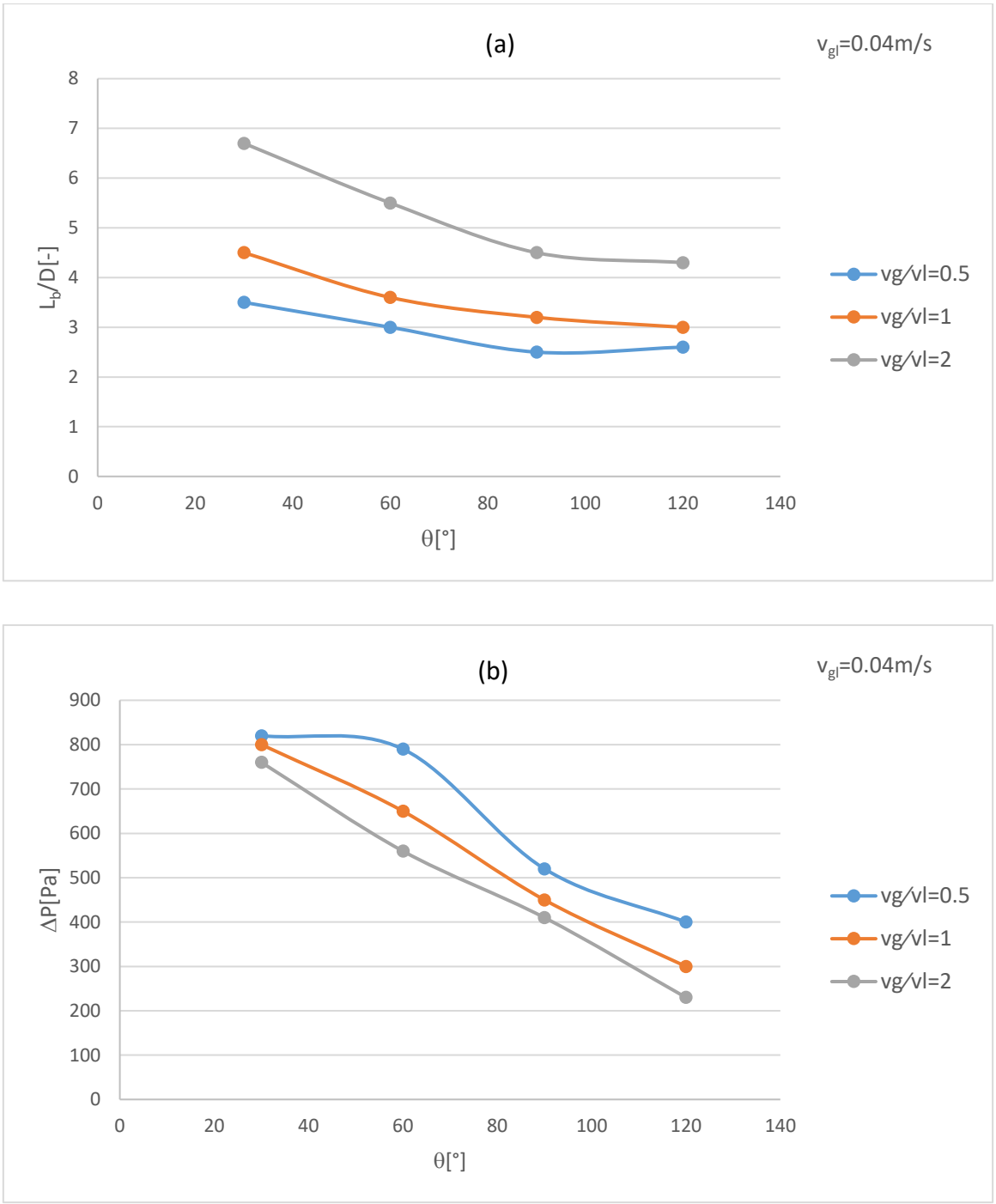

Figure 6.2 Effect of the contact angle at gas–liquid flow ratios of 0.5, 1.0, 2.0 on (a) bubble length, and (b) total pressure drop (measured from the inlet of gas to the outlet of the main microchannel). Liquid surface tension σ=37.6 mN/m, dynamic viscosity μ_l=2.7 mPa s, two-phase mixture velocity V_{gl}=0.04 m/s.

The increase of the contact angle results in a decrease of the adhesive force on the wall, which further leads to a reduction in the overall resistance to the flow and therefore contributes to the generation of bubbles (Garstecki et al., 2006; Bashir et al., 2011). More specifically, the bubble length decreases with the contact angle being increased from $30°$ to $90°$. This is mainly caused by the fact that the change of bubble shape which will result in a decrease in the bubble length if the bubble is considered as a given volume in direct contact with the microchannel wall. It is revealed that no liquid film in the channel was around the bubble body at large contact angle ($120°$) which corresponds to the literature observations (Cubaud et al., 2006; Oskooei et al., 2010; Yue et al., 2013). For a relatively small contact angle like $30°$, however, the bubble body is surrounded by a liquid film along the microchannel wall which implying a relatively long bubble. Therefore, it is possible that the bubble length decreases with the increase of the contact angle. In summary, the numerical results show that the effect of the contact angle on the bubble length becomes more significant at higher gas-liquid flow ratios.

The total pressure drop in the simulation of microbubble generation, which is measured from the gas inlet to the outlet of the microchannel, under various gas-liquid flow ratios and contact angles with constant mixture velocity is shown in Figure 6.2b. It can be seen that the total pressure drop decreases with increasing contact angle under constant gas-liquid flow ratio, which is due to the significant reduction of pressure drop over bubble tips caused by the shape change, resulting in a total pressure drop including the pressure drop from the liquid slug, the bubble body and its tips reduction. At constant contact angle, the total pressure drop with microbubble flow decreases when the gas-liquid flow ratio increases. The decrease of the total pressure drop is mainly caused by the reduction in the pressure drop contributed from the liquid slug because the liquid holdup is decreased upon increasing gas-liquid flow ratio; such lower liquid holdup, the decrease of pressure drop from the liquid will become more pronounced when the slug velocity is fixed (Yue et al., 2009).

6.2.3 Effect of the surface tension

The effect of the surface tension under various gas-liquid flow ratios and contact angles on the bubble length (Figure 6.3a and b) is investigated here. The simulation results have shown that the bubble length increase with an increase of the surface tension at contact angle $\theta =$

60° and gas-liquid flow ratio $v_g/v_l = 0.5$ and 2.0 (Figure 6.3a), and at $v_g/v_l = 1.0$, $\theta = 30°$ and 120° (Figure 6.3b), which agree with the results from the literature (Qian et al., 2006). The results can be explained by the reason that the surface tension is the only conservative force that hinders the expansion and the rupture of the emerging bubble (Bashir et al., 2011). Therefore, it is more difficult to reach a balance of forces at higher surface tension, leading to slower bubble formation and hence larger bubble size. Different from the effect of the contact angle, the effect of the surface tension on the bubble length is on the contrary, which indicates the slight increase of bubble length along with the surface tension increase (Figure 6.3a and b). It was also found that the surface tension has less influence on the shape of the bubble and the liquid film around the bubble body in simulations.

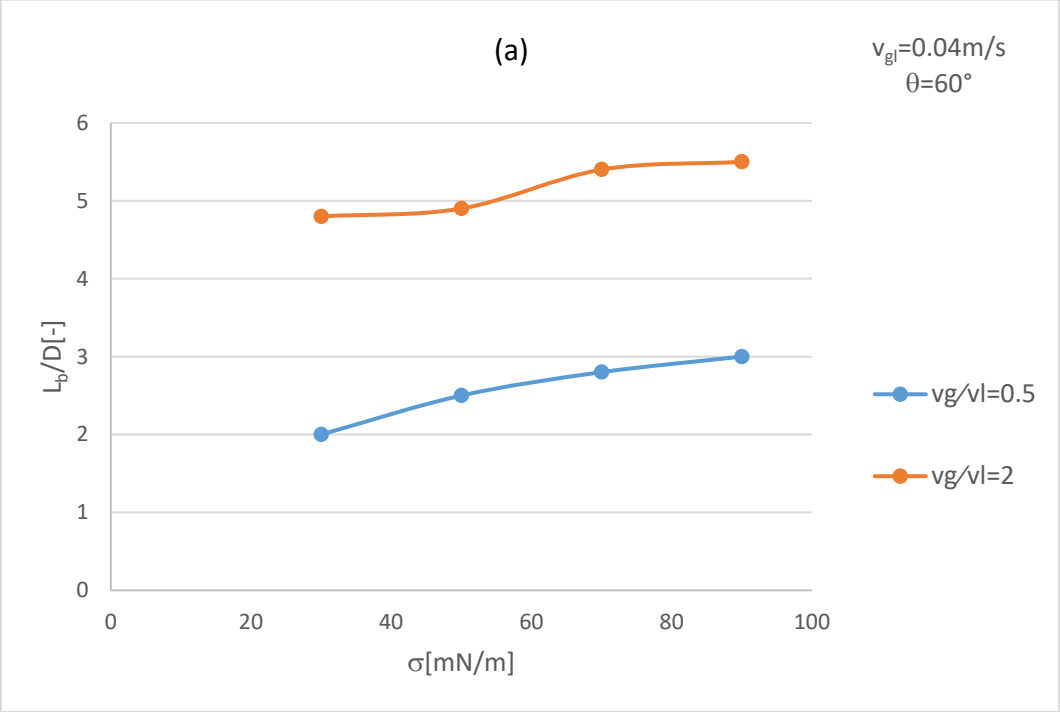

Figure 6.3 *Effect of the surface tension under various gas–liquid flow ratios (a) and contact angles on the bubble length (b). Liquid dynamic viscosity μ_l=2.7 mPa s, two-phase mixture velocity V_{gl}=0.04 m/s.*

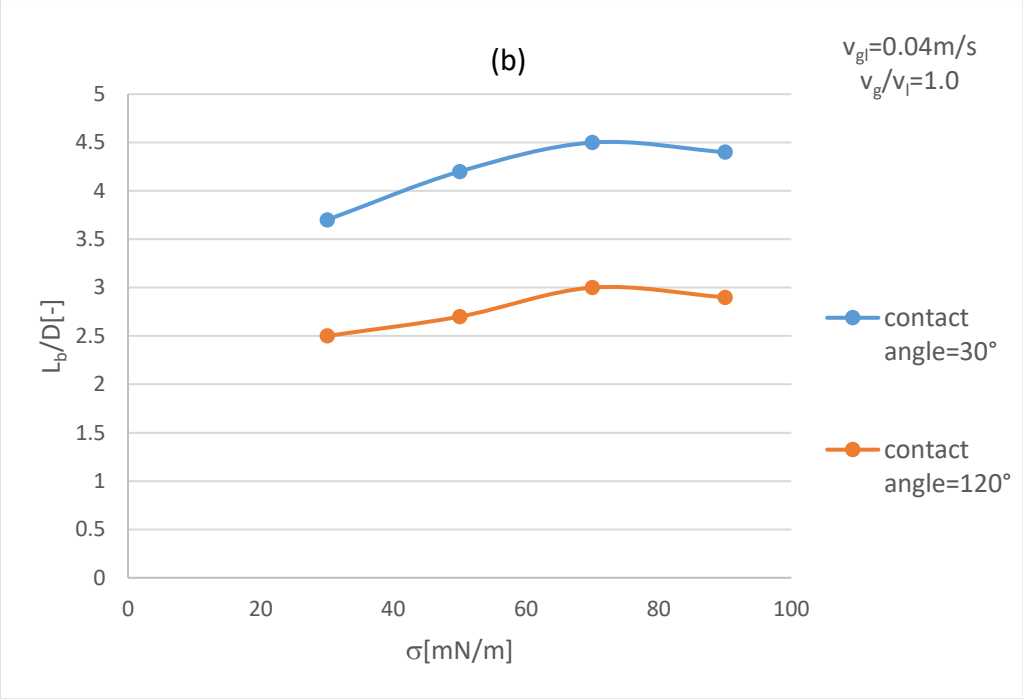

Figure 6.3 Effect of the surface tension under various gas–liquid flow ratios (a) and contact angles on the bubble length (b). Liquid dynamic viscosity μ_l=2.7 mPa s, two-phase mixture velocity V_{gl}=0.04m/s(continued).

6.2.4 Effect of the liquid viscosity

The results in Figure 6.4a-b have shown the effect of the liquid viscosity on the bubble size. It is found that the effect of the contact angle on the bubble length (Figure 6.4a) varies at different liquid viscosities (1.7 and 6.6 mPa s). The bubble length decreases with the increase of the contact angle under low liquid viscosity (μ_l = 1.7 mPa s) and keeps stable under relatively high liquid viscosity (μ_l = 6.6 mPa s) when surface tension is low (38 mN/m). However, for high surface tension (80 mN/m), the bubble length decreases in both low and high viscosity conditions (1.7 and 6.6 mPa s) with the increase of the contact angle. In Figure 6.4b, it can be further concluded that at a relatively high liquid viscosity (μ_l = 6.6 mPa s), the bubble length decreases dramatically with the increase of the contact angle. The bubble (regardless of its volume change) can experience a significant decrease in its length with increasing contact angle because of the combined effect caused by change of bubble shape and the decrease of the liquid film volume around the bubble; this combined effect is also present at the current condition of μ_l = 6.6 mPa s.

Figure 6.4a indicates that for a relatively high liquid viscosity of μ_l= 6.6 mPa s, the bubble length almost remains constant with the increasing contact angle at surface tension σ= 38 mN/m. However, it shows a significant decrease with increasing contact angle at σ = 80 mN/m (Figure 6.4b). This can also be explained by the two factors that cause the decrease of the bubble length with increasing contact angle as discussed before, which are the change of bubble shape and the decrease of the normalized liquid film volume surrounding the bubble body.

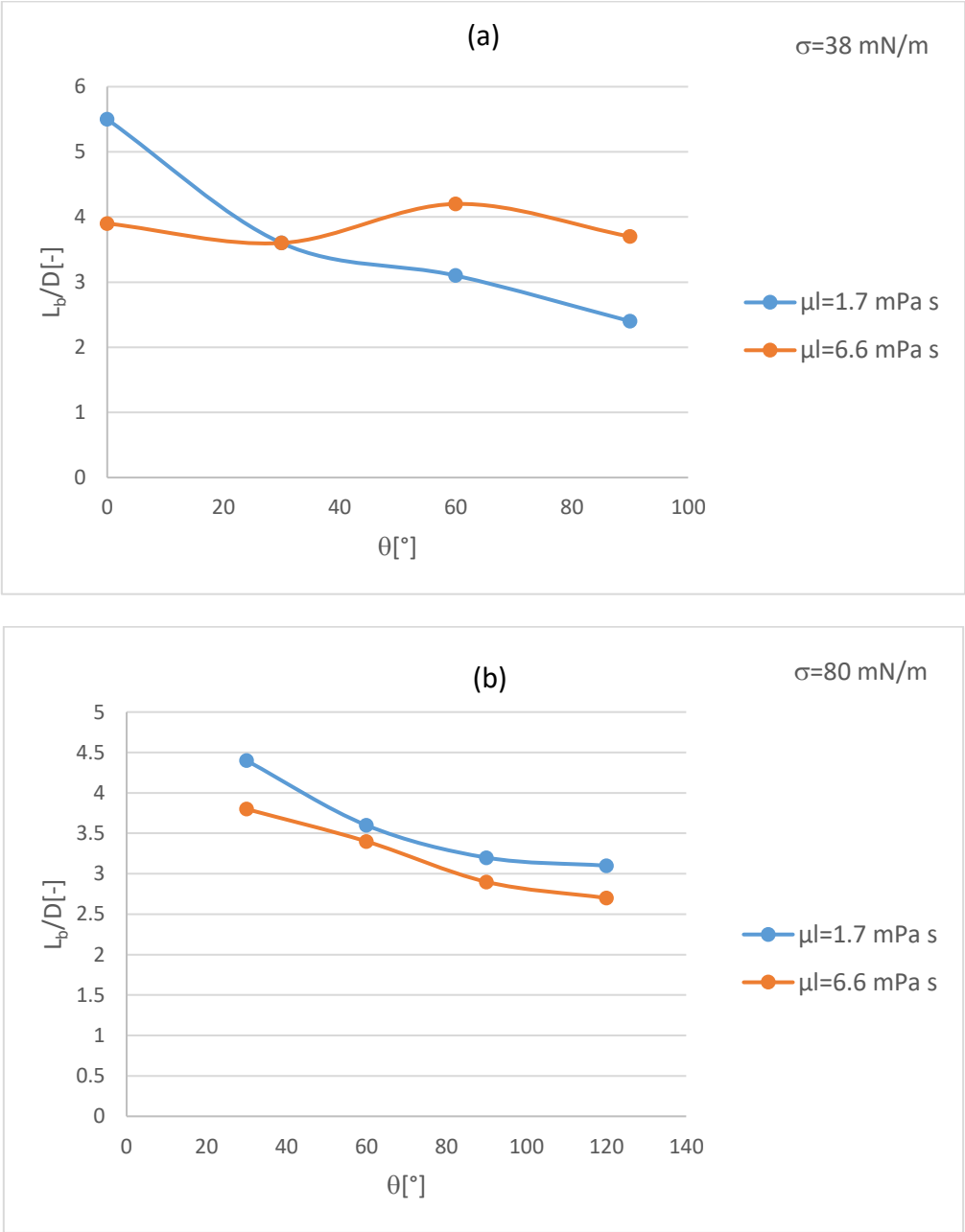

Figure 6.4 Effect of the liquid viscosity on (a) the bubble length at σ = 38 mN/m, (b) the bubble length at σ = 80 mN/m. Gas velocity V_g = 0.2 m/s, liquid velocity V_l= 0.2 m/s.

6.3 Experimental results

6.3.1 Microbubble generation

Microbubbles were generated at various gas pressures under constant liquid flow rate. Microbubbles could only be consistently produced within a limited range of gas pressures (P_{min} and P_{max}). For gas pressures lower than P_{min}, only liquid droplets were formed as the gas phase would be pushed back towards the gas inlet by the liquid stream because of capillary force applied by the liquid phase. In such instances, gas inlet capillary might be blocked. On the contrary, at gas pressures higher than P_{max} the stability of both gas and liquid flow was interrupted inside the intersection chamber, which prevented the pinch off process at the outlet channel so that only long gas slugs were consistently produced.

The high-speed camera was used to capture image sequences of the bubble generation process (Figure 6.5). The bubble generation process can be classified into four stages: (1) expansion stage; (2) fluctuation stage; (3) stretching stage; and (4) pinch off stage. Initially, the gas column entered the intersection chamber inside the junction area where it expanded to a large gas core until it reached the outlet channel. The shape of the gas core fluctuated and then gradually became stable. The gas column near the outlet was stretched at this point and then the liquid phase finally pinched off the gas column so that gas slugs were formed with remarkable repeatability. Microbubble generation could only successfully proceed when the gas pressure and the liquid flow rate reached an equilibrium state.

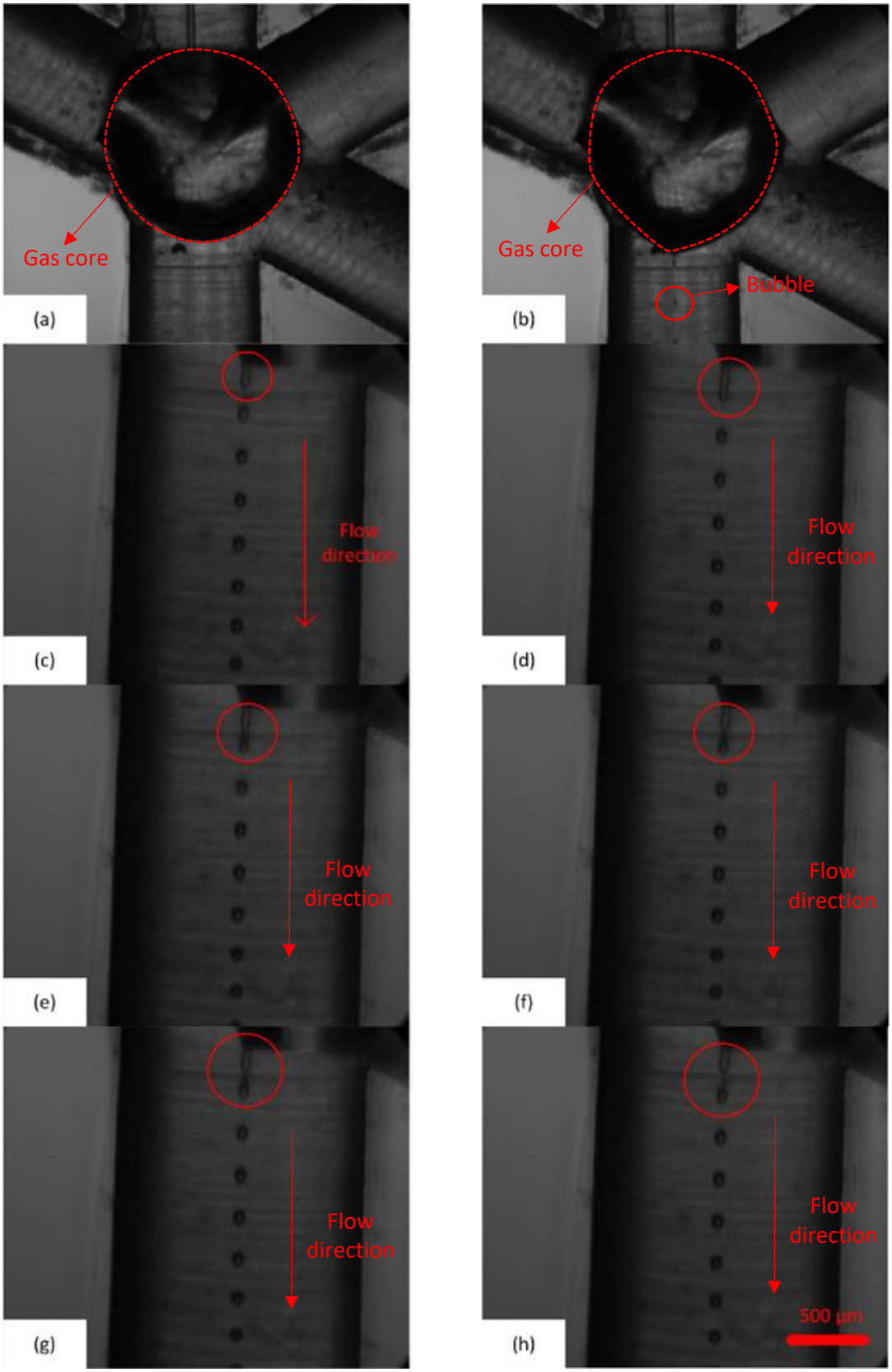

Figure 6.5 Bubble generation process in the K-junction. Solution with viscosity of 2.7 mPas and flow rate of 0.2 m/s was used. (a), (b) Images are taken at (c)0 ms; (d)0.22 ms; (e)0.44 ms; (f)0.49 ms; (g)0.56 ms; (h)0.67 ms. In the first two images, the mixing chamber dominated by the gas core is shown. In the last 6 images, pinch-off and the bubble train in the outlet capillary are shown.

6.3.2 Influence of the gas inlet pressure

Figure 6.6 shows the effect of the gas inlet pressure on the average bubble size under a constant liquid flow rate of 0.2m/s. The liquids used were 5% PEG with increasing concentrations of PVA (from 1% to 5%) with the viscosity increasing from 1.7 to 6.7 mPa s. The properties of these polymer solutions are shown in Table 6.2.

Components	**Density (kgm^{-3})**	**Dynamic viscosity (mPa s)**	**Surface tension (mNm^{-1})**
A)5% wt PEG+1% wt PVA	993	1.7	38.4
B)5% wt PEG+2% wt PVA	997	2.7	37.6
C)5% wt PEG+3% wt PVA	999	3.8	37.3
D)5% wt PEG+4% wt PVA	1002	5.1	38.2
E)5% wt PEG+5% wt PVA	1013	6.6	38.3

Table 6.2 Properties of polymer solutions used for pressure influence experiments.

The average bubble diameter increased with increasing inlet gas pressure. The expansion time of the gas core decreased with increasing gas pressure but the fluctuation time increased as well as the stretching time so that a longer gas slug/bubble was formed. It was observed that the bubble generation process occurred within a specific range of gas pressures for liquids with different viscosities. Based on Figure 6.6, it was found that the difference between gas pressure to create the smallest and biggest bubbles for low viscosity liquids (5%PEG+1%PVA, 5%PEG+2%PVA, and 5%PEG+3% PVA) is about 170 kPa. However, for high viscosity liquids (5%PEG+4% PVA and 5%PEG+5% PVA) the gas pressure difference is about 120 kPa, which indicates a smaller range of gas pressures for microbubble generation at high viscosity than that at low viscosity. It is also clear that bubbles were generated at low gas pressure for low viscous liquids while for high viscous liquids the gas pressure required was much higher because of the increased resistance to microchannels by shear stress; therefore, high gas pressure was required to overcome the friction between the liquid and

microchannels in order to keep the fluid moving. The microbubbles generated in the experiments were collected on glass microscope slides. It was found that microbubbles were highly monodispersed when collected on water wetted glass slides. The microscope slides were then placed on the optical microscope Nikon Eclipse ME-600 (Nikon Co, Tokyo, Japan) for observation and images were captured immediately. In each image under specific liquid and gas pressure conditions, the diameter of 100 bubbles were measured by using an open source software ImageJ developed by Wayne Rasband (Schneider et al., 2012) and the average value of microbubble diameter was taken as result.

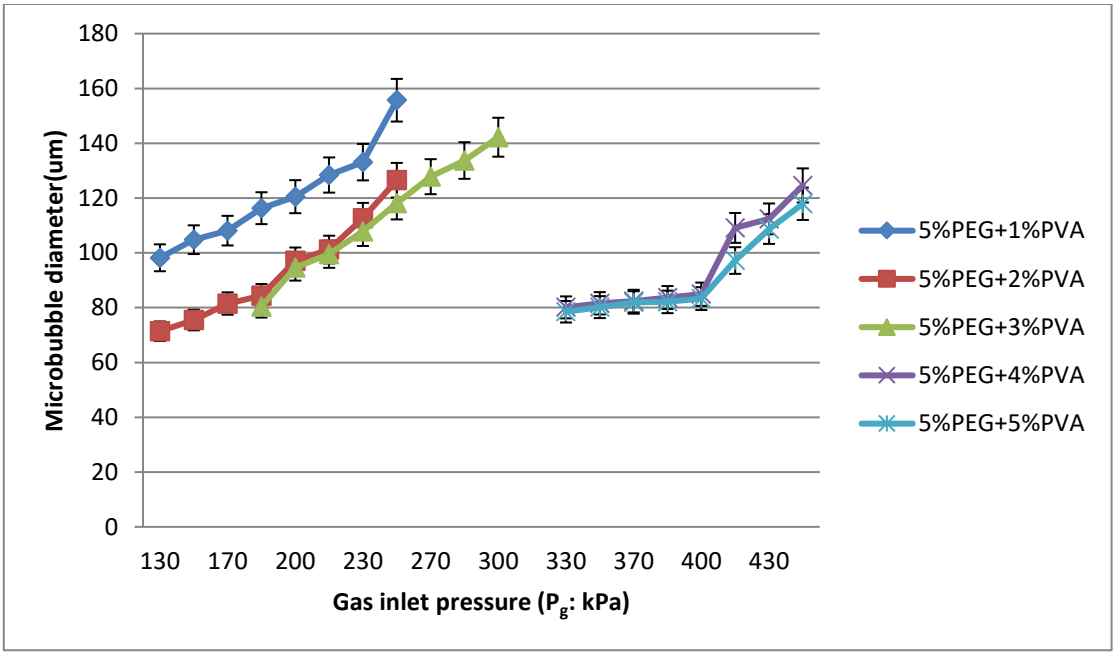

Figure 6.6 Bubble diameter variation plotted as a function of inlet gas pressure for solutions of different viscosities. The liquid flow rate was kept constant at 0.1ml/min with ±5% error bar.

6.3.3 Influence of the liquid viscosity

Due to its good stability regarding the microbubbles generated by the K-junction, aqueous solution with surfactant PEG and polymer PVA was chosen for further experiments. The viscosity was adjusted by increasing the percentage of PVA from 1% to 5% with constant 5% PEG. It was revealed (Figure 6.7) that microbubbles with the highest diameter were obtained by using solutions with the lowest viscosity while for solutions with higher viscosities the microbubbles formed have lower diameters. As it is also shown in Figure 6.8, bubble diameter

decreases with increasing liquid viscosity under constant gas pressure and liquid flow rate. Microbubbles with relatively smaller sizes were produced at a fixed liquid flow rate by using high viscosity solutions because of the increasing shear force in the liquid flowing through capillaries from three different directions and meeting at the intersection chamber of the junction.

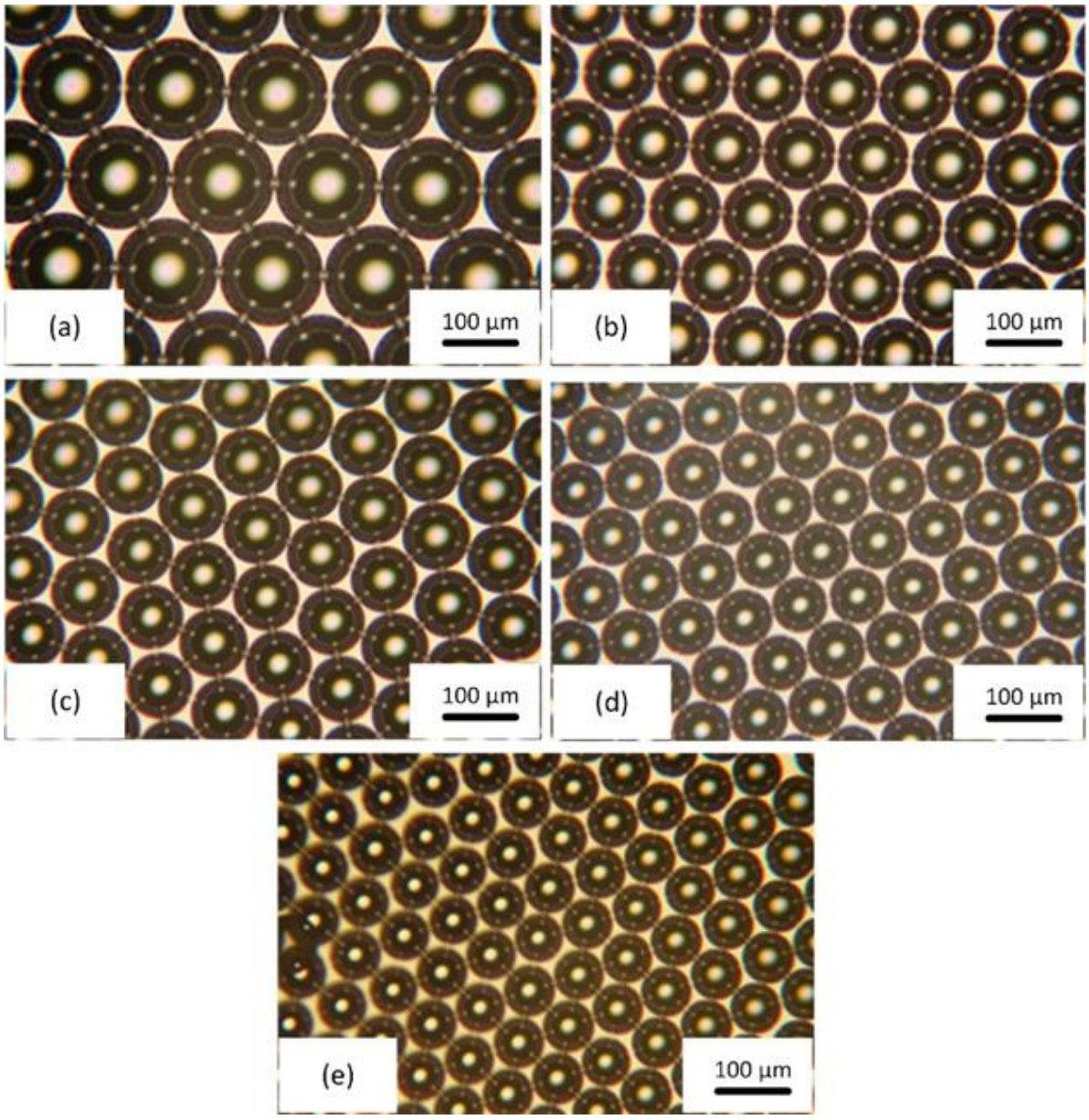

Figure 6.7 Micrographs showing bubbles formed under a constant liquid flow rate (0.2m/s) and gas to liquid flow ratio (Q_g/Q_l) of 2 and viscosities of: (a) 1.7 mPa s, (b) 2.7 mPa s, (c)3.8 mPa s, (d)5.1 mPa s, and (e)6.6 mPa s.

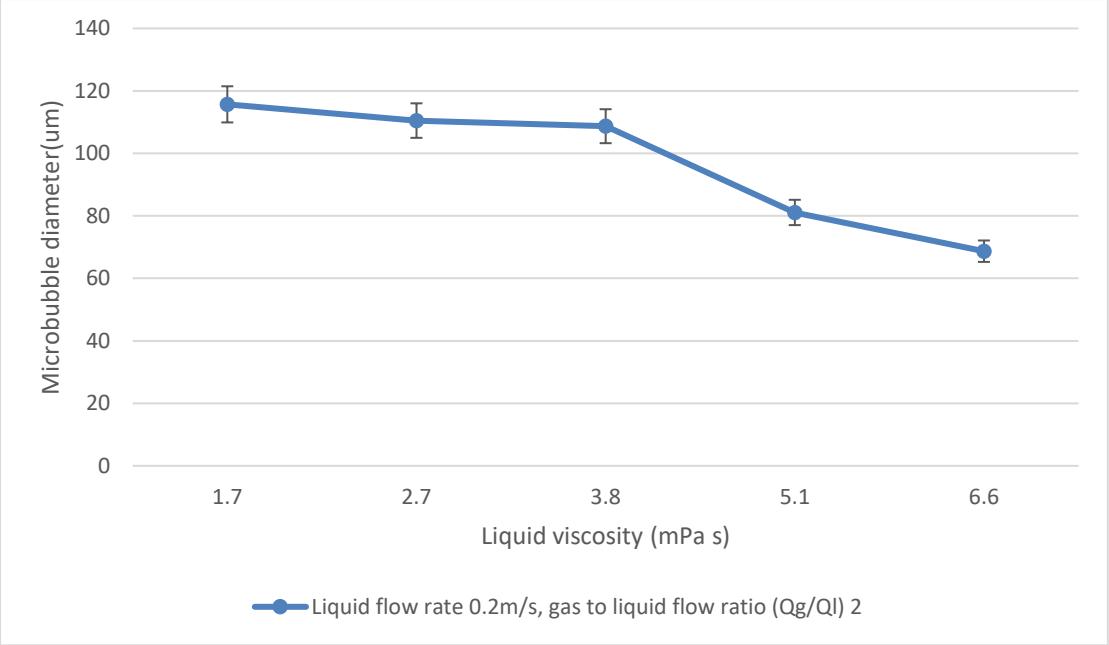

Figure 6.8 Microbubble size variation with different liquid viscosities under constant liquid flow rate and gas to liquid flow ratio with ±5% error bar.

6.3.4 Influence of the gas-liquid flow ratio

Figure 6.9 shows the variation of microbubble diameter as a function of gas to liquid flow ratio (Q_g/Q_l) for different viscosities. It is clear that the bubble size increased with increasing flow ratio. At a given gas pressure, the bubble size decreased with increasing liquid flow rates and the bubble size increased when the gas flow rates increased under constant liquid flow rates. This result has also revealed that the bubbles can only be generated under relatively high gas-liquid flow ratios especially for high viscosity solutions in order to overcome the viscous forces when the liquid moves through microchannels. Similar results were found in previous work conducted using T-junctions (Parhizkar et al. 2013; Garstecki et al. 2006). According to Garstecki et al. (2006), at low capillary numbers it was the pressure drop across the bubble that controlled the dynamic process of immiscible thread break-up in the T-junction and the size of the bubbles was only dependent on the ratio of the volumetric rates of flow between the two immiscible fluids. Thus, a simple scaling equation of the size of bubble/slug/droplet was proposed:

$$L/w = 1 + \beta Q_{in}/Q_{out} \tag{6.1}$$

where L is the length of the bubble/slug/droplet, w is the width of the channel, $Q_{in/out}$ represents the rates of discontinuous and continuous fluid volumes, respectively, and β is a constant of order one which depends on the geometry of the T-junction. In the present study, the capillary number for the low viscous solutions was below 10^{-2} and this equation can be used in this work to compare with experimental observations. In Figure 6.10, the dimensionless length of the microbubbles (L/w) is plotted according to the scaling Equation (6.1) and from experimental results for different gas-liquid flow ratios. The comparisons show good agreement between the experimental results and the scaling equation, the similarities between the conventional T-junction and the K-junction used in this work.

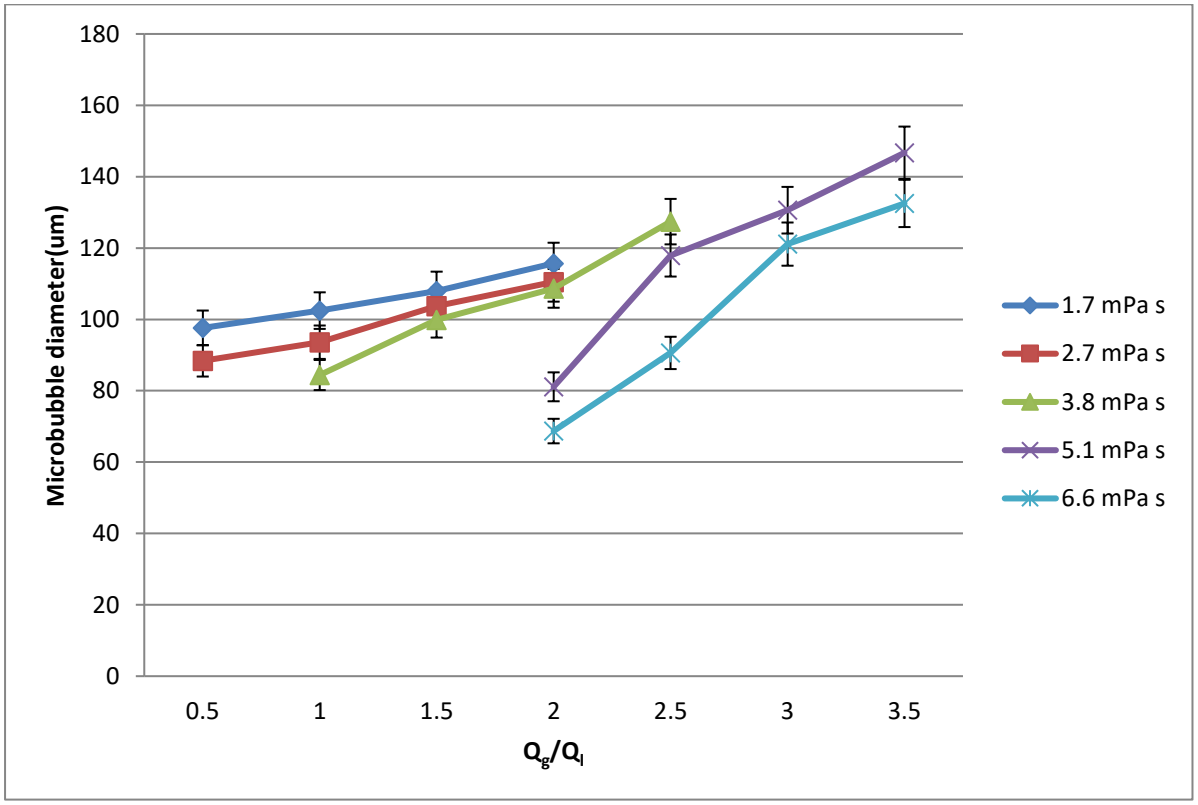

Figure 6.9 Bubble size at different gas to liquid flow ratios and liquid viscosities at constant Q_l=0.1ml/min with ±5% error bar.

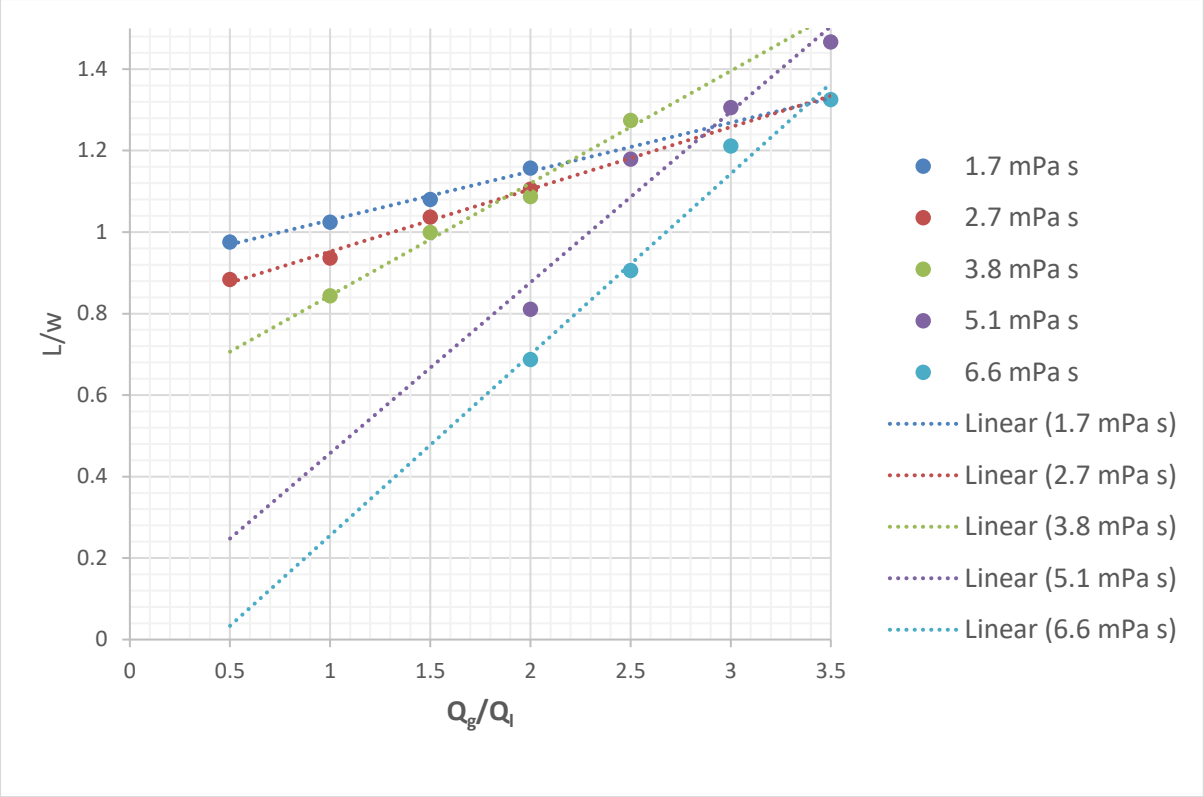

Figure 6.10 Dimensionless length of the microbubbles (L/w) plotted as a function of the ratio of flow rates of gas and liquid for the K-junction at constant Q_l=0.1ml/min.

6.3.5 Multiple fluids mixing

Three different kinds of polymeric solutions with specific liquid flow rate under certain gas pressure were applied in the experiments in order to investigate multiple fluids mixing phenomenon of the microfluidic K-junction. A series of high-speed camera images illustrating the microbubble generation and fluid mixing process are shown in Figure 6.11-6.13. The images are extracted from video clips recorded during experiments, visualizing the flow in the junction area (Figure 6.11), periodic bubbling at the outlet capillary (Figure 6.12) and bubbles in the blob at the capillary tip (Figure 6.13).

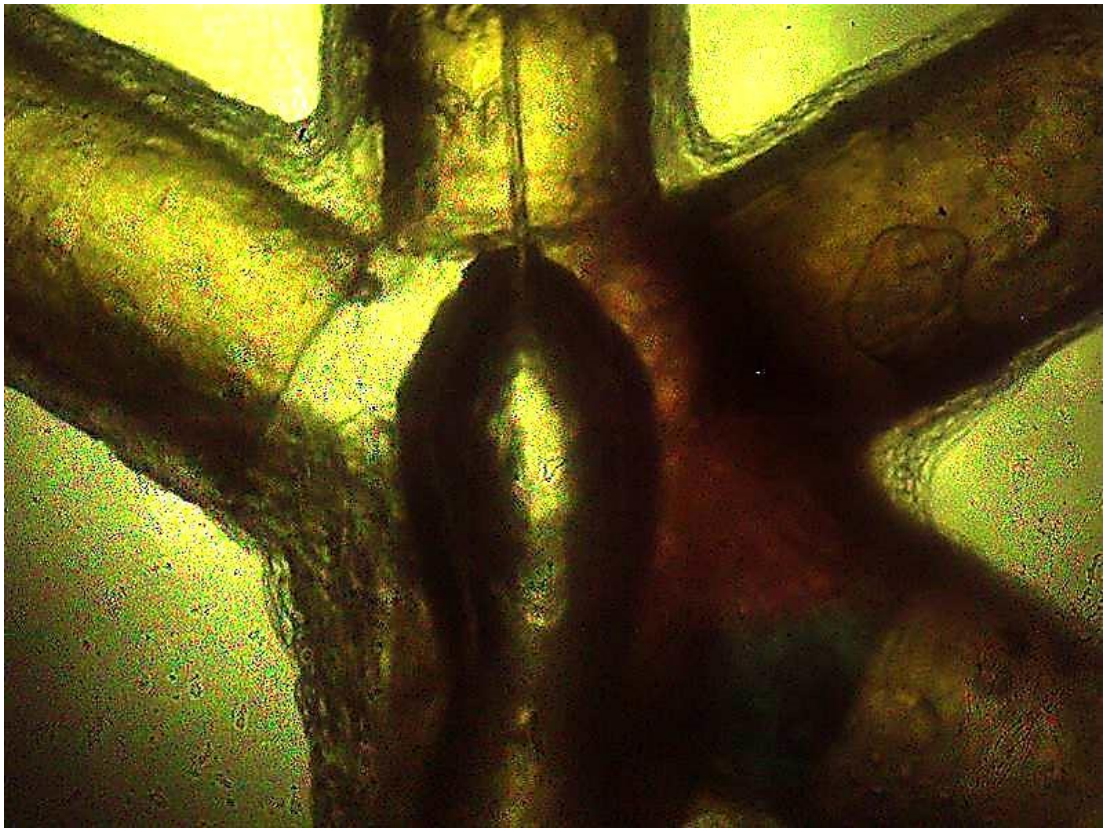

Figure 6.11 Image of periodic flow in the K- junction mixing area captured by high speed camera with solutions (PLGA, PMSQ and PEG) containing three different dyes which are recognised as yellow (left), red (top right) and blue/green (bottom right) respectively.

Figure 6.11 shows the flow in the junction area where three polymer solutions and nitrogen gas mix. The solutions can be distinguished by adding three different dyes and were identified by naked eyes, which are yellow (Perylene/PLGA, left channel), red (Neutral Red/PMSQ, top right channel) and blue/green (Methyl Green/PEG, bottom right channel). The microbubbles were generated continuously when the junction area is filled with polymer solutions and nitrogen. The monodispersed and continuous bubble generation was also captured in the outlet capillary tube shown in Figure 6.12, where the arrows show the trail of a single bubble at 0ms, 33ms, 66ms and 100ms; in the end, the bubble leaves the outlet for collection.

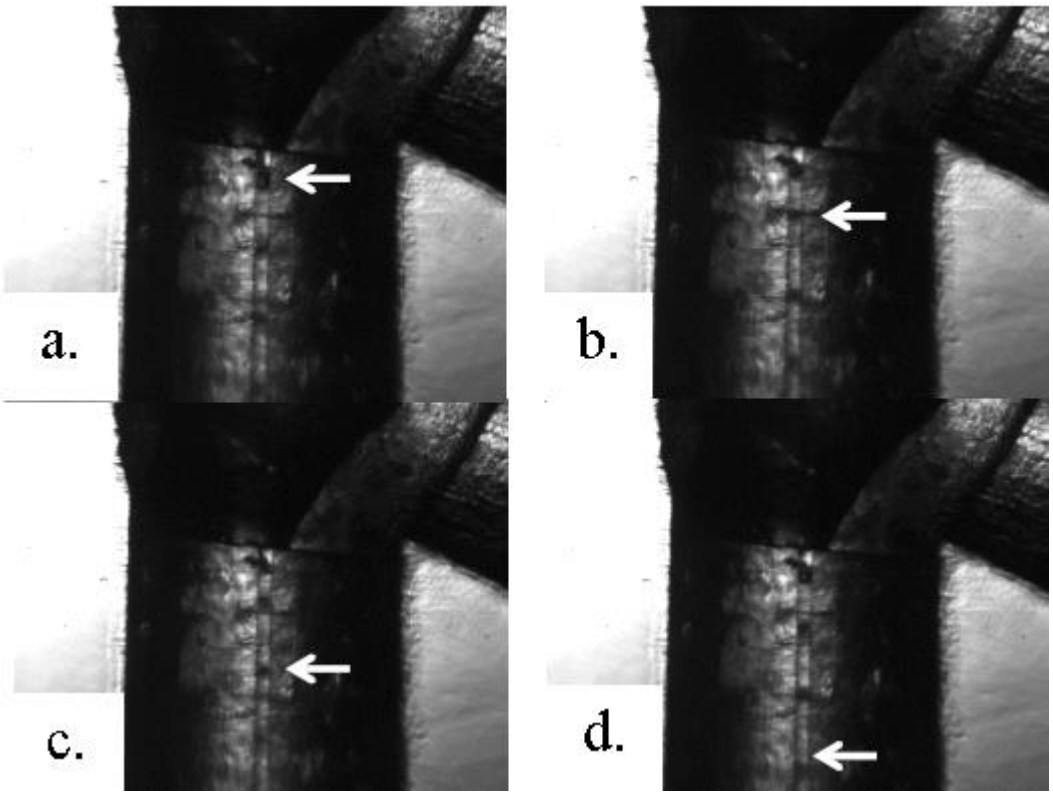

Figure 6.12 Formation of bubbles in the outlet capillary of the K-Junction microfluidic device with a flow rate of 200 µl/min at **a.** t = 0ms **b.** t = 33ms **c.** t = 66ms. t = 100ms. Arrows tracing an individual bubble.

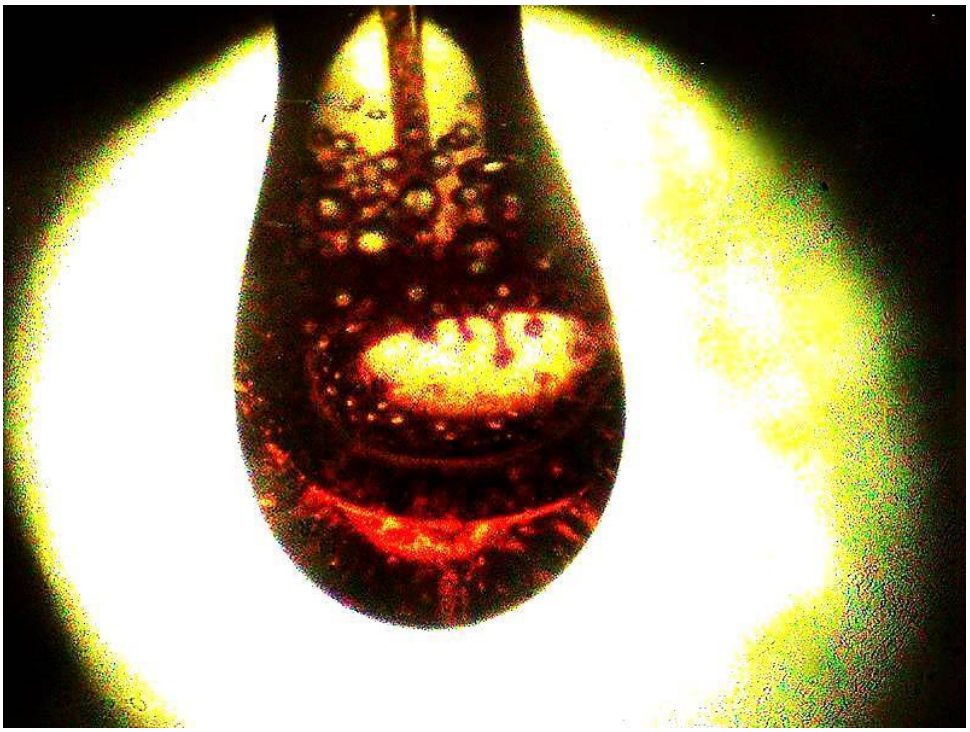

Figure 6.13 Image of bubble accumulation in the blob at the outlet tip of the K-junction by using nitrogen and three different solutions.

The bubbles accumulate in a blob at the tip of the outlet microchannel just before dripping to the glass slide for collection (Figure 6.13). If the liquid to bubble conversion efficiency is considered as 100%, it can be estimated that approximately 3 x 10^5 are accumulated within the blob per second. The periodic production adds to the weight of the blob leading to pinch-off and these bubbles are collected on a glass slide covered with distilled water as shown in Figure 6.14.

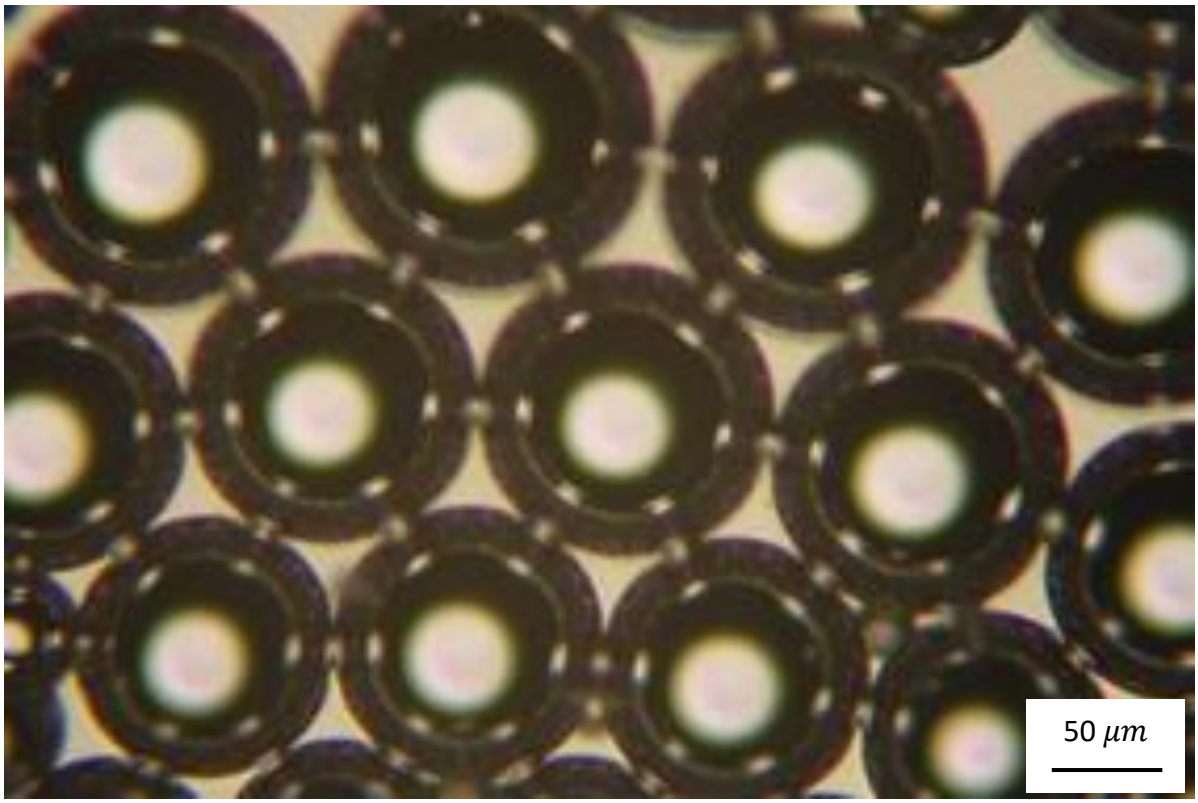

Figure 6.14 Microbubbles collected on a glass slide from K-junction by using three different liquids (PLGA, PMSQ and PEG solutions) under the observation of microscope with 5x magnification.

6.4 Comparison between numerical and experimental results

Numerical simulations with 500000 mesh cells by using the multiple liquids were then conducted by using STAR-CCM+ (CD-adapco Ltd, Melville, New York), which improved insight into the mechanism and allowed a direct comparison between experimental and numerical results (Figure 6.15).

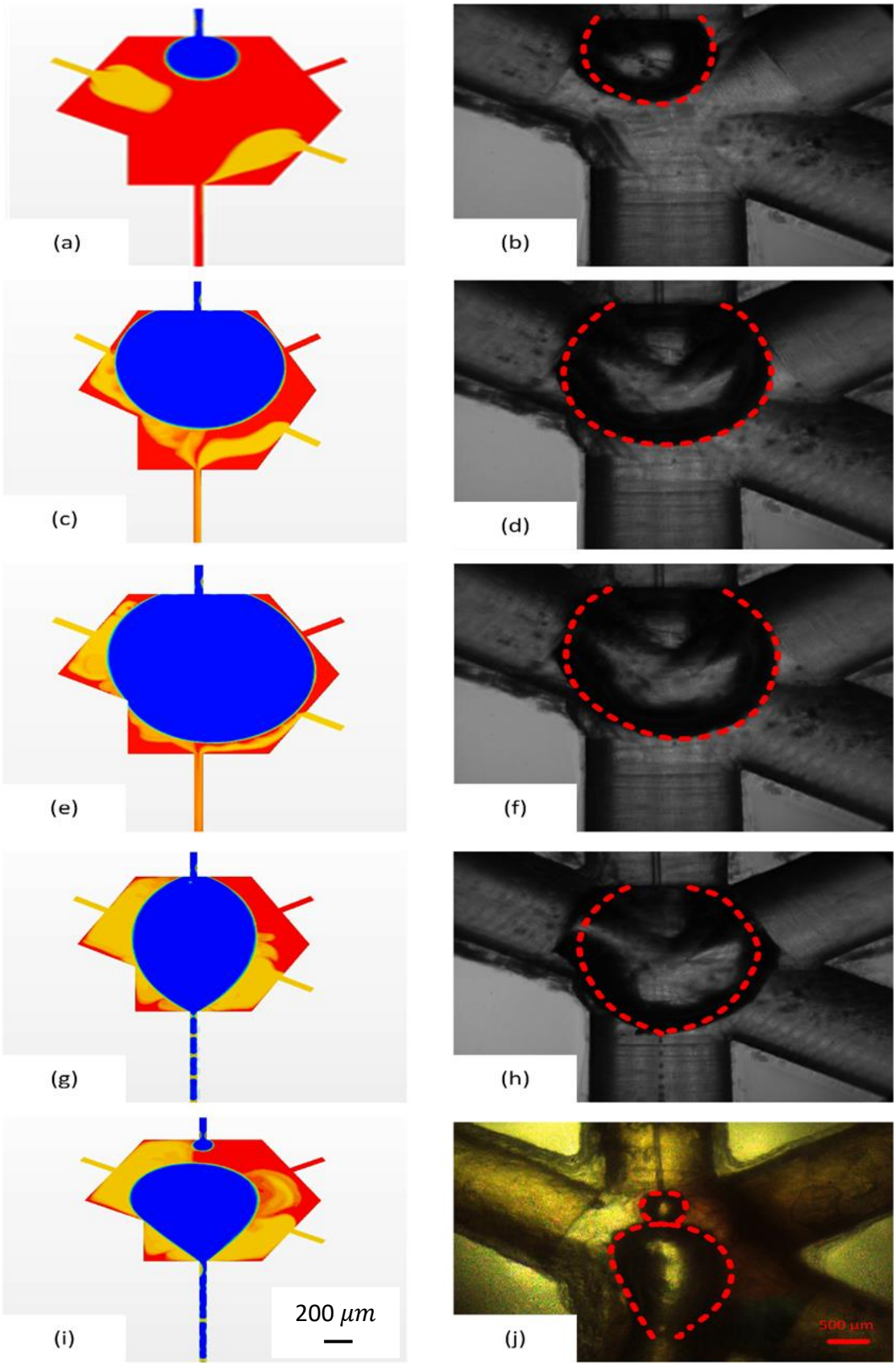

Figure 6.15 Comparison between numerical simulation results (left) and experimental observations (right where red dashed curves represent the interface between gas core and liquids) as a function of time: (a)(b) 0.1 ms; (c)(d) 0.57 ms; (e)(f) 1.14 ms; (g)(h) 1.25 ms; (i) (j) 2.01ms.

The simulations were carried out by using the same material properties as in the multiple liquids mixing experiments, which were nitrogen as the gas phase and PVA-water, PEG-water and ethanol mixture and PLGA-acetone solution as the liquid phases. The simulation results have shown the expanding gas core inside the intersection chamber until it touched the outlet channel, which is in very good agreement with the experimental observations. After some fluctuations of the gas core, the gas and liquid flow rates came to a balance when bubbles with uniform size were produced continuously. According to Christopher et al. (2008), the break up mechanism and bubble size is dependent on three forces: the viscous stress acting on the emerging interface of the droplet, the capillary force resisting deformation of the interface, and the "squeezing" pressure. Bubble generation occurs after the balancing of these three forces. Thus, it was found that in both experiments and numerical simulations, a certain period of time was needed to elapse before bubble generation starts, during which the size of the gas core first increased and then fluctuated. Uniform bubble formation could be obtained within a specific time interval of about 35s after these three forces reached an equilibrium. Meanwhile, throughput of microbubbles in both numerical simulations and experiments with various gas-liquid flow ratios under identical gas and liquid phases was investigated and shown in Table 6.3. For the simulations, the throughput of microbubbles was measured from the animation generated by the software STAR-CCM+ (CD-adapco Ltd, Melville, New York) while for the experiments, video clips captured by high-speed camera and inbuild image processing software were used to measure the microbubble throughput. It was found that the microbubble throughput in simulations and experiments was close but slightly different. The throughput values in experiments were higher than that in simulations. It was mainly caused by bigger bubble size obtained in the 2D simulations with no dimension constrain in channel thickness instead of 3D simulation which is closer to experimental observation. Therefore, under identical gas/liquid velocity flow ratio more bubbles in experiments were captured when flowing through the outlet of the K-junction because of smaller size. However, the error between computational and experimental throughput varies from 14.3% to 27% and the error decreased when gas/liquid velocity flow ratio increased. In addition, measurement error when monitoring bubble throughput in both numerical and practical approaches also contributed to the difference.

Gas/liquid velocity flow ratio	Throughput in simulations(bubble/s)	Throughput in experiments(bubble/s)
0.5	0.8	1.1
1	1.1	1.3
1.5	1.2	1.4
2	1.4	1.8

Table 6.3 Bubble throughput for the K-junction in simulation and experiments.

The bubble size distribution was also compared between numerical simulations and experiments with different gas-liquid flow ratios and liquid viscosity. Microbubbles were measured from both numerical simulations and experiments with increasing gas-liquid flow ratios ranging from 0.5 to 2 with identical material properties such as viscosity, surface tension and contact angle. The difference between simulation and experiments can be calculated and the error is obtained after dividing the difference by experimental measurement. The bubble size distribution from simulations was in relatively good agreement with experimental results, with an average error around 27.2% (based on size), probably attributable to the 2D/3D discrepancy. Moreover, the trend that indicates the increase of gas to liquid flow ratio leads to increased bubble diameter, as observed in experiments, was also captured by the simulations, as shown in Figure 6.16.

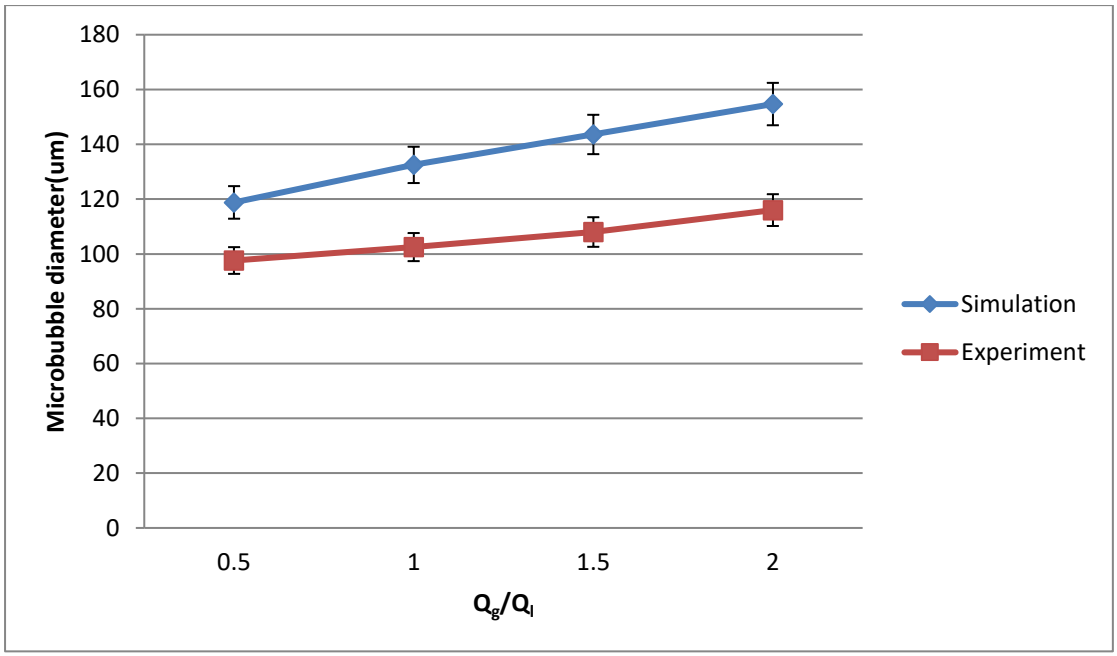

Figure 6.16 Comparison of bubble diameter generated for different gas to liquid flow ratios in simulations and experiments at liquid viscosity 1.7 mPa s and surface tension 38.4 mNm^{-1} with ±5% error bar.

For microbubbles generated in both numerical simulations and experiments with increasing viscosity from 1.7 mPa s to 6.6 mPa s (fixed gas-liquid flow ratio, surface tension and contact angle), the comparison of microbubble size distribution was conducted. It can be seen from Figure 6.17 that the bubble size decreases with the increase of viscosity in both simulations and experiments, and the bubble sizes from experiments are slightly smaller than those from simulations but with reasonable errors (average error of 15.6%) due to the limitation of the 2D geometry used in numerical simulations, which is only a simplification of the 3D experiments.

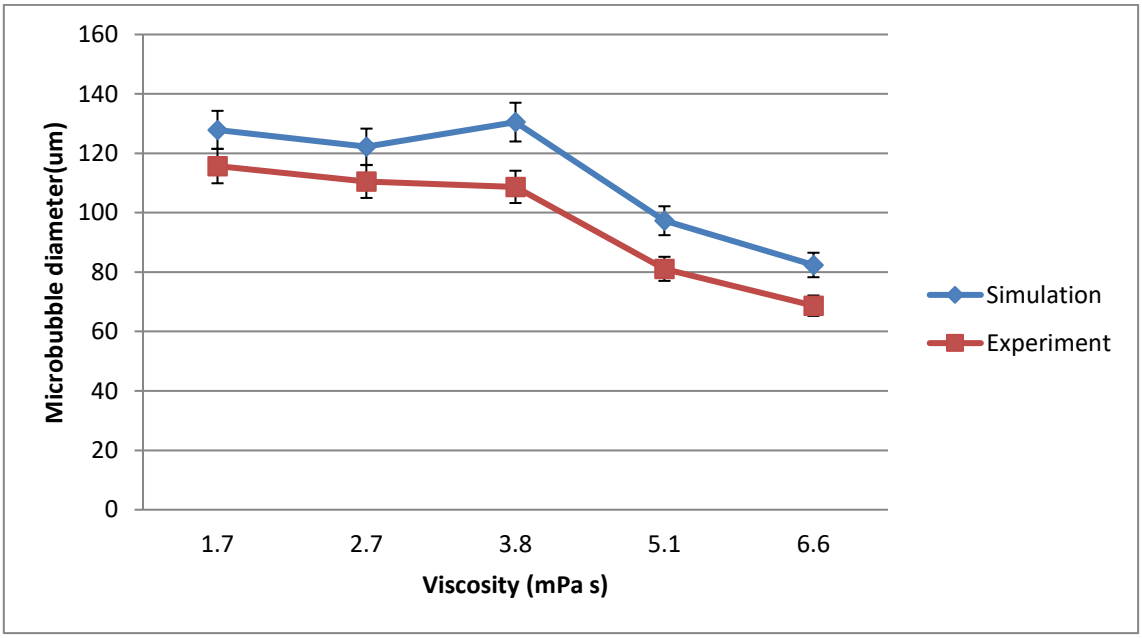

Figure 6.17 Comparison of bubble diameter generated for different liquid viscosities in simulations and experiments at fixed gas-liquid flow ratio of 2 with ±5% error bar.

6.5 Summary

The microbubble generation in a microfluidic K-junction has been investigated using both computational and experimental approaches. The effects of the gas-liquid flow ratio, contact angle, surface tension and liquid viscosity in microbubble generation have been studied. It can be concluded that the Volume of Fluid (VOF) method is able to acquire relative accurate

gas-liquid interface especially at the bubble pinch off and generation process, and bubbles obtained from simulations are consistent with the experimental results. For relatively high gas-liquid flow ratio, the bubble length decreases significantly when the contact angle increases from $30°$ to $120°$. When the gas-liquid flow ratio is relatively low, the bubble length decreases with increasing contact angle. The bubble length increase with an increase of the surface tension. For comparatively high liquid viscosity, the bubble length remains about the same with increasing contact angle at low surface tension. While at high surface tension and liquid viscosity, the bubble length decreases with increasing contact angle. The experimental results have shown that the average bubble diameter increased with increasing inlet gas pressure and gas-liquid flow ratios but it decreases with increasing liquid viscosity. It is also indicated that the microbubble generation process captured in experiments has good agreement with simulations but there still exist errors in bubble size distribution.

Chapter 7 : Chaotic mixing in microfluidic junctions

7.1 Overview

In this chapter, the theory of chaotic mixing and its implementation on microfluidic systems have been presented. An additional conventional microfluid cross-junction is introduced, and investigated numerically and experimentally in the multiple fluids mixing domain. The microbubble generation process in the cross-junction is also studied in both simulation and experiments. Experiments of cross-junction are conducted to analyze microbubble size variation with different gas pressure, liquid viscosity. A numerical approach is applied to the qualitative research of multiphase mixing phenomenon between K-junction and cross-junction.

7.2 Introduction to chaotic mixing

Chaotic mixing is a process by which flow tracers develop into complex multiply folded and stretched patterns, often of a fractal nature, under the action of a fluid flow. An example of chaotic mixing is shown in Figure 7.1 below.

Figure 7.1 Snapshot of the concentration field for transient magnetically forced chaotic mixing. Fluid labelled with fluorescein was initially confined to the right half of the cell (Rothstein et al. 1999).

The flow is characterized by an exponential growth of fluid filaments (Ottino, 1989). Simple flows such as the blinking vortex, or finitely resolved wind fields can also generate exceptionally complex patterns from an initially simple tracer field (Methven and Hoskins, 1999). Fluid mixing is based on two basic mechanisms: diffusion, turbulence and advection. Molecular diffusion alone in liquids is often not as efficient for mixing. We shall exclude the topic of turbulent mixing from our discussion, since it falls outside the scope of this work. Enhanced mixing in low Reynolds number flows can be achieved by advection which is the transport of matter by a flow. Chaotic mixing can be regarded as stirring water soluble polymer into water to prepare solution. If it is stirred in a circular motion, the efficient of mixing polymer in water is very low leading to the result that most of polymers go around in a circle in the solution. However, if it is stirred in a circular fashion away from the center, then stirring in a similar circle on the other side, and then alternated back and forth between the two stirring circles, the polymer will mix much more efficiently in the solution. This protocol is called the blinking vortex flow for mixing, and is shown in Figure 7.2.

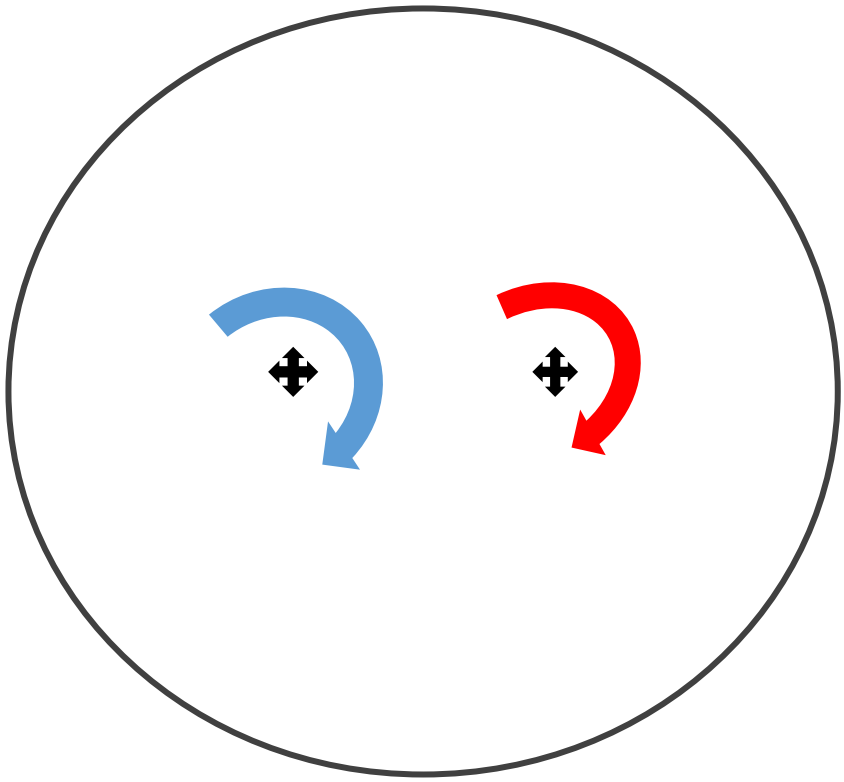

Figure 7.2 Illustration of blinking vortex flow and the flow circulates alternately back and forth around the left and right '+' marks.

Tracers which are particles of substance that trace trajectories like the polymer in the solution moving in the blinking vortex flow can undergo either ordered trajectories (if far enough away from the vortex centers) or chaotic trajectories (if closer). The trajectory of a single tracer in the flow is shown in Figure 7.3(a) and determined from the equations describing the mixing plotted in Figure 7.2.

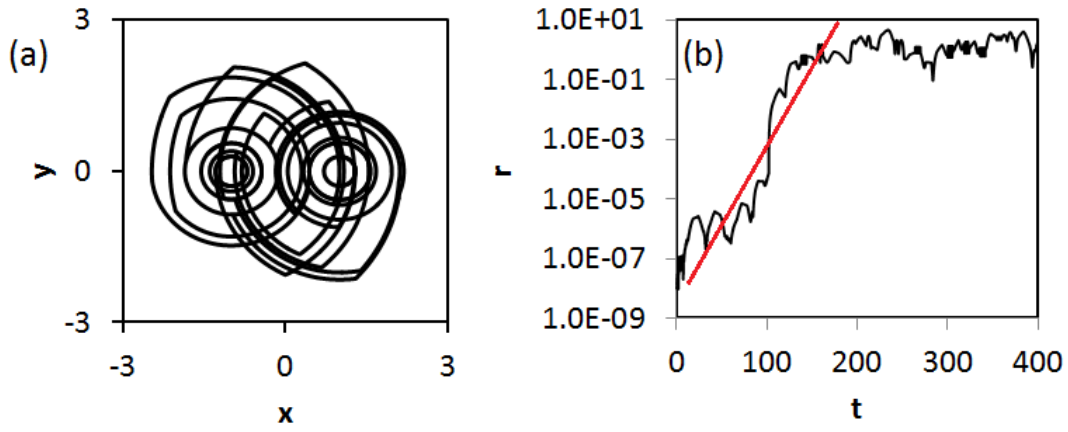

Figure 7.3 (a) Chaotic particle trajectory in a blinking vortex flow where x, y represents the horizontal and vertical axis (b) Separation r between two nearby tracers in the blinking vortex flow, plotted logarithmically as a function of time t to emphasize the rapid growth. The tracers separate roughly exponentially in time until the separation reaches a scale close to the size of the system, as indicated by the linear curve in the diagram (Solomon, 2015).

The logarithmic scale shown in Figure 7.3(b) is one where each mark represents a multiple of the quantity represented by the previous mark. Each mark on the r axis represents a distance 100 times the distance denoted by the one before it, whereas the difference between two marks on the time t axis is a constant of 100 units thus compressing the large distances into a convenient graph. These chaotic trajectories are very sensitive to differences in initial conditions. Simulating the motion of two tracers which are initially very close together (the two tracers simulated for Figure 7.3(b) are initially 10^{-8}apart) as in the work by Solomon (2015), have shown this result. The separation of these two tracers is illustrated in Figure 7.3(b) and it was indicated that the separation between the tracers fluctuates erratically, but on the mean grows roughly exponentially in time until saturating at a distance comparable to the size of the system.

A large number of tracers like polymer molecules, will mix efficiently due to the quick separation of chaotic trajectories in time. Images of the evolution of an initial line of 10^4 tracer particles in the blinking vortex flow in chronological order are shown in Figure 7.4. A well-mixed region has formed in the central region of the flow after a few periods of the blinking.

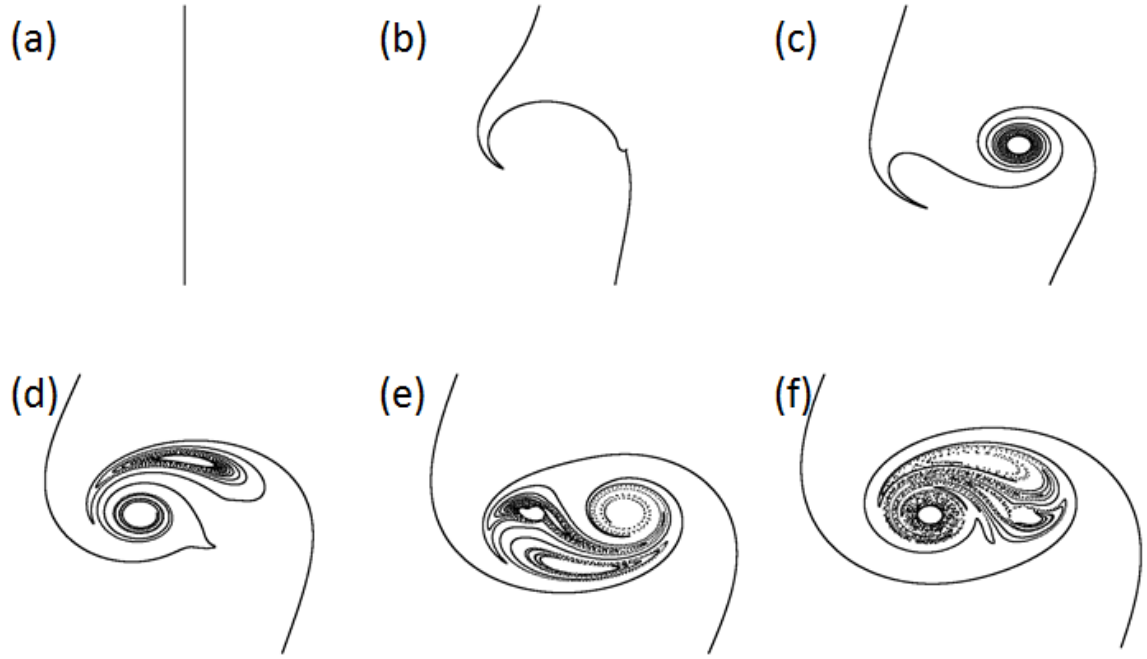

Figure 7.4 Numerical simulation of mixing of a line of tracers in the blinking vortex flow based on recurrence equation. Images (a)-(f) represents 0, 0.5, 1.0, 1.5, 2.0 and 2.5 blinking periods after start respectively (Solomon, 2015).

As microfluidic systems are now widely used in biology and biotechnology, a series of applications are based on mixing of the fluid flowing in microchannels. Examples include the homogenization of solutions of reagents used in chemical reactions, and the control of dispersion of material along the direction of Poiseuille flows (Jones and Young, 1994). Pressure induced flow in simple channels with smooth walls are laminar and uniaxial at low Reynolds number, thus the mixing of material between streams in the flow is purely diffusive. However, the diffusive mixing rate is slow compared with the convection of material along the channel, especially in microchannels resulting in length extension of microchannels for mixing.

Transverse components of flow which stretch and fold volumes of fluid over the cross section of the channel could be used to reduce the mixing length. Several designs for mixing based on chaotic flows have been developed and tested in macroscopic systems (Ottino,1989), but it is still difficult for mixing at the microscale. A helical microchannel demonstrated chaotic stirring which occurs due to eddies at bends in the channel in flows of intermediate Re (Re>1) (Liu et al.,2000). However, this mixer is complicated to manufacture and inefficient at low Re (Re<1). External, variable-frequency pumps off microfluidic chip or internal moving components on chip are necessary for activating these mixers (Stroock et al., 2002). Besides, passive methods for mixing streams of steady pressure-driven flows in microchannels at low Reynolds number were also investigated (Stroock et al., 2002). This is achieved by placing ridges on the floor of the channel at an oblique angle. Thus, transverse flows in microchannels were generated under the influence of a steady axial pressure. The structure can be easily fabricated with commonly used methods of planar lithography. The schematic graph of the two trajectories in Figure 7.5 has indicated that the entire flow has helical streamlines. It was found that these ridges present an anisotropic resistance to viscous flows, therefore less resistance exists in the direction parallel to the peaks and valleys of the ridges leading to an average transverse component in the flow generated by an axial pressure gradient. The increasing length of the channel required for mixing has shown to possess a logarithmical relation with the Péclet number, and hydrodynamic dispersion along the channel is reduced relative to that in a simple, smooth channel.

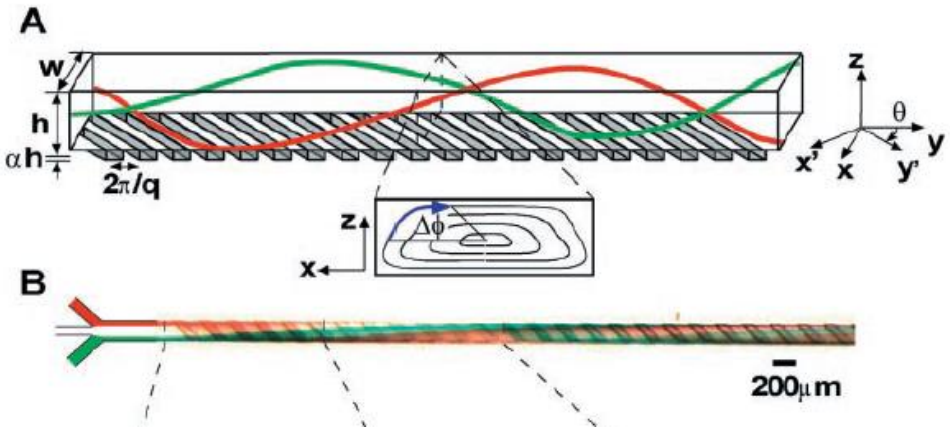

Figure 7.5 Three-dimensional twisting flow in a channel with obliquely oriented ridges on one wall. Schematic diagram of channel with ridges (up), Optical micrograph showing a top view of a red stream and a green stream flowing on either side of a clear stream in a channel(lower) (Stroock et al., 2002).

Although various mixing device designs have now been investigated numerically, there are still advantages to obtain a better understanding at a basic level and to use this knowledge to suggest improvements for further experiments and simulations. In the current study, most of the mixer were focused on geometrical detail such as extending the length of channel or modifying the shape of the inner channel. The mixing properties of the system are examined by changing the governing parameters. For instance, cavity driven flow can be considered as a generic mixing flow, since one of the walls provides a shearing force resulting in mechanical agitation or stirring of the fluid. Four distinct flow regimes have been found in this simple system, and the transition from steady to chaotic flow, as well as the behaviour in between, have been examined in detail. Therefore, the influence of modifications to parameters governing the system on mixing has been illustrated. In this work, microfluidic devices with different geometries (such as the shape of mixing area) were studied numerically and experimentally to compare and evaluate the effect of geometry on mixing, thus providing information on the optimisation of mixing.

7.3 Mixing in cross-junction

In addition to the conventional microfluidic T-junction which is commonly used in producing microbubbles, another flow-focusing microfluidic cross-junction (shown in Figure 7.6) is also widely used in forming droplets and microbubbles (Christopher et al., 2007; Van Loo et al., 2016). In the cross-junction device, the main channel used for the droplets/bubbles flowing and the continuous phase channels is perpendicular to the main channel. The dispersed phase channel has to be connected to the continuous phase channels and the main channel (Figure 7.6). The droplets'/bubbles' size can be controlled by input pressure driven flow. Droplet/bubble size is also dependent on the characteristic dimension of the tubes and junctions with more flexibility for flow-focusing method (cross-junction).

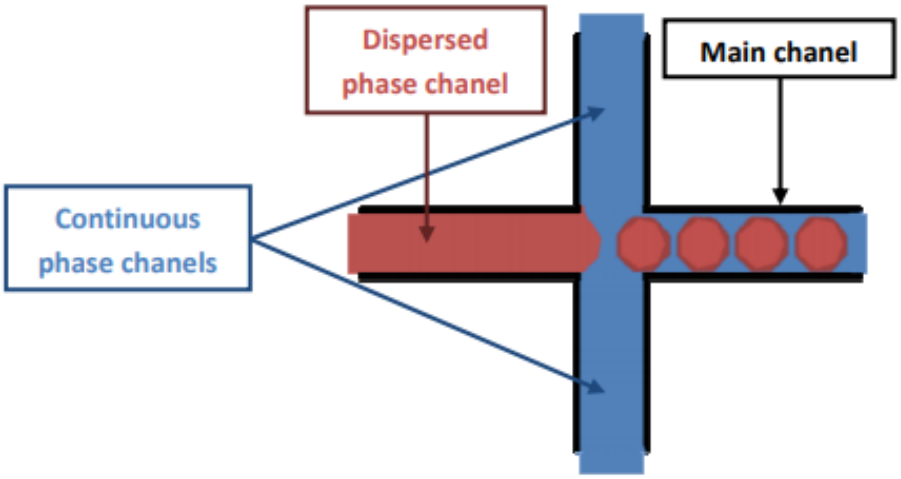

Figure 7.6 Schema of droplets formation at a cross-junction (flow focusing).

In this work, the novel microfluidic K-junction used in both simulations and experiments possesses the potential of multiple fluids (one gas and three different liquids) mixing due to its multiple liquid inlet channels design and unique mixing chamber inside the junction. The flow focusing microfluidic cross-junction is also capable of mixing multiple fluids (one gas and two different liquids). Therefore, it is necessary to introduce this cross-junction in this study and compare multiple fluids mixing effect between the K-junction and cross-junction. Figure 7.7 shows the geometry of the cross-junction used in the following section, and according to the graph of the cross-junction, there are four channels with diameter and length (without a screw thread) of 1.58 mm and 5 mm respectively which can be inserted by capillaries. The structure is similar to the aforementioned regular flow focusing cross-junction with small regular shaped mixing chamber, as opposed to the large irregular shaped mixing chamber in the K-junction. Numerical and experimental studies were conducted for the cross-junction thus the influence of the microfluidic junction geometry on multiple fluids mixing efficiency can be investigated. It also helps to improve the mixing process in microfluidic device based on the obtained results.

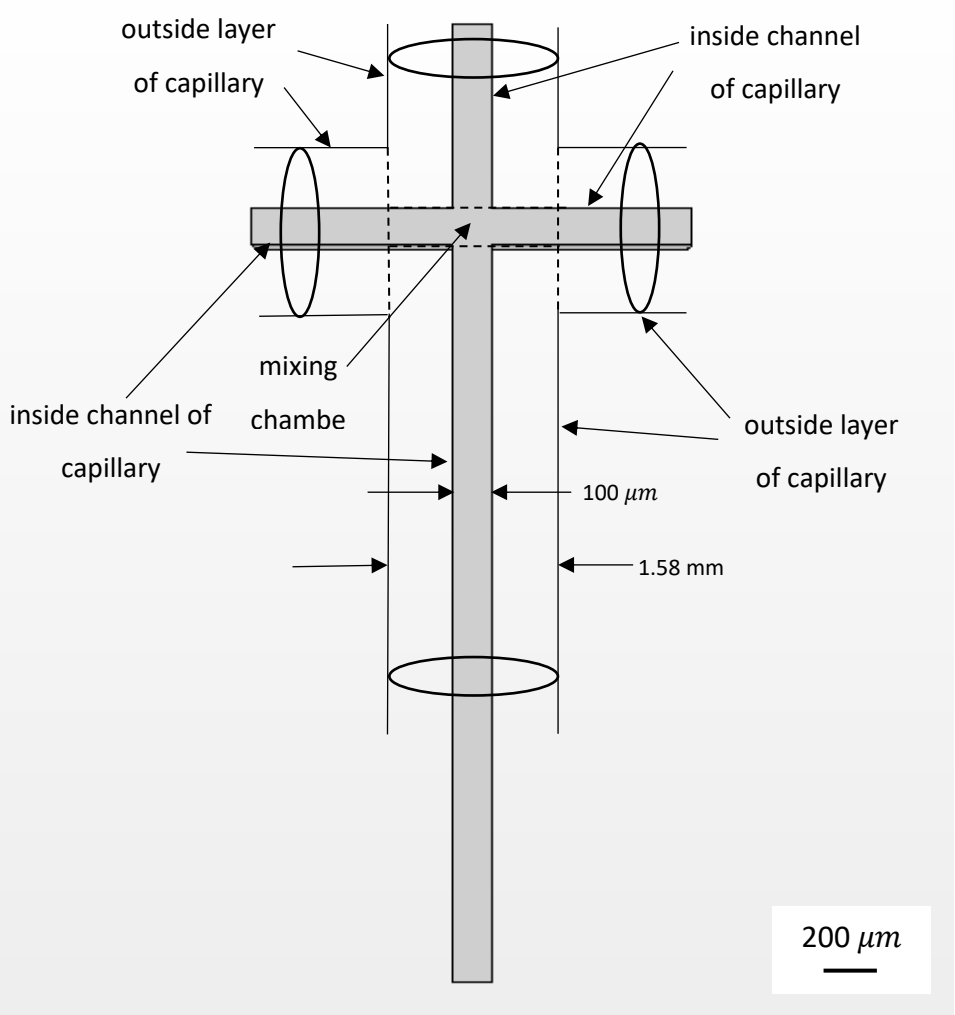

Figure 7.7 Geometry of cross-junction created in the numerical simulation inserted with four capillaries with inner diameter of 100 μm and outer diameter of 1.58 mm.

The square shaped mixing area is formed when the edges of four capillaries with inner diameter of 100 μm meet. Three of the channels are considered as inlet channels (one for gas and two for liquid) and the last one as outlet channel. Gaseous phase flows through the internal channel in the capillary are fed in the vertical inlet channels, liquid phase flows through the inner channel of the capillaries inserted in the horizontal inlet channels, and gas slug/bubble is collected at the end of the outlet channel (see Figure 7.8).

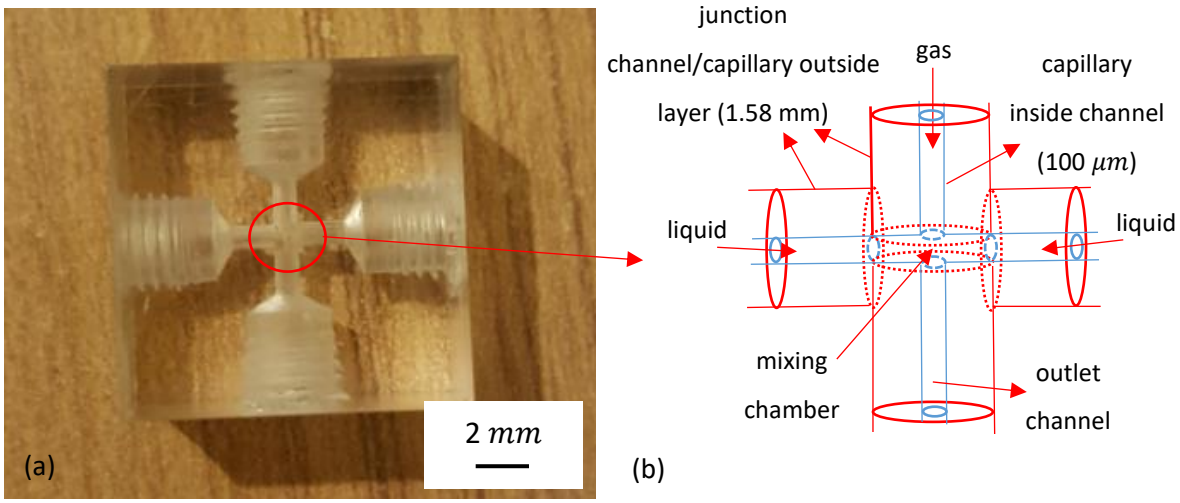

Figure 7.8 Cross-junction (a) and the close-up of cross-sectional representation of the center in the red circle (b).

This microfluidic cross-junction was constructed using polydimethylsiloxane(PDMS) and fabricated by the process of precision mechanical machining in the workshop. Capillaries were inserted and fixed in the cross-junction via connectors with a screw thread. Experiments were then conducted by using this cross-junction with similar setups as for K-junction. In experiments, aqueous solutions with PEG and PVA were used as liquid phase and nitrogen as gas phase under specific gas pressure and liquid flow rate. Therefore, microbubbles could be generated frequently and mixing was easy to observe under this condition. For the simulations, same materials were used and the physical geometry of the cross-junction can be regarded as four channels with diameter 100 μm and a regular square shaped mixing chamber with side length of 100 μm formed by the edges of capillaries. When applying the physics models in the form of simulations, inlet boundaries were assigned to the tip and both sides of inlet channels, outlet boundaries were assigned to the tip of the last channel, and the wall of both channels and the mixing chamber were set as surface boundaries with an applied no-slip condition. The length of outlet channels which are used to collect gas slug/bubble was extended compared to the rest of the channels in order to clearly observe the bubble generation and distribution. The whole geometry used in simulations is shown in Figure 7.9.

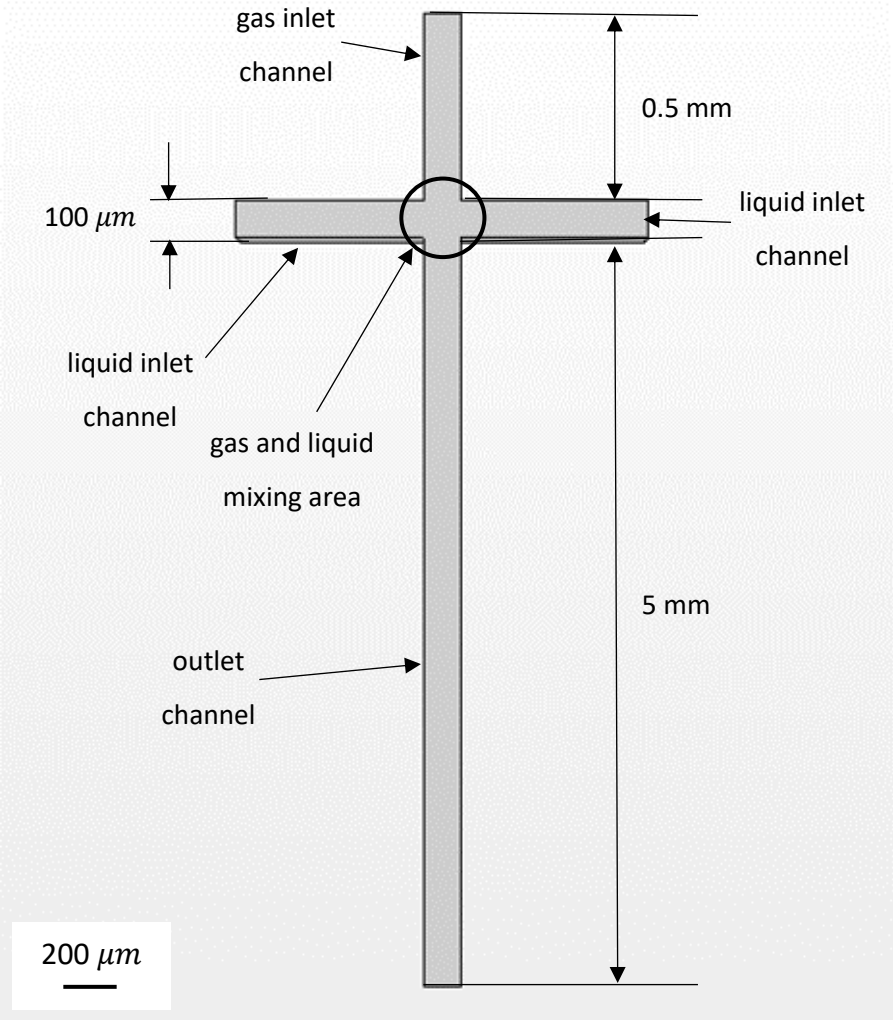

Figure 7.9 Simplified 2D cross-junction geometry generated and used in the simulation made of only capillary inner channel with dimensions in mm.

The microbubble generation process of a cross-junction was captured by a Phantom V5.1 high-speed camera (Vision Research Ltd. Bedford, UK) in experiments and is then compared with simulation results and is shown as a function of time in Figure 7.10.

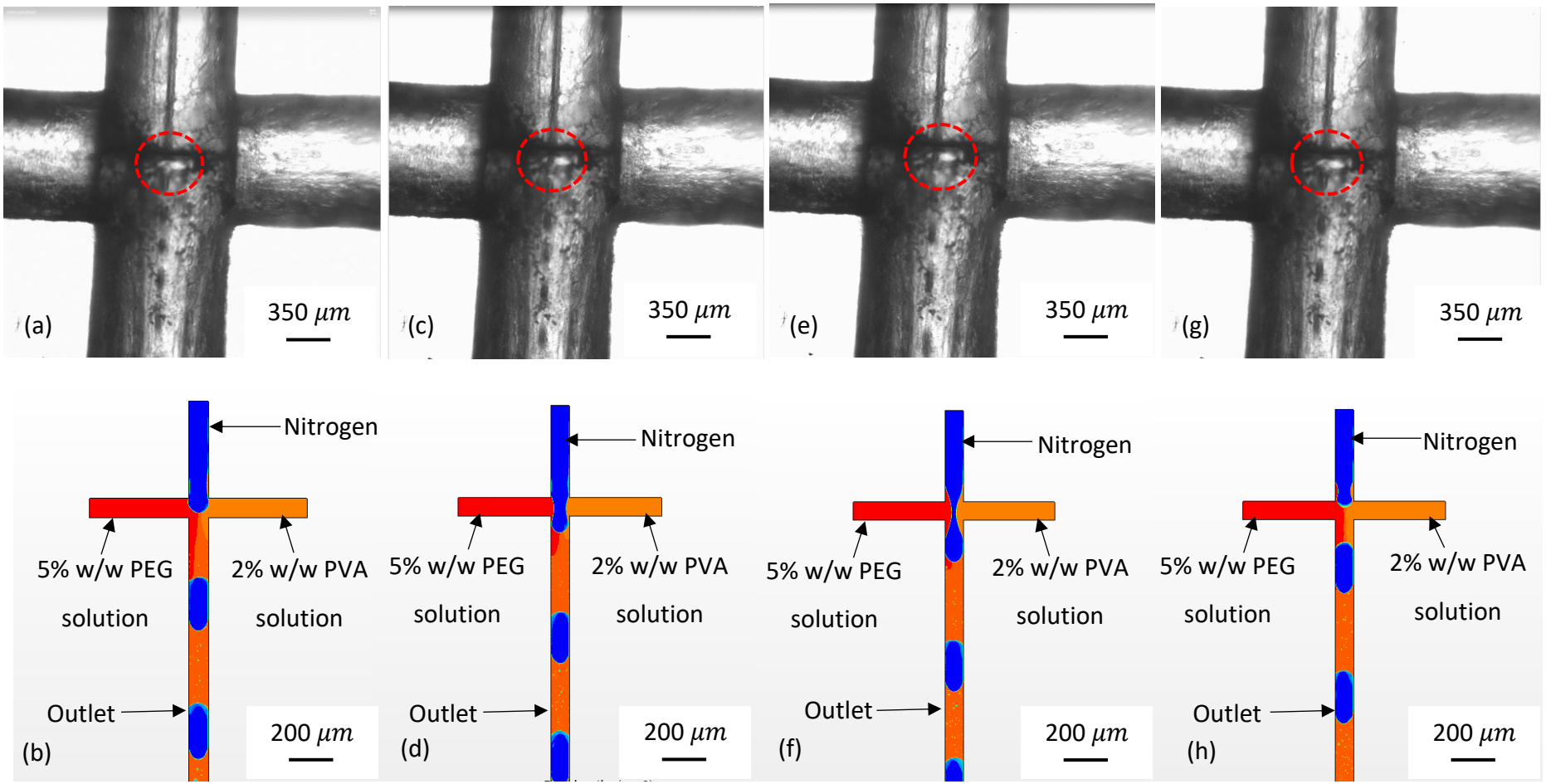

Figure 7.10 Microbubble generation process in the cross-junction in experiment (a), (c), (e), (g) and simulation (b), (d), (f), (h) at a series of time point under constant gas pressure 200 kPa and liquid flow rate 0.1 ml/min. (a), (b) are taken at t=9.8 ms; (c), (d) are taken at t =10.6 ms; (e), (f) are taken at t=11.05 ms; (g), (h) are taken at t=11.6 ms. 5% w/w PEG water solution and 2% PVA water solution were injected through left and right liquid inlet channels respectively in both experiments and simulations and the red circle in experimental images displays individual bubble generation.

It was found in both experiments and simulations that bubbles are generated at the square shaped mixing area and gas phase firstly inflates at this area and then pinched off in the middle by the liquid phase from left and right inlet capillary channels. The bubble generation process was very similar to that in a conventional T-junction (Parhizkar et al., 2013) which can be classified into an expansion stage, fluctuation stage, stretching stage and pinch-off stage. Uniform and continuous bubbles were also observed in the outlet capillary. The length of the bubbles and the distance between the bubble tips in both experiment and simulation were obtained, as shown in Figure 7.11 for comparison.

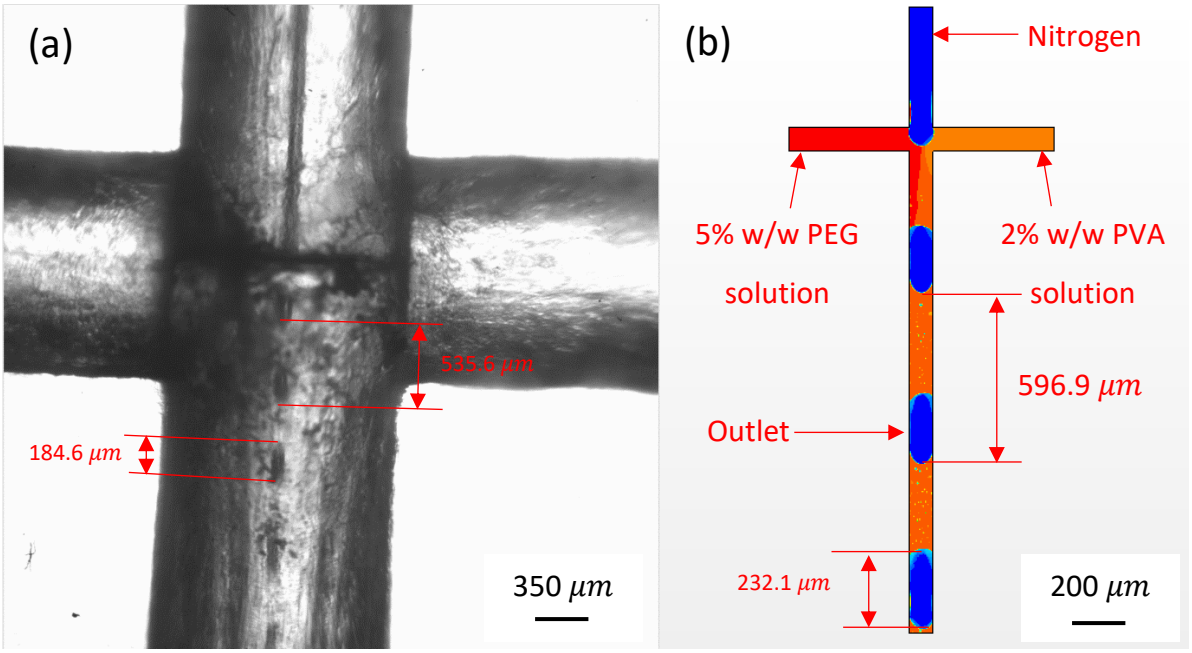

Figure 7.11 Experimental(a) and numerical(b) results of the bubble length and the distance between bubble tips under the condition of constant gas-liquid flow ratio of 2 and liquid flow rate of 0.1ml/min with 5% w/w PEG water solution and 2% w/w PVA solution.

It is noted that under the same boundary conditions and material properties, the differences of the bubble length and distance between two consecutive bubble tips between simulation and experiment reaches to 25.7% and 11.4% respectively. We believe that he bulk of this discrepancy can be attributed to the 2D model used in the simulations, nevertheless the model still shows reasonable agreement with experimental results confirming the effectiveness of numerical method we choose to investigate the bubble generation and fluid mixing.

The liquid phase used were 5% w/w PEG water solution with density of 1013.2 $\mathrm{kg \cdot m^{-3}}$, dynamic viscosity of 5.7 $\mathrm{mPa\ s}$, surface tension of 38.2 $\mathrm{mNm^{-1}}$, 2% w/w PVA water solution with density of 1006 $\mathrm{kg \cdot m^{-3}}$, dynamic viscosity of 2.6 $\mathrm{mPa\ s}$, surface tension of 42.2 $\mathrm{mNm^{-1}}$, and 5% w/w PEG+2% w/w PVA water solution with density of 986 $\mathrm{kg \cdot m^{-3}}$, dynamic viscosity of 4.14 $\mathrm{mPa\ s}$, surface tension of 54 $\mathrm{mNm^{-1}}$ separately in the experiments. The influence of gas inlet pressure and liquid viscosity on microbubble diameter was also explored in experiment and simulation. Figure 7.12 has shown the bubble size distribution under constant liquid flow rate (0.1ml/min) with increasing gas pressure from 100 kPa to 180 kPa by using 5% w/w PEG+2% w/w PVA water solution.

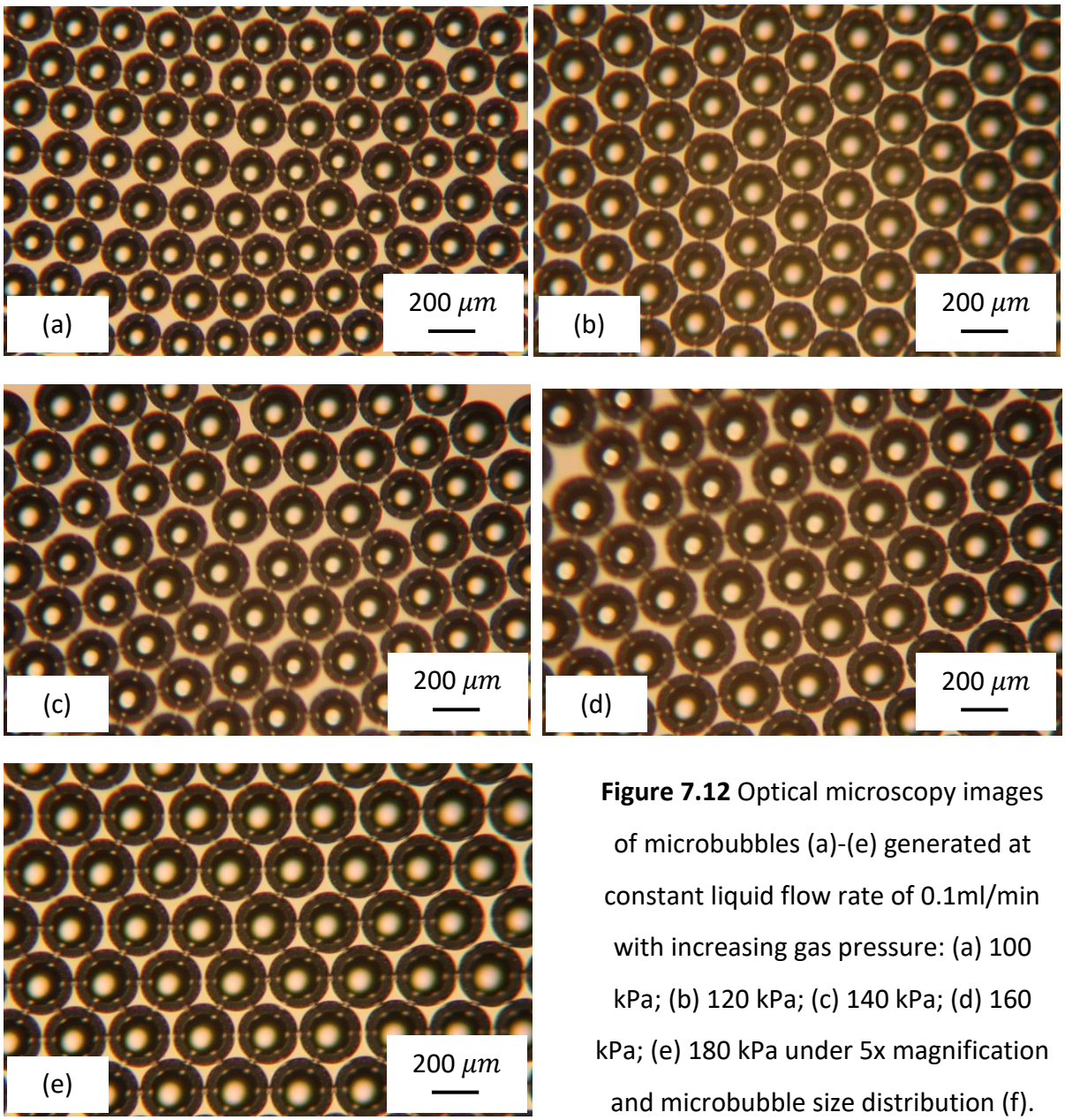

Figure 7.12 Optical microscopy images of microbubbles (a)-(e) generated at constant liquid flow rate of 0.1ml/min with increasing gas pressure: (a) 100 kPa; (b) 120 kPa; (c) 140 kPa; (d) 160 kPa; (e) 180 kPa under 5x magnification and microbubble size distribution (f).

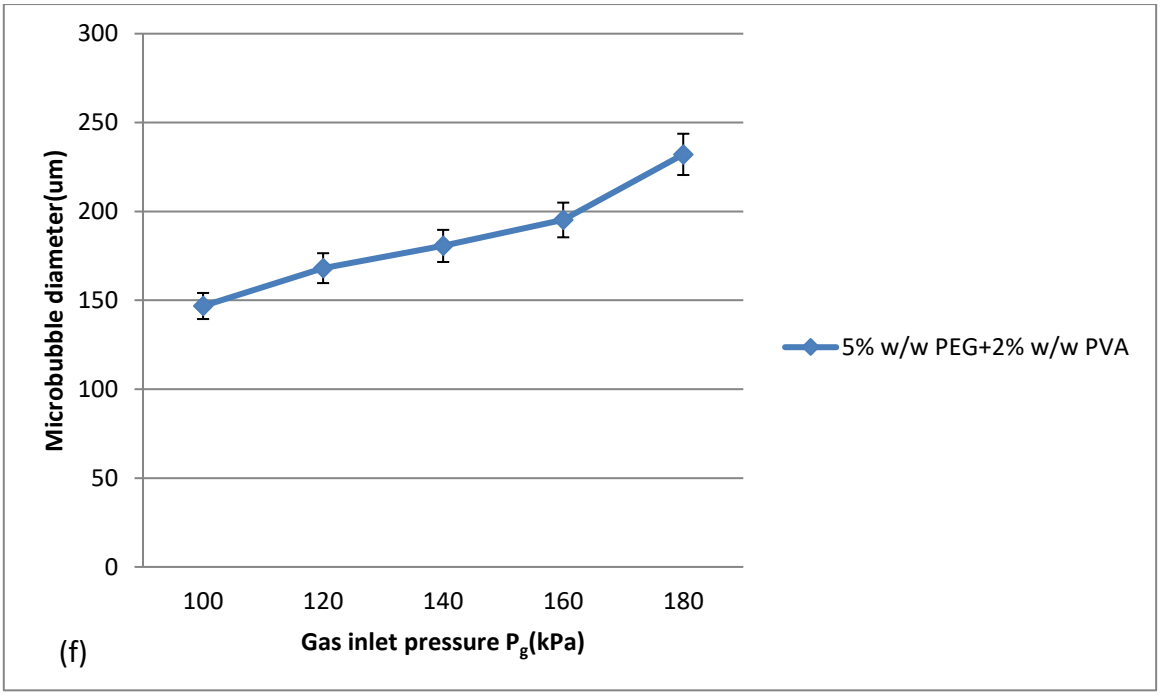

Figure 7.12 Optical microscopy images of microbubbles (a)-(e) generated at constant liquid flow rate of 0.1ml/min with increasing gas pressure: (a) 100 kPa; (b) 120 kPa; (c) 140 kPa; (d) 160 kPa; (e) 180 kPa under 5x magnification and microbubble size distribution (f) with ±5% error bar (continued).

The result showed that similar phenomena in the K-junction occurred in the cross-junction as well. The average bubble diameter increases with increasing inlet gas pressure due to the decrease of expansion time of gas cavity, which is generated by gas phase. In addition, the bubble fluctuation and stretching time also increases with increasing gas pressure. The bubble size distribution is shown in Figure 7.13 by using polymer solutions (mentioned in Table 6.2) with increasing liquid viscosity under constant liquid flow rate of 0.1ml/min and a gas pressure of 200 kPa. Similar results were observed, in that microbubble diameter decreases with increasing liquid viscosity under fixed gas pressure and liquid flow rate due to the increase of shear force exerted in the flow through capillary channels when using high viscosity liquids.

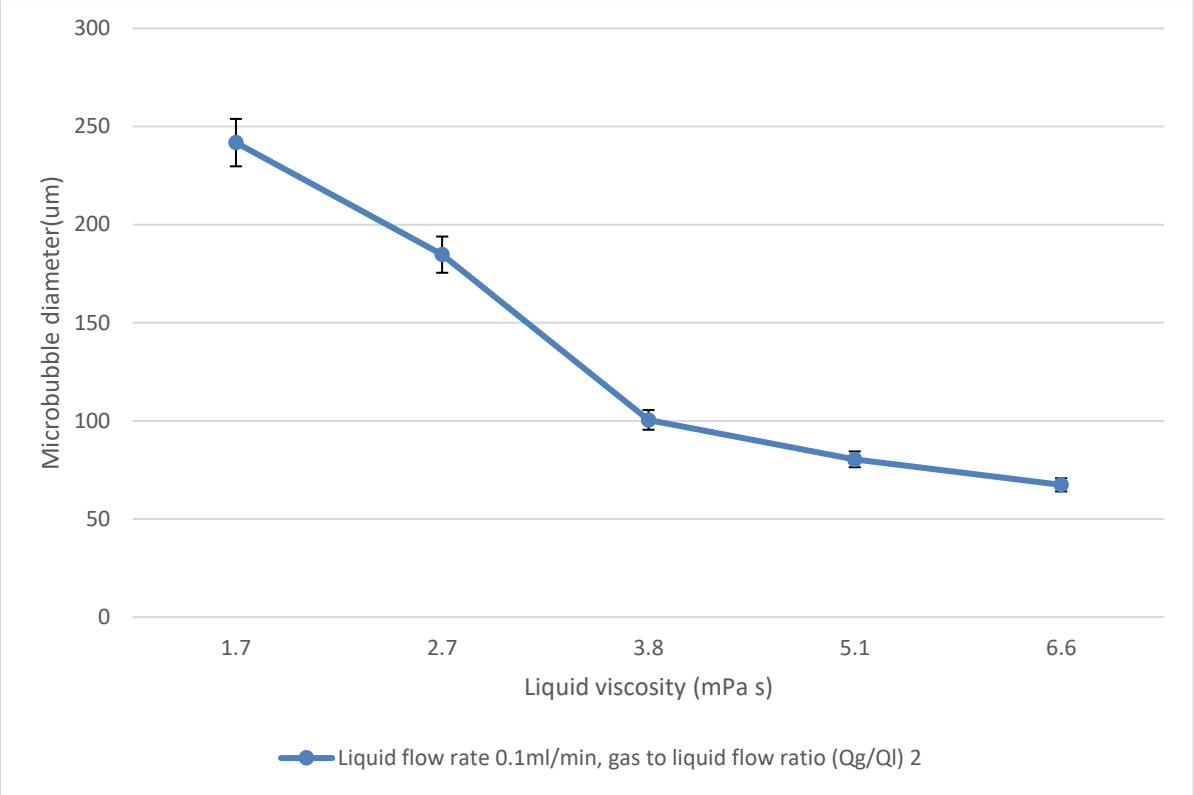

Figure 7.13 Microbubble size variation with different liquid viscosities under constant liquid flow rate and gas to liquid flow ratio for cross-junction with ±5% error bar.

In addition, it was also observed that monodispersed microbubble microbubbles were easy to occur within a range of gas pressures with constant liquid flow rate for longer time than the K-junction during experiment and gas pressure with too high or low values results in gas slug or liquid slug respectively. According to the comparison of microbubble size distribution between experiment and simulation by using 5% w/w PEG+2% w/w PVA water solution as liquid phase with increasing gas-liquid flow ratios in Figure 7.14, reasonable agreement was achieved with smaller error (7.8%-9.2%) than the K-junction (10.6%) due to the compact and regular mixing area in the cross-junction, which is more convenient to build high quality mesh and reduce numerical divergence hence to obtain more accurate simulation results.

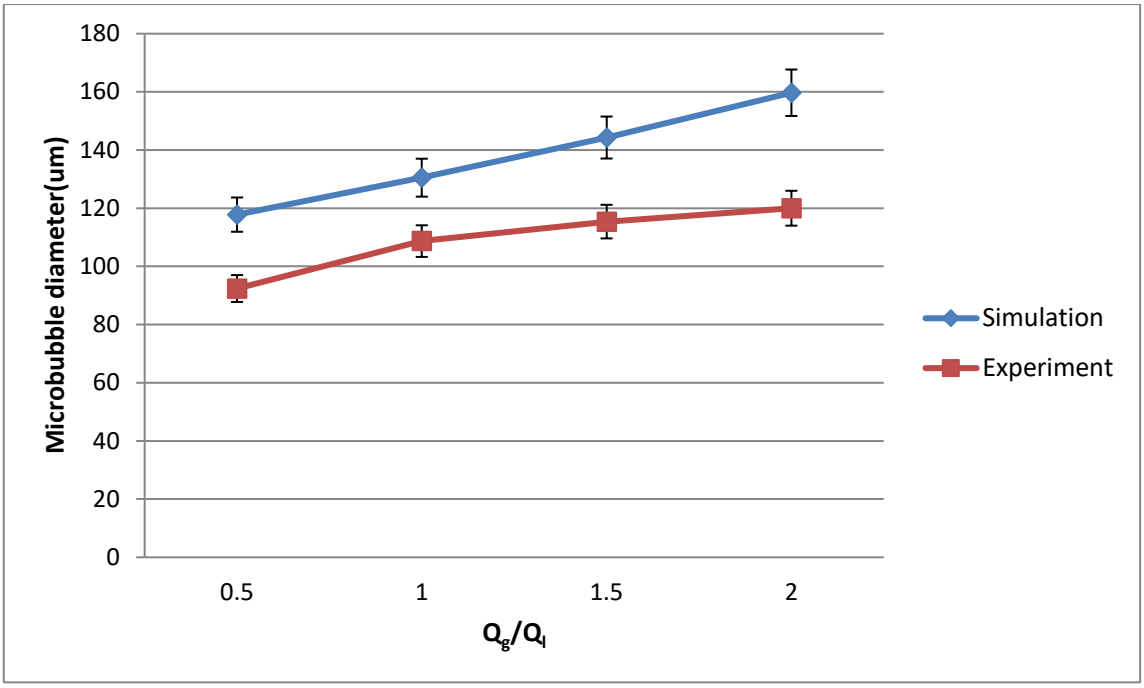

Figure 7.14 Comparison of bubble diameter generated from cross-junction with different gas to liquid flow ratios in both simulation and experiment with ±5% error bar.

7.4 Multiphase mixing study in K-junction and cross-junction

The main advantage of using the proposed microfluidic K-junction and cross-junction devices is the capability to mix multiple components added to the liquid phase and distribute them on the shell of bubbles. For the K-junction, three different liquids: PVA water solution, PEG-Neutral Red water/ethanol solution, and PLGA-perylene acetone solution were used in both experiments and simulations with nitrogen as the gas phase (see Table 7.1).

Components	**Density (kgm^{-3})**	**Dynamic viscosity (mPa s)**	**Surface tension (mNm^{-1})**
5% wt PVA +water	1012	6.4	46.9
5% wt PEG +50/50 water/ethanol	796	3.5	30.2
5% wt PLGA+acetone	932	0.64	23.3

Table 7.1 Properties of three different polymer solutions used for K-junction.

Glycerol was added to the aqueous solution of PVA to improve the stability of bubbles, while microbubbles were labelled with fluorescent dyes Neutral Red and Perylene, respectively for observation under fluorescent microscope. For the cross-junction, PEG and PVA water solutions were used as liquid phase and nitrogen as gas phase in numerical and experimental studies.

The experimental results of K-junction have shown that microbubbles aggregated in a close packing pattern and there was a variation in bubble size from centre to edge, those at the centre being larger and more monodispersed which is shown in Figure 7.15.

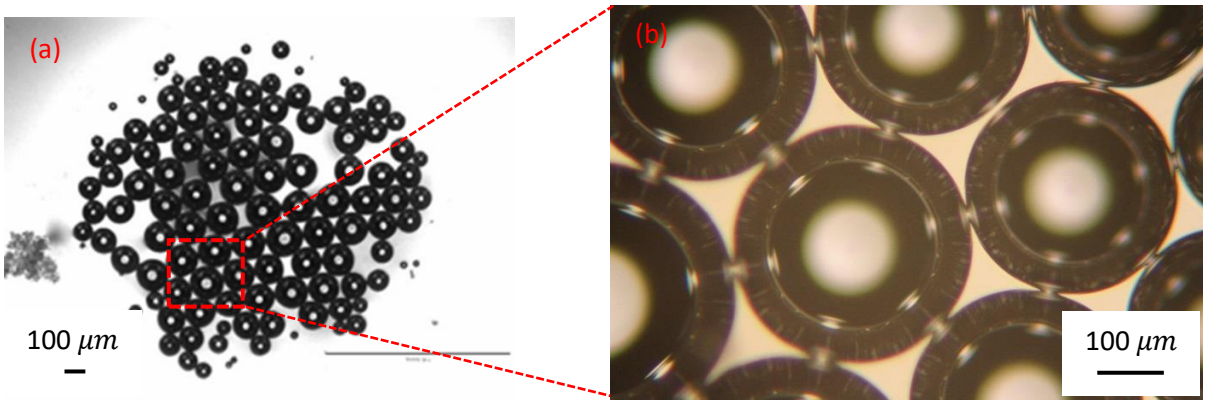

Figure 7.15 Microbubble droplet formed by using three different liquids (polymer solutions containing PVA, PEG and PLGA separately) for observation on glass slides under optical microscope with 5x magnification (a) and 20x magnification (b) under the condition that gas pressure 160 kPa and liquid flow rate 150 µl/mn.

This is mainly caused by bubble coalescence, liquid diffusion and evaporation as bubbles merged in the centre driven by the surface tension and slowed by the inertia and viscosity of the surrounding fluid (Stover et al. 1997). Thus, the bubbles gradually grew in the centre and the size of bubbles in the edge decreased because of liquid diffusion from the edge to centre and evaporation. Monodispersed bubbles were only observed in small quantities which were generated within a very short time. In addition, the gas to liquid flow ratios were lower than that of a single liquid case when bubbles were obtained due to the mixture viscosity changing after liquid mixing of all three solutions. Therefore, as the viscosity change caused by different liquids mixing in the intersection chamber of the K-junction takes effect, more time is needed for the gas core to fluctuate and stabilise and bubbles could only be generated when the

liquids were properly mixed so that duration was quite short. According to previous research with the T-junction (Parhizkar et al. 2013), the effect of viscosity has significant influence on microbubble size. In this study, because of the use of multiple liquids with different viscosities, the viscosity of the liquid mixture varied before it reached a specific value as proposed by Maples (2000) who used the kinematic viscosity (η) of a mixture of two or more liquids. A Viscosity Blending Number (VBN) of each component was calculated and then used to determine the VBN of the liquid mixture:

$$VBN_i = 14.534 \times \ln(\ln(\eta_i + 0.8)) + 10.975 \quad (7.1)$$

where η_i is the kinematic viscosity, VBN_i is the viscosity blending number. The VBN of the liquid mixture can be calculated as follows:

$$VBN_{mixture} = \sum_{i=0}^{N} y_i \times VBN_i \quad (7.2)$$

where y_i represents the weight fraction of each component of the blend and VBN_i is the viscosity blending number. All the viscosities are determined at the same temperature. Finally, the kinematic viscosity of the mixture can be estimated by using the viscosity blending number of the mixture shown below:

$$\eta_{mixture} = \exp\left(\exp\left(\frac{VBN_{mixtre} - 10.975}{14.534}\right)\right) - 0.8 \quad (7.3)$$

where VBN_i is the viscosity blending number. The bubble size varies because of the viscosity change, so that most of the generated bubbles were not uniform, and only few monodispersed bubbles were generated. One may stipulate that this is indicative of the fact that the mixing process in the chamber is a continuously evolving, possibly aperiodic process (Sotiropoulos et al., 2001; Ottino,1989), resulting in a condition where the specific pinch-off for every bubble, or every few bubbles, is always slightly different, due to the difference in the original viscosity at specific position. Meanwhile, the influence of gas and liquid flow rates on microbubble size variation was not as significant as the viscosity change (Figure 7.16), and viscosity variation at the liquid film between two gas slugs in the outlet capillary in the simulation (Figure 7.17) revealed that the viscosity value was in between all three different liquids (1.325-1.4 mPa s) which indicates the liquid film may be a mixture of these liquids (6.4 mPa s, 3.5 mPa s, 0.64 mPa s).

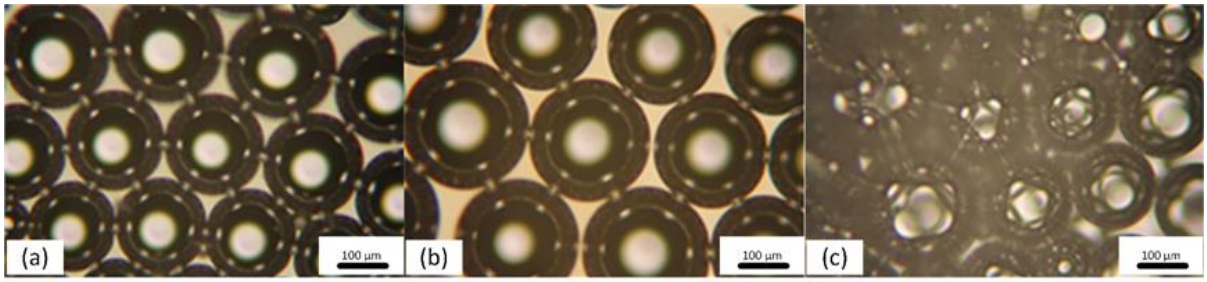

Figure 7.16 Optical micrographs of bubbles formed by multiple liquids and gas with constant liquid flow rate of 0.15 ml/min at different gas pressures of: (a) 160 kPa; (b) 180 kpa; (c) 230 kPa.

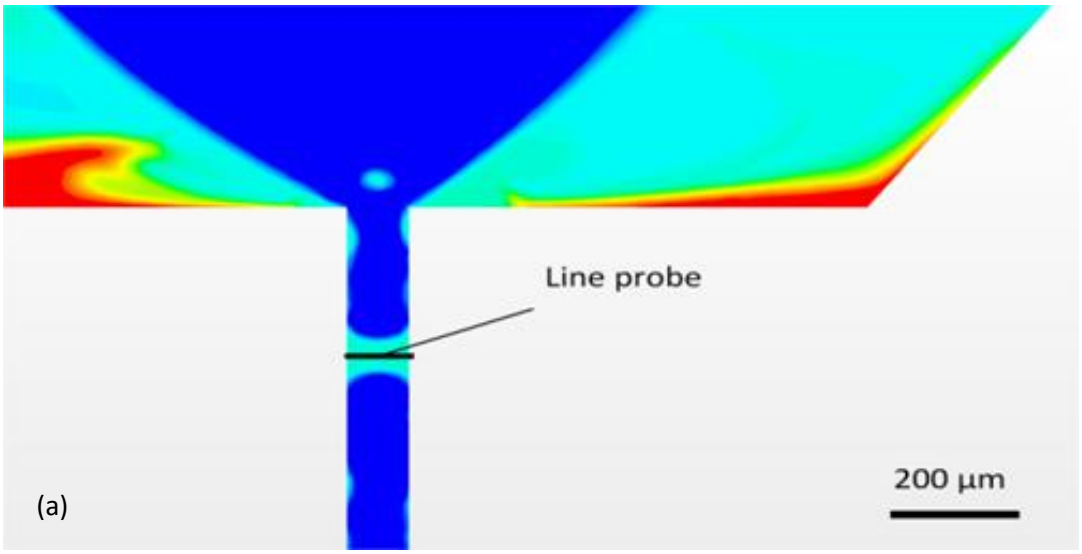

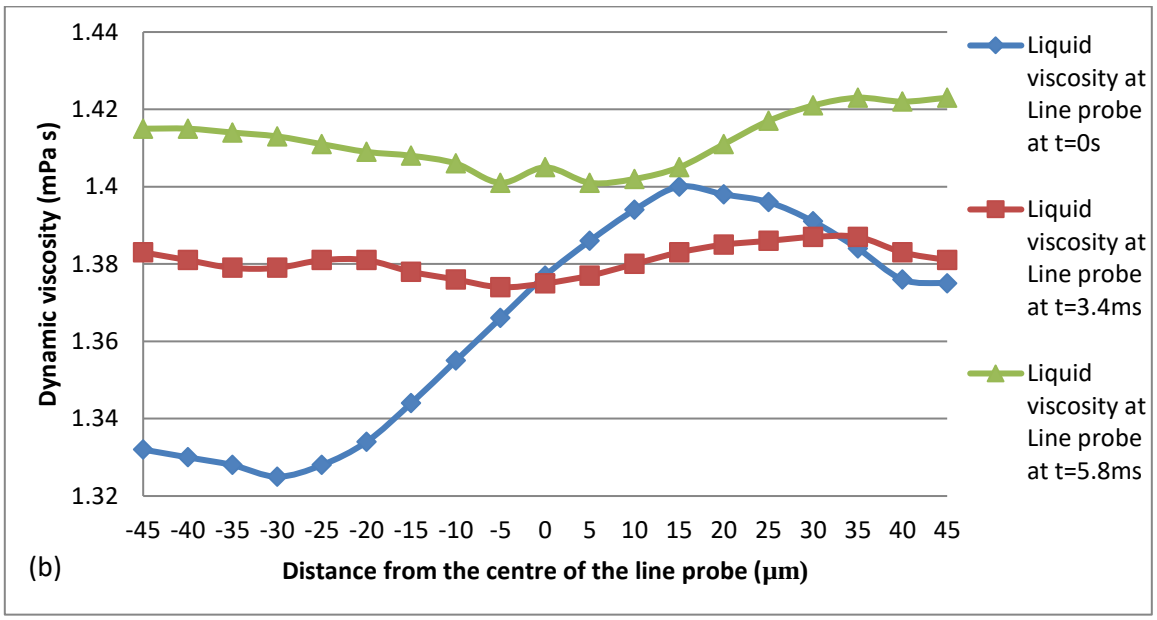

Figure 7.17 Liquid viscosity at the liquid film between gas slugs at line probe shown in (a) and liquid film viscosity distribution at fixed point of time (b) with three liquids used viscosity of 6.4 mPa s, 3.5 mPa s, 0.64 mPa s separately for reference.

Multiple fluids mixing process with time sequence in K-junction was also simulated under initial condition that the whole junction was filled with one of the liquids as shown in Figure 7.18.

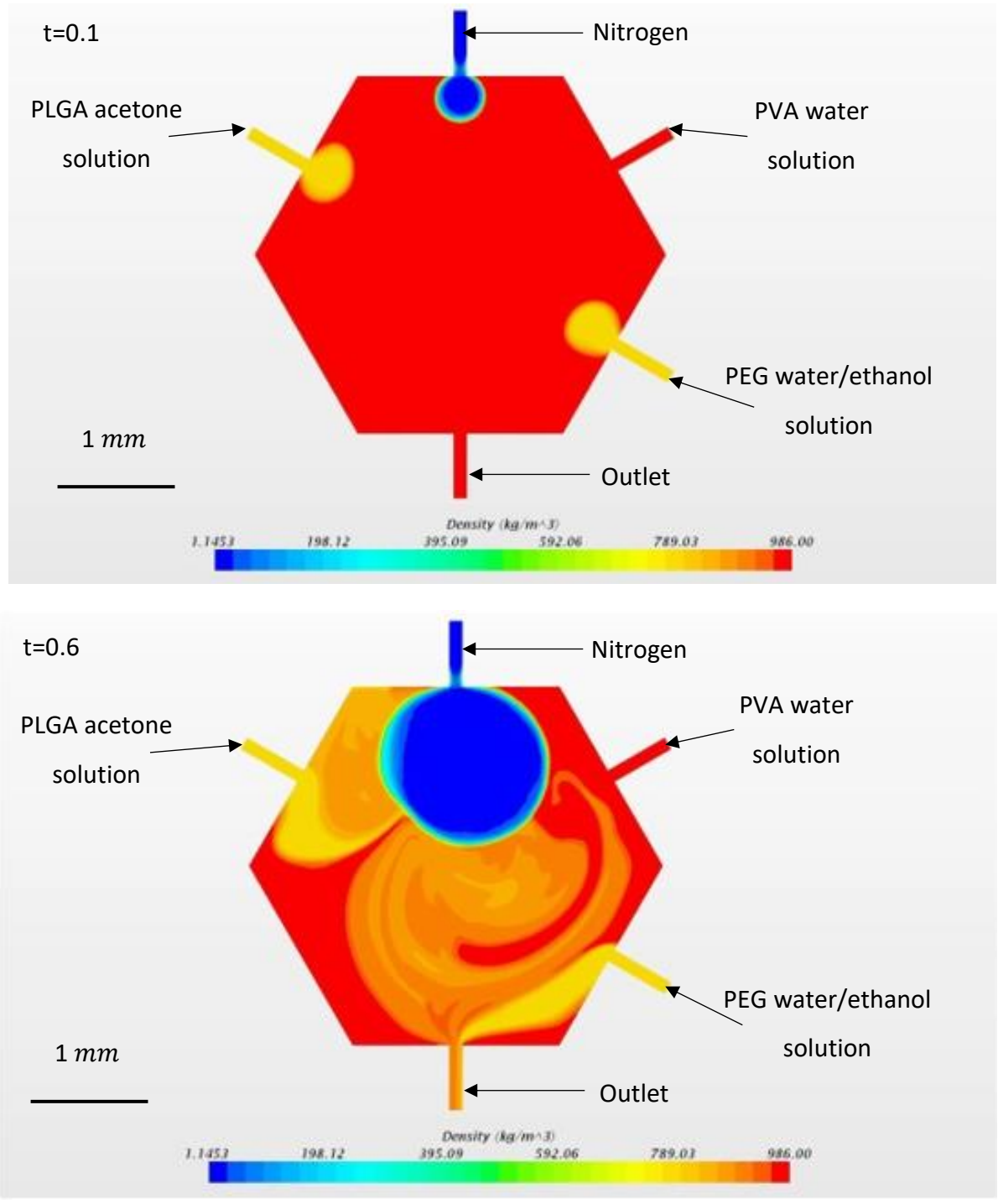

Figure 7.18 The simulation of three different liquids (PEG, PVA and PLGA solutions mentioned in Table 5.1) mixing inside of K-junction with time sequence where PVA water solution was injected through liquid inlet on the top right, PEG water/ethanol solution was injected through liquid inlet on the bottom right, and PLGA acetone solution was injected through liquid inlet on the left with constant liquid flow rate of 150 µl/min and gas pressure of 170 kPa.

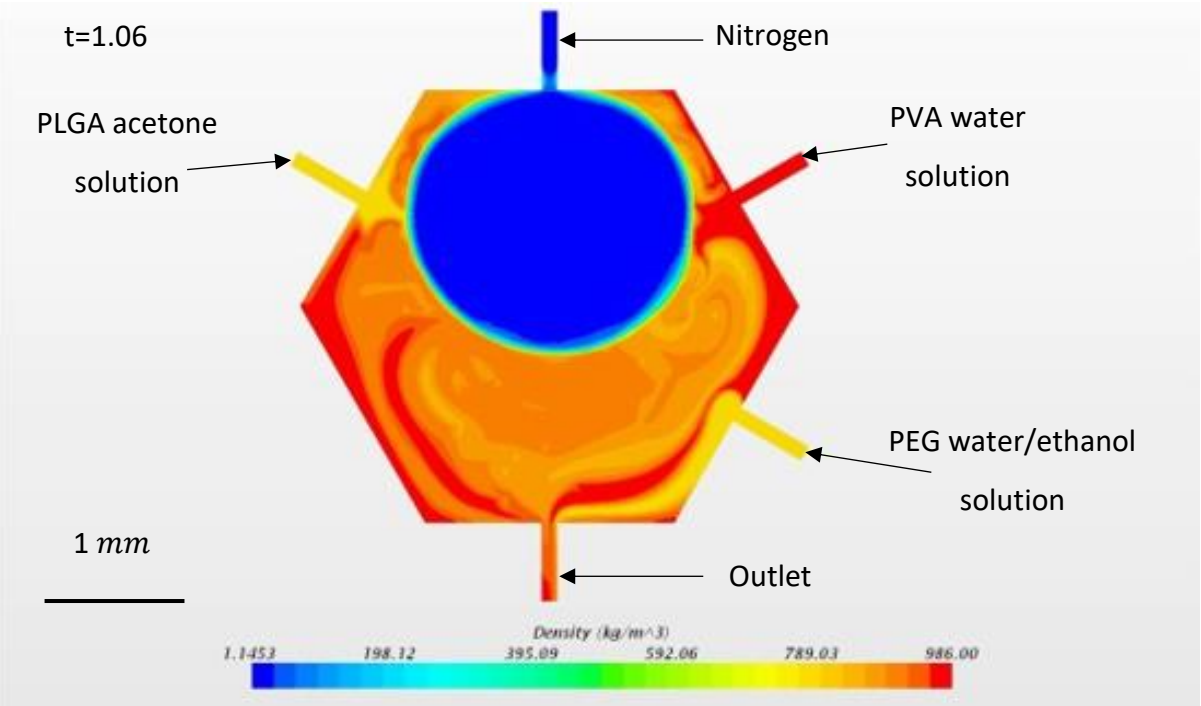

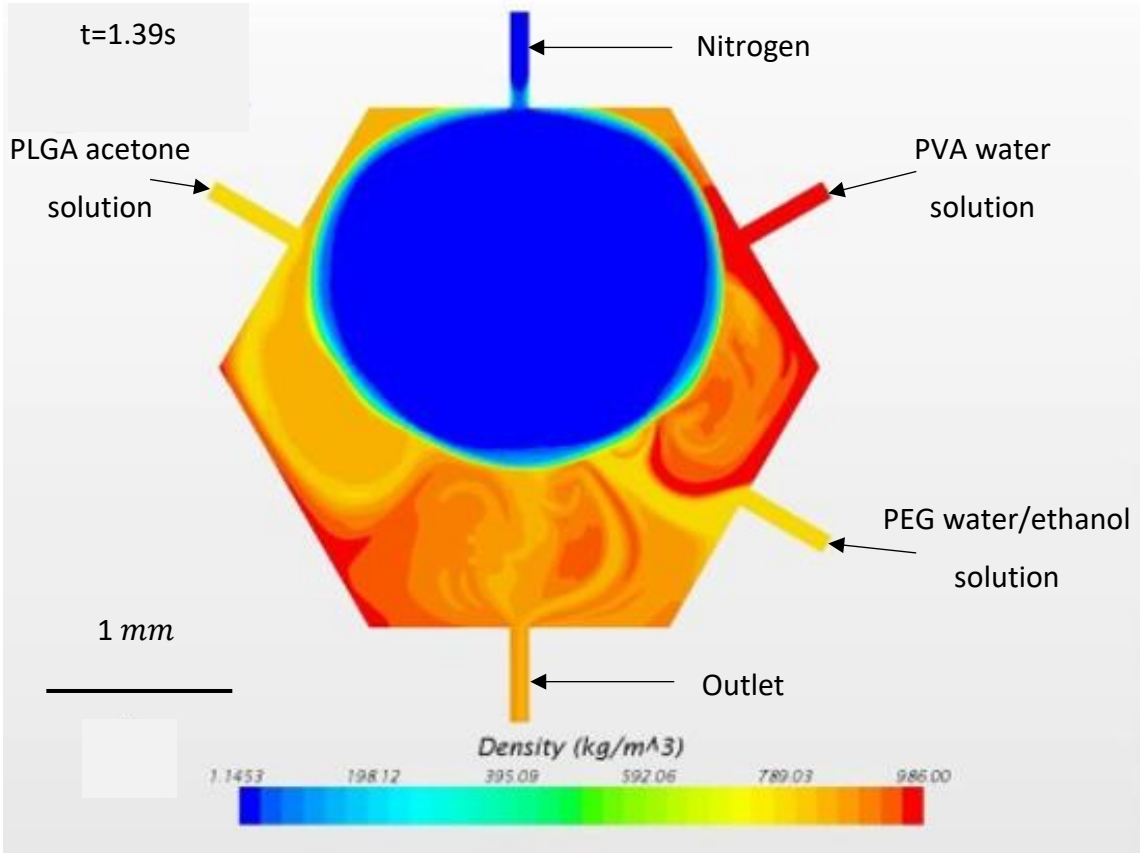

Figure 7.18 The simulation of three different liquids (PEG, PVA and PLGA solutions mentioned in Table 5.1) mixing inside of K-junction with time sequence where PVA water solution was injected through liquid inlet on the top right, PEG water/ethanol solution was injected through liquid inlet on the bottom right, and PLGA acetone solution was injected through liquid inlet on the left with constant liquid flow rate of 150 µl/min and gas gas pressure of 170 kPa (continued).

It can be seen from these simulation results that gas phase has formed a big bubble in the mixing chamber inside of the K-junction and it continues growing along with the running of simulation. Meanwhile, it blocks the original path of liquid phase from the other three liquid inlets thus it can be considered as transverse components of flow like ridges on the floor of the channel at a specific angle which is illustrated in the research of Stroock et al (2002). It also has shown some similarities in mixing occurred in the staggered herringbone mixer developed by the same authors (Figure 7.19) as the streamlines of the flow in the mixing area rotate when it comes across the ridges in the channel or bubble core thus generates the upwelling and downwelling of the liquid flow and chaotic mixing.

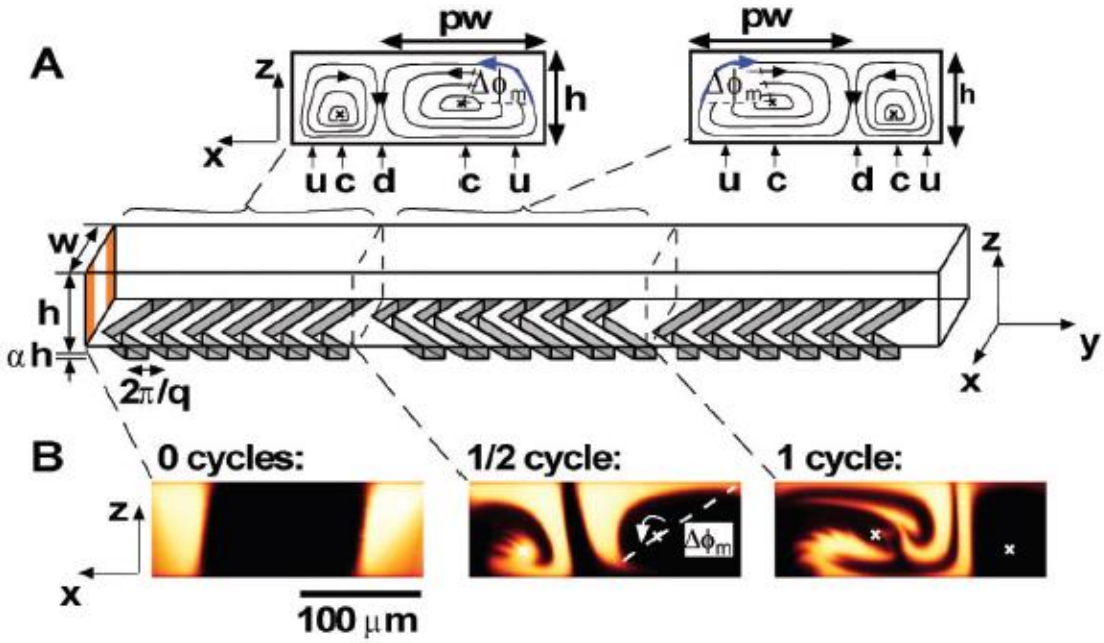

Figure 7.19 Staggered herringbone mixer (SHM). (**A**) Schematic diagram of one-and-a-half cycles of the SHM. (B) Confocal micrographs of vertical cross sections of a channel as in (A) (Stroock et al.,2002).

In the K-junction, different liquids have enough time and space to complete mixing in the mixing chamber instead of outlet capillary channel and the liquid mixture was pushed to the outlet because of the expansion of the big bubble and pressure accumulated in the chamber. A grid independence test was conducted before running multiple fluids mixing simulation. Five sets of quadrilateral mesh cell ranging from 10^3 to 10^4 were adopted with identical condition in this test. It was found that when the number of mesh cell exceeds 8×10^3 the length change of the gas slug was not significant (Figure 7.20). Therefore, the

mesh cell count of 8×10^3 was chosen for the mixing simulation in the cross-junction as a compromise of saving computation effort and accuracy.

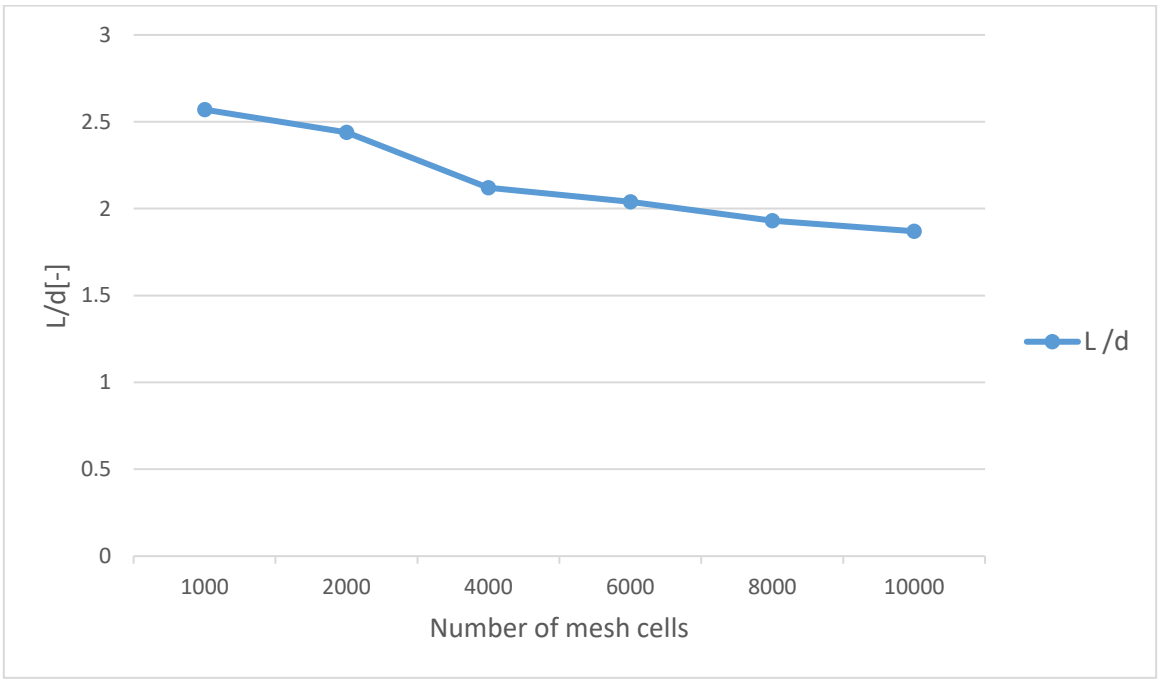

Figure 7.20 Grid dependence study of the microbubble length/channel diameter ratio(L/d) using 5% w/w PEG water solution as the liquid phase with viscosity μ_l=5.7 mPa s, surface tension σ= 38.2 mN/m and velocity v_l of 0.01 m/s. Nitrogen is the gas phase with velocity v_g=0.02 m/s.

It is observed that when the number of mesh cell reaches to 8×10^3, the microbubble length/channel diameter ratio still decreases slightly with the increasing of mesh cells. But bubbles were generated constantly with uniform size instead of the instability when the number of mesh cell was less than 8×10^3. Therefore, the grid impendence is achieved at this point and the following simulations were based on the mesh cell of 8×10^3 although it is still a coarse mesh for simulations in high accuracy. As this coarse mesh (8×10^3) was used for simulation and only one set of diffusion between all of three liquids was defined, numerical diffusion and incomplete mixing issue still existed. Following simulations on this geometry in 2D and 3D need to be carried out and then compared with experiment observation to obtain results with better accuracy.

The images captured by fluorescence microscopy, Figure 7.21, showed the specific close-packed pattern of microbubbles. As mentioned previously, the diameter of these

bubbles decreased from centre to edge, except in the case of some monodispersed bubbles near the centre. This visualisation also revealed that fluorescent dyes used in the experiment (Neutral Red and Perylene) were encapsulated in a thin film and distributed uniformly on the shell of bubbles. From images in Figure 7.21(e), (f) it can be concluded that the reflecting shades of Neutral Red and Perylene also occurred around and inside the shell of bubbles. Thus, this novel K-junction has the potential of encapsulating fluorescent dyes and polymers on the shell of bubbles formed and could be adopted as a method to encapsulate active pharmaceutical ingredients for potential applications in drug delivery.

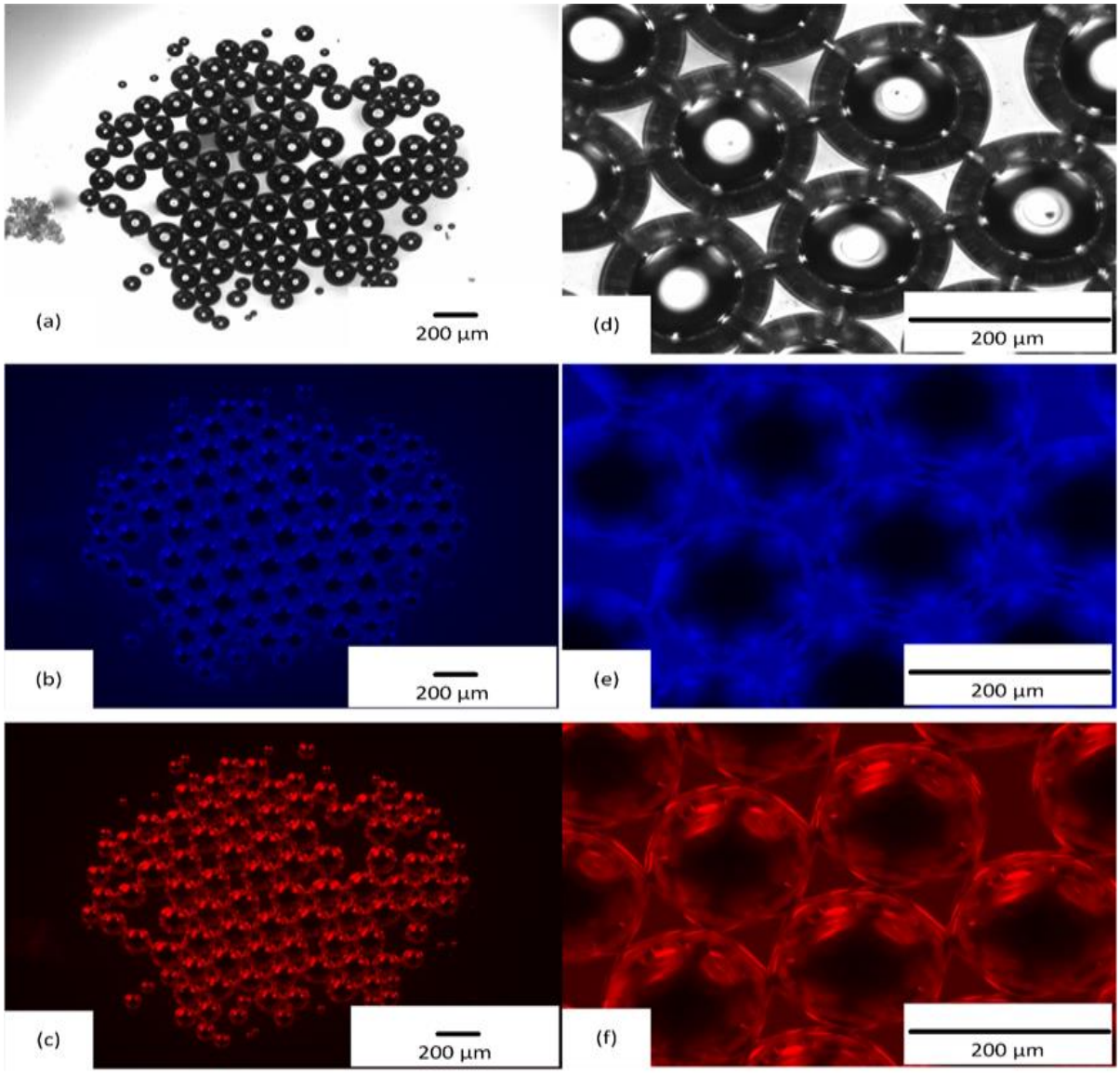

Figure 7.21 Fluorescent microscopy images of microbubbles formed by different solutions containing fluorescent dyes: (a), (d) without fluorescent light; (b), (e) transmission of Perylene; (c), (f) transmission of Neutral Red.

For cross-junction, mixing experiments were conducted by using two different solutions: 5% w/w PEG water solution and 2% w/w PVA water solution under the condition of constant liquid flow rate of 0.1ml/min and gas pressure ranging from 180 kPa to 240 kPa. The microbubble size variation along with the increase of gas pressure is shown in Figure 7.22.

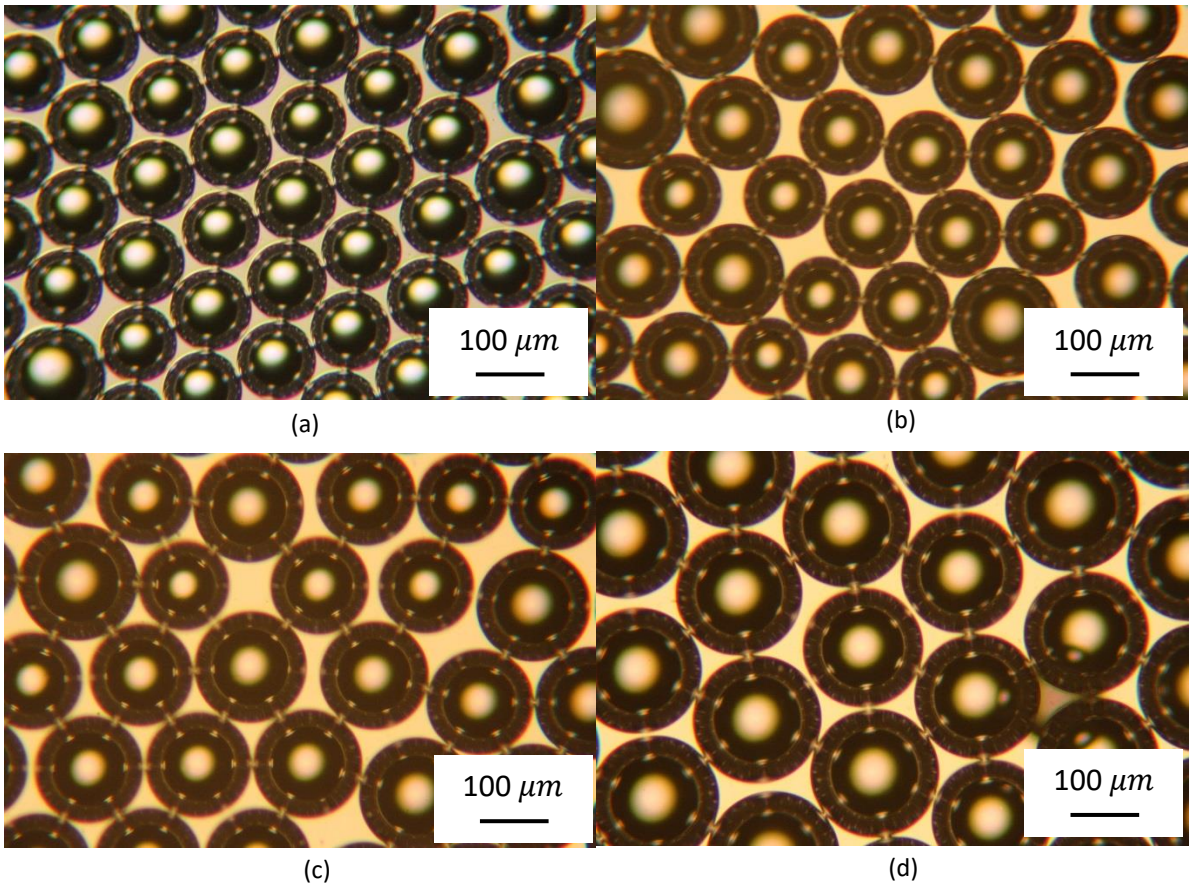

(a) (b)

(c) (d)

Figure 7.22 Optical micrographs with 5x magnification of bubbles formed by multiple liquids and gas with constant liquid flow rate of 0.1 ml/min at different gas pressures of: (a) 180 kPa; (b) 200 kpa; (c) 220 kPa; (d) 240 kPa.

Apparently, the microbubbles diameter increases with the increase of gas pressure when other boundary conditions remains the same by using cross-junction just like what happened in T-junction and K-junction. Monodispersed microbubble distributed normally as other conventional microfluidic junction like T-junction.

Numerical simulations were operated under the same condition as in experiments and the mixing and bubble generation process inside of cross-junction is shown in Figure 7.23.

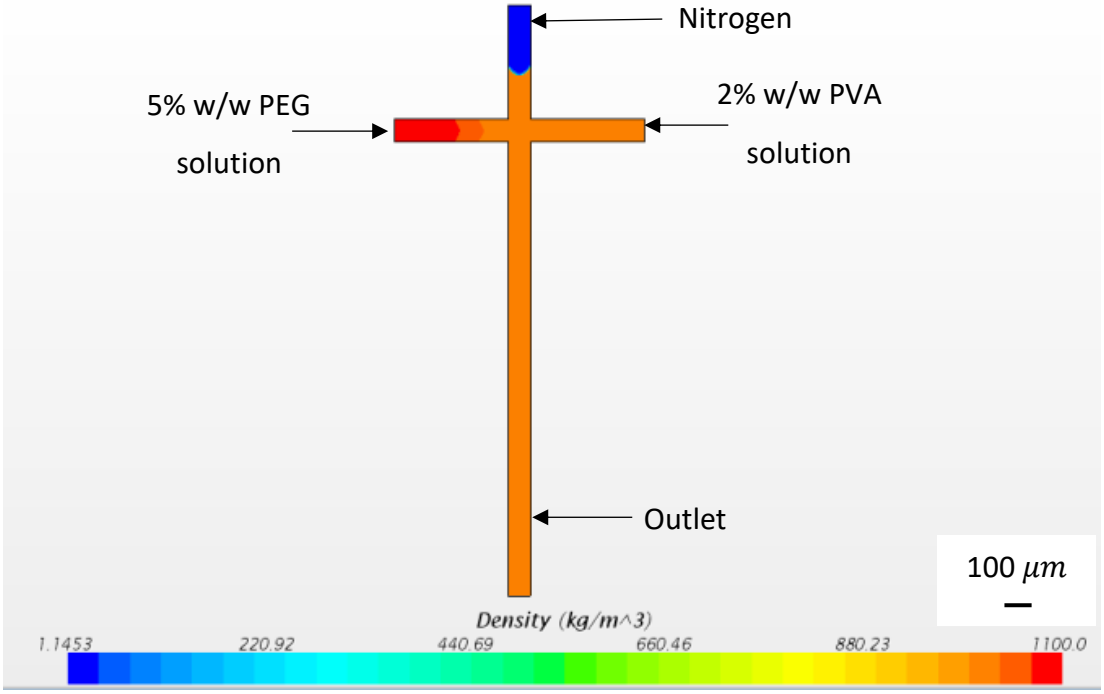

(a) t=2.85ms

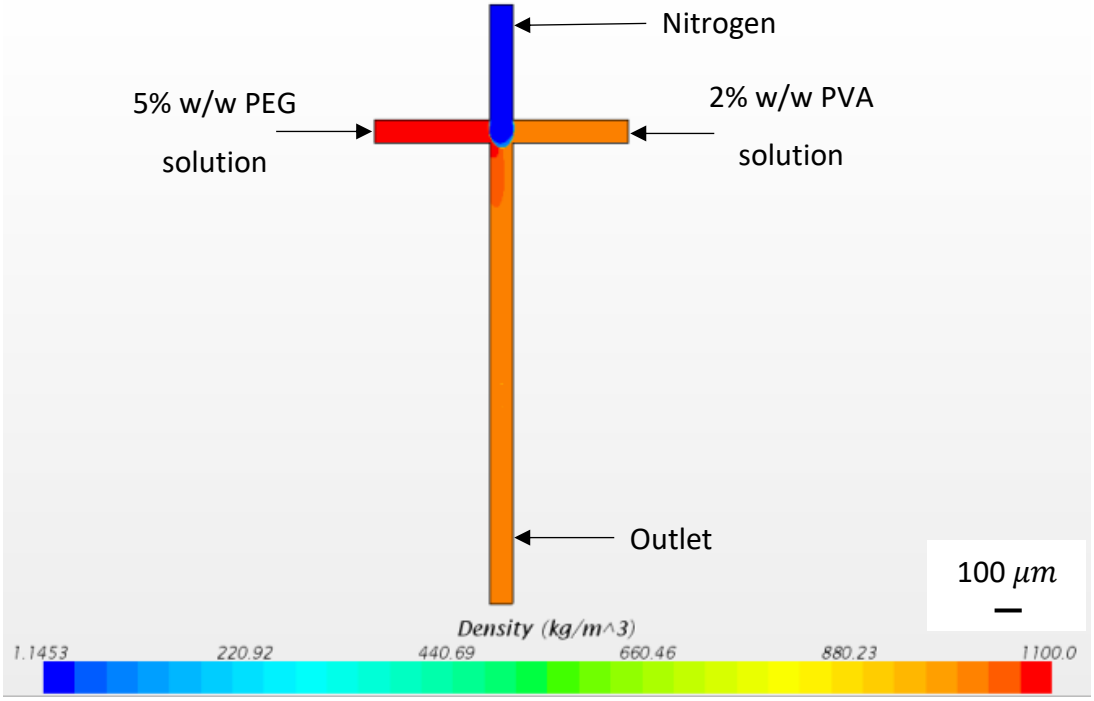

(b)t=5.85ms

Figure 7.23 The simulation of two different liquids mixing and microbubble generation inside of cross-junction with time sequence with solutions of 5% w/w PEG water solution (in left channel), 2% w/w PVA water solution (in right channel) and nitrogen (in the top channel) under the same boundary conditions as in experiments (gas pressure 200 kPa and liquid flow rate 0.1 ml/min).

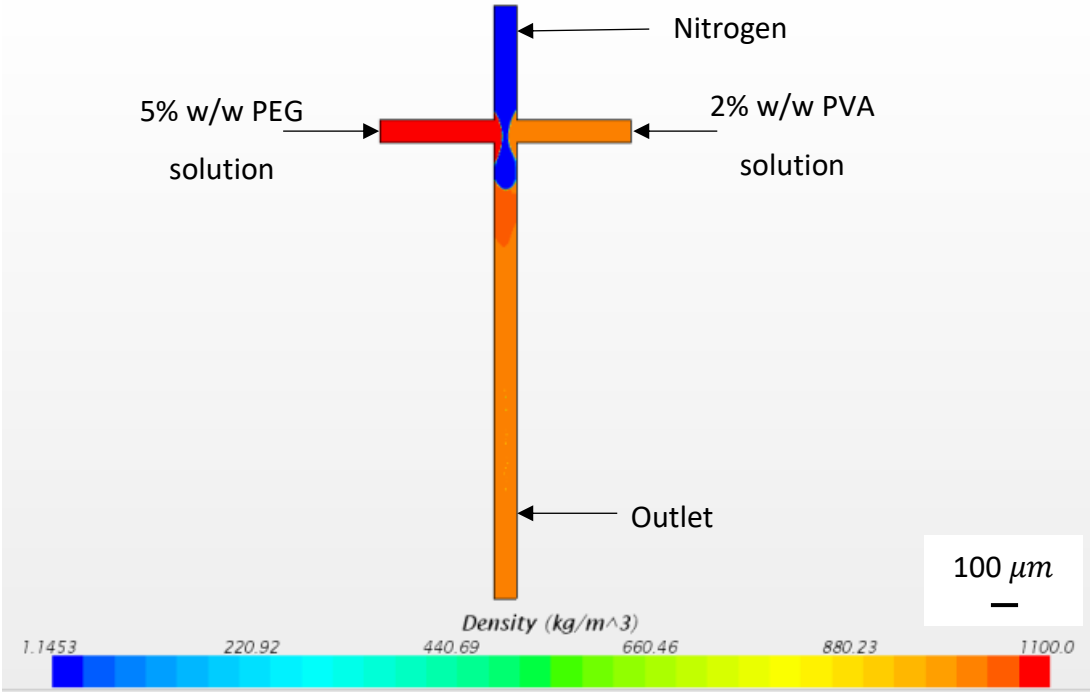

(c) t=6.55ms

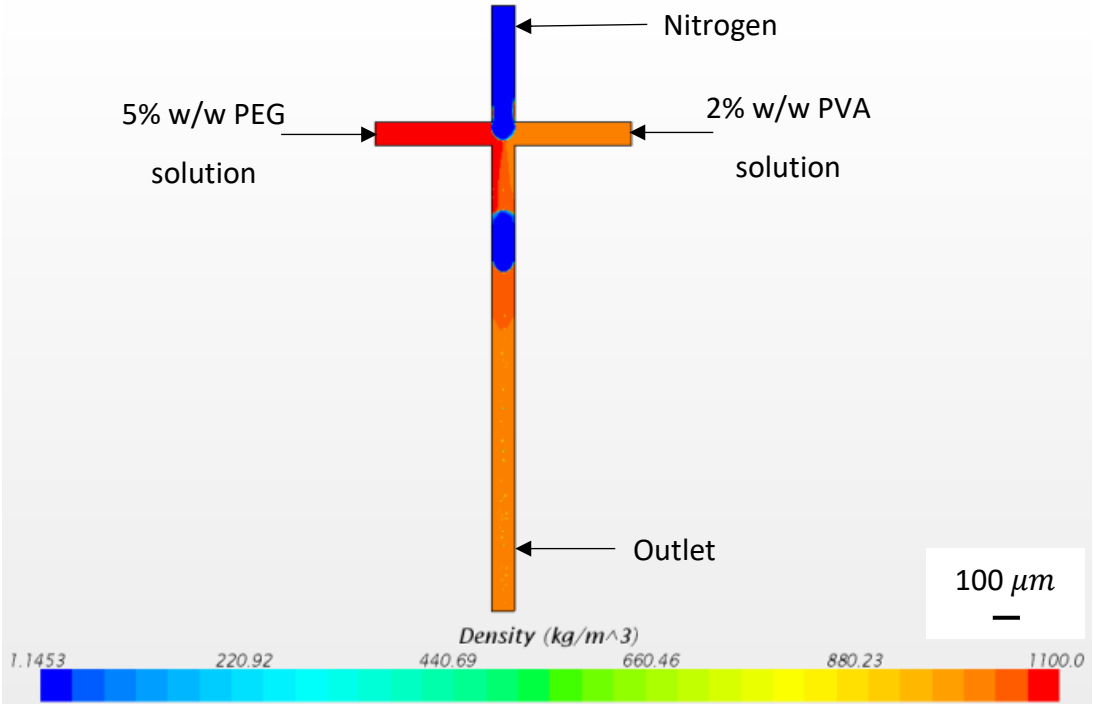

(d)7.51ms

Figure 7.23 The simulation of two different liquids mixing and microbubble generation inside of cross-junction with time sequence with solutions of 5% w/w PEG water solution (in left channel), 2% w/w PVA water solution (in right channel) and nitrogen (in the top channel) under the same boundary conditions as in experiments (gas pressure 200 kPa and liquid flow rate 0.1 ml/min) (continued).

A probe line with the length of capillary diameter was place at a fixed position near the outlet of the mixing area in the capillary to investigate viscosity change at the liquid film between two gas slugs in the channel and the results are shown in Figure 7.24.

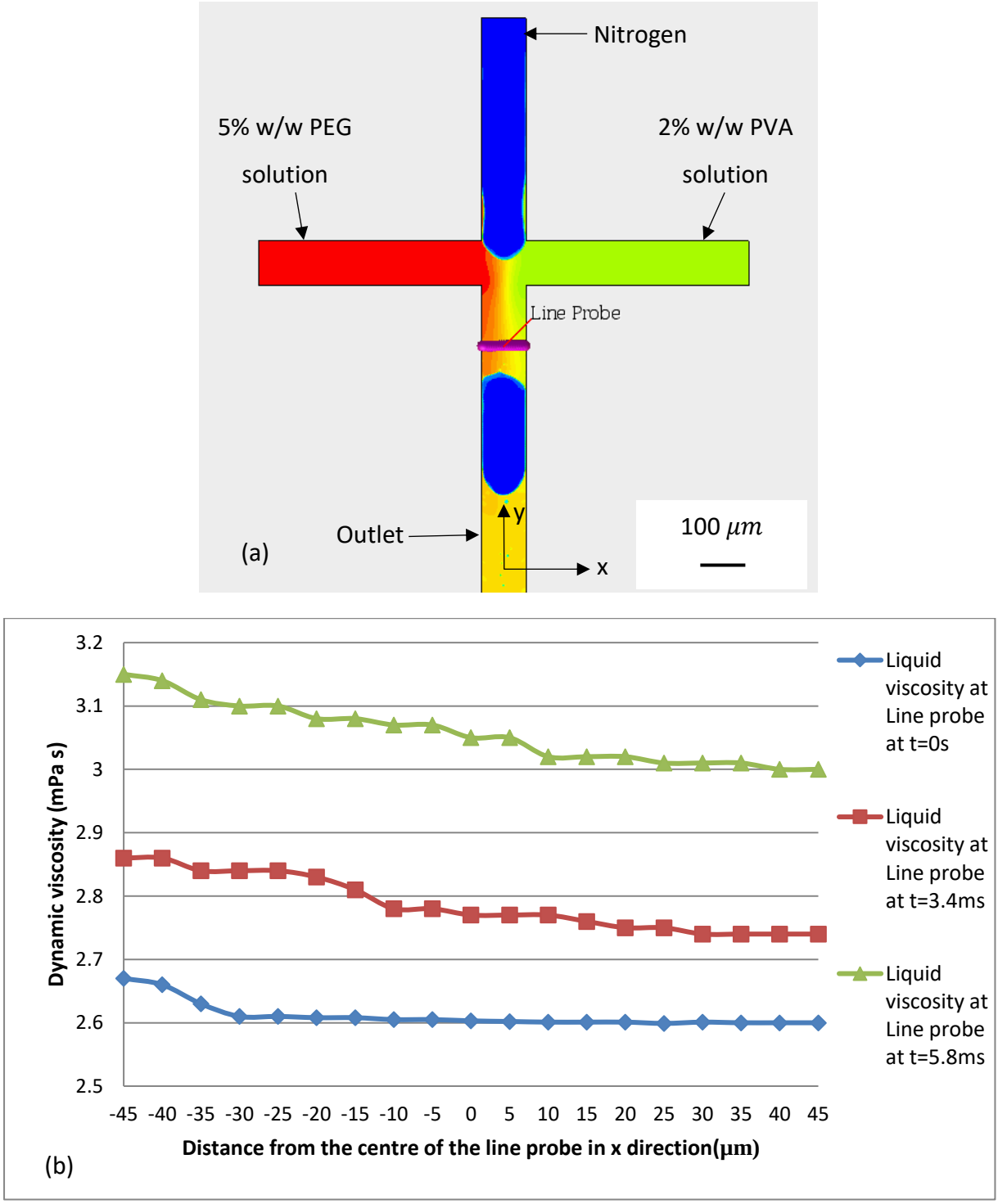

Figure 7.24 Liquid viscosity at the liquid film between gas slugs at line probe shown in (a) liquid film viscosity distribution at fixed point of time (b) with two liquids used viscosity of 5.7 mPa s, 2.6 mPa s separately for reference.

The dynamic viscosity change of multiple fluids was observed at varies temporal points to evaluate the occurrence of mixing. It can be seen from the multiple fluids mixing simulations in the cross-junction with grid density of 8×10^3 that the viscosity value of the liquid film between two gas slugs was in the range of 2.6-3.15 mPa s due to the mixing of these two liquids. However, no streamlines of the flow rotating in the mixing area was found and the viscosity at the line probe changed slightly at specific time point due to limit space of the mixing area hence most of the mixing process occurred in the outlet channel instead as time passed by. Thus, the mixing in the cross-junction is dependent the length of the outlet channel and shows relatively slower viscosity change and mixing process than the K-junction at the same time interval.

7.5 Summary

Chaotic mixing in both K-junction and cross-junction has been investigated experimental and numerically in this chapter Microfluidic devices have a wide variety of chemical and biological applications, including medical diagnostics, DNA and protein analysis, and drug development. They can be miniaturized, allowing for quick analysis using portable instrumentation. They also use minimal amounts of samples and consume little reagents, reducing the waste generated and leading to overall low-cost operations. However, microfluidic devices also have limitations. One of the challenges is mixing, which is often required for sample dilution, reagent homogenization, and chemical or biological reactions. The difficulty in achieving sufficient mixing in a microfluidic device results from laminar flows that can be explained by low Reynolds numbers determined by the channel's hydraulic diameter, flow velocity, and solution's kinetic viscosity.

Several methods have been developed to enhance mixing in microfluidic devices for a variety of applications. One of the methods is passive mixing, which involves using ridges or slanted wells in the microchannel, changing geometry and patterns to improve mixing performance, changing the properties of channel surfaces, and optimizing via simulations. The other method is active mixing, which including microstirrers, acoustic mixers, and flow pulsation. This method has been investigated and integrated into microfluidic devices to enhance mixing in a more controllable manner. Generally, passive mixers have advantage of convenient integration, but users find it difficult to control externally after fabrication.

However, active mixers can be controlled by users to a certain degree for tuned mixing but integration within a device requires external components (e.g. power sources) to operate and could be much more difficult. In this work, passive method which uses microfluidic devices K-junction and cross-junction with different shapes of mixing area were investigated through simulations and experiments. It was found that the cross-junction performs like conventional microfluidic junction behaviour in both experiments and simulations such as four stages of microbubble generation and microbubble diameter distribution under the influence of different gas pressure and liquid viscosity. According to the simulation results such as viscosity variation at specific position as a function of time, chaotic mixing was found in the mixing area of the K-junction rather than the cross-junction. Therefore, it can be concluded that the mixing process depends on the geometry of the mixing area in microfluidic junctions. In this study, K-junction has shown similar chaotic mixing phenomena occurs in passive mixing device by using ridges and exhibits better mixing efficiency due to sufficient fluid mixing inside of the large mixing chamber than the cross-junction.

Chapter 8 : Conclusions and future work

8.1 Conclusions

Numerical simulations and experiments were conducted to investigate the microbubble generation and multiple fluids mixing in the microfluidic K-junction and cross-junction with the effect of gas pressure, liquid flow rate, viscosity, density, and surface tension It is concluded that the numerical simulations performed by using the Finite Volume method and Volume of Fluid (VOF) technique is verified through using simple T-junction for test simulation to produce multiple fluids which is one gas and two more liquids mixing and microbubble generation process in both K-junction and cross-junction under specified boundary conditions.

Appropriate operating conditions, such as contact angle, liquid viscosity and surface tension were explored and determined in simulations and the influence of gas pressure, liquid viscosity and gas-liquid flow ratios were investigated in experiments respectively. It was indicated that for high gas-liquid ratio such as $v_g/v_l = 2$, the bubble volume decreases with the increase of the contact angle ranging from $30°$ to $120°$ rapidly. The increase of the contact angle results in the decrease of the adhesive force on the wall which leads to a reduction in the overall resistance to flow thus is helpful in the generation of bubbles. However, for a low gas-liquid ratio like $v_g/v_l = 0.5$, the change of the bubble volume is not as significant as that of the bubble length with the increase of the contact angle while the bubble length decreases with the contact angle being increased from $30°$ to $90°$ but the bubble volume slightly decreases.

The simulation results have shown that the bubble length and bubble volume increase with an increase of the surface tension at contact angle $\theta = 60°$ and gas-liquid flow ratio $v_g/v_l = 0.5$ and 2.0 or at $v_g/v_l = 1.0$, $\theta = 30°$ and or $120°$ which is agree with the results concluded in literatures. It was also found that bubble size decreases with increasing liquid viscosity while it increases with increasing gas-liquid flow ratios and gas pressure, and these numerical results are in good agreement with experimental results for the microfluidic K-junction and cross-junction devices. Moreover, it was found that for the K-junction the bubble generation process only occurred when the gas core inside the intersection chamber of the junction

became stable, after a long initialisation operating time, monodispersed bubbles were produced only in a specific time interval during bubble formation, when using a single liquid.

Numerical simulation results have shown good agreement with experiments on bubble generation and size distribution under the influence of gas-liquid flow ratios and liquid viscosity in the K-junction, and have elucidated processes that are inaccessible for the experimental apparatus to investigate, like mixing processes inside the microfluidic chamber. Furthermore, for the multiple liquids containing different components in the experiments, it was revealed that the novel K-junction was capable of creating bubbles with good distribution of fluorescent dyes on the bubble shell and has potential applications in encapsulating targeting species. Numerical simulations of the K-junction and cross-junction with multiple liquids have highlighted and illustrated the mixing efficiency in the chamber with different geometry. Chaotic mixing was found in the mixing area of the K-junction rather than the cross-junction based on the simulation results such as viscosity variation at specific position as a function of time. As a result, the mixing efficiency depends on the geometry of the mixing area in microfluidic junctions and K-junction has shown similar chaotic mixing phenomena occurs in passive mixing device by using ridges leading to better mixing efficiency than conventional cross-junction due to sufficient fluid mixing inside of the large mixing chamber than the cross-junction.

8.2 Future work

The numerical simulations were performed on the K-junction and cross-junction using 2D geometries, in order to reduce the computation load and obtain general results more quickly. The grid dependence test in Section 4.4.2 has shown that although 500 thousand mesh cells is a reasonable choice for the following numerical simulations in multiple fluids mixing, the microbubble length, liquid slug length and total length of bubble still increase with the increasing number of mesh cells leading to slight errors in the numerical results. Moreover, because of the complexity of junction 2D geometries and large number of mesh cells on them, the simulation process run slowly on the available computers (slow on desktop, long waiting queues on computer cluster). In addition, the results from simulations of 2D geometries can only show the length and width of the microbubbles or gas slug in the outlet of the K-junction or cross-junction, but the real circular cross-section cannot be assessed. In the simulations of

the corresponding 3D geometry, all of the dimensions such as length, width, and radius would be well defined with fixed volume resulting in a more accurate numerical result. Such difference between 2D and 3D geometry simulations has been investigated in the numerical analysis of microbubble formation in microfluidic devices by Weber and Shandas (2007). In their study, bubble formation in a microfluidic flow-focusing device is simulated using the Volume of Fluid approach for the gas and liquid phases. It was found that one important difference between 2D and 3D simulation is the extra radius of curvature which must be considered when calculating the pressure difference between the gas and liquid phases. Although there is difference, both simulations have shown the same qualitative behaviours, including the bubble size variation during bubble formation as shown in Figure 8.1.

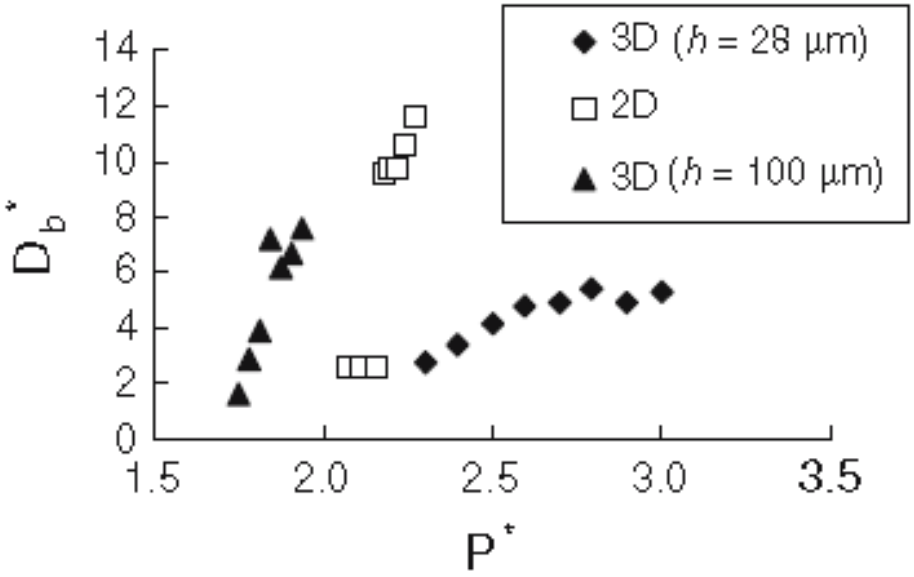

Figure 8.1 Dimensionless bubble diameter (D_b^*) distribution for both 2D and 3D simulations as a function of normalized gas inlet pressure (P^*) where h is the height of the microfluidic device (Weber & Shandas, 2007).

It was indicated that the bubble diameter for 2D simulation is almost three times bigger than that for 3D simulation at gas inlet pressure of 230 kPa. Therefore, similar phenomenon is also very likely to happen between 2D and 3D simulations in this study with huge difference in bubble size distribution.

During the simulation, the effect of boundary conditions such as gas pressure and liquid flow rate and fluid properties like density, viscosity, surface tension was taken into consideration despite of contact angle because it was assumed as 0 degree to simplify the simulation. Thus, it could have an effect on the accuracy of the simulation results when comparing with experimental observations. In terms of experiments, when using three different kinds of solutions in the K-junction to investigate multiple fluids mixing process, the inner channels of the capillaries were often blocked by the liquid. This is mainly caused by the corrosion and damage of the channel inside of the K-junction by using acetone which will dissolve PDMS material as solvent in PLGA solution resulting in discontinuous microbubble generation and insufficient fluids mixing.

Furthermore, in order to investigate the influence of gas-liquid flow ratios on microbubble size distribution in both K-junction and cross-junction through simulation and experiment. The gas inlet boundary condition has to change from gas pressure inlet to volumetric flow rate in the simulations. The conversion process of pressure to flow rate is mentioned in Section 4.3.4 and Poiseuille equation, Bernoulli's equation are used for the rearrangement. However, there is still difference between theoretical calculation and actual measurement due to the assumption that gas and other external environment are in ideal condition when using these equations. Therefore, when using theoretical calculation data in simulation this difference also effects the accuracy of numerical results and the agreement with experimental results as well.

In terms of the experiment, the control of the gas valve and gas flow meter connected to the gas tank is problematic, as it could be difficult to keep a stable gas pressure output for a long time. Thus, the actual gas pressure applied to the microfluidic junction may have introduced an error, compared to the reading in the digital pressure gauge. Meanwhile, the pumps used for pumping liquid into the junction through plastic syringes also introduce error as some particles in the solution may block the capillary and cause liquid backflow or the malfunction of the pumps.

Future work can be classified into the following parts:

1) Conducting numerical simulations in 3D geometry of the K-junction with multiple fluids and refined mesh under a variety of boundary conditions such as gas pressure, gas-liquid flow ratios to obtain more realistic simulation results compared to experiments and further investigate microbubble generation process, microbubble size distribution and multiple fluids mixing which helps to optimize the design of microfluidic device and understand the mechanism of microbubble generation and fluid mixing in microscale.

2) As it has been shown that K-junction has potential applications in encapsulating targeting species, further experiments of K-junction by drug components combined with different liquids such as 5wt%PEG+2wt%PVA water solution, 5wt%PMSQ ethanol solution, and 5wt%PLGA acetone solution have to be conducted with a series of boundary conditions such as gas/liquid flow rate ratio to investigate the effeteness of producing drug delivery carrier by using this novel microfluidic devices like K-junction.

3) The influence of capillary size along with liquid viscosity and gas to liquid flow ratios has to be investigated in depth, in order to explore possible further reduction in microbubble diameter, for those application where small size is required (for example medical imaging contrast agents). In addition, measurement of dynamic contact angle instead of static contact angle used in this work between fluid and microchannel in the junction has to be made through an appropriate experimental method and taken into consideration in the rest of simulation due to its significant influence on the microbubble size and shape from literature.

4) The materials of K-junction can be upgrade to glass instead of PDMS as solvent (such as acetone) can't cause damage to the channel inside of the junction in the case of glass. Therefore, a greater variety of solutions could be allowed for use in the experiments of the K-junction and more stable and continuous microbubble generation processes could be achieved.

5) The investigation on chaotic mixing in the K-junction and cross-junction only shows the qualitative analysis of the mixing occurred but no quantitative analysis is provided. Therefore, further simulations should be conducted to track particles in the liquid phase for quantitative study. The distance of these particle has to be displayed as it grows exponentially

during the mixing process so that it could be more supportive for the existence of chaotic mixing in the K-junction.

References

Agarwal, A., Xu, H., Ng, W.J. and Liu, Y., 2012. Biofilm detachment by self-collapsing air microbubbles: a potential chemical-free cleaning technology for membrane biofouling. Journal of materials chemistry, 22(5), 2203-2207.

Agarwal, A., Ng, W.J. and Liu, Y., 2011. Principle and applications of microbubble and nanobubble technology for water treatment. Chemosphere, 84(9), 1175-1180.

Albijanic, B., Ozdemir, O., Nguyen, A. V., & Bradshaw, D., 2010. A review of induction and attachment times of wetting thin films between air bubbles and particles and its relevance in the separation of particles by flotation. Adv Colloid Interface Sci, 159(1), 1-21.

Baroud, C.N., Gallaire, F. and Dangla, R., 2010. Dynamics of microfluidic droplets. Lab on a Chip, 10(16), 2032-2045.

Bashir, S., Rees, J.M. and Zimmerman, W.B., 2011. Simulations of microfluidic droplet formation using the two-phase level set method. Chemical Engineering Science, 66(20), 4733-4741.

Bhatt, Y., & Shah, D., 2012. Influence of additives on fabrication and release from protein loaded microparticles. Iranian Journal of Pharmaceutical Sciences, 8(3), 171-179.

Blomley, M.J., Cooke, J.C., Unger, E.C., Monaghan, M.J. and Cosgrove, D.O., 2001. Science, medicine, and the future: Microbubble contrast agents: a new era in ultrasound. BMJ: British Medical Journal, 322(7296), 1222-1225

Brackbill, J.U., Kothe, D.B. and Zemach, C., 1992. A continuum method for modeling surface tension. Journal of computational physics, 100(2), 335-354.

Chen, C. et al., 2009. Production of monodispersed micron-sized bubbles at high rates in a microfluidic device. Applied Physics Letters, 95(14), 144101

Chen, S. and Doolen, G.D., 1998. Lattice Boltzmann method for fluid flows. Annual review of fluid mechanics, 30(1), 329-364.

Chern, I.L., Glimm, J., McBryan, O., Plohr, B. and Yaniv, S., 1986. Front tracking for gas dynamics. Journal of Computational Physics, 62(1), 83-110.

Clayden, J., Greeves, N., & Warren, S. (2012). Organic chemistry (Second ed.). New York: Oxford University Press.

Christopher, G.F, Noharuddin N.N, Taylor J.A, Anna S.L., 2008. Experimental observations of the squeezing-to-dripping transition in T-shaped microfluidic junctions. Phys Rev E 78(3), 036317

Christopher, G.F. and Anna, S.L., 2007. Microfluidic methods for generating continuous droplet streams. Journal of Physics D: Applied Physics, 40(19), 319.

Ciskowski, R.D. and Brebbia, C.A. eds., 1991. Boundary element methods in acoustics. Springer.

Clayden, J., Greeves, N., & Warren, S., 2012. Organic Chemistry: OUP Oxford

Clift, R., Grace, J. R., & Weber, M. E., 2005. Bubbles, Drops, and Particles: Dover Publications.

Cubaud, T., Ulmanella, U. and Ho, C.M., 2006. Two-phase flow in microchannels with surface modifications. Fluid Dynamics Research, 38(11), 772-786.

Dang, M., Yue, J. and Chen, G., 2015. Numerical simulation of Taylor bubble formation in a microchannel with a converging shape mixing junction. Chemical Engineering Journal, 262, 616-627.

Davidson, M. W., & Abramowitz, M., 2002. Optical microscopy. Encyclopedia of imaging science and technology.

Dayton, P.A. and Rychak, J.J., 2007. Molecular ultrasound imaging using microbubble contrast agents. Front Biosci, 12(23), 5124-5142.

De Menech, M., Garstecki, P., Jousse, F. and Stone, H.A., 2008. Transition from squeezing to dripping in a microfluidic T-shaped junction. journal of fluid mechanics, 595, 141-161.

Demello, A.J., 2006. Control and detection of chemical reactions in microfluidic systems. Nature, 442(7101), 394-402.

DeMerlis, C. C., & Schoneker, D. R., 2003. Review of the oral toxicity of polyvinyl alcohol (PVA). Food and Chemical Toxicology, 41(3), 319-326.

Dreyfus, R., Tabeling, P., & Willaime, H., 2003. Ordered and Disordered Patterns in Two-Phase Flows in Microchannels. Physical Review Letters, 90(14), 144505.

Farook, U., Stride, E. and Edirisinghe, M.J., 2009. Preparation of suspensions of phospholipid-coated microbubbles by coaxial electrohydrodynamic atomization. Journal of the Royal Society Interface, 6(32), 271-277.

Fauci, L.J. and Peskin, C.S., 1988. A computational model of aquatic animal locomotion. Journal of Computational Physics, 77(1), 85-108.

Fedkiw, R.P., Aslam, T., Merriman, B. and Osher, S., 1999. A non-oscillatory Eulerian approach to interfaces in multimaterial flows (the ghost fluid method). Journal of computational physics, 152(2), 457-492.

Ferziger, J.H. and Peric, M., 2012. Computational methods for fluid dynamics. Springer Science & Business Media.

Fogelson, A.L. and Peskin, C.S., 1988. A fast numerical method for solving the three-dimensional Stokes' equations in the presence of suspended particles. Journal of Computational Physics, 79(1), 50-69.

Fu, T., Ma, Y., Funfschilling, D., Zhu, C. and Li, H.Z., 2010. Squeezing-to-dripping transition for bubble formation in a microfluidic T-junction. Chemical engineering science, 65(12), 3739-3748.

Fu, T., Ma, Y., Funfschilling, D. and Li, H.Z., 2009. Bubble formation and breakup mechanism in a microfluidic flow-focusing device. Chemical Engineering Science, 64(10), 2392-2400.

Garstecki, P., 2010. Formation of droplets and bubbles in microfluidic systems. In Microfluidics Based Microsystems (163-181). Springer, Dordrecht.

Garstecki, P., Fuerstman, M.J., Stone, H.A. and Whitesides, G.M., 2006. Formation of droplets and bubbles in a microfluidic T-junction—scaling and mechanism of break-up. Lab on a Chip, 6(3), 437-446.

Garstecki, P., & Whitesides, G. M., 2006. Formation of droplets and bubbles in a microfluidic T-junction-scaling and mechanism of break-up. Lab on a Chip, 6(3), 437-446.

Garstecki, P., Stone, H.A. and Whitesides, G.M., 2005. Mechanism for flow-rate controlled breakup in confined geometries: a route to monodisperse emulsions. Physical Review Letters, 94(16), 164501.

Garstecki, P., Gitlin, I., DiLuzio, W., Whitesides, G.M., Kumacheva, E. and Stone, H.A., 2004. Formation of monodisperse bubbles in a microfluidic flow-focusing device. Applied Physics Letters, 85(13), 2649-2651.

Glimm, J., Graham, M.J., Grove, J., Li, X.L., Smith, T.M., Tan, D., Tangerman, F. and Zhang, Q., 1998. Front tracking in two and three dimensions. Computers & Mathematics with Applications, 35(7), 1-11.

Glimm, J., Grove, J., Lindquist, B., McBryan, O.A. and Tryggvason, G., 1988. The bifurcation of tracked scalar waves. SIAM Journal on Scientific and Statistical Computing, 9(1), 61-79.

Gordillo, J.M. et al., 2004. A new device for the generation of microbubbles. Physics of Fluids, 16(8), 2828–2834

Grossmann, C., Roos, H.G. and Stynes, M., 2007. Numerical treatment of partial differential equations (Vol. 154). Berlin: Springer.

Gunduz, O., Ahmad, Z., Stride, E., & Edirisinghe, M., 2013. Continuous Generation of Ethyl Cellulose Drug Delivery Nanocarriers from Microbubbles. Pharmaceutical Research, 30(1), 225-237.

Gunduz, O., Ahmad, Z., Stride, E., & Edirisinghe, M., 2012. A device for the fabrication of multifunctional particles from microbubble suspensions. Materials Science and Engineering: C, 32(4), 1005-1010.

Guo, F., Chen, B., 2009. Numerical Study on Taylor Bubble Formation in a Micro-channel T-Junction Using VOF Method. Microgravity Science Technology, 21(1), 51-58

Gunther, A., Jensen, K.F., 2006. Multiphase microfluidics: from flow characteristics to chemical and material synthesis. Lab on a Chip, 6(12), 1487–1503

Hawker, N.A. and Ventikos, Y., 2012. Interaction of a strong shockwave with a gas bubble in a liquid medium: a numerical study. Journal of Fluid Mechanics, 701, 59-97.

Heiszwolf, J.J., Kreutzer, M.T., van den Eijnden, M.G., Kapteijn, F. and Moulijn, J.A., 2001. Gas–liquid mass transfer of aqueous Taylor flow in monoliths. Catalysis Today, 69(1), 51-55.

Hong, J., Hong, C. K., & Shim, S. E., 2007. Synthesis of polystyrene microspheres by dispersion polymerization using poly(vinyl alcohol) as a steric stabilizer in aqueous alcohol media. Colloids and Surfaces A: Physicochemical and Engineering Aspects, 302(1–3), 225-233.

Hosokawa, S., Tanaka, K., Tomiyama, A., Maeda, Y., Yamaguchi, S. and Ito, Y., 2009. Measurement of micro Bubbles generated by a pressurized dissolution method. In Journal of Physics: Conference Series (Vol. 147, No. 1, p. 012016). IOP Publishing.

Iliescu, C., Taylor, H., Avram, M., Miao, J., & Franssila, S., 2012. A practical guide for the fabrication of microfluidic devices using glass and silicon. Biomicrofluidics, 6(1), 016505-016516.

Issa, R.I., Gosman, A.D. and Watkins, A.P., 1986. The computation of compressible and incompressible recirculating flows by a non-iterative implicit scheme. Journal of Computational Physics, 62(1), 66-82.

Jacqmin, D., 1999. Calculation of two-phase Navier–Stokes flows using phase-field modeling. Journal of Computational Physics, 155(1), 96-127.

Jones, S.W. and Young, W.R., 1994. Shear dispersion and anomalous diffusion by chaotic advection. Journal of Fluid Mechanics, 280, 149-172.

Kashid, M.N., Platte, F., Agar, D.W. and Turek, S., 2007. Computational modelling of slug flow in a capillary microreactor. Journal of Computational and Applied Mathematics, 203(2), 487-497.

Kee, R.J., Almand, B.B., Blasi, J.M., Rosen, B.L., Hartmann, M., Sullivan, N.P., Zhu, H., Manerbino, A.R., Menzer, S., Coors, W.G. and Martin, J.L., 2011. The design, fabrication, and evaluation of a ceramic counter-flow microchannel heat exchanger. Applied Thermal Engineering, 31(11), 2004-2012.

Khalil, A.M., Fateen, S.E.K. and Bonilla-Petriciolet, A., 2016. Gravitational search, monkey, and krill herd swarm algorithms for phase stability, phase equilibrium, and chemical equilibrium problems. Chemical Engineering Communications, 203(3), 389-406.

Khirani, S., Kunwapanitchakul, P., Augier, F., Guigui, C., Guiraud, P. and Hébrard, G., 2011. Microbubble generation through porous membrane under aqueous or organic liquid shear flow. Industrial & Engineering Chemistry Research, 51(4), 1997-2009.

Kiessling, F., Fokong, S., Koczera, P., Lederle, W. and Lammers, T., 2012. Ultrasound microbubbles for molecular diagnosis, therapy, and theranostics. Journal of nuclear medicine, 53(3), 345-348.

Kreutzer, M.T., Kapteijn, F., Moulijn, J.A., Kleijn, C.R. and Heiszwolf, J.J., 2005. Inertial and interfacial effects on pressure drop of Taylor flow in capillaries. AIChE Journal, 51(9), 2428-2440.

Kukizaki, M. and Goto, M., 2007. Spontaneous formation behavior of uniform-sized microbubbles from Shirasu porous glass (SPG) membranes in the absence of water-phase flow. Colloids and Surfaces A: Physicochemical and Engineering Aspects, 296(1), 174-181.

Kumacheva, E. and Garstecki, P., 2011. Methods for the Generation of Polymer Particles. Microfluidic Reactors for Polymer Particles, 7-15.

Kumagai, I., Takahashi, Y. and Murai, Y., 2015. Power-saving device for air bubble generation using a hydrofoil to reduce ship drag: theory, experiments, and application to ships. Ocean Engineering, 95, 183-194.

Leng, Y., 2008a. Light Microscopy Materials Characterization (1-44): John Wiley & Sons (Asia) Pte Ltd.

Leonard, B.P., 1991. The ULTIMATE conservative difference scheme applied to unsteady one-dimensional advection. Computer methods in applied mechanics and engineering, 88(1), 17-74.

Liu, R.H., Stremler, M.A., Sharp, K.V., Olsen, M.G., Santiago, J.G., Adrian, R.J., Aref, H. and Beebe, D.J., 2000. Passive mixing in a three-dimensional serpentine microchannel. Journal of microelectromechanical systems, 9(2), 190-197.

Logan, D.L., 2011. A first course in the finite element method. Cengage Learning.

Maesumi, B.L. and Mcbryan, O., 1988. Pages: 89-103 Article Author: P. Daripa, J. Glimm, M. Month, 89-103.

Mahalingam, S., Raimi-Abraham, B.T., Craig, D.Q. and Edirisinghe, M., 2015. Formation of protein and protein-gold nanoparticle stabilized microbubbles by pressurized gyration. Langmuir, 31(2), 659-666.

Makuta, T., Suzuki, R. and Nakao, T., 2013. Generation of microbubbles from hollow cylindrical ultrasonic horn. Ultrasonics, 53(1), 196-202.

McDonald, J. C., & Whitesides, G. M. (2000). Fabrication of microfluidic systems in poly(dimethylsiloxane). Electrophoresis, 21(1), 27-40.

Methven, J. and Hoskins, B., 1999. The advection of high-resolution tracers by low-resolution winds. Journal of the atmospheric sciences, 56(18), pp.3262-3285.

Moretti, G., 1987. Computation of flows with shocks. Annual Review of Fluid Mechanics, 19(1), 313-337.

Mukumoto, M., Ohshima, T., Ozaki, M., Konishi, H., Maeda, N. and Nakamura, Y., 2012. Effect of microbubbled water on the removal of a biofilm attached to orthodontic appliances—An in vitro study—. Dental materials journal, 31(5), 821-827.

Mustin, B. and Stoeber, B., 2008, June. Design considerations for robust suspension-based microfluidic systems for biomedical applications. In Mixed-Signals, Sensors, and Systems Test Workshop, 2008. IMS3TW 2008. IEEE 14th International (1-6). IEEE.

Muzaferija, S., 1998. A two-fluid Navier-Stokes solver to simulate water entry. In Proc. of the 22nd Symp. on Naval Hydro..

Nie, Z. et al., 2008. Emulsification in a microfluidic flow-focusing device: effect of the viscosities of the liquids. Microfluidics and Nanofluidics, 5(5), 585–594

Nguyen, N.T., Lassemono, S. and Chollet, F.A., 2006. Optical detection for droplet size control in microfluidic droplet-based analysis systems. Sensors and actuators B: Chemical, 117(2), 431-436.

Noh, W.F., Woodward, P. (1976) SLIC (Simple Line Interface Calculation). In proceedings of 5th International Conference of Fluid Dynamics, edited by A. I. van de Vooren & P.J.

NUMAKURA, T., KASHIWAGURA, K. and MAKUTA, T., 2014. Development and Optimization of a Microbubble Generator with a Hollow Cylindrical Ultrasonic Horn. Journal of the Japanese Society for Experimental Mechanics, 14(Special_Issue), 52-56.

Olsson, E., Kreiss, G. (2005) A conservative level set method for two phase flow. Journal of Computational Physics, 210(2005): 225–246

Osher, S. and Sethian, J.A., 1988. Fronts propagating with curvature-dependent speed: algorithms based on Hamilton-Jacobi formulations. Journal of computational physics, 79(1), 12-49.

Oskooei, S.A.K. and Sinton, D., 2010. Partial wetting gas–liquid segmented flow microreactor. Lab on a Chip, 10(13), 1732-1734.

Ottino, J.M., 1989. The kinematics of mixing: stretching, chaos, and transport (Vol. 3). Cambridge university press.

Parhizkar, M., Edirisinghe, M. and Stride, E., 2013. Effect of operating conditions and liquid physical properties on the size of monodisperse microbubbles produced in a capillary embedded T-junction device. Microfluidics and nanofluidics, 14(5), 797-808.

Park, J.I. et al., 2010. Small, stable, and monodispersed bubbles encapsulated with biopolymers. Macromolecular Rapid Communications, 31(2), 222–227

Patankar, S.V., 1980. Numberical Heat Transfer and Fluid Flow, Hemisphere, Washington, DC

Pawell, R.S., Inglis, D.W., Barber, T.J. and Taylor, R.A., 2013. Manufacturing and wetting low-cost microfluidic cell separation devices. Biomicrofluidics, 7(5), 056501.

Peskin, C.S., 1977. Numerical analysis of blood flow in the heart. Journal of computational physics, 25(3), 220-252.

Power, H. and Wrobel, L.C., 1995. Boundary integral methods in fluid mechanics. Computational mechanics.

Prevenslik, T., 2011. Stability of nanobubbles by quantum mechanics. In Proceedings of conference Topical Problem of Fluid Mechanics (113-116).

Qian, D. and Lawal, A., 2006. Numerical study on gas and liquid slugs for Taylor flow in a T-junction microchannel. Chemical Engineering Science, 61(23), 7609-7625.

Quintanar-Guerrero, D., 1998. Preparation techniques and mechanisms of formation of biodegradable nanoparticles from preformed polymers. Drug Dev Ind Pharm, 24(12), 1113-1128.

Richtmyer, R.D. and Morton, K.W., Difference methods for initial-value problems. 1967. Interscience, New York.

Rong, S., Chen, B., 2010. Numerical Simulation of Taylor Bubble Formation in Micro-channel by MPS Method. Microgravity Science and Technology, 22(3): 321–327

Santos, R.M. and Kawaji, M., 2010. Numerical modeling and experimental investigation of gas–liquid slug formation in a microchannel T-junction. International Journal of Multiphase Flow, 36(4), 314-323.

Schneider, C.A., Rasband, W.S. and Eliceiri, K.W., 2012. NIH Image to ImageJ: 25 years of image analysis. Nature methods, 9(7), 671-675.

Sethian, J.A. and Wiegmann, A., 2000. Structural boundary design via level set and immersed interface methods. Journal of computational physics, 163(2), 489-528.

Sethian, J.A., 1999. Level set methods and fast marching methods: evolving interfaces in computational geometry, fluid mechanics, computer vision, and materials science (Vol. 3). Cambridge university press.

Shapira, Y., 2008. Matrix-based multigrid: theory and applications (Vol. 2). Springer Science & Business Media.

Sirsi, S., Borden, M., 2009. Microbubble Compositions, Properties and Biomedical Applications. Bubble Science, Engineering & Technology, 1(1-2), 3–17

Smolianski, A., 2001. Numerical modeling of two-fluid interfacial flows. University of Jyväskylä.

Solomon, T., 2015. Chaos and chaotic fluid mixing.

Stride, E., Porter, C., Prieto, A.G. and Pankhurst, Q., 2009. Enhancement of microbubble mediated gene delivery by simultaneous exposure to ultrasonic and magnetic fields. Ultrasound in medicine & biology, 35(5), 861-868.

Stride, E., Edirisinghe, M., 2008. Novel microbubble preparation technologies. Soft Matter, 4(12), 2350–2359

Stroock, A.D., Dertinger, S.K., Ajdari, A., Mezić, I., Stone, H.A. and Whitesides, G.M., 2002. Chaotic mixer for microchannels. Science, 295(5555), 647-651.

Suslick, K.S., 1990. Sonochemistry. science, 247(4949), 1439-1446.

Tabeling, P., & Chen, S., 2010. Introduction to Microfluidics: OUP Oxford.

Tryggvason, G., Bunner, B., Esmaeeli, A., Juric, D., Al-Rawahi, N., Tauber, W., Han, J., Nas, S. and Jan, Y.J., 2001. A front-tracking method for the computations of multiphase flow. Journal of Computational Physics, 169(2), 708-759.

Umbanhowar, P. B., Prasad, V., & Weitz, D. A., 2000. Monodisperse Emulsion Generation via Drop Break Off in a Coflowing Stream. Langmuir, 16(2), 347-351.

Unger, E.C., Hersh, E., Vannan, M., Matsunaga, T.O. and McCreery, T., 2001. Local drug and gene delivery through microbubbles. Progress in cardiovascular diseases, 44(1), 45-54.

Van Loo, S., Stoukatch, S., Kraft, M. and Gilet, T., 2016. Droplet formation by squeezing in a microfluidic cross-junction. Microfluidics and Nanofluidics, 20(10), 146.

Wan, J. and Stone, H.A., 2011. Coated gas bubbles for the continuous synthesis of hollow inorganic particles. Langmuir, 28(1), 37-41.

Wan, J. and Stone, H.A., 2010. Microfluidic generation of a high volume fraction of bubbles in droplets. Soft Matter, 6(19), 4677-4680.

Wang, K., Xie, L., Lu, Y. and Luo, G., 2013. Generating microbubbles in a co-flowing microfluidic device. Chemical Engineering Science, 100, 486-495.

White, F.M., 1999. Fluid mechanics, WCB. Ed McGraw-Hill Boston.

Xiong, R., Bai, M. and Chung, J.N., 2007. Formation of bubbles in a simple co-flowing micro-channel. Journal of Micromechanics and Microengineering, 17(5), 1002.

Xu, S., Nie, Z., Seo, M., Lewis, P., Kumacheva, E., Stone, H.A., Garstecki, P., Weibel, D.B., Gitlin, I. and Whitesides, G.M., 2005. Generation of monodisperse particles by using microfluidics: control over size, shape, and composition. Angewandte Chemie, 117(5), 734-738.

Xu, Q., Nakajima, M., Ichikawa, S., Nakamura, N. and Shiina, T., 2008. A comparative study of microbubble generation by mechanical agitation and sonication. Innovative food science & emerging technologies, 9(4), 489-494.

Xu, J.H., Li, S.W., Chen, G.G. and Luo, G.S., 2006a. Formation of monodisperse microbubbles in a microfluidic device. AIChE journal, 52(6), 2254-2259.

Xu, J.H., Li, S.W., Wang, Y.J. and Luo, G.S., 2006. Controllable gas-liquid phase flow patterns and monodisperse microbubbles in a microfluidic T-junction device. Applied Physics Letters, 88(13), 133506.

Yamamoto, K. and Ogata, S., 2013. Effects of T-junction size on bubble generation and flow instability for two-phase flows in circular microchannels. International Journal of Multiphase Flow, 49, 24-30.

Yasuno, M., Sugiura, S., Iwamoto, S., Nakajima, M., Shono, A. and Satoh, K., 2004. Monodispersed microbubble formation using microchannel technique. AIChE journal, 50(12), 3227-3233.

Youngs, D.L. (1982) Time-dependent multi-material flow with large fluid distortion. Numerical Methods for Fluid Dynamics, 273–285.

Yu, Z., Hemminger, O. and Fan, L.S., 2007. Experiment and lattice Boltzmann simulation of two-phase gas–liquid flows in microchannels. Chemical Engineering Science, 62(24), 7172-7183.

Yue, J., Falke, F.H., Schouten, J.C. and Nijhuis, T.A., 2013. Microreactors with integrated UV/Vis spectroscopic detection for online process analysis under segmented flow. Lab on a Chip, 13(24), 4855-4863.

Yue, J., Luo, L., Gonthier, Y., Chen, G. and Yuan, Q., 2009. An experimental study of air–water Taylor flow and mass transfer inside square microchannels. Chemical Engineering Science, 64(16), 3697-3708.

Zandbergen, Lecture Notes in Physics 59, 330–340

Zhang, J., Yan, S., Yuan, D., Alici, G., Nguyen, N.-T., Ebrahimi Warkiani, M., & Li, W., 2016. Fundamentals and applications of inertial microfluidics: a review. Lab on a Chip, 16(1), 10-34.

Zhang, Y., Wang, L., 2009. Experimental investigation of bubble formation in a microfluidic t-shaped junction. Nanoscale and Microscale Thermophysical Engineering, 13(4), 228–242

Zhao, S., Wu, X., Wang, L., & Huang, Y., 2004. Electrospinning of ethyl–cyanoethyl cellulose/tetrahydrofuran solutions. Journal of Applied Polymer Science, 91(1), 242-246.

Zimmerman, W.B., 2006. Multiphysics modeling with finite element methods (Vol. 18). World Scientific Publishing Co Inc. (432)